PROCEEDINGS OF THE INTERNATIONAL SYMPOSIUM ON RELIABILITY OF MULTI-DISCIPLINARY ENGINEERING SYSTEMS UNDER UNCERTAINTY, TAIPEI, TAIWAN, DECEMBER 8-11, 2019

ISRMES2019

International Symposium on Reliability of Multi-Disciplinary Engineering Systems Under Uncertainty (ISRMES2019)

Proceedings

Edited by

Shi-Shuenn Chen
Distinguished Professor,
National Taiwan University of Science and Technology, Taiwan

Alfredo H-S. Ang
Emeritus Chair Professor, University of California, Irvine, USA

Publication Date: June, 2020

Published by: National Taiwan University of Science and Technology (Taiwan Tech)
Address: No. 43, Sec. 4, Keelung Rd., Taipei 106, Taiwan, R.O.C.
E-mail : tbtc@mail.ntust.edu.tw
Website: http://www.ntust.edu.tw

ISBN: 978-986-98537-1-2 (pbk)

Table of Contents

Organized Sessions

Session Topic: Structural Resilience and Reliability

Session Topic: Engineering System Risks Under Extreme Storm Conditions

Session Topic: Reliability-Based Codes for Design and Maintenance

Preface

The International Symposium on Reliability of Multi-disciplinary Engineering Systems under Uncertainty, held on 8-11 December 2019, is organized by the National Taiwan University of Science and Technology (Taiwan Tech) in Taipei, Taiwan.

The performance reliability and safety of built infrastructure systems are issues that are of major concern to all disciplines of engineering. Invariably, the determination of the reliability or safety of any engineering system must be considered or evaluated under conditions of uncertainty, and thus requires quantitative assessment in terms of probability. Since such issues are common and important in all disciplines of engineering, the international symposium is organized to address many of the relevant issues related to major infrastructure systems. As engineers, our mission is to improve the public safety, facilitate the economic growth, and protect the environment as well as eco systems. With this international symposium, we hope to strengthen the consensus of all sectors of government, academy, industry, and research institutions.

This Symposium contains 14 keynote speeches and 10 organized sessions contributed by those from many parts of the world, including USA, Denmark, China, Japan, Korea, Singapore, Indonesia, Vietnam, Taiwan, etc. The total number of participants from the government, the academia and the industry are expected to be more than 200.

The Symposium is held under the sponsorship of the Ministry of Education, the Ministry of Science and Technology, the Taiwan Tech, and a number of supporting organizations. In particularly, the faculty and staff of the Department of Civil and Construction Engineering and Taiwan Building Technology Center (TBTC) are responsible for the Secretariat of the Symposium.

Finally, I would like to express my sincere gratitude to all the keynote speakers, the session organizers, the authors, the sponsors, and the participants for their contributions; to the members of the Steering Committee, the International Scientific Committee, and the Local Organizing Committee for their devoted time and efforts that makes ISRMES2019 a successful event.

Prof. Shi-Shuenn Chen
Symposium Chair

Organizing Committees

Steering Committee

Prof. Shi-Shuenn Chen	Former President & Director of TBTC, Taiwan Tech, Chair
Mr. Jeou-Rong Yan	Deputy Minister of Public Construction Commission, Executive Yuan, Advisory-Chair
Mr. R.J. Wang	Director, Architecture and Building Research Institute, Ministry of the Interior, Advisory-Chair
Prof. I-Tung Yang	Chairman, Department of Civil and Construction Engineering, Taiwan Tech, Co-Chair
Prof. Alfredo H-S. Ang	University of California, USA
Prof. Liang-Jenq Leu	President, Taiwan Construction Research Institute, Taiwan
Prof. Shyh-Jiann Hwang	Director, National Center for Research on Earthquake Engineering, Taiwan
Prof. Hongey Chen	Director, National Science and Technology Center for Disaster Reduction, Taiwan
Dr. Shen-Hsien Chen	Chairman, SINOTECH Engineering Consultants, LTD., Taiwan
Dr. Shun-Min Lee	President, CECI Engineering Consultants, Inc., Taiwan
Prof. Chung-Yue Wang	Department of Civil Engineering, National Central University, Taiwan
Prof. Kuo-Wei Liao	Department of Civil Engineering, for Sustainable Environment, National Taiwan University
Prof. Chien-Kuo Chiu	Vice Dean, College of Engineering, Taiwan Tech
Prof. Rwey-Hua Cherng	Department of Civil & Construction Engineering, Taiwan Tech
Prof. Min-Yuan Cheng	Department of Civil & Construction Engineering,

	Taiwan Tech
Prof. Jui-Sheng Chou	Department of Civil & Construction Engineering, Taiwan Tech
Prof. Ting-Yu Hsu	Department of Civil & Construction Engineering, Taiwan Tech
Prof. Jun-Yang Shi	Taiwan Building Technology Center, Taiwan Tech

International Scientific Committee

Prof. Alfredo H-S. Ang	University of California, USA, Chair
Prof. Dan Frangopol	Lehigh University, USA, Co-Chair
Prof. Shi-Shuenn Chen	Taiwan Tech, ex-officio
Prof. Bilal Ayyub	University of Maryland, USA
Prof. Jianbing Chen	Tongji University, China
Prof. David De Leon	Mexico State University, Mexico
Prof. Bruce Ellingwood	Colorado State University, USA
Prof. L. Esteva	National University of Mexico
Prof. M. Faber	Aalborg University, Denmark
Prof. H. Fujino	Yokohama University, Japan
Prof. H. Furuta	Kansai University, Japan
Prof. Paolo Gardoni	University of Illinois at Urbana-Champaign, USA
Prof. Huawei Huang	Tongji University, China
Prof. Armen Der Kiureghian	University of California at Berkeley, USA
Prof. Sang-Hyo H. Kim	Yonsei University, Korea
Prof. Hasan Kamal	Kuwait University, Kuwait
Prof. Jie Li	Tongji University, China
Prof. X.L. Liu	Jaio-Tung University, China
Prof. Zhao-Hui Lu	Central South University, China

Prof. R. Melcher	University of Newcastle, Australia
Prof. K.K. Phoon	National University of Singapore, Singapore
Prof. S.T. Quek	National University of Singapore, Singapore
Prof. John Dalsgaard Sørensen	Aalborg University, Denmark
Prof. Junho Song	Seoul National University, Korea
Prof. P.D. Spanos	Rice University, USA
Prof. H. K. Tung	Hong Kong University of Science & Technology, Hong Kong
Prof. C.B. Yun	Zhejiang University, China
Prof. Yangang Zhao	Kanagawa University, Japan
Prof. Limin. Zhang	Hong Kong University of Science & Technology, Hong Kong, China
Prof. Jeng-Tzong Chen	Department of Harbor and River engineering, National Taiwan Ocean University
Prof. Jianye Ching	Department of Civil Engineering, National Taiwan University

Local Organizing Committee

Prof. I-Tung Yang	Chair, Taiwan Tech
Prof. Chien-Kuo Chiu	Co-Chair, Taiwan Tech
Prof. Ting-Yu Hsu	Co-Chair, Taiwan Tech
Prof. Chao-Lung Hwang	Taiwan Tech
Prof. Cheng-Cheng Chen	Taiwan Tech
Prof. Rwey-Hua Cherng	Taiwan Tech
Prof. Chun-Tao Chen	Taiwan Tech
Prof. Min-Yuan Cheng	Taiwan Tech
Prof. Jun-Yang Shi	Taiwan Tech
Prof. Yin-Nan Huang	National Taiwan University

Prof. Yu-Chen Ou	National Taiwan University
Prof. Kuo-Hsin Yang	National Taiwan University
Prof. Po-Hua Albert Chen	National Taiwan University
Prof. Kuang-Yen Liu	National Cheng Kung University
Prof. Chien-Cheng Chou	National Central University
Prof. Tzu-Kang Lin	National Chiao Tung University
Prof. Rong-Yau Hwang	Taiwan Construction Research Institute
Prof. Cheng Tao Yang	National Center for Research on Earthquake Engineering

List of Organizers & Sponsors

Organizers

National Taiwan University of Science and Technology (NTUST), Taiwan Tech

Taiwan Building Technology Center, NTUST, Taiwan Tech

Department of Civil and Construction Engineering, NTUST, Taiwan Tech

Sponsors

Ministry of Education

Ministry of Science and Technology

Co-Sponsors

International Association for Structural Safety and Reliability

International Association for Life Cycle Civil Engineering

International Association for Bridge Maintenance and Safety

Architecture and Building Research Institute, MOI (ABRI)

Taiwan Construction Research Institute(TCRI)

The Chinese Institute of Engineers (CIE)

Chinese institute of Civil and Hydraulic engineering

Chinese Union of Professional Civil Engineers Association

Taipei Professional Civil Engineers Association

Taiwan Regional Engineering Contractors Association (TRECA)

CTCI Education Foundation

CTCI Foundation

CASTO Engineering Consultants Co., Ltd.

Sinotech Engineering Consultants. LtdCECI Engineering Consultants, Inc., Taiwan

Keynote Lectures

RELIABILITY-BASED OPTIMAL DESIGN OF CIVIL INFRASTRUCTURE SYSTEMS

Alfredo H-S. Ang

Professor Emeritus, University of California, Irvine, USA

RELIABILITY-BASED APPROACH FOR OPTIMAL DESIGN OF INFRASTRUCTURE SYSTEMS

Alfredo H-S Ang
University of California, Irvine, CA, USA
E-mail: ahang2@aol.com

Abstract: Optimality in the design of engineering systems is invariability one of the primary objectives of engineering design. For aerospace systems minimum weight is of primary concern, whereas for civil structures or infrastructure minimum cost is invariably a more mundane objective.

Optimality, of course, must be achieved subject to a specified level of safety or reliability. In this regard, the reliability-based design of structural components has been well established. However, the reliability-based design of structures as a complete system remains an issue that has not been addressed adequately. This issue requires the assessment of the system reliability of a complete structure, considering the effects of both the aleatory and epistemic types of uncertainty. Proposed is a systematic approach for this purpose. The main issue can be addressed effectively using the PDEM (probability density evolution method) for the effects of the aleatory uncertainty, resulting in the PDF of the critical state of a system. The effects of the epistemic uncertainty can be included systematically as the error in the estimation of the critical state of the system.

Two examples of complex systems demonstrate the effectiveness of the method; namely (1) the minimum life-cycle cost aseismic design of an existing high-rise building in Mexico City; and (2) the optimal design of high voltage transmission towers for life-cycle performance and reliability in China.

Keywords: Optimal design, reliability-based design, life-cycle cost, 3D finite element models

1 Introduction

Optimal design is a major goal in the design of engineering systems. Reliability-based optimal design of engineering systems, including structures must take into account the complexity of the engineering system, such as the response of a structure when subjected to imposed loadings that may include static loads (structure's own weight), dynamic loads (earthquake or wind loads), and the deterioration of the system capacity with time and usage. The design must also resolve the effects of the underlying uncertainties (aleatory and epistemic types) in terms of the required allowable failure probability, or the corresponding specified reliability index. Moreover, the optimality goal or objective of the optimization process is paramount; this may be in terms of the minimum cost of the design for many civil engineering systems. The pertinent cost may be the life-cycle cost – that is, the total cost over the useful life of the system which would include the initial cost in its design and construction, its whole life maintenance cost that should include repair, retrofitting, and reconstruction in case of failure or serious damage, the chance of life loss and cost of injuries in the event of building damages, and related economic losses.

In the case of a structural system, there cannot be a uniform or prescribed standard for its optimal design. A procedure is needed, particularly for the design of a complete system. A practical procedure is proposed for the probabilistic approach for the reliability-based optimal design of a complete structure as a system. That is, the proposed procedure will determine the reliability-based safety index for the optimal design of a complete structure as a system.

2 On Optimal Structural System Design

Optimality in the design of structures depends on the field of application. For civil structures and infrastructure, cost of the structure may be a more mundane and important design goal, in particular design to achieve the minimum life-cycle cost may be most meaningful. That is, minimizing the total cost over the whole life of a structure.

2.1 Expected Life-Cycle Cost, E(LCC), of Structures

In minimizing the cost of a land-based structure, it is the expected whole life cost, or expected life-cycle cost, E(LCC), that is most pertinent. This should include all the cost items over the life (normally >40-50 years) of the structure. Specifically, the total E(LCC) would consist of the following expected costs:

$$C_T = C_I + C_M + C_S \tag{1}$$

where, C_I = the initial cost, including the design and construction costs;

C_M = the cost of *maintenance*, including the costs of inspection and repair, potential damage and failure or reconstruction, retrofit and demolition, etc;

C_S = social cost, including possible loss of lives, injuries, loss of revenues.

For consistency, all cost items must be transformed or expressed in "present value" taking into account the discount rate of the region under consideration.

Graphically, all the expected life-cycle cost items can be displayed as shown in Figure 1 which shows the E(*LCC*) versus the mean safety index E(β) used in the design of the structure. Observe that the initial cost, C_I, increases monotonically with increasing mean safety index, whereas the maintenance cost plus the social cost, $C_M + C_S$, will decrease monotonically with increasing mean safety index. The sum of these two cost items will give the total expected life-cycle cost, from which the mean safety index that will yield the minimum E(*LCC*) design can be identified.

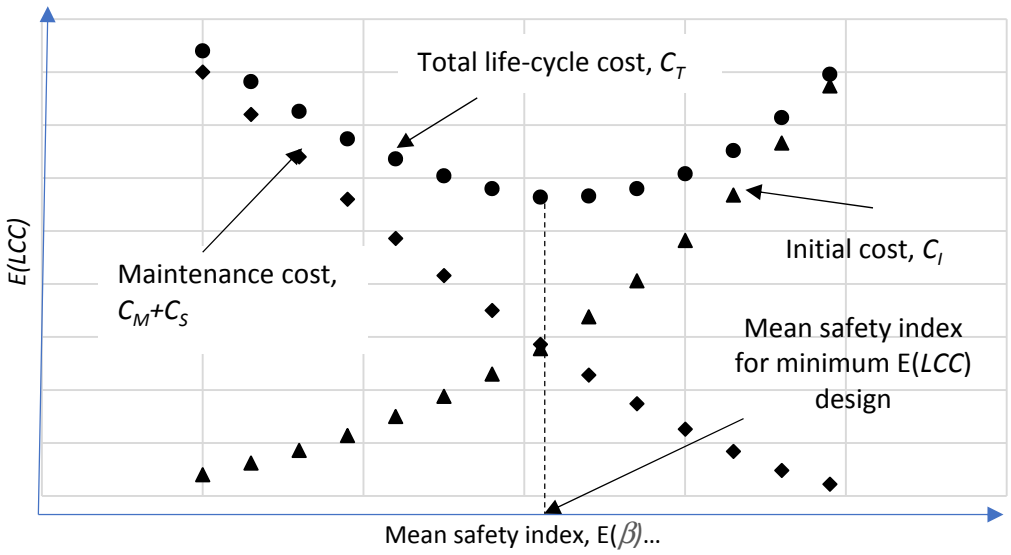

Figure 1. E(*LCC*) versus mean safety index for respective cost items

2.2 Practical Procedure for Determining the Optimal Design

To determine the structural design with the minimum expected life-cycle cost, E(*LCC*), proceed to design the structure with varying design safety indices, β, and estimate the corresponding E(*LCC*). Plot the resulting designs as shown in Figure 1 displaying the total life-cycle cost, C_T , of the various specific designs. From Figure 1, the optimal design with the minimum E(*LCC*) and corresponding mean β can be identified.

2.2.1 Confidence Level Appropriate for Optimal Design of Engineering Systems

The reliability index for design is a random variable associated with a cumulative probability or "confidence level". An important remaining question for the optimal approach is "what confidence level is appropriate for specifying the reliability or safety index for the design of the complete system?" This is the key question for the design of a complex structure as a system.

The answer to this important question, depends on the confidence levels that underlie good professional practice; particularly in the successful design of existing major critical systems. In this regard, and for this purpose, consider the following.

Design of Offshore Oil Production Platforms -- The industry standards (American Petroleum Institute, 1993; and the Mexican PEMEX, 2000) for the design of offshore oil production platforms require the safety index for the design of such production platforms to be within β = 3.3 – 3.5

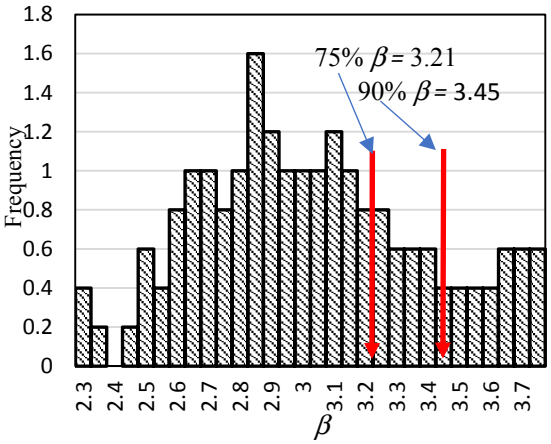

Figure 2. Histogram *of* β for minimum expected life-cycle cost design

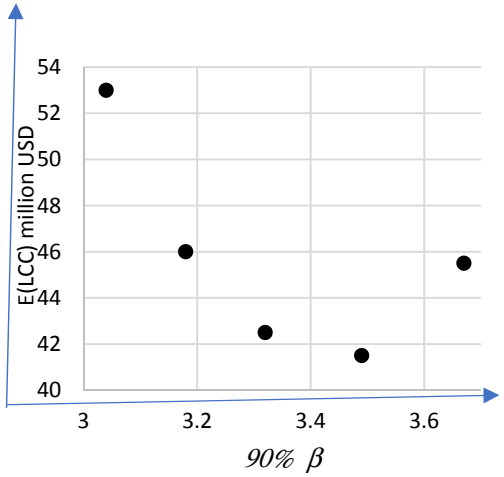

Figure 3. 90% β versus expected life-cycle cost E(*LCC*)

In the study of life-cycle cost (*LCC*) design of offshore platforms, De Leon and Ang (2008) showed the histogram of β for the minimum *LCC* design in Figure 2. Whereas Figure 3 summarizes the 90% β for different designs with an optimal 90% β = 3.45. Clearly, in the case of offshore production platforms, designing with a safety index associated with a confidence level of 90% is consistent with good professional practice, i.e., within β = 3.3 – 3.5.

Design of Cable-Stayed Bridges – In the case of the design of cable-stayed bridges, Han and Ang

(2008) have shown that a confidence between 90%-95% for optimal design is also consistent with good professional practice.

3 Illustrated Examples of Optimal System Design

3.1 Example 1: Optimal Design of High-Rise Reinforced Concrete Buildings

For examples of complex systems, consider first the 15-story reinforced concrete building in Mexico City shown in Figure 4; its three dimensional finite element model (3D FEM) is shown in Figure 5.

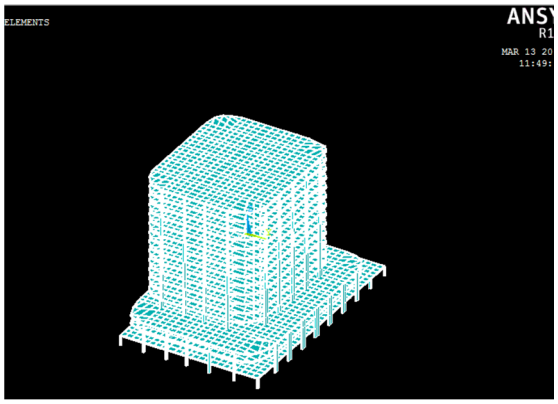

Figure 4. A 15-Story R/C building in Mexico City

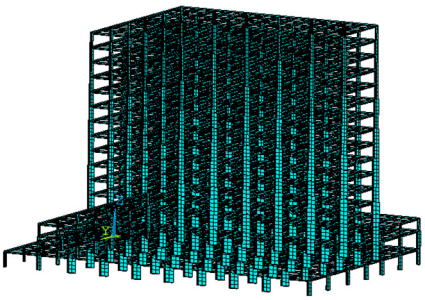

Figure 5. 3D FEM of 15-story building

The building was subjected to the Mexico earthquake of 1985; the two directions (EW and NS) of the earthquake ground motions are shown in Figure 6.

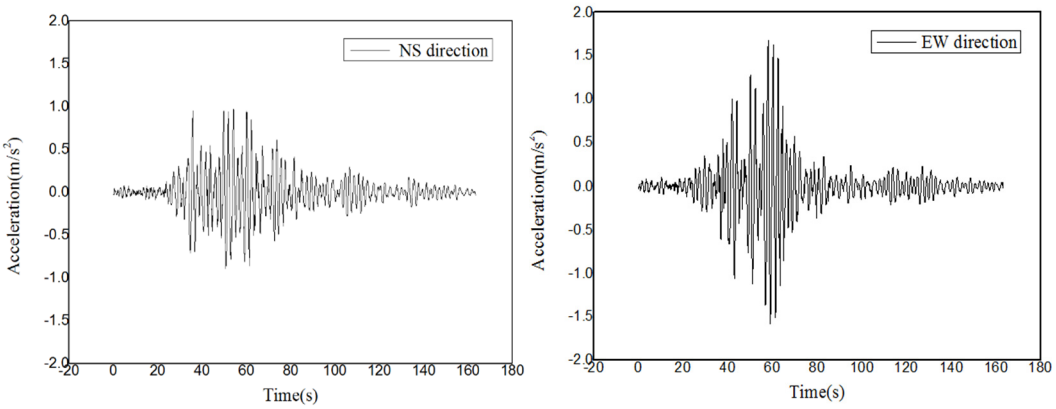

Figure 6. The 2 directions of ground motions

3.1.1 Response Analysis and Optimal Design of Building

For this building, the calculations of its response with the 3D FEM model of the building is highly complex. The number of finite elements is over 72,000, and the total number of nodes and dofs are over 63,000 and 200,000, respectively, for the 3D model used in the response analysis.

With the PDEM (Li and Chen, 2007), 135 representative points or samples of deterministic building responses, with their respective probabilities, were used to obtain the PDF of the ultimate

performance function, Z_{max} of the building response as shown in Figure 7 (with twin modes); and the mean safety index β = 2.63. This PDF represents only the effect of the underlying aleatory uncertainty. The same response result can be modeled approximately with the fitted lognormal PDF with a mean value of 0.9 and standard deviation of 0.035 (also shown in Figure 7); the corresponding mean safety index of the fitted lognormal PDF would be β = 2.73.

For this example, assume that the epistemic uncertainty (representing the inaccuracy of the mean-value of Z_{maxx}) can be modeled also with a lognormal PDF with a mean-value of 1.0 and a c.o.v. of 0.10. By convolution integration of this lognormal PDF and the lognormal PDF of the aleatory uncertainty with a mean of 0.9 and standard deviation of 0.035, then yields the histogram of all possible values of the safety index for the 15-story building as shown in Figure 8.

On Effectiveness of the PDEM – The effectiveness of the PDEM can be demonstrated in this example. In this regard, observed the following:

- Only 135 sample points, with corresponding associated probabilities, of the building responses were used to calculate the reliability for each case of the building design. For each case, the solution by PDEM is performed with the Dirac δ sequence method (Fan, Chen, Li, 2009).
- To verify the accuracy with this small sample size of 135, calculations with 226 sample points were also performed for the case of the original as-built building design – the results are as follows: with 135 sample points, the range of safety index with 90% to 95% confidence is β = 3.05-3.18, whereas with 226 sample points, the corresponding range of the safety index is β = 3.07-3.20.
- The difference between the results for the two sample sizes is around 0.6%, indicating that with only 135 sample points for the original case, gives reasonably accurate safety indices for the 15-story building. It is reasonable to assume that the other cases of the same building will have the same accuracy

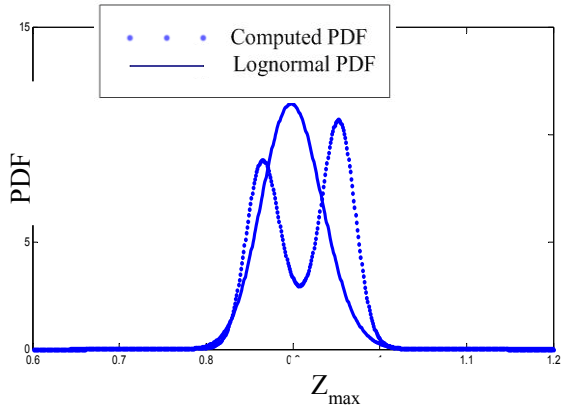

Figure 7. Computed PDF of Z_{max} of the building and corresponding fitted lognormal PDF

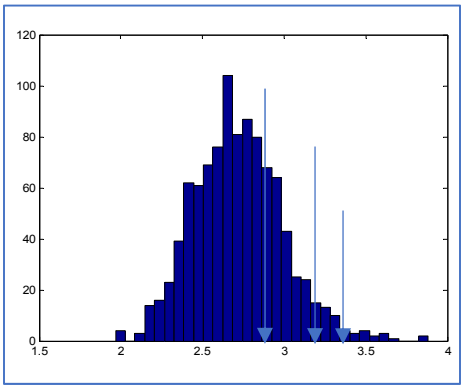

Figure 8. Histogram of β of the 15-story building

The main statistics of the histogram in Figure 8 can be summarized a follows:

Mean β = 2.72

90% confidence β = 3.05

95% confidence β = 3.18

Similar PDEM calculations were performed for the same building with different percentages of the original building design; namely, 80%, 90%, 95%, and 105%, 110%, 120%, 130% of the original as-built structure. The results of all these cases, namely the safety indices β together with the corresponding expected life-cycle costs, E(*LCC*) in million U.S. dollars, are summarized below in Table 3.

Table 3. Safety Index β and E(*LCC*) for all cases

Case (% of original)*	80%	90%	95%	100%	105%	110%	120%	130%
Mean E(*LCC*) **	0.023 876	0.465 576	1.71 82.86	2.72 11.24	2.85 9.59	2.99 8.46	3.31 7.34	3.74 7.21
90% conf. E(*LCC*)**	0.025 875	0.524 539	1.91 55.14	3.05 7.46	3.23 6.80	3.39 6.59	3.71 6.69	4.22 7.07
95% conf. E(*LCC*)**	0.026 874	0.545 526	2 45.67	3.18 6.73	3.37 6.36	3.55 6.30	3.87 6.60	4.39 7.05

*in percentage capacity of the original as-built structure

**in million U.S. dollars

Plots of the safety index β (for 90% and 95% confidences) versus the corresponding E(*LCC*), are shown below in Figures 9 and 10, respectively.

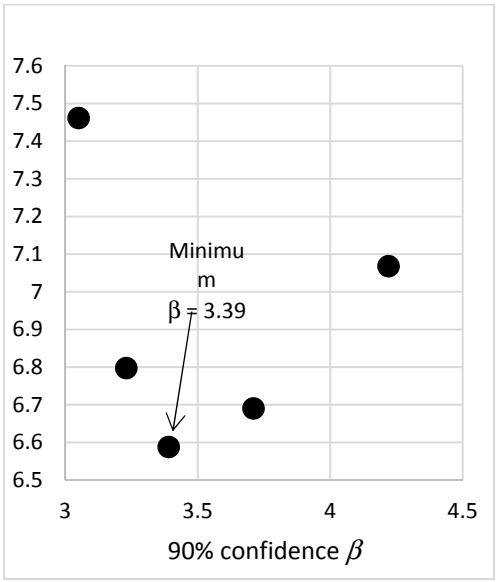

Figure 9. Designs with 90% confidence β versus respective E(*LCC*)

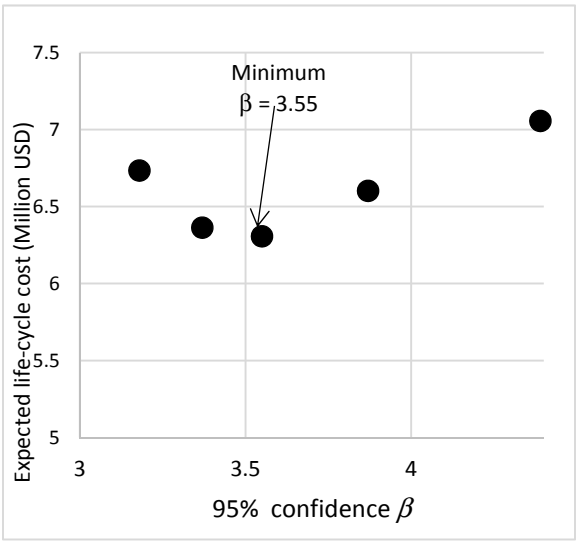

Figure 10. Designs with 95% confidence β versus respective E(*LCC*)

Figures 9 and 10 clearly show that with 90%-95% confidence, the optimal design of the 15-story building would have required a safety index of β = 3.39-3.55 which is 110% of the original building design (see column marked in red) in Table 3; i.e., to obtain the minimum E(*LCC*) design would require 110% capacity of the original as-built building. Observe also from Table 3 (column marked in blue), that the original as-built structure was designed with a safety index of β = 3.05-3.18

with the same 90%-95% confidence.

3.2 Example 2: Optimal Design of Electrical Transmission Towers

The same procedure is applied and illustrated for the design of high-voltage electrical transmission towers (Ang, Wan, and Chen). Such a tower-line structural system is shown in Figure 11. It is shown as a single-tower-two-lines model. The major loading on the transmission tower-line is wind. The height of the transmission tower is 76.5m, whereas the span distance between 2 adjacent towers is 400m. The materials for the tower include Chinese steel of Q235, Q345 and Q420, whereas the material for the transmission line is 4×LGJ-400/35.

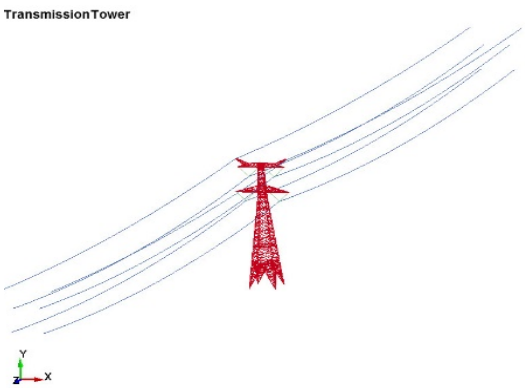

Figure 11. Typical high-voltage transmission tower

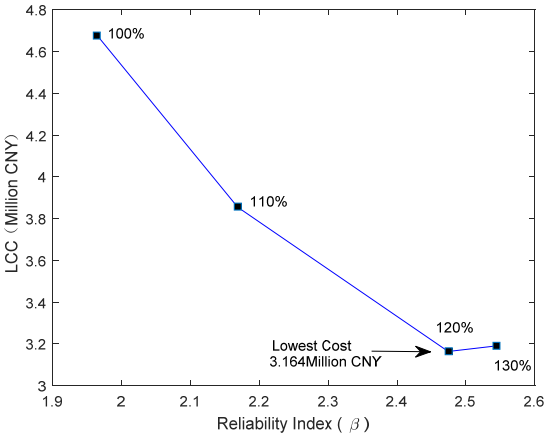

Figure 12. Life-cycle cost versus reliability index

3.2.1 The Optimal Tower Design

In this case, four alternative designs of the transmission tower were examined; namely 100%, 110%, 120%, and 130% of the standard design. The total expected life-cycle cost of each design is:

$$C_T = C_I + C_D + C_S$$

or

$$C_T = C_I \times \mathrm{RF} + C_M + (C_R + C_{DP}) \times P_f \times \mathrm{PVF} \qquad (2)$$

where, C_I = present cost of the standard original design;
RF = the ratio of the standard design; i.e., 1.00, 1.10, 1.20 and 1.30;
P_f = the collapse probability of the tower;
PVF = the present-value factor $= \{1-\exp(-\alpha L)\}/(\alpha L)$;
in which $\alpha = \ln(1+i_R)$, and i_R = the annual discount rate; L = the service life of the structure.

The sum of the two cost items, $C_I + C_D$, will give the total expected life-cycle cost E(LCC). Figure 12 shows the E(LCC) versus the reliability index β for the alternative designs that were examined, from which the reliability index of β = 2.47 that will yield the minimum expected life-cycle cost design with E(LCC) = 3.164 million (Chinese yuan) can be determined as shown in Figure 12.

From Figure 12, observe that this optimal design is 1.20% of the standard design. The PDF of the corresponding $Z_{max,}$ based on the energy criterion (Xu and Li, 2015), is shown in Figure 13 with its corresponding fitted lognormal PDF. It should be emphasized that the results in Figure 13 is strictly due to the effect of the aleatory uncertainty.

For design, the effect of the epistemic uncertainty must be included. Assuming an epistemic uncertainty of 10%, represented by a lognormal PDF with a mean of 1.0 and a c.o.v. of 0.10, convolution integration of this lognormal PDF with the fitted lognormal PDF (approximating the Z_{max} of Figure 13) will yield the PDF of the reliability index of the tower, as shown in Figure 14 with the following values:

With 10% epistemic uncertainty	With 20% epistemic uncertainty
Mean value = 2.47	Mean value = 2.47
75% value =2.61	75% value =2.73
90% value = 2.78	90% value = 3.12

If the epistemic uncertainty is 20%, the corresponding mean, 75% and 90% values would be those given in the second column above. Figure 14 shows the respective histograms for the 10% and 20% epistemic uncertainties.

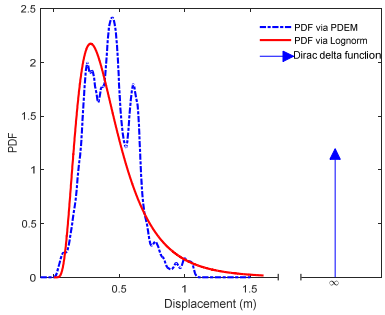

Figure 13. PDF of Z_{max} for collapse limit-state

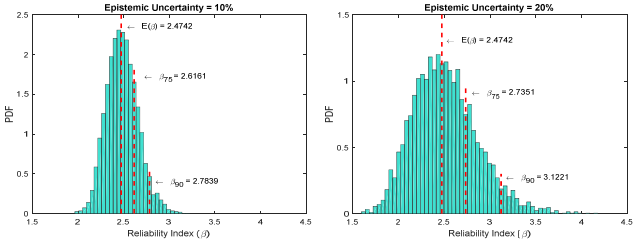

Figure 14. Two histograms of reliabiity indices with 10% and 20% epistemic uncertainties, respectively

4 Main Conclusions

Based on this study and with the two illustrative examples, the major conclusions can be summarized as follows:

1. For civil structures and infrastructure, minimum life-cycle cost is an important consideration in optimal design. Proposed is a systematic reliability-based approach for this purpose.

2. Engineering problems that are inherently three dimensional require 3D model idealizations; results obtained with 2D model idealizations could be mis-leading. As in the case of the 15-story building, the 3D model analysis shows that the optimal design could be 110% higher structural capacity and at 6% -12% lower E(*LCC*) than the as-built building (presumably designed with a 2D model).

3. The recently developed PDEM is a most effective numerical simulation method available for calculating the ultimate performance function of the relevant system due to the effects of the aleatory uncertainty of a system.

4. For design, the effects of the epistemic uncertainty must also be included. This can be

combined systematically and effectively with the effects of the aleatory uncertainty obtained by the PDEM .

5 Acknowledgements

The results of the two examples were based on work previously reported with international colleagues. In particular, the results for the 15-story building were obtained with the assistance of Prof. David de Leon of Tuluca, Mexico and Prof. Wenliang Fan of Chongqing, China; whereas the results for the power transmission tower were obtained with the assistance of Prof. Jianbing Chen and his colleagues of Tongji University, Shanghai, China. These assistances are gratefully acknowledged.

6 References Cited

Alfredo H-S. Ang, David de Leon, and Wenliang Fan, "Optimal Reliability-Based Aseismic Design of High-Rise Buildings", *XXI National Congress of Seismic Engineering*, Mexico City, 2018

A.H-S. Ang, Z. Wan, and JB Chen, "Optimal Design of High Voltage Transmission Towers for Life-Cycle Performance and Reliability", *Workshop in Shandong Jianzhu University*, China (in press)

American Petroleum Institute, "Recommended Practice for Planning, Designing and Constructing Fixed Offshore Platforms, Load and Resistance Factor Design", *API RP 2ª LRFD*, 1st Ed, July 1993, Washington, D.C.

D. De Leon, and A.H-S. Ang, "Confidence Bounds on Structural Reliability Estimations for Offshore Platforms", *Journal of Marine Science and Technology*, Vol. 13, No 3, 2008

Fan, W., Chen, JB., Li, J., "Solution of Generalized Evolution Equation via a Family of δ Sequences", *Computational Mechanics*, 43, pp.781-796, 2009

Han, S.H., and Ang, A. H-S., "Optimal Design of Cable-Stayed Bridges Based on Minimum Life-Cycle Cost" *Proceedings. IABMAS'08*, Seoul, Korea, 2008

J.Xu, J.Li. An Energy Criterion for Dynamic Instability of Structures Under Arbitrary Excitations. *International*

Journal *of Structural Stability & Dynamics*, 15(2), 1450043, 2015.

Jie Li and Jianbing Chen, *Stochastic Dynamics of Structures*, John Wiley & Sons, Singapore, 2009

PERFORMANCE-BASED ENGINEERING OF BUILDINGS FOR NATURAL HAZARDS: PRACTICAL IMPLEMENTATION OF RELIABILITY AND RISK-INFORMED DECISION

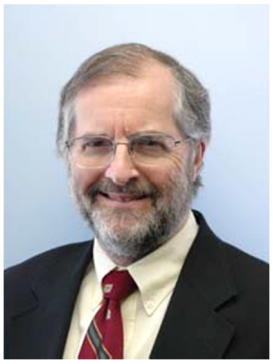

Bruce R. Ellingwood

Professor and College of Engineering Eminent Scholar,
Colorado State University, USA

PERFORMANCE-BASED ENGINEERING OF BUILDINGS FOR NATURAL HAZARDS

Practical Implementation of Reliability and Risk-informed Decision

Bruce R. Ellingwood, Ph.D., P.E., N.A.E.
Department of Civil and Environmental Engineering, Coloraco State University
Fort Collins, CO 80523 USA
bruce.ellingwood@colostate.edu

Abstract: Civil infrastructure facilities must be designed to withstand demands imposed by their service requirements and by environmental events such as windstorms or earthquakes. In an era of heightened public awareness of infrastructure performance and community resilience, structural engineers are seeking improvements to building and construction practices to achieve levels of performance beyond what currently is provided by prescriptive code provisions and to better meet owner, occupant and public expectations. This paper describes the new paradigm of performance-based engineering (PBE), which enables structural engineers to achieve more reliable control of civil infrastructure performance across a range of hazards, and has gained acceptance in earthquake engineering and fire-resistant structural design and, most recently, in wind engineering. Modern risk-informed decision tools will be essential to the successful implementation of PBE in providing a framework for managing the impact of uncertainties on performance and for guiding engineering decisions in an era of social and economic development, technological innovation and community resilience concerns.

Keywords: Buildings (codes), design (buildings), reliability, risk, structural engineering.

1 Introduction

While buildings and other structures designed by current prescriptive provisions usually possess adequate levels of safety, extreme environmental or man-made events may cause them to suffer severe damage and economic losses. In an era of heightened public awareness of infrastructure performance and community resilience, structural engineers are seeking improvements to building and construction practices to achieve levels of performance beyond what currently is provided by prescriptive code provisions and to better meet owner, occupant and public expectations. The new paradigm of *performance-based engineering (PBE)* enables structural engineers to achieve reliable control of civil infrastructure performance across a range of natural hazards. PBE has gained acceptance in earthquake engineering and fire-resistant structural design, where the incentives to seek alternatives to prescriptive methods are strongly economic in nature, and in design for disproportionate collapse resistance, where the shortcomings of traditional prescriptive approaches to design are immediately apparent. Recent developments in performance-based approaches to wind engineering and other hazards will ensure that competing hazards are addressed in a balanced manner and that investments in risk reduction are targeted appropriately within financial constraints. Finally, the international focus of engineers, social scientists and policy makers to enhance the resilience of urban communities against natural disasters [McAllister 2013] will necessitate new approaches toward performance-based engineering of buildings and other structures [McAllister 2016; Ellingwood et al 2019] and accelerate its development.

2 Performance-based engineering for buildings – current status

Performance-based engineering is aimed at providing a connection between the building design and the performance expectations of the owner and occupant [Hamburger 1996]. These expectations, of course, include the traditional engineering requirements for life safety that are embedded in current codes and standards, but often extend to monetary loss, disruption of service or loss of function. Specifying a level of expected performance to a given hazard scenario and quantifying the consequences to the owner if such a hazard were to occur provides a basis for more informed decisions for achieving the desired performance. The basic premises of PBE are that performance levels can be quantified and tailored to stakeholder needs; that engineering computation has advanced to the point where performance can be predicted analytically with sufficient confidence; that uncertainties can be modeled; and that risk can be managed at an acceptable level. Perhaps most important, PBE provides a vehicle for implementing risk-based concepts into structural design and for communicating risk among stakeholders in the building process and to the client. Indeed, modern probabilistic risk assessment methods are essential to the successful implementation of PBE, since they provide a framework for managing the impact of uncertainties on performance and guide engineering decisions in an era of technological innovation, competition and financial constraints.

The application of PBE is most mature in earthquake engineering and in fire engineering. Performance-based earthquake engineering in the United States has been supported over the past two decades by research on building seismic performance factors conducted by the Applied Technology Council (ATC), including ATC-63 (FEMA, 2009) and ATC-58 (FEMA, 2018), and implemented through *ASCE Standard 7-16* and *ASCE Standard 41-17* (ASCE, 2017). The motivation to adopt PBE for earthquake-resistant design is three-fold [Hamburger 1996]: to enhance building performance for clients who insist on a higher level of performance than is guaranteed by current code minimums; to better upgrade existing structures that are judged unsafe following an earthquake; and to limit the economic and social consequences of structural damage to communities following an earthquake. In fire engineering, the motivation is clearly economic. Fire protection traditionally has relied on component qualification testing [*ASTM Standard E119*; *ISO Standard 834]*, with acceptance criteria relying on survival to a "standard" fire for a prescribed rating period. Many of these test procedures have been in existence for nearly a century, and are archaic [NIST, 2009]. Perhaps most importantly, they focus on fires that are localized in compartments and do not address the impact of the fire on a structural system. As a result, many structural components and systems that are known to perform acceptably under realistic fire exposures are penalized or proscribed. The Society of Fire Protection Engineers [SFPE, 2007] and the European Convention for Constructional Steelwork [ECCS, 2001] have developed model performance-based fire engineering codes. Implementation of PBE for both fire and earthquake-resistant design generally requires an explicit consideration of the behavior of the structure as a system, an obvious departure from traditional prescriptive structural design methods based on individual member performance.

Most recent proposals for PBE distinguish levels of performance for different building categories where life safety or economic consequences differ. Historically codes and standards, including *ASCE Standard 7*, often have made such distinctions using an "importance factor" leading to a higher design load, a step that may not lead to better performance, especially when performance requires additional ductility rather than strength. PBE takes this relation to the next stage through a matrix, such as that in Table 1, in which the target reliabilities depend on

the building Risk Categories (designated by Roman numerals), ranging from negligible risk to life to post-disaster functioning, and on failure mode. Ordinary buildings fall within Risk Category II. PBE might require that a hospital (Risk Category IV) remain functional and provide continued service following an extreme event. In *ASCE Standard 7-16*, buildings designed by PBE must meet these performance targets, expressed in terms of reliability indices or annual probabilities. It should be noted that current prescriptive codes limit their focus (for ordinary building occupancies) to life safety. The role played by probability and structural reliability principles in the development of such a table is evident. The structural engineering profession is only beginning to consider other dimensions of risk, as described subsequently.

3 Performance-based engineering for buildings – new initiatives

Several new initiatives for PBE in the United States are pending. A first is in wind engineering, where a pre-standard for performance-based wind design [ASCE, 2019] recently has been developed by the Structural Engineering Institute of ASCE, as an alternative to the prescriptive procedures for wind design of buildings contained in *ASCE Standard 7*. This new activity is motivated, in part, by the damage to building construction and enormous economic losses suffered in Hurricanes Katrina (2005), Superstorm Sandy (2012) and the Tuscaloosa, AL and Joplin, MO tornados (2011) [NIST, 2014]. Although there are examples of limited uses of PBE for wind on a project-by-project basis, little information has found its way into practitioner usage, and performance requirements and acceptability criteria beyond the customary life safety objectives remain to be developed. This pre-standard is intended to resolve conflicts in performance objectives that exist with using prescriptive procedures for wind design or when using performance-based procedures originally developed in earthquake engineering. Major innovations include nonlinear dynamic analysis, limited inelasticity in the main wind force-resisting system [Chuang & Spence, 2019], system-based performance criteria [Mohammadi et al, 2018], enhanced criteria for designing the building envelope, a known area of vulnerability, and requirements to use wind tunnel testing to determine lateral wind forces.

Table 1. Acceptable reliability for non-earthquake events

Limit state	Risk category I (temp. storage)	Risk category II (normal)	Risk category III (public assembly)	Risk category IV (hospitals)
Benign	1.25×10^{-4} /yr β = 2.5	3.0×10^{-5} /yr β = 3.0	1.25×10^{-5} /yr β = 3.25	5.0×10^{-6} /yr β = 3.5
Sudden or severe	3.0×10^{-5} /yr β = 3.0	5.0×10^{-6} /yr β = 3.5	2.0×10^{-6} /yr β = 3.75	7.0×10^{-7} /yr β = 4.0
Sudden and severe	5.0×10^{-6} /yr β = 3.5	7.0×10^{-7} /yr β = 4.0	2.5×10^{-7} /yr β = 4.25	1.0×10^{-7} /yr β = 4.5

A second initiative is a proposed ASCE Standard for disproportionate collapse, with publication scheduled for later in 2020. The design requirements are based on the perceived *hazard*, and

the *vulnerability* of the building in the community, and *consequences* of total or partial collapse. The fundamental mathematical framework for assessing risk due to disproportionate collapse is provided by the following equation [e.g., Ellingwood, 2007; NIST 2007], which measures *consequences* in terms of annual losses (severe injury or death, direct damage costs, loss of opportunity costs, etc.):

$$\lambda_{Loss > c} = \Sigma_H \Sigma_{DS} \Sigma_D \, P[Loss > c|DS] P[DS|H] \, \lambda_H \quad (1)$$

in which λ_H = mean annual frequency of *hazard*, H; P[DS|H] = conditional probability of a damage state, DS, given the hazard, H; P[Loss >c|DS] = conditional probability that loss exceeds limit c, given damage state DS (often determined from insurance records); and $\lambda_{Loss > c}$ = mean annual frequency of losses that exceed a limit, c. The term P[DS|H] describes the *vulnerability* (or fragility) of the structural system to specific hazards and falls within the domain of structural engineering. The term $\lambda_{Loss > c}$, as a measure of *consequences*, is the *metric* of risk. Proper management of risk from disproportionate collapse to a civil infrastructure facility involves examining each of the terms in Eq (1). For purposes of standard implementation, Eq (1) is rewritten as,

$$\text{Risk} = \text{Hazard Likelihood x Vulnerability x Consequences} \quad (2)$$

and each of the terms is assigned an ordinal rank, based on the terms in Eq (1). The resulting risk is used to assign a *collapse-resistant design category (CRDC)*, similar to the *seismic design category (SDC)* stipulated in *ASCE Standard 7-16*, which determines the nature of the permissible structural systems and the design method(s) that can be used.

In the areas of hurricane storm surge and coastal inundation, current performance requirements are completely qualitative in nature and rely more on land use requirements and facility siting than on design. There are no performance-based design metrics for either individual buildings or communities, and the design premise has always been that evacuation is the primary mitigation strategy for life safety. In an era of climate change and its impact on coastal communities, this premise warrants re-examination.

4 Risk communication

In first-generation probability-based design (and in PBE to date), the performance (or risk) metric of choice has been the annual (or 50-year) failure probability; see Table 1 (Ellingwood 2001). Situations identified as having progressively more severe consequences of failure are addressed indirectly by reducing their target probability. This approach, while useful for the narrow scope of probability-based code development, has some drawbacks for performance-based engineering. For one thing, most stakeholders and public decision-makers are not trained in or comfortable with the tools of quantitative risk analysis, especially when the decision process involves rare events. Indeed, regulators often are skeptical of quantitative risk assessment, and may suspect that it might be used to justify socially or politically unacceptable decisions. For another, focusing solely on the probability without considering the consequences omits an important dimension of the assessment and decision process, noted previously [Faber & Stewart, 2003]. Low-probability events can be exceedingly risky. While it is difficult to quantify consequences in terms of economic loss, it is clear that this is what many building owners, engineers and regulatory officials in the civil arena want. The “average annual loss” is sometimes cited as an appropriate risk measure but the distribution of loss determined from Equation (1) (due to the epistemic uncertainties involved in loss estimation) can be very broad,

and no central measure – mean, median or mode – represents loss adequately. So, while the average annual loss might be meaningful for an insurance provider underwriting a large portfolio, it is not particularly useful for the individual attempting to measure risk to an individual facility. Other metrics must be sought. Consideration of acceptable risk in quantitative terms for civil infrastructure facilities, the construction of which often has been regulated by public codes, is a relatively new development (Ellingwood 2001). Risk communication [Mileti and Fitzpatrick, 1991], to the client and to the building regulatory authority, remains a challenge for risk-informed PBE. A life-cycle perspective, which seems important in an era of rapid economic development and climate change, also seems essential [Frangopol & Maute, 2003].

5 The role of performance-based engineering in community resilience assurance

The resilience of communities under disruptive natural hazard events depends on the performance of the built environment, as well as on supporting social, economic and public institutions which are essential for immediate community response and long-term recovery [e.g., Bruneau et al, 2003; Miles & Chang, 2006; Bocchini & Frangopol 2012; Ellingwood et al 2016]. Investigations conducted in the aftermath of recent disasters have revealed the importance of planning, development and mitigation policies that focus on the resilience of the community as a whole, rather than those that address safety and functionality of individual buildings and other civil infrastructure facilities [McAllister 2013]. Nevertheless, the performance of individual buildings and other infrastructure facilities, which are key to community resilience, is largely determined by codes and standards (e.g., *ASCE Standard 7-16* [ASCE 2016]), which with one exception (hospitals) do not consider the functionality of the community as a whole. Furthermore, these codes and standards are, and have been, focused on life safety goals and do not address response and recovery explicitly, which are key aspects of resilience. The role played by the performance of individual buildings in fulfilling community resilience goals is unknown. Moreover, design requirements for civil infrastructure facilities have been developed by different professional groups, often with different objectives, and the consistency of these governing standards with community goals seldom has been achieved [McAllister 2016].

The importance of the built environment to community resilience means that a fundamental change must occur in the way that code and standard-writing groups for buildings and other civil infrastructure approach their tasks to ensure that performance of physical infrastructure systems will support a resilient community. Community resilience planning requires communication across broad disciplines and stakeholder groups, including engineers, socioeconomic sciences, information technology, urban planning, government and the public at large. The National Institute of Standards and Technology (NIST) *Resilience Planning Guide* [NIST 2015] provides a general framework for developing resilience plans with the aim of ensuring that the performance objectives for building clusters and lifeline systems are aligned with specific functionality goals defined at the community level, which are based on the needs of their social institutions. However, the *Guide* stops short of providing the technical approach to linking component, system and community-level performance goals with the design standards for individual facilities. It is clear that traditional prescriptive approaches to design will be totally inadequate for the task at hand. On the other hand, a PBE approach can provide the framework for engineers and planners to respond to evolving public expectations and to achieve desired levels of performance and functionality of civil infrastructure systems that are essential

for community resilience and support community resilience goals. A key aspect of this work lies in de-aggregating the community performance goals to the individual building level, where they can be addressed in codes and standards. Work on this essential task has been initiated [Wang & Ellingwood, 2015; Lin et al, 2016; Ellingwood, 2019], as shown in Figure 1 below.

6 Conclusions

Performance-based engineering provides a vehicle for implementing risk-informed concepts into structural design and for communicating risk among stakeholders in the building process and to the client. PBE has already gained acceptance in earthquake engineering and fire-resistant structural design. Current initiatives to extend PBE to other hazards, such as extreme wind, flooding, storm surge and coastal inundation, and tsunami effects, and to develop design procedures in which investments in risk reduction can be targeted appropriately will bear fruit in the next decade. These initiatives will require risk-based performance assessment tools for buildings and other structures that are accessible to a spectrum of stakeholders with different skills and talents. The benefits of such an approach are an improved ability to assess the effectiveness of various risk mitigation strategies in terms of risk reduction per dollar invested, and thus a better allocation of public and private resources for managing risk.

Public demands to enhance community resilience in an era of climate change, prompted by recent extreme natural hazard events, will require a fundamental change in the way that code and standard-writing groups approach their tasks to achieve community-wide resilience goals. Here, too, risk-informed decision tools will be essential to the successful implementation of PBE for managing the impact of uncertainties on performance of buildings and for guiding engineering decisions in an era of social and economic development, technological innovation and community resilience concerns.

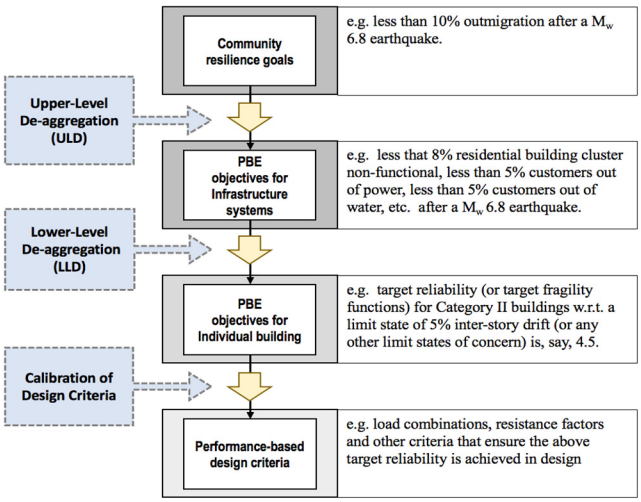

Figure 1. De-aggregation of community resilience goals for structural design

Acknowledgement

Preparation of this paper was supported, in part, by the Center of Excellence for Risk-Based Community Resilience Planning, established by The National Institute of Standards and Technology at Colorado State University and supported under NIST Financial Assistance Award

Number: 70NANB15H044. This support is gratefully acknowledged. The views expressed are those of the authors/presenter, and may not represent the official position of the National Institute of Standards and Technology.

7 References

ASCE (2016). *Minimum design loads for buildings and other structures (ASCE Standard 7-16)*. American Society of Civil Engineers, Reston, VA.

ASCE (2018). *Seismic evaluation and retrofit of existing buildings (ASCE Standard 41-17*). American Society of Civil Engineers, Reston, VA.

ASCE (2019). *Prestandard for performance-based wind design*. American Society of Civil Engineers, Reston, VA.

ASTM (2011). *Standard methods of fire test of building construction and materials (ASTM E119-11a)*. American Society for Testing and Materials, West Conshohocken, PA, USA

P. Bocchini, P., & D. M. Frangopol (2012). Restoration of bridge networks after an earthquake: multicriteria intervention optimization. *Earthquake Spectra, 28*, 426–455.

M. Bruneau, S. Chang, R. Eguchi, G. Lee, T. O'Rourke, A.M. Reinhorn, & D.V. Winterfelt (2003). A framework to quantitatively assess and enhance the seismic resilience of communities. *Earthquake Spectra, 19*, 733–752.

W.-C. Chuang & S.M.J. Spence (2019). An efficient framework for the inelastic performance assessment of structural systems subject to stochastic wind loads." *Engrg. Struct.* **179**:92-105.

ECCS 2001. *Model Code on Fire Engineering*, 1st Edition. European Convention for Constructional Steelwork Technical Committee 3, Brussels, Belgium.

B.R. Ellingwood (2001). Acceptable risk bases for design of structures," *Progress in Struct. Engrg. and Mat.* 3(2):170 - 179.

B.R. Ellingwood (2007). Strategies for mitigating risk to buildings from abnormal load events. *Int. J. of Risk Assessment and Mgt.* 7(6/7):828-845.

B.R. Ellingwood, H. Cutler, P. Gardoni, W.G. Peacock, J.W. van de Lindt & N. Wang (2016). "The Centerville virtual community: a fully integrated decision model of interacting physical and social infrastructure systems." *Sustainable and Resilient Infrastructure* 1(3-4): 95-107.

B.R. Ellingwood, N. Wang, J.R. Harris & T.P. McAllister (2019). The role of performance-based engineering in achieving community resilience. Ch. 6 in *Handbook of Sustainable and Resilient Infrastructure*, Routledge (ed. by P. Gardoni); 94-112 ISBN 978-1-138-30687-5.

Faber, M. & Stewart, M.G. 2003. Risk assessment for civil engineering facilities: a critical appraisal. *Reliability Engrg. & System Safety* 80: 173-184.

FEMA 2009. *Quantification of building seismic performance factors. FEMA Report P-695*, Prepared by the Applied Technology Council under Project ATC-63. Washington: Federal Emergency Management Agency.

FEMA 2018. Seismic performance assessment of buildings. ATC Project 58

D.M. Frangopol & K. Maute (2003). Life-cycle reliability-based optimization of civil and aerospace structures. *Comput. & Struct.* 81:397-410.

R.O. Hamburger (1996). Implementing performance-based seismic design in structural engineering practice. *Proc. 11th World Conf. On Earthquake Engrg.* , (Paper 2121). Elsevier Science Ltd.

ISO (1999). *Fire Resistance Tests - Elements of Building Construction - Part 1: General Requirements (ISO 834-1:1999)* International Organization for Standardization, Geneva.

P. Lin, N. Wang, N. & B.R. Ellingwood (2016). A risk de-aggregation framework that relates community resilience goals to building performance objectives, Sustainable & Resilient Infrastructure, 1(1-2): 1-13.

T.P.McAllister, T. (2013). *Developing guidelines and standards for disaster resilience of the built environment: A research needs assessment*. NIST Technical Note 1795, National Institute of Standards and Technology, Gaithersburg, MD [dx.doi.org/10.6028/NIST.TN.1795]

T.P.McAllister, T. (2016). Research Needs for Developing a Risk-Informed Methodology for Community Resilience, *J. Struct. Eng., ASCE* 142(8): DOI: 10.1061/(ASCE)ST.1943-541X.0001379

Mileti, D. S. & Fitzpatrick, C. (1991). Communication of public risk: its theory and its application. Sociological Practice Review 2(1):20-28.

S.B. Miles & S.E. Chang (2006). Modeling community recovery from earthquakes. *Earthquake Spectra*, 22(2): 439–458.

A. Mohammad, A. Azazinamini, L. Griffis & P. Irwin (2018). Performance assessment of an existing 47-story high-rise building under extreme wind loads." *J. Struct. Engrg.* 145:04018232.

NIST (2007). *Best practices for reducing the potential for progressive collapse in buildings* (NISTIR 7396, D. Duthinh & H.-S. Lew editors). National Institute of Standards and Technology, Gaithersburg, MD.

NIST (2009). *Best practice guidelines for structural fire resistance design of concrete and steel buildings* (NISTIR 7563, L. Phan, editor). National Institute of Standards and Technology, Gaithersburg, MD.

NIST (2014). 2014. *Measurement science R&D roadmap for windstorm and coastal inundation impact reduction (*GCR 14-973). National Institute of Standards and Technology, Gaithersburg, MD.

NIST (2015). *Community resilience planning guide for buildings and infrastructure systems (in two volumes)*. Special Publication 1190 (Vols. 1 and 2), National Institute of Standards and Technology, Gaithersburg, MD..

SFPE (2007). *Engineering Guide - Performance-Based Fire Protection*. Quincy: National Fire Protection Association.

N. Wang & B.R. Ellingwood (2015). Disaggregating community resilience objectives to achieve building performance goals. *Proc., Int. conference on applications of statistics and probability to civil engineering (ICASP12)*, University of British Columbia, Vancouver, BC, July.

RELIABILITY, RISK, RESILIENCE AND SUSTAINABILITY OF INFRASTRUCTURE SYSTEMS

Dan M. Frangopol

Professor, Lehigh University, USA

RELIABILITY, RİSK, RESILIENCE AND SUSTAINABILITY OF INFRASTRUCTURE SYSTEMS

Dan M. Frangopol[1],* and David Y. Yang[1]
[1]Department of Civil and Environmental Engineering, ATLSS Engineering Research Center, Lehigh University, Bethlehem, PA, USA
*E-mail: dan.frangopol@lehigh.edu

Abstract: Reliability analysis evaluates the probability of failure of engineering systems under various performance limits. It has been extensively used in structural design/standardization and more recently performance-based life-cycle management of infrastructure systems. In a multi-disciplinary setting, reliability analysis lends itself to a number of performance assessment processes associated with civil and marine infrastructure systems. These include risk, resilience, and sustainability performance of deteriorating and hazard-susceptible infrastructure assets and networks. This paper summarizes some of the recent advances in risk, resilience, and sustainability of infrastructure systems. The role of reliability analysis is highlighted.

Keywords: Reliability; Risk; Resilience; Sustainability; Life-cycle Management.

1 Introduction

In the United States and many parts of the developed world, civil and marine infrastructure systems are facing a number of pressing challenges posed by structural deterioration, lack of financial resources for maintenance, and ever-increasing and diversifying needs from the public. For instance, the latest Report Card by American Society of Civil Engineers (ASCE 2017) rated the overall infrastructure in the US a grim D+. Within transportation sector, one in eleven bridges was rated structurally deficient, and a total investment of US $123 billion is needed to clear this backlog; even worse situation exists in public transit systems that received a D- rating citing "overdue maintenance and underinvestment", which lead to aging transit infrastructure and a US$90 billion rehabilitation backlog. These symptoms of infrastructure systems are further compounded by growing population and changing climate. Therefore, ASCE recently outlined the grand challenge for civil engineers to (a) significantly enhance the performance and value of infrastructure projects over their life cycles by 2025 and (b) foster the optimization of infrastructure investments for society.

In order to tackle this challenge, life-cycle management has drawn growing attention from both the research community and practicing engineers. Life-cycle oriented planning, design, and maintenance have been embraced to address the continuously increasing societal, political, economic, and environmental demand for sustainable development. Considering the long life-cycle of many infrastructure assets, a major challenge of infrastructure life-cycle management is to take into account the various uncertainties involved in the decision-making process. To this end, structural reliability theory, which was initially developed to quantify structural safety margin under uncertainties, plays a central role. Reliability analysis of engineering systems attempts to determine the probability of failure under various performance limits. A generic performance function can be represented as

$$g = f(X_1, X_2, \dots, X_n) \tag{1}$$

where the performance g is measured by a function f of n random variables X_1 to X_n that are associated with the uncertainties involved. For life-cycle analysis, the performance function becomes time-variant due to structural deterioration. The corresponding time-variant reliability index can be used for the purpose of structural and infrastructure management (e.g. maintenance planning) (Frangopol 2011; Frangopol, Dong, and Sabatino 2017; Frangopol and Kim 2019). Reliability-based life-cycle management has been widely used for highway and railway bridges, marine and offshore structures, aerospace structures, and underground structures, among others (Frangopol, Saydam, and Kim 2012).

In recent years, novel reliability-based indicators for life-cycle performance have been developed to better assist infrastructure management under more complex conditions. Examples of these indicators include life-cycle risk (Decò and Frangopol 2011), lifetime resilience (Yang and Frangopol 2018a), and sustainability utility (Sabatino, Frangopol, and Dong 2016). Centered around these indicators, this paper overviews the reliability, risk, resilience, and sustainability of deteriorating infrastructure systems with emphasis on the recent progress at Lehigh University in all these regards.

2 Life-Cycle Risk

Structural reliability analysis provides the probability of failure of a structure. This probability can be considered as the indicator of the structural performance to fulfil its functional requirements. However, failure probability itself does not offer the consequence of failure. Hence, it does not draw a full picture of the impact of structural failure and its threat posed to infrastructure users. To this end, risk is used to combine probability of failure (PoF) and consequence of failure (CoF). In general, risk can be defined as the expected consequences associated with the adverse event that a structure fails to perform its functional requirements. Mathematically, risk is defined as the product of PoF and CoF:

$$R = p_f \cdot C_f \tag{2}$$

where R is the risk associated with structural failure; p_f and C_f are PoF and CoF, respectively. Similar to reliability, when used in a life-cycle context, both PoF and CoF become time-variant.

For infrastructure systems, two issues arise from the general definition of risk. The first is the evaluation of CoF at the network level. In a connected infrastructure network, the failure of one asset may have cascading effects on its surrounding assets. For instance, in a bridge network, a failed bridge may drastically alter the traffic pattern in the entire transportation network. Therefore, consequence evaluation of interconnected infrastructure assets should be conducted at the network level where the aforementioned interaction is explicitly considered. Yang and Frangopol (2018b) compared the risk assessment results for bridges at the project and the network levels. They found that failure to consider the network effect can significantly affect the risk-based ranking of bridge vulnerability and its maintenance priorities.

The second issue that needs to be addressed in risk assessment is to consider the climate change impact on life-cycle risks of infrastructure systems. It has been found from various studies that climate change is responsible for the increasing frequency and intensity of various natural hazards (e.g. floods, hurricanes, heatwaves, and wildfires) (ASCE 2015; Mondoro, Frangopol, and Liu 2018a). Given the long service life of infrastructure assets, the impact of climate change should be included in the risk assessment process. A recent study by Yang and Frangopol (2019c)

investigated the bridge scour risks under a wide array of climate change scenarios and global climate predictions. The results are shown in Figure 1. The deep uncertainty of future risks under climate change, as uncovered in this study, inspires the use of robust optimization for life-cycle management of intervention actions (Mondoro, Frangopol, and Liu 2018b; Yang and Frangopol 2019b).

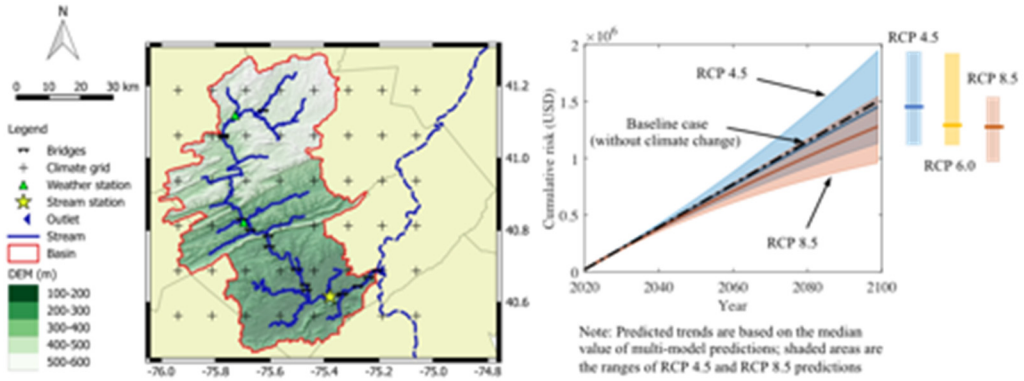

Figure 1. Physics-based regional bridge scour risk under climate change – Lehigh River Watershed (adapted from Yang and Frangopol (2019c))

3 Lifetime Resilience

In the life-cycle of infrastructure systems, structural deterioration is not the only stressor that can jeopardize their performance. An array of hazards can also lead to punctuated performance drop or even catastrophic structural failure. The recovery of structural performance after these hazards is usually studied under the name of "structural resilience". As witnessed in recent disasters such as Hurricane Maria, structural resilience acts as the physical foundation of the broader community resilience. Therefore, it is of paramount importance to incorporate the facet of structural resilience into the overall infrastructure management process. Formally, resilience is defined as (Frangopol and Bocchini 2011)

$$R_i = \frac{\int_{t_i}^{t_i+t_h} Q(t)dt}{Q_0 \cdot t_h} \tag{3}$$

where $Q(t)$ is the structural performance at time; Q_0 is the initial structural performance; R_i is the quantified resilience under the hazard i; t_i is the time of hazard occurrence; t_h is the time horizon under consideration. The value of resilience in Eq. (3) can be interpreted as the area under the performance recovery path $Q(t)$. For structural resilience, reliability index can be used to represent structural performance.

In the life-cycle context, gradual deterioration and sudden performance drop are usually coupled: under the same hazard, the recovery of an aged structure may take much longer than that of a new one due to the more extensive damage of the former. To model this interaction between structural deterioration and structural resilience, Yang and Frangopol (2018a) proposed a novel concept termed as lifetime resilience. Instead of only considering one hazard event, lifetime resilience combines structural deterioration and resilience assessment of deteriorated structures by investigating all hazards that may be encountered by a structure in its life-cycle. A schematic representation of lifetime resilience is shown in Figure 2. Since the occurrence time and the hazard impact are all random variables, a stochastic process approach based on renewal theory

is developed to efficiently evaluate the expected lifetime resilience under multiple hazards (Yang and Frangopol 2019a).

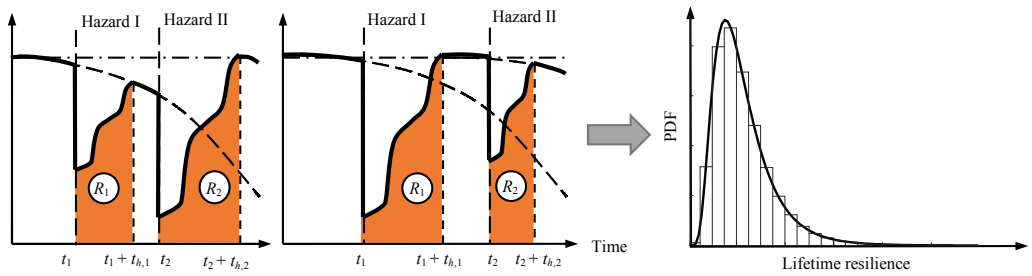

Figure 2. Lifetime resilience of a deteriorating and repairable engineering system (adapted from Yang & Frangopol (2018a))

4 Infrastructure Sustainability

In recent years, the norm for infrastructure management has shifted from economy-centric practice to a sustainability-informed paradigm. Infrastructure sustainability can be reflected from two aspects: structural longevity and functional integrity (Yang and Frangopol 2018a). The former requires that infrastructure system should be durable and meet intergenerational needs, while the latter mandates a more holistic viewpoint towards infrastructure projects that covers economic, social, and environmental criteria (i.e. three pillars of sustainability). To achieve infrastructure sustainability, Sabatino, Frangopol, and Dong (2016) proposed a novel life-cycle performance indicator — sustainability utility — based on multi-attribute utility theory. To determine the value of this indicator, economic, social, and environmental risks associated with infrastructure failure, which are usually measured in different units, are first converted to a unified utility value according to decision-makers' risk attitude. For instance, for infrastructure management, exponential utility functions in the following form has been wide used (Sabatino, Frangopol, and Dong 2016)

$$u_a = \frac{1}{1-exp[-\gamma]}\left(1 - exp\left[-\frac{a_{max}-a}{a_{max}-a_{min}}\right]\right) \tag{4}$$

where u_a is the attribute (economic, social, or environmental) utility; a is the attribute value (e.g. economic loss, fatalities, or CO_2 emissions); γ represents the decision-maker's risk attitude ($\gamma > 0$, $\gamma = 0$, and $\gamma < 0$ for risk-averse, risk-neutral and risk-taking decision-makers, respectively); a_{max} and a_{min} are the maximum and minimum attribute values, respectively. Sustainability utility is then defined as a weighted sum of all three utility values:

$$u_{sus} = w_{eco}u_{eco} + w_{soc}u_{soc} + w_{env}u_{env} \tag{5}$$

where u_{sus} is the sustainability utility and its weight; u_{eco} and w_{eco} are the economic utility and its weight, respectively; u_{soc} and w_{soc} as well as u_{env} and w_{env} are those for social and environmental aspects, respectively. The risk attitude of decision-makers γ as well as the attribute weights can be obtained by conducting surveys among stakeholders (Cheng, Yang, and Frangopol 2019). Sustainability assessment based on utility theory has been used in life-cycle management for both civil and marine structures (L. Liu et al. 2018; Y. Liu and Frangopol 2018). It has been shown that decisions based on sustainability can have drastically different outlook than those based solely on economic risks. This again demonstrates the importance of adopting sustainability-informed decision-making in life-cycle assessment and management.

5 Concluding Remarks

Reliability, risk, resilience and sustainability of infrastructure systems are playing an increasingly important role in modern life-cycle assessment and management. The changing climate and the growing demand for sustainable development aspire to new paradigms and criteria for infrastructure management. This paper summarizes several recently developed performance indicators used in infrastructure life-cycle management in order to mitigate risk, enhance resilience, and achieve sustainability. All these indicators pivot on reliability assessment of engineering systems and incorporate various additional factors such as failure consequences, climate change impacts, lifetime hazards, and social and environment considerations.

6 Acknowledgements

The authors are grateful for the financial support received from (a) the U.S. National Science Foundation (Grant CMMI 1537926), (b) the U.S. Department of Transportation Region 3 University Transportation Center (Grant CIAM-UTC-REG6), and (c) the Pennsylvania Infrastructure Technology Alliance (PITA). The opinions and conclusions presented in this paper are those of the authors and do not necessarily reflect the views of the sponsoring organizations.

7 References

ASCE. 2015. Adapting Infrastructure and Civil Engineering Practice to a Changing Climate. Edited by J. Rolf Olsen. Reston, VA: American Society of Civil Engineers (ASCE). doi:10.1061/9780784479193.

ASCE. 2017. Report Card for America's Infrastructure. Reston, VA: American Society of Civil Engineers (ASCE).

Cheng, Minghui, David Y. Yang, and Dan M. Frangopol. 2019. "Investigation of the Effects of Time Preference and Risk Perception on Life-Cycle Management of Civil Infrastructure." ASCE-ASME Journal of Risk and Uncertainty in Engineering Systems, Part A: Civil Engineering, (in press).

Decò, Alberto, and Dan M. Frangopol. 2011. "Risk Assessment of Highway Bridges under Multiple Hazards." Journal of Risk Research 14 (9): 1057–1089. doi:10.1080/13669877.2011.571789.

Frangopol, Dan M. 2011. "Life-Cycle Performance, Management, and Optimisation of Structural Systems under Uncertainty: Accomplishments and Challenges." Structure and Infrastructure Engineering 7 (6): 389–413. doi:10.1080/15732471003594427.

Frangopol, Dan M., and Paolo Bocchini. 2011. "Resilience as Optimization Criterion for the Bridge Rehabilitation of a Transportation Network Subject to Earthquake." In Proceedings of the ASCE Structures Congress 2011, edited by Dana Ames, Theodore L. Droessler, and Marc Hoit, 2044–2055. Las Vegas, Nevada.

Frangopol, Dan M., You Dong, and Samantha Sabatino. 2017. "Bridge Life-Cycle Performance and Cost: Analysis, Prediction, Optimisation and Decision-Making." Structure and Infrastructure Engineering 13 (10). Taylor & Francis: 1239–1257. doi:10.1080/15732479.2016.1267772.

Frangopol, Dan M., and Sunyong Kim. 2019. Life-Cycle of Structures under Uncertainty: Emphasis on Fatigue-Sensitive Civil and Marin Structures. Boca Raton, FL: CRC Press.

Frangopol, Dan M., Duygu Saydam, and Sunyong Kim. 2012. "Maintenance, Management, Life-Cycle Design and Performance of Structures and Infrastructures: A Brief Review." Structure and Infrastructure Engineering 8 (1): 1–25. doi:10.1080/15732479.2011.628962.

Liu, Liang, Dan M. Frangopol, Alysson Mondoro, and David Y. Yang. 2018. "Sustainability-Informed Bridge Ranking under Scour Based on Transportation Network Performance and Multi-Attribute Utility." Journal of Bridge Engineering, ASCE 23 (10): 04018082. doi:10.1061/(ASCE)BE.1943- 5592.0001296.

Liu, Yan, and Dan M. Frangopol. 2018. "Probabilistic Risk, Sustainability, and Utility Associated with Ship Grounding Hazard." Ocean Engineering 154 (April). Elsevier Ltd: 311–321. doi:10.1016/j.oceaneng.2018.01.101.

Mondoro, Alysson, Dan M. Frangopol, and Liang Liu. 2018a. "Bridge Adaptation and Management under Climate Change Uncertainties: A Review." Natural Hazards Review, ASCE 19 (1): 04017023.

Mondoro, Alysson, Dan M. Frangopol, and Liang Liu. 2018b. "Multi-Criteria Robust Optimization Framework for Bridge Adaptation under Climate Change." Structural Safety 74. Elsevier: 14–23. doi:10.1016/j.strusafe.2018.03.002.

Sabatino, Samantha, Dan M. Frangopol, and You Dong. 2016. "Life Cycle Utility-Informed Maintenance Planning Based on Lifetime Functions: Optimum Balancing of Cost, Failure Consequences and Performance Benefit." Structure and Infrastructure Engineering 12 (7). Taylor & Francis: 830–847. doi:10.1080/15732479.2015.1064968.

Yang, David Y., and Dan M. Frangopol. 2018a. "Bridging the Gap between Sustainability and Resilience of Civil Infrastructure Using Lifetime Resilience." In Handbook of Sustainable and Resilient Infrastructure, edited by Paolo Gardoni, 419–442. Abingdon, UK and New York, USA: Routledge.

Yang, David Y., and Dan M. Frangopol. 2018b. "Risk-Informed Bridge Ranking at Project and Network Levels." Journal of Infrastructure Systems, ASCE 24 (3): 04018018. doi:10.1061/(ASCE)IS.1943-555X.0000430.

Yang, David Y., and Dan M. Frangopol. 2019a. "Life-Cycle Management of Deteriorating Civil Infrastructure Considering Resilience to Lifetime Hazards: A General Approach Based on Renewal-Reward Processes." Reliability Engineering & System Safety 183 (March): 197–212. doi:10.1016/j.ress.2018.11.016.

Yang, David Y., and Dan M. Frangopol. 2019b. "Risk-Based Portfolio Management of Civil Infrastructure Assets under Deep Uncertainties Associated with Climate Change: A Robust Optimisation Approach." Structure and Infrastructure Engineering, July. Taylor & Francis, 1–16. doi:10.1080/15732479.2019.1639776.

Yang, David Y., and Dan M. Frangopol. 2019c. "Physics-Based Assessment of Climate Change Impact on Long-Term Regional Bridge Scour Risk Using Hydrologic Modeling: Application to Lehigh River Watershed." Journal of Bridge Engineering, ASCE 24 (11): 04019099. doi:10.1061/(ASCE)BE.1943-5592.0001462.

RELIABILITY ASSESSMENT OF WIND ENERGY STRUCTURES

John Dalsgaard Sørensen

Professor, Aalborg University, Denmark

RELIABILITY ASSESSMENT OF WIND ENERGY STRUCTURES

John Dalsgaard Sørensen
Department of Civil Engineering, Thomas Manns Vej 23, 9220 Aalborg, Denmark
E-mail: jds@civil.aau.dk

Abstract: Wind energy is a main contributor to the increasing demand for renewable energy. During the recent decades significant reductions in Levelized Cost of Energy (LCoE) for wind energy have been obtained through technological innovations. Wind turbines are exposed to highly dynamic loads that cause fatigue and extreme load effects which are subject to significant uncertainties. Continued reduction of cost of energy for wind energy should be performed such that the turbine components and system is designed to have sufficient reliability with respect to both extreme and fatigue loads. This paper presents models for uncertainty modelling and reliability assessment of critical wind turbine components. The turbine components are designed to have sufficient reliability with respect to both extreme and fatigue loads but they should not be too safe (and costly). In this paper focus is failure modes related to degradation / fatigue of the considered components. This is especially important when planning inspections and maintenance. Planning of inspections in relation to lifetime extension is considered in this paper and illustrative examples are presented.

Keywords: Wind turbines, reliability, stochastic modelling, inspections, lifetime extension.

1 Introduction

Wind energy is one of the most important renewable energy sources, and an increasing focus is on reducing the levelized cost of energy (LCOE) such that wind energy becomes even more competitive compared to other energy sources. LCOE is obtained on basis of the life-cycle costs and the energy produced. Thus turbine components and systems have to be designed to have sufficient reliability, but also not be too costly considering both APEX and OPEX. Both these cost contributions as well as the energy produced depends on the reliability of the components and systems.

Wind turbines are exposed to highly dynamic loads and the response is dependent on the wind turbine control system. Wind turbines have to be verified to have sufficient reliability with respect to fatigue and extreme load effects which are subject to significant uncertainties. In this paper probabilistic models are presented for uncertainty modeling and reliability assessment of especially the structural components such as tower, substructure and blades. Since reliable function of wind turbines is highly dependent on the control system, electrical and mechanical components reliability assessment of these components are also presented in this paper. Probabilistic analysis and design of wind turbines are considered e.g. in (Veldkamp 2006), (Toft 2010), (Agarwal 2008), (Sørensen & Toft 2010, 2015).

2 Reliability modelling

Structural components in wind turbines are designed considering a number of load combinations, see (IEC 61400-1, 2019):

- Failure during normal operation in extreme load or by fatigue (DLC 1)

- Failure under fault conditions (e.g. failure of electrical / mechanical components or loss of grid connection) due to extreme loads or by fatigue (DLC 2)
- Failure during start up, normal shut down or emergency shut down (DLC 3, 4 and 5)
- Failure when the wind turbine is idling / parked and does not produce electricity. Failure can be by extreme loads or by fatigue (DLC 6)
- Failure during transportation and installation (DLC 7)
- Failure during transport, assembly, maintenance and repair (DLC 8)

Generally sufficient of wind turbines systems is performed on a component level, and the components can generally be divided in two groups:

(i) Electrical and mechanical components modelled using classical reliability models, with the main descriptor being the failure rate, λ which are estimated on the basis of time-to-failure data. The failure rate / hazard rate typically follow a bath-tub model describing the time dependent behaviour of the failure rate / hazard rate. The reliability is typically modelled using basically a Weibull model for the time to failure. Using e.g. FMEA (Failure Mode and Effect Analysis), system models can be established and the systems reliability can be estimated, see e.g. (Tavner 2012).

(ii) Structural elements such as tower, main frame, blades and the support structure / foundation with failure modes that can be described by limit state equations, $g_i(\mathbf{X})$. Failure of the tower can e.g. be yielding failure, buckling stability failure or fatigue. The parameters in the limit state equation $g(\mathbf{X})$ are assumed to be modelled by n stochastic variables $\mathbf{X} = (X_1, ..., X_n)$. The probability of failure, P_f can be estimated using Structural Reliability Methods, e.g. FORM / SORM / simulation methods, see e.g. (Madsen et al. 1986) and (JCSS 2002).

In many cases fault of an electrical component or the control system results in increased load effects in the structural components; both for extreme and fatigue failures of the structural components. Examples are design load cases (DLC 2.3) and (DLC 6.2). The annual failure rate for a component can be estimated from, see also (Sørensen & Toft 2015):

$$\lambda_{F_j} = P\left(F \middle| \text{fault } j\right) \cdot \nu_{\text{fault},j} \tag{1}$$

where $\lambda_{\text{fault},j}$ is the annual failure rate for the considered fault (e.g. grid loss or loss of electrical network connection) which e.g. can be estimated directly based on observed data. $P\left(F \middle| \text{fault } j\right)$ is the conditional probability of failure for the structural component given fault *j*. $P\left(F \middle| \text{fault } j\right)$ can be estimated by structural reliability methods simulating the fault conditions.

For wind turbines the risk of loss of human lives in case of failure of a structural element is generally very small. Further, it can be assumed that wind turbines are systematically reconstructed in case of collapse or end of lifetime. Therefore, an appropriate target reliability level corresponding to a minimum, target annual probability of failure is considered to be $5 \cdot 10^{-4}$ (annual reliability index equal to 3.3), see (IEC 61400-1 2019) and (Sørensen & Toft 2015).

2.1 Extreme loads

This section describes the basic assumptions used for calibration of material partial safety factors for extreme loads in (IEC 61400-1 2019), see (Sørensen & Toft 2015) for details.

The following generic limit state equation for extreme load effects (ultimate limit states) in operation or standstill / parked is considered:

$$g = z\ b\ \delta\ R(\mathbf{X}, a) - X_{dyn} X_{\exp} X_{aero} X_{str} L \tag{2}$$

where z is a design parameter, e.g. cross-sectional area, $R(\ )$ model for the load bearing capacity / resistance, δ model uncertainty for resistance assumed to have a mean value equal to 1 and coefficient of variation V_δ, b bias in the resistance model, $R(\ )$, see Annex K in (IEC 61400-1 2019). $\mathbf{X}$ is a vector with stochastic variables (e.g. strength parameters), a is set of deterministic variables, e.g. geometrical parameters, X_{dyn} models uncertainty related to modeling of the dynamic response, including uncertainty in damping ratios and eigenfrequencies, X_{exp} models uncertainty related to the modeling of the exposure (site assessment) - such as the terrain roughness and the landscape topography, X_{aero} models uncertainty in assessment of lift and drag coefficients and additionally utilization of BEM, dynamic stall models, etc., X_{str} models uncertainty related to the computation of the load-effects given external load and L models uncertainty related to the extreme load-effect due to wind loads. For simplicity no permanent loads are introduced, but could easily be included. The stochastic model in Table 1 is 'representative' in the sense that it is used as basis for calibration of material partial safety factors.

The design equation for deterministic design corresponding to Eq. (2) is written

$$\frac{z\ b\ R_k}{\gamma_R} - \gamma_f L_k \geq 0 \tag{3}$$

where R_k is the characteristic value of load bearing capacity, L_k is the characteristic value of variable load, γ_R is a partial safety factor for resistance and γ_f is a partial safety factor for load effect assumed to be 1.35.

Table 1. Stochastic models for physical, model and statistical uncertainties. LN: Lognormal; G: Gumbel; W: Weibull.

Variable	Distribution	Mean	COV	Quantile	Comment
R	LN	-	V_R	5%	Strength
δ	LN	-	V_δ	Mean	Model uncertainty
L – DLC 1.1	W	-	0.15	0.98	Annual maximum load effect obtained by load extrapolation
L – DLC 6.1	G	-	0.2	0.98	Annual maximum wind pressure - European wind conditions
X_{dyn}	LN	1	0.05	Mean	
X_{exp}	LN	1	0.15	Mean	
X_{aero}	G	1	0.10	Mean	
X_{str}	LN	1	0.03	Mean	

Table 2 shows the partial safety factor for resistance, γ_R for various values of the coefficient of variation for model uncertainty, V_δ calibrated to the target annual failure probability equal to 5 10^{-4} assuming the bias, *b* = 1. It is seen that the required partial safety factor, γ_R increases with the uncertainty of the model, V_δ. It is also seen that γ_R does not depend on the coefficient of variation of the strength, V_R .The reason is that the characteristic value (5% quantiles) for *R* approximately accounts for changes in V_R .

Table 2. γ_R - partial safety factor for model uncertainty.

Coefficient of variation for model uncertainty for resistance model in model 1, V_δ	5 %	10 %	15 %	20 %
γ_R	1.20	1.25	1.35	1.45

As an example for a structural steel component with yielding failure criteria it can be assumed that V_R =0.05, V_δ =0.05 and b =1.1 (ductile failure with extra load bearing capacity) implying that γ_R 1.18 and thus the resulting partial safety factor equal to 1.18 / 1.1 ~ 1.1. The above calibrated partial safety factors can similarly be used for other materials and for different resistance models if the bias, *b* and the coefficients of variation of the model uncertainty as well as the strength parameters are known.

2.2 Fatigue loads

This section describes the basic assumptions used for calibration of material partial safety factors for fatigue limit states for welded details in (IEC 61400-1 2019), see (Sørensen & Toft 2015) for details. For wind turbine steel substructures fatigue can be a critical failure mode for welded details.

If a linear SN-curves is considered the SN relation is written

$$N = K\left(\Delta\sigma\right)^{-m} \tag{4}$$

where N is the number of stress cycles to failure with constant stress ranges $\Delta\sigma$. K and m are dependent on the fatigue critical detail. For a wind turbine in free wind flow the design equation in deterministic design is written

$$G(z) = 1 - \int_{U_{in}}^{U_{out}} \frac{\nu \cdot FDF \cdot T_L}{K_C} D_L\left(m; \alpha_{\Delta\sigma}(U)\hat{\sigma}_u(U)/z\right) f_U(U)\, dU = 0 \tag{5}$$

where z is a design parameter (e.g. proportional to cross sectional area) and

$$D_L\left(m;\sigma_{\Delta\sigma}\right) = \int_0^\infty s^m f_{\Delta\sigma}\left(s\left|\sigma_{\Delta\sigma}(U)\right.\right) ds \tag{6}$$

is the expected value of $\Delta\sigma^m$ given standard deviation $\sigma_{\Delta\sigma}$ and mean wind speed U , ν is the total number of fatigue load cycles per year (determined by e.g. rainflow counting), T_L is the design life time, FDF is the Fatigue Design Factor (equal to $(\gamma_f\gamma_m)^m$ where γ_f and γ_m are partial safety factors for fatigue load and fatigue strength). K_C is the characteristic value of K

(here assumed to be obtained from $\log K_C$ as mean of $\log K$ minus two standard deviations), U_{in} is the cut-in wind speed (typically 3 m/s), U_{out} is the cut-out wind speed (typically 25 m/s). $f_{\Delta\sigma}\left(s\left|\sigma_{\Delta\sigma}(U)\right.\right)$ is the density function for stress ranges given standard deviation of $\sigma_{\Delta\sigma}(U)$ at mean wind speed U. This distribution function can be obtained by e.g. rainflow counting of response, and can generally be assumed to be Weibull distributed.

It is assumed that the standard deviation of the stress ranges, $\sigma_{\Delta\sigma}(U)$ can be written:

$$\sigma_{\Delta\sigma}(U) = \alpha_{\Delta\sigma}(U)\frac{\sigma_u(U)}{z} \tag{7}$$

where $\alpha_{\Delta\sigma}(U)$ is the influence coefficient for stress ranges given mean wind speed U and $\sigma_u(U)$ is the standard deviation of turbulence given mean wind speed U.

$\sigma_u(U)$ is modelled as LogNormal distributed with characteristic value $\hat{\sigma}_u(U)$ defined as the 90% quantile and standard deviation equal to $I_{ref}\cdot 1.4$ [m/s]. The characteristic value of the standard deviation of turbulence, $\hat{\sigma}_u(U)$ given average wind speed U is modelled by:

$$\hat{\sigma}_u(U) = I_{ref}\cdot(0.75\cdot U + b) \quad ; \; b = 5.6 \text{ m/s} \tag{8}$$

where I_{ref} is the reference turbulence intensity and $\hat{\sigma}_u$ is the ambient turbulence.

The corresponding limit state equation is written

$$g(t) = \Delta - \int_{U_{in}}^{U_{out}}\int_{0}^{\infty}\frac{\nu\cdot t}{K}\left(X_{Wind}X_{SCF}\right)^m D_L\left(m;\alpha_{\Delta\sigma}(U)\sigma_u(U)/z\right) f_{\sigma_u}\left(\sigma_u\left|U\right.\right) f_U(U)\, d\sigma_u dU \tag{9}$$

where Δ is a stochastic variable modelling the model uncertainty related to the Miner rule for linear damage accumulation, t is time in years, X_{Wind} is the model uncertainty related to assessment of the fatigue wind load effects and is due to uncertainties related to site assessment, assessment of lift and drag coefficients, dynamic response calculations, X_{SCF} is the model uncertainty related to local stress analysis given global fatigue load effects, $\sigma_u(U)$ is the standard deviation of turbulence given average wind speed U.

The design parameter z is determined from the design equation and next used in the limit state equation to estimate the reliability index or probability of failure with the reference time interval $[0;t]$.

Next, it is assumed that the SN-curve is bilinear (thickness effect not included) with slope change at

$N_D = 5\cdot 10^6$:

$$\begin{aligned} N &= K_1 S^{-m_1} \quad \text{for} \quad S \geq \Delta\sigma_D \\ N &= K_2 S^{-m_2} \quad \text{for} \quad S < \Delta\sigma_D \end{aligned} \tag{10}$$

where K_1, m_1 are material parameters for $S \geq \Delta\sigma_D$ and K_2, m_2 are material parameters for $S < \Delta\sigma_D$:

$$\Delta\sigma_D = \left(\frac{K_1}{5 \cdot 10^6} \right)^{1/m_1} \tag{11}$$

The fatigue strength $\Delta\sigma_F$ is defined as the value of S for $N_D = 2 \cdot 10^6$.

In case the SN-curve is bilinear $D_L\left(m; \sigma_{\Delta\sigma}\right)$ in design equations and limit state equations is exchanged with

$$D_{BL}\left(m_1, m_2, \Delta\sigma_D; \sigma_{\Delta\sigma}\right) = \int_0^{\Delta\sigma_D} s^{m_2} f_{\Delta\sigma}\left(s \left| \sigma_{\Delta\sigma}(U)\right.\right) ds + \int_{\Delta\sigma_D}^{\infty} s^{m_1} f_{\Delta\sigma}\left(s \left| \sigma_{\Delta\sigma}(U)\right.\right) ds \tag{12}$$

The probability of failure in year *t* given survival up to year *t* is estimated by

$$\Delta P_{F,t} = \left(P\left(g(t) \leq 0\right) - P\left(g(t-1year) \leq 0\right)\right) / P\left(g(t) \leq 0\right) \tag{13}$$

Table 3 shows a representative stochastic model. It is assumed that the design lifetime is T_L = 25 year.

Table 3. Stochastic model or fatigue failure of welded details.

Variable	Distri-bution	Expected value	Standard deviation / Coefficient Of variation	Comment
Δ	N	1	COV_Δ = 0.30	Model uncertainty Miner's rule
X_{Wind}	LN	1	COV_{Wind}	Model uncertainty wind load
X_{SCF}	LN	1	COV_{SCF}	Model uncertainty stress concentration factor
m_1	D	3		Slope SN curve
$\log K_1$	N	determined from $\Delta\sigma_D$	$\sigma_{\log K_1}$ = 0.2	Parameter SN curve
m_2	D	5		Slope SN curve
$\log K_2$	N	determined from $\Delta\sigma_D$	$\sigma_{\log K_2}$ = 0.2	Parameter SN curve
$\Delta\sigma_F$	D	71 MPa		Fatigue strength
$\log K_1$ and $\log K_2$ are fully correlated				

It is assumed that γ_m = 1.25 can be used a basic partial safety factor for fatigue strength. With the minimum / target annual probability of failure 5 10^{-4} (corresponding to normal/high consequence of failure) Table 4 shows the required product of the partial safety factors for the fatigue load γ_f as function of the total coefficient of variation of the fatigue load: $COV_{load} = \sqrt{COV_{Wind}^2 + COV_{SCF}^2}$. It is seen that the required partial safety factor product, γ_f highly depends on the coefficient of variation for the fatigue load, COV_{load}. If COV_{load} is in the range 15-20% then a fatigue load partial safety factor γ_f equal to1.00 is obtained for the target failure probability equal to 5 10^{-4}. Information about assessment of COV_{Wind} and COV_{SCF} can be found

in (Sørensen 2012) and (Sørensen & Toft 2015). Table 5 and 6 show examples of assessment of COV_{Wind} and COV_{SCF} .

Table 4. Recommended partial safety factor for fatigue stress ranges, γ_f .

Coefficient of variation, COV_{load}	5-10 %	10-15 %	15-20 %	20-25 %	25-30 %
γ_f	0.90	0.95	1.00	1.10	1.20

Table 5. Examples of COV_{Wind} .

COV_{Wind}	Uncertainty is assessment of fatigue wind load
0.10-0.15	*Site assessment:* • More than 2 years of climatic data, corrected with MCP techniques. • Wind measurements above and below wind turbine hub height. • Flat terrain with low roughness
0.15-0.20	*Site assessment:* • Minimum 1 year of climatic data. • Wind measurements at hub height and below. • Non-complex site with medium roughness.
0.20-0.25	*Site assessment:* • Less than 1 year of data, not corrected with MCP techniques Wind measurements below hub height. • Complex terrain.

Table 6. Examples of COV_{SCF} .

COV_{SCF}	Fatigue critical detail
0.00	Statically determinate systems with simple fatigue critical details (e.g. girth welds) where FEM analyses are performed
0.05	Statically determinate systems with complex fatigue critical details (e.g. multi-planar joints) where FEM analyses are performed
0.10	Statically in-determinate systems with complex fatigue critical details (e.g. doubler plates) where FEM analyses are performed
0.15	2 dimensional tubular joints using SCF parametric equations
0.20	Tubular joints in structures where tubular stiffness is modeled by Local Joint Flexibility (LJF) models and SCF parametric equations are used

3 Existing wind turbines – Life extension

In this section it is described how life extension can be assessed for structural details in wind turbines exposed to fatigue failure. Since structural components are assumed to be designed to satisfy the requirement that the annual probability of failure does not exceed 5 10^{-4} the extreme load cases do not need to be considered in relation to life extension unless there are changes in the environmental conditions compared to the design assumptions, or new information about the materials / resistances are obtained. Therefore focus is here on the fatigue limit state.

The following procedure can be followed considering a life extension from e.g. T_L = 20 years to e.g. T_L^U = 25 years:

- Calculate the annual reliability (index) as function of time using the SN-approach using

  - Markov matrix to represents the long-term distribution of stress ranges
  - Stochastic model for fatigue strength for SN-approach, fatigue load and model uncertainties, see section 2.2
- Calibrate a (1- or) 2-dimensional Fracture Mechanics model to give the same annual reliability (index) as function of time using
  - Same fatigue load as for SN-approach
  - Stochastic model for fracture mechanics model and the same stochastic model for the fatigue load as for the SN-approach
    See e.g. (Sørensen 2012).
- Assess if a reduced reliability level can be accepted during the life extension. A reduced reliability level can be argued in higher cost of safety measure for an existing wind turbines compared to a new wind turbine. Based on Table G.4 in (ISO 2394 2015) the annual probability of failure could e.g. be increased from 5 10^{-4} to than 10^{-3} corresponding to an annual reliability index equal to 3.1.
- Assume that inspections have been performed or are planned with the result that no cracks are detected. If cracks are detected they are assumed to be repaired by grinding, welding or replacement depending on the size of the crack.
- Model the reliability of inspections by POD (Probability Of Detection) curves, e.g. using the POD-curves for Visual, MPI, EC, … inspections in (DNVGL-RP-C210 2015)
- Determine an inspection and repair strategy, incl. inspection methods and inspection times such that the annual probability of failure does not exceed smaller than 5 10^{-4} during the extended lifetime [0, T_L^U]. No-find of cracks are assumed. If cracks are detected and repaired, then a new reliability assessment is necessary.

Table 7 shows examples of required inspections considering life extension from 20 to 25 years for three different inspection techniques. The decision is made in year 15 and three different levels of updated knowledge on the fatigue load uncertainty COV_{load} are considered. The POD curve for Eddy current follows (DNVGL-RP-C210 2015), and for close / normal visual inspection it is assumed exponential with mean detectable cracks widths equal to 5mm and 10mm. Figure 1 shows an example of updated annual reliability index given an updated COV_{load} = 20-25%, use of close visual inspection and thus required inspections at years 18, 21 and 24.

Table 7. Required inspection time intervals ΔT_I for life extension (in years).

COV_{load}	Eddy current	Close visual	Normal Visual
10-15%	no	no	no
15-20%	20	20 + ΔT_I = 4	20 + ΔT_I = 3
20-25%	18 + ΔT_I =5	18 + ΔT_I = 3	18 + ΔT_I = 2

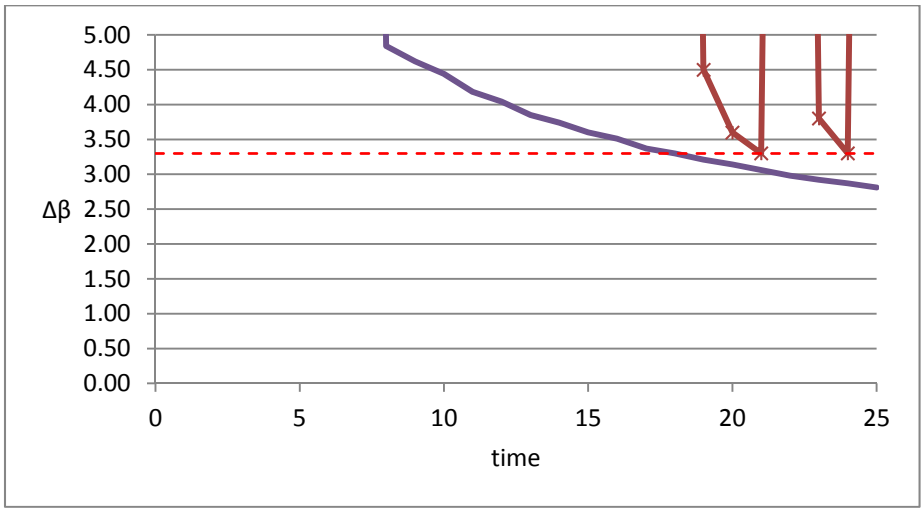

Figure 1. Example of annual reliability index as function of time given inspections assuming updated COV_{load} = 20-25%. Red curve shows the updated annual reliability index given inspections at year 18, 21 and 24.

4 Conclusions

This paper presents a probabilistic model for design of wind turbines, and the link to the partial safety factors used for design of structural wind turbine components according to IEC 61400:2019. The main Design Load Cases to be verified in both a semi-probabilistic design and in a probabilistic design are presented and probabilistic models are described for extreme loads and for fatigue loads.

Further aspects are considered of using a reliability-based approach for decision making / planning inspections in relation to life extension where additional information may be available for the fatigue load. An illustrative example is presented based on the probabilistic models used for calibration of the partial safety factors in IEC 61400:2019, and also using the required reliability level for structural failure modes, 5 10^{-4} per year. It is noted that it may be considered to lower the requirement to the reliability level for life extension since the relative cost of safety measures can be assumed to be larger than for design of a new wind turbine.

Acknowledgements

This research is partly conducted under the project titled “Demonstration of Requirements for Life Extension of Wind Turbines beyond their Design Life” (LifeWind) funded by the Danish Energy Technology Development and Demonstration Program (EUDP).

5 References

Agarwal, P. 2008. Structural Reliability of Offshore Wind Turbines. PhD thesis, University of Texas at Austin.

DNVGL-RP-C210. 2015. Probabilistic methods for planning of inspection for fatigue cracks in offshore Structures.

IEC 61400-1. 2019 Wind turbine generator systems – Part 1: Safety requirements. 4th edition.

ISO 2394. 2015. General principles on reliability for structures.

JCSS. 2002. (Joint Committee on Structural Safety): Probabilistic Model Code. http://www.jcss.byg.dtu.dk/

Madsen, H. O., Krenk, S. & Lind, N.C. 1986. Methods of Structural Safety, Dover Publications, Inc.

Sørensen, J.D. & Toft, H.S. 2010. Probabilistic design of wind turbines. Energies, Vol. 3, pp. 241-257.

Sørensen, J.D. 2012. Reliability-based calibration of fatigue safety factors for offshore wind turbines. International Journal of Offshore and Polar Engineering. Vol. 22, No. 3, pp. 234–241.

Sørensen, J.D. & Toft, H.S. 2015. Safety Factors – IEC 61400-1 ed. 4 - background document. DTU Wind Energy-E-Report-0066 (EN).

Tavner, P. 2012. Offshore Wind Turbines: Reliability, Availability and Maintenance. Institution of Engineering and Technology.

Toft, H.S. 2010. Probabilistic Design of Wind Turbines. PhD thesis, Aalborg University.

Veldkamp, D. 2006. Chances in Wind Energy - A Probabilistic Approach to Wind Turbine Fatigue Design. PhD thesis, DUWIND Delft University, Wind Energy Research Institute, Delft.

CHICKEN (METHOD) AND EGG (DATA) – WHICH COMES FIRST?

Kok-Kwang Phoon

Distinguished Professor, National University of Singapore, Singapore
Vice-Provost (Academic Personnel), National University of Singapore

CHICKEN (METHOD) AND EGG (DATA) - WHICH COMES FIRST?

Kok-Kwang Phoon[1], Yu Wang[2]
[1]Department of Civil and Environmental Engineering, National University of Singapore, Singapore
E-mail: kkphoon@nus.edu.sg
[2]Department of Architecture and Civil Engineering, City University of Hong Kong, Hong Kong
E-mail: yuwang@cityu.edu.hk

Abstract: Geotechnical uncertainty representation has hitherto been focused on the method. The small sample size encountered in geotechnical engineering will not be viewed as a "curse" if methods were to be developed with the MUSIC (multivariate, uncertain and unique, sparse, incomplete, partially corrupted) nature of site data as the starting point. We have the curse of small sample size. We have the curse of de-trending. These problems emerge from methods that are developed somewhat independently of the data we actually have at hand. The authors advocate a "data-driven" perspective that requires: (1) a detailed understanding of the features of geotechnical data, which include uncertainty and spatial variability and (2) a method that can operate on all data, not simply data that fit the method. Preliminary research shows that the Bayesian compressive sampling is a possible candidate data-driven method in terms of its ability to accommodate geotechnical data features and its responsiveness to changes in these features. The chicken (method) has always come before the egg (data). It is time to put the egg before the chicken.

Keywords: Geotechnical data, MUSIC, Data-driven method, Bayesian compressive sampling.

1 Introduction

The uncertainty in geotechnical site data is known for at least five decades (Lumb 1966). It is natural to adopt probabilistic methods to manage such data (National Research Council 1995). The generalization from a random variable model to a random field model (Vanmarcke 1977) is also natural, given the spatial variations exhibited by natural geo-materials. In short, two features of site data are reasonably well studied, namely uncertainty and spatial variability. There are many sophisticated variations of the basic random variable idea to other uncertainty representations such as imprecise probability (Beer et al. 2013) and generalizations of the basic Gaussian random field idea to vector fields, third or higher order fields, and copula fields, among others. These more recent theoretical developments will be not pursued in this paper.

In the opinion of the authors, more attention has been focused on the method thus far. Let's call this perspective "method-driven". This perspective has been highly successful in many disciplines, particularly in scientific disciplines where the modeler has full control on the collection of data. Experiments can be designed at great cost to collect the right kind and sufficient amount of data to test the proposed model with as much precision as desired. The Large Hadron Collider, which is the world's largest and most powerful particle accelerator, is an almost ideal example of the extreme cost and efforts invested to collect data. It seeks to validate a Theory of Everything (TOE) that can explain all physics, big and small, in a single equation without any fitting parameters called fundamental constants. After all, any number that emerges must be explainable by this TOE equation. This perspective is awkward for geotechnical engineering, because we do not and could not exercise this degree of control over our data. Even the right kind of data (inputs to a physical model such as the effective friction angle) is rarely collected from field tests for various practical reasons. It is not possible to

increase the site investigation budget just to estimate statistical parameters such as the mean, coefficient of variation, and correlation with sufficient precision. The emphasis on a neat classical random variable model could have hobbled the adoption of probabilistic methods in geotechnical engineering, because practitioners feel this model is at odds with the limited data they have at hand (Phoon 2017). The problem does not lie with probability theory, but the difficulty of validating the fairly strong assumptions underlying these classical methods and computing the model parameters in these methods from available data alone. Another well-known example of this characterization problem is the separation of trend from stationary fluctuations (the "de-trending" problem) (Ching and Phoon 2017, Ching et al. 2017). Thus far, practitioners and clients are not inclined to collect additional data to mitigate these problems. The prevailing sentiment is to ask for a value proposition to decision making in practice, whatever the combination of method and data, before more investment in data collection will be considered. It is hard to argue with this sentiment from a business standpoint. In addition, a method-driven perspective is less sensitive to the detailed features of the available data, because it assumes that the *data it needs* will somehow be made available. A method-driven perspective may have also inadvertently resulted in geotechnical engineers being less responsive to the digital transformation taking place elsewhere (Gerbert et al. 2016, State of the Nation Report 2017) where the features of available data in terms of volume, variety, velocity, and veracity (the four "V"s of big data) are changing rapidly. In the authors' opinion, there is a growing gap between the *data we need* and the *data we have* in geotechnical engineering. It is timely for us to address this gap explicitly in light of rapid advances in digital technologies.

At this point, we do not quite understand what is meant by a "data-driven" perspective in geotechnical uncertainty representation. We know that the focus should be data, not method. Data is now a core asset. This immediately re-orientates our goal to seek insights from data *we have*, rather than data *we need*. Hence, there is need to deal with the entire data estate (which is evolving), not simply those that fit the needs of certain methods.. A detailed understanding of the features of geotechnical data is now of fundamental importance, rather than an afterthought in a method-driven perspective. This is the first piece of knowledge we need to explore this new perspective. The features of site data are more complicated that "uncertain" and "spatially variable". We present our current understanding in the next section. The authors submit that the value of a method should be defined as the value it brings to decision making in practice as a result of drawing insights from *all available data* with minimum assumptions, regardless of their varied features. This means addressing the detailed data features *explicitly* as the primary research goal. The statistician George Box once said: "All models are wrong, but some are useful". We believe this adage is an important guidepost in exploring this data-driven perspective. The objective of this paper is to examine the Bayesian compressive sampling (BCS) as a possible candidate data-driven method in terms of its ability to accommodate geotechnical data features and its responsiveness to changes in these features.

2 Features of Site Data

Soils are natural geo-materials, which are affected by many spatially varying factors during the geological processes they have undergone, such as their parent materials, weathering and erosion processes, transportation agents, and sedimentation conditions. The occurrence of geo-materials and their properties therefore vary spatially (e.g., Lacasse and Nadim 1996, Phoon and Kulhawy 1999). Furthermore, surface outcrops do not say much about the subsurface

conditions. Site investigation is therefore necessary before construction of any geotechnical project can commence. However, due to the technical difficulties and cost of testing subsurface soils in an undisturbed state, only a small volume fraction is actually characterized within any project site (e.g., Mayne et al. 2002). This leads to the so-called "curse of small sample size" in geotechnical engineering (Phoon 2017).

Besides possible sparsity, geotechnical site data are generally multivariate as shown in Table 1. It is uneconomical to mobilize equipment just to conduct a single test. In addition, genuine multivariate data are rarely collected in a site investigation program, because it is not cost effective to conduct multiple tests in close proximity. There is an obvious tradeoff between conducting different tests in different locations and conducting different tests in the same location. The former strategy collects more information on the spatial variability of the site. The latter strategy collects information on the cross-correlations among different tests. In practice, it is common to adopt an intermediate strategy involving conducting different test combinations at different depths and locations. The grayed out cells in Table 1 denote absent measurements. Hence, geotechnical site data are almost always "incomplete" in this multivariate sense.

Table 1. Site investigation results for a silty clay layer at a Taipei site (Ou and Liao 1987).

Depth (m)	s_u (kN/m^2)		s_u(mob) (kN/m^2)	Test results						
				LL (Y_1)	PI (Y_2)	LI (Y_3)	s'_v/P_a (Y_4)	s'_p/P_a (Y_5)	$s_u(mob)/s'_v$ (Y_6)	q_{t1} (Y_9)
12.8	UU	55.2	46.9	30.1	9.1	1.20	1.26	1.71	0.37	3.35
14.8	VST	50.7	52.9	32.8	12.8	1.43	1.43		0.36	3.34
16.1	UU	61.9	51.7	36.4	14.5	1.24	1.54		0.33	3.15
17.8	UU	54.2	42.8	41.9	18.9	0.90	1.68	1.79	0.25	2.74
18.3	VST	59.5	59.3				1.72		0.34	2.76
20.2	UU	73.1	60.5	38.1	17.3	0.70	1.88		0.32	2.73
22.7	VST	63.3	64.4	37.0	16.0	0.58	2.08		0.31	2.97
24.0	UU	82.2	67.5	38.0	16.2	0.75	2.19	2.19	0.30	2.80
26.6	UU	98.1	82.1	34.8	13.8	0.80	2.41		0.34	3.92

Phoon (2018) suggested that the features of geotechnical site data can be succinctly described as *MUSIC*: Multivariate, Uncertain and Unique, Sparse, and InComplete. Phoon et al. (2019) generalized *MUSIC* to include presence of some outliers ("*C*" for partially corrupted data). The "unique" and "incomplete" features have not received the attention they deserve in the literature, although they are surely present to different degrees in geotechnical databases. In fact, site investigation is mandated in many building regulations, because of this "unique" feature of geotechnical site data. It is also a practical recognition that a broad qualitative understanding of geology is not sufficiently refined in terms of quantifying differences in soil properties in numerical terms between two sites. Otherwise, the minimum site investigation effort mandated in building regulations should depend on this appreciation of geology, rather than cast-in-stone (literally) regardless of how much data are known in adjacent sites. Table 1 is a site-specific example of a *MUSIC* database. Each row (record) in a *MUSIC* database is treated as independent. This assumption is reasonable if the depth interval between each record is larger than the spatial correlation length. Ching and Phoon (2019a, 2019b) extended *MUSIC* to *MUSIC-X* to account for spatial correlation between two records measured in close proximity. The symbol "*X*" is adopted to foreground the spatial/temporal dimension in *MUSIC* data. Spatial variability is a well-recognized feature in many geo-disciplines such as

geostatistics. Spatial variation is used in the broad sense where stratigraphic changes and other variable geologic features are included. These data features pose significant challenges to classical methods. This section describes what we know about the features of site investigation data in a typical project. In general, geotechnical data can cover remote sensing, monitoring, load testing, and possibly a proliferation of new types emerging from the internet of things.

The challenge to deal with this impending "data explosion" (not unlike the Cambrian explosion in speciation) is likely to involve rethinking our motivation, how we develop our methods, and exploring non-classical data-driven methods, such as compressive sampling or sensing, as described in the next section.

3 Compressive Sampling

Compressive sampling (or sensing, CS) is a novel sampling paradigm in digital signal processing to reconstruct a signal (e.g., an image with 1000 × 1000 = 1 million pixels) from a small number of measurements on that signal (Candès et al. 2006, Donoho 2006, Candès and Wakin 2008, Wang and Zhao 2016, Comerford et al. 2016, 2017). In the context of signal processing, Table 1 is a 9 × 9 matrix and can be considered as an image with 9 × 9 = 81 pixels and missing values at 9 pixels. Then, the *MUSIC-X* problem associated with Table 1 becomes a problem of how to estimate or recover the 9 missing values or how to add a new row to Table 1 at a new given depth. Indeed, many geotechnical site data are images, such as geology maps and subsurface geological cross-section, and direct measurements on the image are often sparse and only taken at a limited number of locations. In linear algebra, a 2D image with $N_{x1} \times N_{x2}$ pixels, such as the color map shown in Figure 1, can be represented by a matrix **F** with a dimension of $N_{x1} \times N_{x2}$ and expressed as a weighted summation of $N_{x1} \times N_{x2}$ number of 2D basis functions, such as cosine or wavelet functions (Zhao et al. 2018):

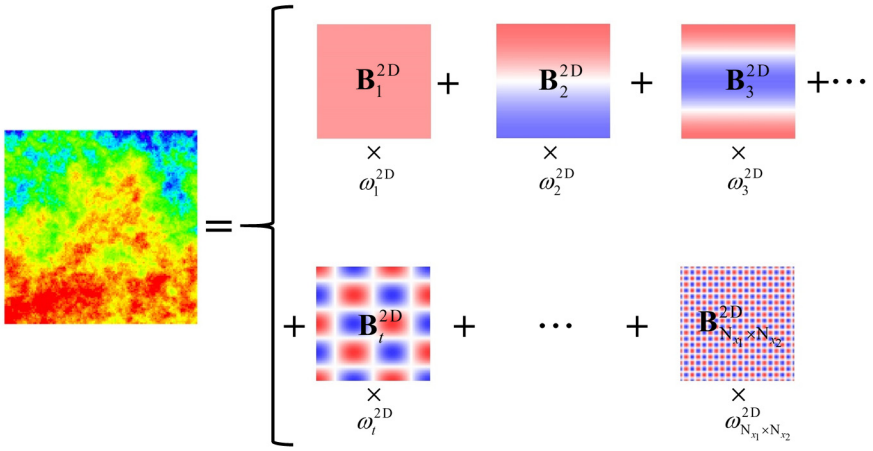

Figure 1. Representation of a 2D image in compressive sampling (Zhao et al. 2018).

$$\mathbf{F} = \sum_{t=1}^{N_{x1}\times N_{x2}} \mathbf{B}_t^{2D} \omega_t^{2D} \tag{1}$$

in which $\mathbf{B}_t^{2D}$ is the t-th 2D basis function that is independent of **F**, while ω_t^{2D} is the weight corresponding to $\mathbf{B}_t^{2D}$. In the context of CS, most images are compressible, suggesting that only a small number of basis functions is necessary to properly represent the image and that the

magnitudes of most ω_t^{2D} are almost zero or trivial except several non-trivial ones (i.e., coefficients with significantly larger magnitudes). Therefore, once the non-trivial coefficients ω_t^{2D} can be identified and estimated using sparse measurements **Y**, signal **F** can be approximately reconstructed. The relation between **Y** and ω_t^{2D} is expressed as (Zhao et al. 2018):

$$\mathbf{Y} = \mathbf{\Psi}_{x_1} \mathbf{F} \mathbf{\Psi}_{x_2} = \sum_{t=1}^{N_{x1} \times N_{x2}} \mathbf{A}_t^{2D} \omega_t^{2D} \tag{2}$$

where $\mathbf{\Psi}_{x1}$ and $\mathbf{\Psi}_{x2}$ are problem-specific measurement matrices, reflecting the locations of elements of **Y** in **F** along row and column directions, respectively. Although Eq. (2) is underdetermined, the non-trivial coefficients in ω_t^{2D} can be obtained using several existing methods, including non-probabilistic methods, such as orthogonal matching pursuit (Pati et al. 1993; Wang and Zhao 2016), and Bayesian methods (Ji et al. 2008, 2009, Wang and Zhao 2017). Once the non-trivial coefficients in ω_t^{2D} are estimated, the ω_t^{2D} can be approximated as $\hat{\omega}_t^{2D}$ by setting those trivial elements of ω_t^{2D} as zero. The methods for identifying non-trivial elements are given in Foucart and Rauhut (2013). Then, the 2D image of interest **F** can be approximated as:

$$\hat{\mathbf{F}} = \sum_{t=1}^{N_{x1} \times N_{x2}} \mathbf{B}_t^{2D} \hat{\omega}_t^{2D} \tag{3}$$

4 Bayesian Compressive Sampling (BCS)

When Bayesian methods is used to estimate $\hat{\omega}_t^{2D}$ (Ji et al. 2008, 2009, Wang and Zhao 2017, Huang et al. 2016, Zhao et al. 2018), both the mean estimate and covariance of $\hat{\mathbf{F}}$ are obtained. Note that when the measurement data **Y** used to derive $\hat{\omega}_t^{2D}$ is too sparse, significant statistical uncertainty is involved in the estimated $\hat{\omega}_t^{2D}$. The uncertainty in $\hat{\omega}_t^{2D}$ propagates to $\hat{\mathbf{F}}$ through Eq. (3). Therefore, quantification of statistical uncertainty in $\hat{\mathbf{F}}$ shall start with the quantification of statistical uncertainty in $\hat{\omega}_t^{2D}$. Note that the uncertainty associated with $\hat{\omega}_t^{2D}$, or equivalently written as a column vector $\hat{\boldsymbol{\omega}}^{2D}$ with a length of $N_{x1} \times N_{x2}$, is explicitly quantified by its probability density function (PDF), which can be obtained under a Bayesian framework (e.g., Sivia and Skilling 2006). Zhao et al. (2018) showed that the posterior PDF of $\hat{\boldsymbol{\omega}}^{2D}$, i.e., $p(\hat{\boldsymbol{\omega}}^{2D} | \mathbf{Y})$ follows multivariate Student's t distribution, with a degree of freedom of $2c_n$, a mean vector of $\boldsymbol{\mu}_{\hat{\omega}^{2D}}$ and covariance matrix of $\mathbf{COV}_{\hat{\omega}^{2D}}$. $\boldsymbol{\mu}_{\hat{\omega}^{2D}}$ and $\mathbf{COV}_{\hat{\omega}^{2D}}$ are expressed as:

$$\begin{aligned} \boldsymbol{\mu}_{\hat{\omega}^{2D}} &= \mathbf{H} \boldsymbol{V}_{tr} = (\mathbf{J} + \mathbf{D})^{-1} \boldsymbol{V}_{tr} \\ \mathbf{COV}_{\hat{\omega}^{2D}} &= \frac{d_n \mathbf{H}}{c_n - 1} = \frac{d_n (\mathbf{J} + \mathbf{D})^{-1}}{c_n - 1} \end{aligned} \tag{4}$$

where $\mathbf{H} = (\mathbf{J}+\mathbf{D})^{-1}$; **D** is a diagonal matrix with diagonal elements $D_{t,t} = a_t$ (t = 1, 2, …, $N_{x1} \times N_{x2}$); **J** is a matrix with element $J_{t,s} = tr[\mathbf{A}_t^{2D}(\mathbf{A}_s^{2D})^T]$ (t, s = 1, 2, …, $N_{x1} \times N_{x2}$) and a dimension of ($N_{x1} \times N_{x2}$)×($N_{x1} \times N_{x2}$), "*tr*" represents trace operation in linear algebra; whereas $\boldsymbol{V}_{tr} = \left\{tr[\mathbf{Y}(\mathbf{A}_1^{2D})^T], tr[\mathbf{Y}(\mathbf{A}_2^{2D})^T], \cdots, tr[\mathbf{Y}(\mathbf{A}_{N_{x1} \times N_{x2}}^{2D})^T]\right\}^T$ is a column vector with a length of $N_{x1} \times N_{x2}$.

$c_n = \mathrm{M}_{tot}/2+c$, where M_{tot} represents the total number of measurements and $\mathrm{M}_{tot} = \mathrm{M}_{x_1} \times \mathrm{M}_{x_2}$ when measurements are collected at grids; $d_n = d+\frac{1}{2}[\|\mathbf{Y}\|_2^2 - \boldsymbol{\mu}_{\hat{\omega}^{2\mathrm{D}}}{}^{\mathrm{T}}\mathbf{H}^{-1}\boldsymbol{\mu}_{\hat{\omega}^{2\mathrm{D}}}]$, where c and d are non-negative constant, e.g., $c = d = 10^{-4}$, and "$\|\mathbf{Y}\|_2^2$" represents the sum of squares of all elements in **Y**. Note that the only unknown parameters in Eq. (4) is a_t (t = 1, 2, …, $N_{x1} \times N_{x2}$), which can be obtained by maximizing the likelihood function of **Y**, i.e., p(**Y**), or equivalently the natural logarithm of p(**Y**) (e.g., Ji et al. 2008, 2009), i.e., ln[p(**Y**)]. Detailed derivation of ln[p(**Y**)] is referred to Wang and Zhao (2017). The log-likelihood ln[p(**Y**)] is expressed as:

$$\ln[\,p(\mathbf{Y})] = -\frac{1}{2}\left[(M_{tot}+2c)\ln(2d+\|\mathbf{Y}\|_2^2 - \boldsymbol{\mu}_{\hat{\omega}^{2\mathrm{D}}}{}^{\mathrm{T}}\mathbf{H}^{-1}\boldsymbol{\mu}_{\hat{\omega}^{2\mathrm{D}}})\right] + \frac{1}{2}\ln[\det(\mathbf{DH})] + const \tag{5}$$

where "det(•)" represents the determinant of a matrix; "*const*" involves all terms that are independent of a_t. Detailed formulation and estimation of a_t are given elsewhere (Tipping 2001, Ji et al. 2008, 2009). After the most probable values of a_t of the non-trivial elements of $\boldsymbol{\omega}^{2\mathrm{D}}$ are identified and estimated, the mean vector $\boldsymbol{\mu}_{\hat{\omega}^{2\mathrm{D}}}$ and covariance matrix $\mathbf{COV}_{\hat{\omega}^{2\mathrm{D}}}$ can be obtained. Then, the mean estimate of the spatially varying geotechnical site data is obtained and statistical uncertainty associated with the interpretation is explicitly quantified.

As an illustration, Figure 2a shows a 2D vertical cross-section with a thickness of 10.20m (in depth direction x_1) and a length of 20.44m (in horizontal direction x_2). A resolution of 0.04m is adopted in this example for both x_1 and x_2 directions, leading to 256×512 = 131,072 data points in total. Suppose that the 10×4 data points grid, as shown by open circles in Figure 4a, are taken as the measured data **Y** and used together with their corresponding locations to recover the complete 2D cross-section with 131,072 data points. Figure 2b shows the mean estimate of the 2D cross-section obtained from BCS (Zhao et al. 2018). A similar spatially varying trend can be observed in Figures 2a and 2b, even when only 40/131,072 = 0.03% of the original data are used as input to BCS. To examine the uncertainty associated with the BCS results, Figure 2c shows standard deviation, SD, obtained from BCS multiplying a factor of 1.96, and Figure 2d shows the absolute residuals between the original 2D data (i.e., Figure 2a) and the BCS mean estimates from **Y** (i.e., Figure 2b). The 1.96 SD surface shown in Figure 2c are generally larger than most residuals shown in Figure 2d, while some residuals at locations far away from the measurement data **Y** are larger than the 1.96 SD. These observations imply that many residuals fall within the region defined by the mean±1.96 SD (i.e., approximate 95% confidence interval or "credible interval" in Bayesian statistics parlance).

CS is data-driven and the CS results improve as the data quantity increases. Figures 3b, 3c, and 3d show the BCS mean estimate for three different measurement grids: 30×15 (0.34%), 50×25 (0.95%) and 100×50 (3.81%), respectively. The 10×4 (0.03%) measurement grid is shown in Figure 3a. When compared with the 10×4 grid in Figure 3a, the mean estimate for the 30×15 grid (see Figure 3b) is more similar to the original 2D data as shown in Figure 2a. As the number of measurement data further increases, the mean estimate of the 2D data (see Figures 3c and 3d) gradually approaches to the original complete 2D data (see Figure 2a), and the BCS SD is reduced to almost zero, as shown by Zhao et al. (2018).

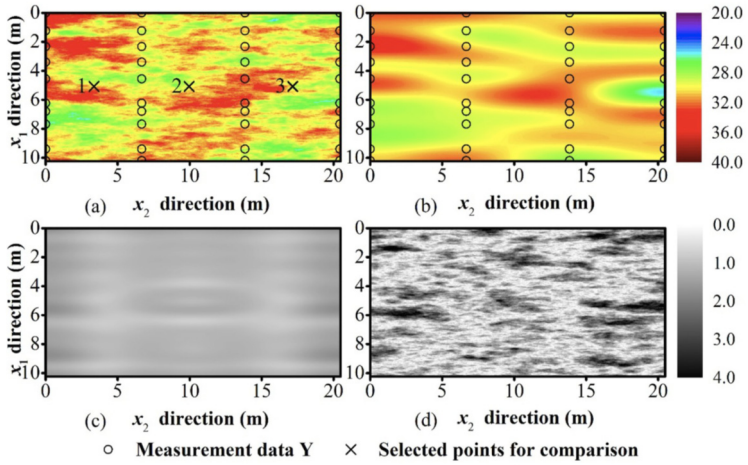

Figure 2. Comparison between the original 2D data and that estimated from the 10×4 measurement grid: (a) Original 2D data; (b) mean estimate of spatially varying 2D data; (c) 1.96 standard deviation of estimated results; and (d) absolute residuals between (a) and (b) (Zhao et al. 2018).

5 Random Field Representation of Site Data from Sparse Measurements

When a sample path (a continuous path or surface in space) is needed for design and analysis, e.g., probabilistic slope stability analysis where the variation of some strength parameters along the critical failure surface is of interest (e.g., Liu et al. 2019), the BCS results can be used together with Karhunen–Loève (KL) expansion to generate random field samples (RFSs) directly from sparse measurements (Wang et al. 2018, Hu et al. 2019). The KL simulation of RFSs generally requires the mean of the random field of interest and deterministic orthogonal eigen-functions and eigenvalues corresponding to the covariance function or covariance matrix (Phoon et al. 2002). In contrast, BCS provides both the mean estimate and the covariance matrix for the signal of interest directly from sparse measurements. Consider, for example, a truncated 2D random field:

$$\hat{\mathbf{H}}(x_1, x_2) = \mu + \sum_{i=1}^{P} \sqrt{\lambda_i}\,\mathbf{f}_i(x_1, x_2)\xi_i \tag{6}$$

in which x_1 and x_2 represents two directions in space or time; μ is mean of the field. $\mathbf{f}_i(x_1, x_2)$ and λ_i are 2D eigen-functions and corresponding eigenvalues, respectively, of the covariance matrix; ξ_i is a standard Gaussian random variable. Eq. (6) suggest that 2D RFSs can be generated through realizations of uncorrelated random variables ξ_i once a covariance matrix is available.

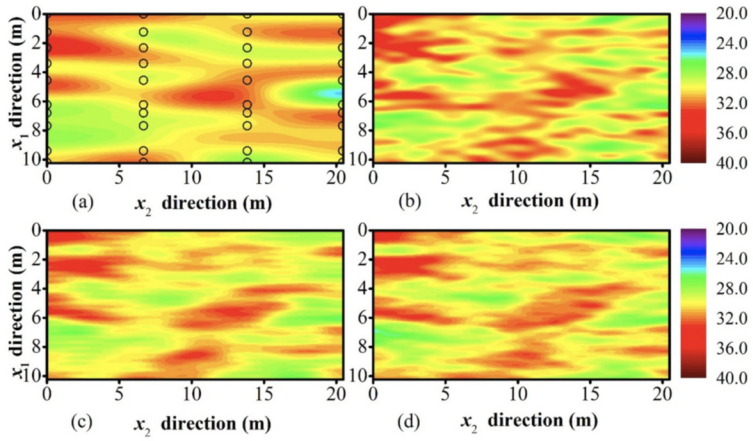

Figure 3. Mean estimate of spatially varying 2D data under different measurement grids: (a) 10×4 (b) 30×15 (c) 50×25 and (d) 100× 50 (Zhao et al. 2018).

Given the mean estimate and covariance matrix of the signal $\hat{\mathbf{F}}$ obtained from BCS, 2D RFSs incorporating interpolation uncertainty and preserving the quantified autocorrelations can be generated using a truncated KL expansion, expressed as (Hu et al. 2019):

$$\hat{\mathbf{F}} = \sum_{t=1}^{N_a} \mathbf{B}_t^{2D} \mu_{\hat{\omega}_t^{2D}} + \sum_{i=1}^{N_a} \sqrt{\lambda_{\hat{\mathbf{F}},i}}\, \mathbf{f}_{\hat{\mathbf{F}},i}(x_1, x_2)\xi_i \tag{7}$$

in which $\hat{\mathbf{F}}$ is a realization or sample path; $\mathbf{f}_{\hat{\mathbf{F}},i}(x_1, x_2)$ is the *i*-th eigen-function of $\mathbf{COV}(\hat{\mathbf{F}})$ with corresponding eigenvalue $\lambda_{\hat{\mathbf{F}},i}$. Because the BCS results are used together with KL expansion, the generator is called the BCS-KL generator. The BCS-KL generator is non-parametric and data-driven. No pre-determined parametric functional forms are needed for the marginal PDF or covariance function of the random field. Therefore, the BCS-KL generator is readily applicable to non-Gaussian and non-stationary RFSs, including RFSs with non-stationary auto-covariance structure (Montoya-Noguera et al. 2019) and RFSs with unknown trend function without de-trending (Wang et al. 2019). In addition, the BCS-KL generator may be readily extended to simulate cross-correlated bivariate RFSs (Zhao and Wang 2018). The following two subsections illustrate the direct simulation of non-Gaussian and non-stationary RFSs from measurements using BCS-KL generator. For clarity of the illustration, only 1D examples are shown below.

5.1 Simulation of non-Gaussian non-stationary random field with trends without de-trending

Consider, for example, a quantity Q that is modeled by a 1D lognormal random field with a quadratic trend in mean $\mu_Q = -4.8\times10^{-6}x^2 + 2.46\times10^{-3}x + 0.90$, a constant variance $\sigma_Q^2 = 0.01$ and an exponential correlation function $\rho = \exp(-2\delta/\lambda_Q)$, where $\delta = |x_i - x_j|$ represents the distance in terms of integer between location x_i and x_j (i, j = 1, 2, …, 512, if the length of the 1D random field is 512 in terms of integer), and λ_Q = 51.2 represents the correlation length used in the random field. In other words, Q is non-stationary in the mean, but stationary in ρ. Given the random field parameters specified above, RFSs can be readily generated using a random field generator, such as KL expansion. Figure 4 plots one example of the Q RFS by a solid line,

together with the quadratic trend by a solid line with open triangles. However, note that the random field parameters used for random field simulation in engineering practice are often unknown and need to be estimated from measurement data of Q before RFS generation (e.g., Stuedlein et al. 2012; Ching et al. 2016).

When the measurement data exhibit a clear trend in the depth or other directions, de-trending is often performed first on the measured data to separate the measurement data into a trend component and stationary residuals before estimating random field parameters from the residuals (i.e., a stationary random field). Figures 5a and 5b show one example, respectively, of 500 unconditional and conditional RFSs generated using this conventional method with removal of a commonly used linear trend from the measurement data, together with average and 95% confidence interval estimated from 500 RFSs. Although the unconditional RFS in Figure 5a looks reasonable, the embedded trend function is incorrect. In contrast, although the conditional RFS in Figure 5b follows the trend of the original Q data, it cannot reflect the uncertainty at the measurement locations. Similarly, Figures 6a and 6b show an example, respectively, of 500 unconditional and conditional RFSs generated using the conventional method with removal of the correct quadratic trend function. Although the trend function is correct, the RFS obviously has different frequency contents when compared with the original Q data. The residuals obtained after removal of the quadratic trend are used to estimate sample auto-covariance function (AF), as shown by circles in Figure 7. Then the random field parameters are estimated by fitting the sample AF to the assumed auto-covariance function (i.e., exponential auto-covariance function) using a least-squares method. The parameters obtained in this example are λ=1.39 and σ^2=0.0093. When compared with the λ_Q = 51.2 in the prescribed random field, the λ=1.39 is grossly underestimated. This is partly due to the limited number of measurement data points (i.e., M = 20 is relatively small when compared with N = 512) used in the analysis (e.g., Wang et al. 2017). The residuals of a limited number of measurement data points cannot effectively capture the auto-correlation of the original random field. It is intriguing that the selection of an incorrect linear trend produces significantly better estimates of σ^2 and λ. This, at least partly, contributes to the reasonable results obtained when a linear trend is removed as shown in Figure 5.

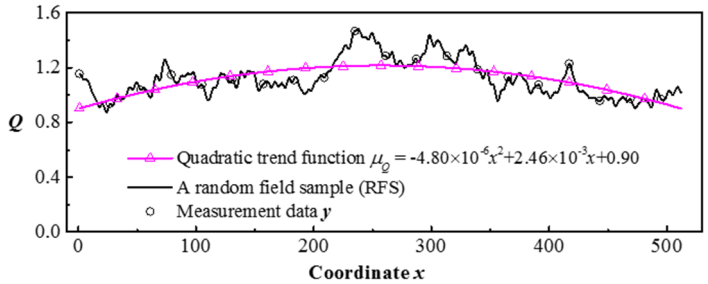

Figure 4. A random field sample (RFS) and limited measurement data y (Wang et al. 2019).

No de-trending is needed when using the BCS-KL generator, and RFSs are directly generated from measurement data without a pre-determined parametric function form of trend function or auto-covariance function. Figure 8 shows an example of 500 RFSs generated from BCS-KL generator with the same set of measurement data in Figures 4, 5, and 6. The average of the 500 RFSs is consistent with the original Q data. In addition, the BCS-KL generator is data-driven, and the RFSs generated converge the original Q data as the data quantity increases, as shown in Figure 9.

5.2 Simulation of non-stationary random field with non-stationary covariance

A Gaussian Wiener-Levy process random process with a non-stationary covariance is used to illustrate the BCS-KL generator in this subsection. The random process has a mean $\mu = 1$ and standard deviation $\sigma = 0.5$. The non-stationary covariance of the Weiner-Levy process is defined as $\boldsymbol{COV}(X_i, X_j) = \min(X_i, X_j)$, and its non-stationary variance function is normalized by the length of RFS (i.e., 512): $K_x^2=\frac{x}{512}\sigma^2$ with covariance function **COV**(x_i, x_j)=min(x_i/512, x_j/512). Figure 10 shows four samples of the Wiener-Levy process. Fifty data points (M = 50) are taken from each of the N_s = 100 RFSs (e.g., four of which are shown in Figure 10) and used as sparse measurement

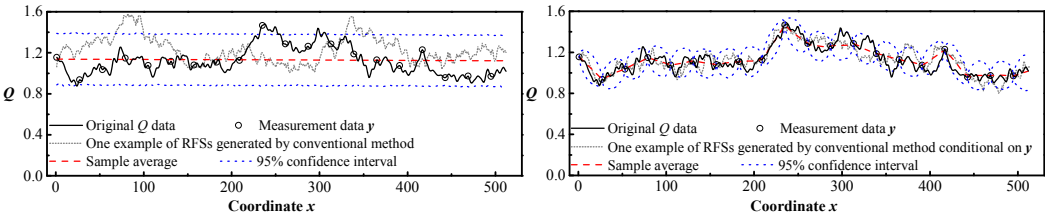

(a) Unconditional RFS (Wang et al. 2019) (b) Conditional RFS

Figure 5. RFSs generated using conventional method with removal of a linear trend.

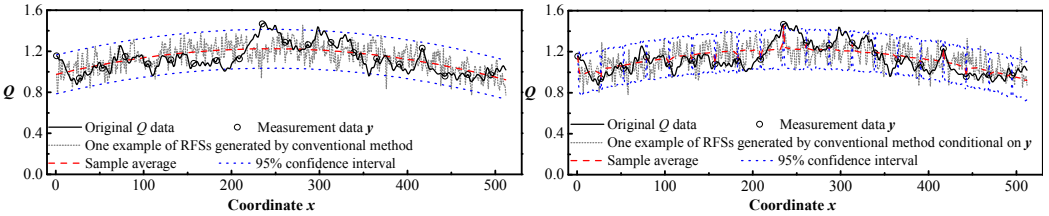

(a) Unconditional RFS (Wang et al. 2019) (b) Conditional RFS

Figure 6. RFSs generated using conventional method with removal of a quadratic trend.

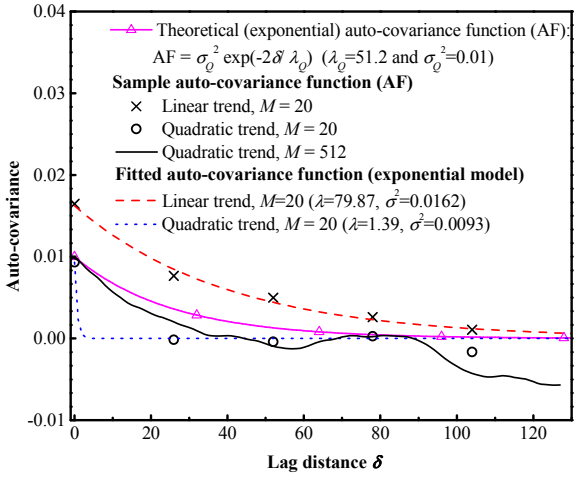

Figure 7. Sample and fitted auto-covariance functions after removal of a linear or quadratic trend (Wang et al. 2019).

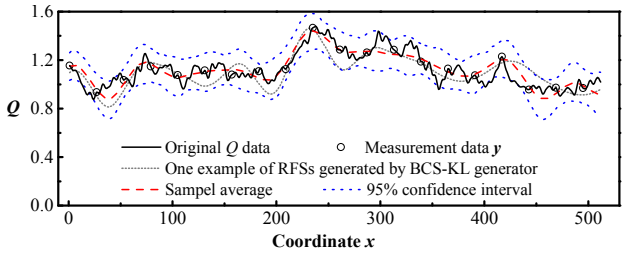

Figure 8. Direct generation of RFSs from measurement data y using the BCS-KL generator (Wang et al. 2019).

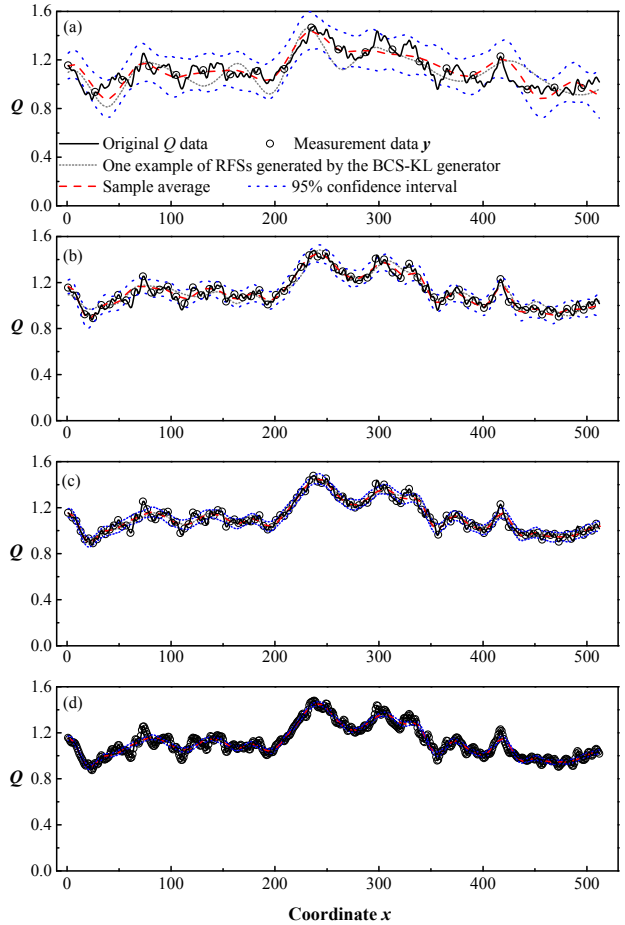

Figure 9. Direct generation of non-stationary RFSs using the BCS-KL generator based on different number of measurement points (M): (a) M = 20; (b) M = 64; (c) M = 128; and (d) M = 512 (Wang et al. 2019).

data and input to the BCS-KL generator, and N_B = 500 RFSs are directly simulated for each set of sparse measurement data. Figures 11a, b and c show the marginal cumulative distribution function (CDF) at x=256, correlation coefficients for x = 128, 256 and 384, and the variance function, respectively. The theoretical functions (see the red solid lines) are compared to the ones obtained from the BCS-KL generator (see the black dotted lines) and the ones obtained

from the original N_s = 100 sets of complete RFSs (see the blue dashed lines). A very good match is observed in the three subplots of Figure 11. The BCS-KL generator not only properly simulates the marginal CDF, but also quantifies the non-stationarity of the correlation matrix and the spatially varying variance function. The BCS-KL generator is able to simulate properly random fields that can be non-Gaussian and non-stationary, using limited and sparse measurement data.

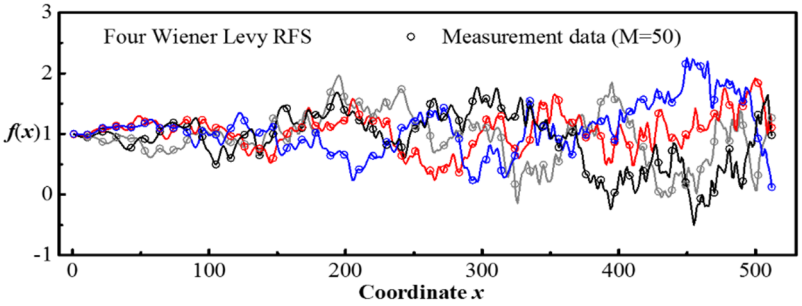

Figure 10. Illustration of non-stationary Wiener-Levy random process with M = 50 measurement data points as input to the BCS-KL generator.

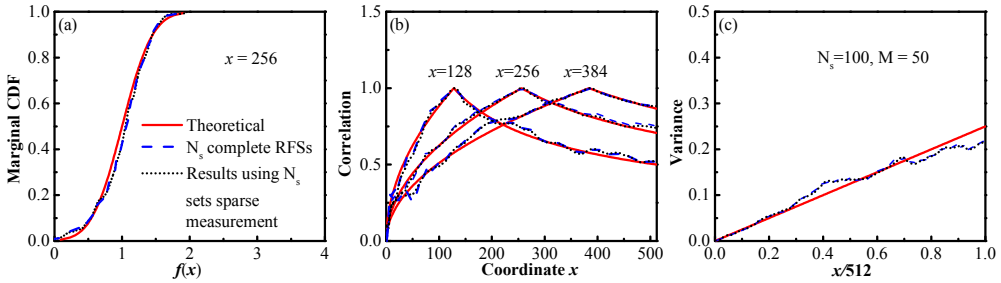

Figure 11. (a) Marginal cumulative distribution function (CDF), (b) Correlation coefficient, and (c) Variance for non-stationary Wiener Levy random process (Montoya-Noguera et al. 2019).

6 Conclusions

The current perspective in geotechnical data analysis is to regard the chicken (method) as preceding the egg (data). This paper explores the alternate data-driven perspective of regarding the egg as preceding the chicken. The entire data estate is therefore a core asset, not simply those that fit the needs of certain methods. A data-driven method is one that best utilizes this data estate for decision making.

The Bayesian compressive sampling (BCS) method is a possible data-driven candidate in terms of its ability to accommodate geotechnical data features and its responsiveness to changes in these features. Phoon et al. (2019) suggested that the features of geotechnical site data can be succinctly described as *MUSIC-X*: Multivariate, Uncertain and Unique, Sparse, Incomplete, and partially Corrupted with "*X*" denoting the spatial/temporal dimension. The results presented in this paper show that uncertainty (one of two "U"s), sparsity ("S"), and non-stationarity in "*X*" can be addressed using BCS with minimal assumptions. Results not covered in this paper show that "M" and "I" can be accommodated for bivariate data as well.

An important open question is whether the basis functions in BCS (which are prescribed) can reproduce the finer details of some sample paths such as those produced by the Whittle-Matérn

AF correctly when there are sufficient measurements (convergence). A second related question is whether it can retain its key practical advantage of representing such "rough" sample paths using sparse measurements (rate of convergence). It will be interesting to further explore the possibility of decoupling BCS from the KL expansion, which contains a fairly strong multivariate Gaussianity assumption.

7 Acknowledgments

The authors would like to thank Mr Yue Hu at City University of Hong Kong for generating Figs. 5b, 6b, and 10 in this paper. This paper was drafted during the lead author's sabbatical at the Institute for Risk and Reliability, Leibniz University, which was funded by the Alexander von Humboldt Foundation. The work on Bayesian compressive sampling described in this paper was supported by a grant from the Research Grants Council of the Hong Kong Special Administrative Region, China [Project No. 9042516 (CityU 11213117)]. The financial support is gratefully acknowledged.

8 References

Beer, M., Zhang, Y., Quek, S. T., and Phoon, K. K. 2013. Reliability analysis with scarce information: comparing alternative approaches in a geotechnical engineering context. Structural Safety, 41, 1-10.

Candès, E. J., Romberg, J. K., and Tao, T. 2006. Stable signal recovery from incomplete and inaccurate measurements. Communications on Pure and Applied Mathematics, 59(8), 1207-1223.

Candès, E. J. and Wakin, M. B. 2008). An introduction to compressive sampling. IEEE Signal Processing Magazine, 25(2), 21-30.

Ching, J. and Phoon, K. K. 2019a. Constructing a site-specific multivariate probability distribution using sparse, incomplete, and spatially variable data. ASCE Journal of Engineering Mechanics, under review.

Ching, J. and Phoon, K. K. 2019b. Modeling multivariate, uncertain, sparse, and incomplete site investigation data with spatial variation (MUSIC-X). Proceedings, 7th International Symposium on Geotechnical Safety and Risk (ISGSR 2019), in press.

Ching, J., Phoon, K. K., Beck, J. L. and Huang, Y. 2017. Identifiability of geotechnical site-specific trend functions. ASCE-ASME Journal of Risk and Uncertainty in Engineering Systems, Part A: Civil Engineering, 3(4), 04017021

Ching, J. and Phoon, K. K. 2017. Characterizing uncertain site-specific trend function by sparse Bayesian learning. Journal of Engineering Mechanics, ASCE, 143(7), 04017028.

Ching, J., Wu, S.-S., and Phoon, K. K. 2016. Statistical characterization of random field parameters using frequentist and Bayesian approaches. Canadian Geotechnical Journal, 53(2), 285-298.

Comerford, L., Jensen, H. A., Mayorga, F., Beer, M., and Kougioumtzoglou, I. A. 2017. Compressive sensing with an adaptive wavelet basis for structural system response and reliability analysis under missing data. Computers and Structures, 182, 26–40.

Comerford, L., Kougioumtzoglou, I. A., and Beer, M. 2016. Compressive sensing based stochastic process power spectrum estimation subject to missing data. Probabilistic Engineering Mechanics, 44, 66–76.

Donoho, D. L. 2006. Compressed sensing. IEEE Transactions on Information Theory, 52(4), 1289-1306.

Foucart, S., and Rauhut, H. 2013. A mathematical introduction to compressive sensing. Boston, USA: Birkhäuser.

Gerbert, P, Castagnino, S., Rothballer, C., Renz, A., and Filitz, R. 2016. Digital in Engineering and Construction. Boston Consulting Group.

Hu, Y., Zhao, T., Wang, Y., Choi, C., and Ng, C. W. W. 2019. Direct simulation of two-dimensional isotropic or anisotropic random field from sparse measurement using Bayesian compressive sampling. Stochastic Environmental Research and Risk Assessment, 33(8-9), 1477-1496.

Huang, Y., Beck, J. L., Wu, S., and Li, H. 2016. Bayesian compressive sensing for approximately sparse signals and application to structural health monitoring signals for data loss recovery. Probabilistic Engineering Mechanics, 31 (46), 62–79.

Ji, S., Dunson, D., and Carin, L. 2009. Multitask compressive sensing. IEEE Transactions on Signal Processing, 57(1), 92–106.

Ji, S., Xue, Y., and Carin, L. 2008. Bayesian compressive sensing. IEEE Transactions on Signal Processing, 56(6), 2346–2356.

Lacasse, S. and Nadim, F. 1996. Uncertainties in characterizing soil properties. Uncertainty in the Geologic Environment: From Theory to Practice, ASCE Geotechnical Special Publication (GSP), 58 (I), 49–75.

Liu, X., Wang, Y., and Li, D. 2019. Investigation of slope failure mode evolution during large deformation in spatially variable soils by random limit equilibrium and material point methods. Computers and Geotechnics, 111, 301-312.

Lumb, P. 1966. Variability of natural soils. Canadian Geotechnical Journal, 3(2), 74-97.

Montoya-Noguera, S., Zhao, T., Hu, Y., Wang, Y. and Phoon, K. K. 2019. Simulation of non-stationary non-Gaussian random fields from sparse measurements using Bayesian compressive sampling and Karhunen-Loève expansion. Structural Safety, 79, 66-79.

National Research Council. 1995. Probabilistic Methods in Geotechnical Engineering. National Academies Press, Washington, DC.

Pati, Y. C., Rezaiifar, R. and Krishnaprasad, P. S. 1993. Orthogonal matching pursuit: recursive function approximation with applications to wavelet decomposition. Proceedings, 27th Asilomar Conference on Signals, Systems and Computers. Pacific Grove, California, USA.

Phoon, K. K. 2017. Role of reliability calculations in geotechnical design. Georisk, 11(1), 4-21.

Phoon, K. K. 2018. Editorial for Special Collection on Probabilistic Site Characterization. ASCE-

ASME Journal of Risk and Uncertainty in Engineering Systems, Part A: Civil Engineering, 4(4), 02018002.

Phoon, K. K., Ching, J., and Wang, Y. 2019. Managing risk in geotechnical engineering – from data to digitalization. Proceedings, 7th International Symposium on Geotechnical Safety and Risk (ISGSR 2019), Taipei, Taiwan, in press.

Phoon, K. K., Huang, S. P., and Quek, S. T. 2002. Simulation of second-order processes using Karhunen–Loève expansion. Computers and Structures, 80(12), 1049–1060.

Phoon, K. K. and Kulhawy, F. H. 1999. Characterization of geotechnical variability. Canadian Geotechnical Journal, 36(4), 612–624.

State of the Nation Report. 2017. Digital Transformation. Institution of Civil Engineers. (Download: https://www.ice.org.uk/news-and-insight/policy/state-of-the-nation-2017-digital-transformation)

Stuedlein, A. W., Kramer, S. L., Arduino, P., and Holtz, R. D. 2012. Geotechnical characterization and random field modeling of desiccated clay. Journal of Geotechnical and Geoenvironmental Engineering, 138(11), 1301-1313.

Tipping, M. E. 2001. Sparse Bayesian learning and the relevance vector machine. Journal of Machine Learning Research, 1, 211-244.

Vanmarcke, E. H. 1977. Probabilistic modeling of soil profiles. Journal of the Geotechnical Engineering Division 103(11), 1227-1246.

Wang, Y. and Zhao, T. 2016. Interpretation of soil property profile from limited measurement data: a compressive sampling perspective. Canadian Geotechnical Journal, 53(9), 1547-1559.

Wang, Y. and Zhao, T. 2017. Statistical interpretation of soil property profiles from sparse data using Bayesian Compressive Sampling. Géotechnique, 67(6), 523-536.

Wang, Y., Akeju, O. V., and Zhao, T. 2017. Interpolation of spatially varying but sparsely measured geo-data: A comparative study. Engineering Geology, 231, 200-217.

Wang, Y., Zhao, T., and Phoon, K. K. 2018. Direct simulation of random field samples from sparsely measured geotechnical data with consideration of uncertainty in interpretation. Canadian Geotechnical Journal, 55(6), 862-880.

Wang, Y., Zhao, T., Hu, Y. and Phoon, K. K. 2019. Simulation of random fields with trend from sparse measurements without de-trending. ASCE Journal of Engineering Mechanics, 145(2), 04018130.

Zhao, T., Hu, Y. and Wang, Y. 2018. Statistical interpretation of spatially varying 2D geo-data from sparse measurements using Bayesian compressive sampling. Engineering Geology, 246, 162-175.

Zhao, T. and Wang, Y. 2018. Simulation of cross-correlated random field samples from sparse measurements using Bayesian compressive sensing. Mechanical Systems and Signal Processing, 112, 384-400.

GAUSSIAN MIXTURE BASED EQUIVALENT LINEARIZATION METHOD (GM-ELM): GENESIS, DEVELOPMENTS AND EARTHQUAKE ENGINEERING APPLICATIONS

Junho Song

Professor, Seoul National University, South Korea

GAUSSIAN MIXTURE BASED EQUIVALENT LINEARIZATION METHOD (GM-ELM): GENESIS, DEVELOPMENTS AND EARTHQUAKE ENGINEERING APPLICATIONS

Junho Song[1], Sang-ri Yi[2], Ziqi Wang[3]
[1] Department of Civil and Environmental Engineering, Seoul National University, Seoul, Korea
E-mail: junhosong@snu.ac.kr
[2] Department of Civil and Environmental Engineering, Seoul National University, Seoul, Korea
E-mail: yisangri@snu.ac.kr
[3] Earthquake Engineering Research & Test Center, Guangzhou University, Guangzhou, China
E-mail: ziqidwang@yahoo.com

Abstract: A new nonlinear random vibration analysis method termed Gaussian mixture based equivalent linearization method (GM-ELM) was recently proposed. GM-ELM approximates the probabilistic distribution of a nonlinear system response by a Gaussian mixture distribution model to decompose the non-Gaussian response of interest into multiple Gaussian responses of linear single-degree-of-freedom oscillators. Using this alternative concept of equivalent linear system (ELS) and random vibration theories, key response statistics including the mean up-crossing rate, first-passage probability and mean peak response can be obtained efficiently and accurately. GM-ELM has been further developed to improve its accuracy and overcome technical challenges with regard to dependency of the ELS on the ground motion intensity and requirement for the stationary condition. This paper summarizes the main idea and recent developments of GM-ELM, and presents GM-ELM based fragility analysis of nonlinear structures under nonstationary excitations. The results will be compared with those by existing random vibration analysis methods to identify merits and future research topics.

Keywords: Equivalent linearization, Fragility analysis, Gaussian mixture, Nonlinear analysis, Random vibration

1 Introduction

Random vibration analysis of structural systems subjected to stochastic excitations such as earthquake, wind or wave loading has been the focus of numerous researchers in the past several decades. Fundamental progresses have been made in analyzing linear structures, yet the analysis of general multi-degree-of-freedom (MDOF) nonlinear systems still poses significant challenges. Various nonlinear random vibration analysis approaches have been developed, among which the equivalent linearization method (ELM) (Atalik and Utku, 1974; Wen, 1980; Casciati et al., 1993) has gained wide popularity because of its applicability to general MDOF nonlinear systems. Other classical methods such as Fokker-Planck equation, stochastic averaging, moment closure and perturbation (Lutes and Sarkani, 2004) might be more accurate, but are mainly restricted to specific (and usually simple) nonlinear systems. Sampling based methods (Rubinstein and Melamed, 1998) have less restrictions, but they are computationally expensive, especially for complex MDOF structural systems with a low level of failure probability.

In ELM, the nonlinear system of interest is replaced by an equivalent linear system with the same DOF. In a conventional approach of ELM, parameters of the equivalent linear system are determined via minimizing the mean-square error between the responses of the nonlinear and linear systems (Atalik and Utku, 1974; Wen, 1980). In general, ELM could be accurate in estimating

the mean-square responses, but it may not capture the non-Gaussianity of the nonlinear responses effectively. As a consequence, using ELM to estimate response statistics such as response probability distributions could be far from correct, especially in the tail region of the distribution. Therefore, as an alternative to the conventional ELM, a non-parametric ELM based on first-order reliability method (FORM) (Der Kiureghian, 2005), namely the tail-equivalent linearization method (TELM) was proposed recently (Fujimura and Der Kiureghian, 2007). In TELM, an equivalent linear system is numerically obtained in terms of a discretized impulse-response function or frequency-response function, using knowledge of the 'design point' determined from FORM analysis. In comparison to the conventional ELM, TELM has superior accuracy in estimating the response probability distributions, especially in the tail region. At the same time, however, TELM is computationally more expensive than the conventional ELM, since TELM involves performing FORM analysis for a sequence of response threshold values. Moreover, in contrast to ELM, TELM is restricted to structural models using smooth constitutive laws with weak stiffening effect.

Motivated by benefits and limitations of conventional ELM and TELM, and using the concept of mixture distribution models (McLachlan and Peel, 2000), a new equivalent linearization method, namely the Gaussian mixture based equivalent linearization method (GM-ELM) was recently developed (Wang and Song, 2017). The initial version of GM-ELM employs a univariate Gaussian mixture (GM) distribution model to approximate the non-Gaussian probabilistic distribution of a nonlinear system response under stationary and ergodic assumptions. Properties of the GM distribution model enable the GM-ELM to decompose the non-Gaussian response of a nonlinear system into multiple Gaussian responses of linear single-degree-of-freedom (SDOF) oscillators. Using a probabilistic combination technique, a mixture of equivalent linear systems identified by GM-ELM can provide accurate estimation of the nonlinear response distribution. The authors further developed GM-ELM to improve its applicability and accuracy (Yi et al., 2018; Yi et al., 2019).

This paper starts by introducing the main theories of the GM-ELM, followed by computational details of the method. Section 3 introduces a further developed version of GM-ELM that incorporates the amount of dissipated hysteretic energy in ELS by finding equivalent damping as well as equivalent stiffness. Section 4 presents the temporal-average GM-ELM to embrace the nonstationary responses. In Section 5, the GM-ELM approach is further generalized by introducing a strategy to obtain the universal ELS which does not depend on the ground motion intensity. Identification of universal ELS provides significant advantages when one aims for efficient seismic fragility analysis. Section 6 demonstrates a numerical example in which a nonstationary earthquake ground motion model and a hysteresis oscillator are used. The paper is concluded by a summary and an outlook on future research topics.

2 Gaussian Mixture based Equivalent Linearization Method

Gaussian Mixture based Equivalent Linearization (GM-ELM) was first developed for random vibration analysis of a nonlinear system under the assumption of stationary responses (Wang and Song, 2017). This chapter summarizes fundamental ideas of how the new equivalent-linear-system concept is retrieved from a Gaussian mixture (GM) probability density function (PDF) model of the structural response.

2.1 Basic ideas of GM-ELM

GM-ELM approximates stochastic responses of a nonlinear structure in terms of those by an equivalent linear system (ELS). Specifically, GM-ELM identifies a group of single degree-of-freedom (SDOF) oscillators as an ELS, which collectively reproduce stochastic properties of nonlinear response in terms of readily formulated combination rules. The ELS achieves the equivalence by capturing the whole shape of the response PDF by the superposition of the response PDFs of the linear oscillators which are randomly activated, constantly switching from one to another. The underlying assumption of GM-ELM analysis is that the input excitation is represented as a stationary Gaussian process, for example, by considering strong and stationary period during an earthquake event, or using a memoryless linear or nonlinear transformation (Soong and Grigoriu, 1993) of a stationary Gaussian process. The non-Gaussian PDF is fitted by a GM model to describe the response by multiple Gaussian PDFs. Because the dynamic response of a linear structure excited by a Gaussian input process also follows a Gaussian distribution, the densities in the fitted GM model lead to multiple linear SDOF oscillators that collectively describe the nonlinear response.

Consider a stationary response of general multi-degree-of-freedom (MDOF) nonlinear structure at time t subjected to the stationary excitation, for which the PDF of the instantaneous responses are time-invariant, i.e. $f_z(z;t) = f_z(z)$. Then, a GM-based approximation of the PDF is

$$f_z(z) \simeq f_{GM}(z;\boldsymbol{\nu}) = \sum_{k=1}^{K} \alpha_k f_{\mathcal{N}}(z;\mu_k,\sigma_k^2) \tag{1}$$

where K is the total number of Gaussian components. The parameter α_k is the relative contribution of each component, and μ_k and σ_k^2 are respectively its mean and variance. The response variable, denoted by z, could represent the response of interest, e.g. displacement at specific location of a nonlinear system. The GM parameters $\{\alpha_k, \mu_k, \sigma_k\}$ provides the information on the corresponding equivalent linear oscillator. While α_k and μ_k respectively represent the relative occurrence rate and underlying displacement shift of the k-th oscillator, σ_k is used to infer its structural parameters. The explicit relationship between a linear SDOF system parameters and its response variance is (Lutes and Sarkani, 2004)

$$\sigma_z^2 = 2\int_0^\infty |H(\omega)|^2 S_g(\omega) d\omega \tag{2}$$

where $H(\omega)$ is the frequency response function (FRF) of the SDOF system. For example, if a system response subjected to ground acceleration excitation is of concern, the following FRF is used:

$$H_k(\omega) = \frac{s_{eq,k}}{m_{eq,k} + i\omega c_{eq,k} - \omega^2 k_{eq,k}} \tag{3}$$

in which $k_{eq,k}$, $c_{eq,k}$ and $m_{eq,k}$ are the stiffness, damping and mass of the k-th linear oscillator, respectively, and $s_{eq,k}$ is a scaling factor which depends on the response quantity of interest. The parameters of FRF in Eq. (4) cannot be determined by using Eq. (3) only. Wang and Song (2017) suggested that $m_{eq,k}$ and $c_{eq,k}$ can be fixed to some pre-specified values, e.g. nodal mass and initial damping, so that only $k_{eq,k}$ needs to be identified from Eq. (4). This heuristic aspect of GM-ELM was later diagnosed and improved by introducing bivariate GM-ELM (Yi et al., 2018).

To determine the parameters $\boldsymbol{\nu}$ of the GM model $f_{GM}(z;\boldsymbol{\nu})$, one needs to obtain the exact or approximate PDF of the response of interest in advance. The most straightforward approach is to directly obtain samples of the response PDF by a small number of dynamic analysis. By introducing

ergodic assumption, a significant amount of computational requirement is reduced. Other approaches such as Fokker-Planck equations, response surface methods, FORM could also be applied to further reduce the computational effort (Yi et al., 2018). Fig. 1 summarizes the concept and procedure of GM-ELM. Further developments in the following sections retain this fundamental concept of linearization.

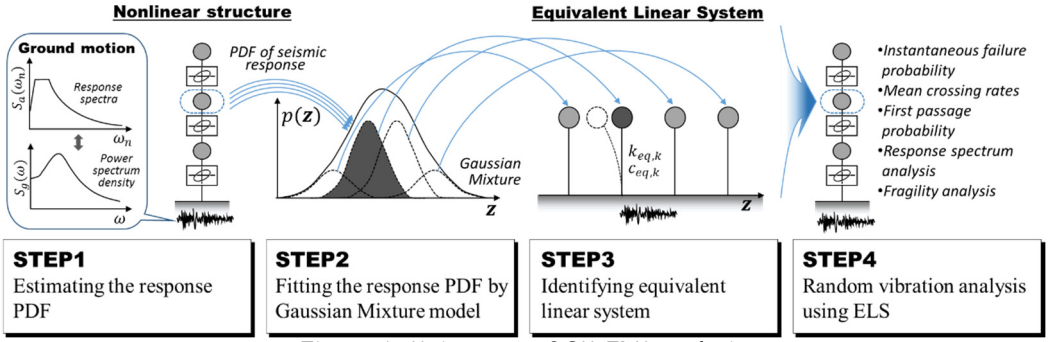

Figure 1. Main steps of GM-ELM analysis

2.2 Random vibration analysis by GM-ELM

The collective response of ELS can approximate the nonlinear response by Step 4 in Fig.1. Firstly, the instantaneous failure probability with respect to a threshold z_0 can be computed as

$$\Pr[Z > z_0] = \sum_{k=1}^{K} \Pr[I_k = 1] \Pr[Z > z_0 | I_k = 1] = \sum_{k=1}^{K} \alpha_k \left[1 - \Phi\left(\frac{z_0 - \mu_k}{\sigma_k}\right)\right] \tag{4}$$

where I_k is the kth element of a K-dimensional random vector in which only one element takes 1 while the others take 0 according to the probabilities α_k, and $\Phi(\cdot)$ denotes the cumulative distribution function (CDF) of the standard normal distribution. Next, from an intuition that, for an infinitesimal δt, it is unlikely that the linear system 'switches' from one of the K equivalent linear systems to another, the mean up-crossing rate of the response is derived as the weighted sum of the crossing rates of each linear oscillators, i.e.

$$\nu^+(z_0) = \lim_{\delta t \to 0} \frac{\sum_{k=1}^{K} \alpha_k \Pr\{Z_k(t) < z_0 \cap Z_k(t+\delta t) > z_0\}}{\delta t} = \sum_{k=1}^{K} \alpha_k \nu_k^+(z_0) \tag{5}$$

and

$$\nu_k^+(z_0) = \frac{1}{2\pi} \sqrt{\frac{\lambda_{2,k}}{\lambda_{0,k}}} \exp\left[-\frac{0.5(z_0 - \mu_{z,k})^2}{\lambda_{0,k}}\right] \tag{6}$$

in which $\lambda_{j,k}$ is the j-th order spectral moment (Lutes and Sarkani 2004) of the k-th linear oscillator. By assuming that the crossing events form a Poisson process, the first passage probability during the excitation duration T_d is also derived as

$$P_f(z_0) = 1 - A\, exp\left(-\sum_{k=1}^{K} \alpha_k \nu_k^+(z_0)\, T_d\right) \tag{7}$$

where A is the probability of the safe start, i.e. $A = Pr(z < z_0)$. In a similar manner, the mean peak response of the structure can be conveniently approximated as a combination of the linear response spectrum analysis results (Yi et al., 2018).

3 Bivariate GM-ELM

In order to identify more precise ELS, Yi et al. (2018) proposed to use the joint PDF of the response $Z(t)$ and its time derivative $\dot{Z}(t)$, which is modeled by a bivariate Gaussian mixture, instead of using the univariate mixture for $Z(t)$ only. By utilizing this additional information, dissipated energy from non-linear hysteretic behaviors can be captured by ELS via the optimized equivalent damping values, while the previous heuristic assumptions are removed. Moreover, this bivariate GM-ELM is consistent with the theoretical backgrounds of Gaussian mixture decomposition discussed in the previous section since the derivative of stationary Gaussian random process for the response of equivalent linear systems is also a Gaussian process.

3.1 Equivalent linear system identified by bivariate Gaussian mixture

In the bivariate GM-ELM, instead of univariate Gaussian mixture model $f_{GM}(z;\boldsymbol{\nu})$ in Section 2.1, bivariate Gaussian mixture model $f_{GM}(\boldsymbol{z};\boldsymbol{\nu})$ is introduced in the space of generic stationary nonlinear response $Z(t)$ and its time derivative $\dot{Z}(t)$, denoted by $\boldsymbol{z}=\{z,\dot{z}\}$ as follows:

$$f_{\boldsymbol{z}}(\boldsymbol{z}) \simeq f_{GM}(\boldsymbol{z};\boldsymbol{\nu}) \sum_{k=1}^{K} \alpha_k f_{\mathcal{N}_2}(\boldsymbol{z};\boldsymbol{\mu}_k,\boldsymbol{\Sigma}_k) \tag{8}$$

where $f_{\mathcal{N}_2}(\boldsymbol{z};\boldsymbol{\mu}_k,\boldsymbol{\Sigma}_k)$ denotes the bivariate Gaussian PDF, each representing equivalent linear oscillators with mean $\boldsymbol{\mu}_k=\{\mu_{z,k},\mu_{\dot{z},k}\}$ and (2×2) covariance matrix of $Z(t)$ and $\dot{Z}(t)$, denoted by $\boldsymbol{\Sigma}_k$. The bivariate GM-ELM uses Eq. (3) and the following equation derived from linear random vibration theories, which provides additional information for identifying equivalent linear systems:

$$\sigma_{\dot{z},k}^2 = \int_{-\infty}^{\infty} \omega^2 |H_k(\omega)|^2 S_g(\omega) d\omega,\ k=1,\dots,K \tag{9}$$

where, $H_k(\omega)$ is the FRF of the equivalent linear systems in Eq. (4). Using knowledge on $\sigma_{z,k}$ and $\sigma_{\dot{z},k}$ available in Eq. (3) and Eq. (9) respectively, the linear system parameter $c_{eq,k}$ and $k_{eq,k}$ can be determined without introducing heuristic constraints.

3.2 Random vibration analysis by bivariate GM-ELM

The bivariate GM-ELM features the following derivation of the mean crossing rate as an alternative to Eq. (5). In theories of linear random vibration analysis (Lutes and Sarkani, 2004), the up-crossing rate of a general stationary response $Z(t)$ can be computed by the joint PDF of $Z(t)$ and $\dot{Z}(t)$, i.e.

$$\nu^{+}(\mathrm{z}) = \int_0^{\infty} \int_{\mathrm{z}-\dot{\mathrm{z}}\Delta\mathrm{t}}^{\mathrm{w}} \mathrm{p}(\mathrm{w},\dot{\mathrm{z}})\mathrm{dw}\,\mathrm{d}\dot{\mathrm{z}} = \int_0^{\infty} \dot{\mathrm{z}}\,\mathrm{p}(\mathrm{z},\dot{\mathrm{z}})\mathrm{d}\dot{\mathrm{z}} \tag{10}$$

Substituting the fitted bivariate GM model $f_{GM}(\boldsymbol{z};\boldsymbol{\nu})$ of Eq. (8) into Eq. (10), we get

$$\nu^{+}(\mathrm{z}) = \sum_{\mathrm{k}=1}^{\mathrm{K}} \alpha_{\mathrm{k}} \int_0^{\infty} \dot{\mathrm{z}} \mathrm{f}_{\mathcal{N}_2}(\mathrm{z},\dot{\mathrm{z}};\boldsymbol{\mu}_{\mathrm{k}},\boldsymbol{\Sigma}_{\mathrm{k}})\mathrm{d}\dot{\mathrm{z}} = \sum_{\mathrm{k}=1}^{\mathrm{K}} \tilde{\alpha}_{\mathrm{k}} \nu_{\mathrm{k}}^{+}(\mathrm{z}) \tag{11}$$

which leads to the same expression as Eq. (5) except the contribution factor of each linear component which is now modified using the statistics derived from the bivariate PDF, i.e.

$$\tilde{\alpha}_{\mathrm{k}} = \sqrt{2\pi}\left(\varphi(\delta_{\dot{\mathrm{z}},\mathrm{k}}) + \delta_{\dot{\mathrm{z}},\mathrm{k}} - \delta_{\dot{\mathrm{z}},\mathrm{k}}\Phi(-\delta_{\dot{\mathrm{z}},\mathrm{k}})\right) \tag{12}$$

where $\varphi(\cdot)$ is the probability density function (PDF) of the standard normal distribution, and $\delta_{\dot{z},k} = \mu_{\dot{z},k}/\sigma_{\dot{z},k}$. Also by replacing α_k in Eq. (7) by $\tilde{\alpha}_k$, the first passage probability can be improved as well. It was shown in Yi et al. (2018) that the use of bivariate GM-ELM could

significantly improve the estimation accuracy for some nonlinear systems.

4 Temporal-average GM-ELM

So far, the choice of excitation models for GM-ELM has been limited, due to the underlying assumption of stationary ergodic responses. In order to overcome these restrictions and incorporate the nonstationary excitation and response, the temporal-average GM-ELM is proposed by Yi et al. (2019)

4.1 Concept of temporal-average ELS

To embrace the nonstationary responses, we first consider the temporal-average PDF of the response. Since the nonstationary response has a time-variant PDF $f_{\boldsymbol{z}}(\boldsymbol{z};t)$, its temporal average is represented as

$$\widehat{\mathrm{f}_{\mathbf{z}}}(\mathbf{z}) = \frac{1}{\mathrm{T_d}}\int_{\mathrm{T_i}}^{\mathrm{T_e}} \mathrm{f_z}(\mathbf{z};\mathrm{t})\mathrm{dt} \tag{13}$$

where T_i and T_e respectively denote the starting and ending time points of the strong motion duration $T_d = T_e - T_i$. By using $\widehat{f_{\boldsymbol{z}}}(\boldsymbol{z})$ in place of $f_{\boldsymbol{z}}(\boldsymbol{z})$ in Eq. (1) or Eq.(8), one could identify the temporal-average ELS. This ELS enables us to utilize the same GM-ELM analysis procedures in Fig. 1. Unlike ELS identified by the existing GM-ELM, which only incorporates stationary responses, temporal-average ELS has the following properties:

- The nonstationary nonlinear response can be approximated by a set of stationary linear responses. The corresponding stationary linear responses are acquired from the equivalent stationary excitation, which is defined as the temporal average of nonstationary PSD. If the nonstationary excitation is represented by an evolutionary PSD $S_g(\omega,t)$ (Lutes and Sarkani, 2004), its temporal average can be calculated as:

$$\hat{\mathrm{S}}_{\mathrm{g}}(\omega) = \frac{1}{\mathrm{T_d}}\int_{\mathrm{T_i}}^{\mathrm{T_e}} \mathrm{S_g}(\omega,\mathrm{t})\mathrm{dt} \tag{14}$$

- While the response statistics such as the instantaneous failure probabilities or the mean up-crossing rate are also time-variant in nonstationary process, the proposed temporal-average GM-ELM analysis produces the time-averaged values of those. Specifically, the mean up-crossing rate obtained using Eq.(5) or Eq.(11) correspond to the time averaged value of the crossing rate, i.e.

$$\hat{\nu}_{\mathrm{k}}(\mathrm{a}) = \frac{1}{\mathrm{T_d}}\int_{\mathrm{T_i}}^{\mathrm{T_e}} \nu_{\mathrm{k}}(\mathrm{a};\mathrm{t})\mathrm{dt} \tag{15}$$

This is a temporal average of the crossing rate formulation of Rice (1945). Under the nonhomogeneous Poisson assumptions of the crossing events, the first passage probability is then estimated by the same formulation in Eq. (7) by replacing $\nu_k(a)$ with $\hat{\nu}_k(a)$.

- For stationary inputs and responses, time-average GM-ELM analysis is identical to the existing GM-ELM.

4.2 Strong motion duration of temporal-average GM-ELM

The strong motion duration of the nonstationary response is identified for the temporal-average GM-ELM as discussed below. Since the critical response of a structure is expected to occur while

the external energy is being supplied, we introduce a criteria defined in terms of the cumulative energy of input ground motions. Particularly, Arias intensity $I_A(t)$, i.e. the integration of the squared excitation history, is adopted. The average Arias intensity is derived in terms of the evolutionary PSD model (Zembaty, 1988), i.e.

$$\mathrm{E}[\mathrm{I_A(t)}] = \mathrm{E}\left[\frac{\pi}{2g}\int_0^t \mathrm{f(t)^2 dt}\right] = \frac{\pi}{g}\int_0^t\int_0^\infty \mathrm{S_g}(\omega,\tau)\,\mathrm{d}\omega\,\mathrm{d}\tau \tag{16}$$

The cumulated amount of energy by time t can be normalized by that of the overall duration T. The starting and ending time of the strong motion duration are defined as the time points when the normalized value reaches 5% and 99% respectively, in order to cover the time interval which critical response is likely to occur.

5 Intensity-augmented GM-ELM

It is noted that fragility analysis using GM-ELM could be inefficient due to the dependency of the ELS on the ground motion intensity. This is because the identification of ELS hinges on the response PDF of the system. In order to overcome this inefficiency, Yi et al. (2019) proposed intensity-augmented GM-ELM which identifies universal ELS that is invariant to the scaling of excitation.

5.1 Concept of universal equivalent linear system

Consider an auxiliary variable I which represents the intensity scale of an earthquake event. By assigning arbitrary distribution, e.g. uniform distribution, to the variable, we define the intensity-augmented PDF as

$$\mathrm{f_{\mathbf{z},I}}(\mathbf{z},\mathrm{I}) = \mathrm{f_{\mathbf{z}|I}}(\mathbf{z}|\mathrm{I})\mathrm{f_I}(\mathrm{I}) \tag{17}$$

which could be approximated using Gaussian mixture distribution model with a higher dimension. By imposing independent condition between I and $\boldsymbol{z}$, we obtain

$$\mathrm{f_{\mathbf{z},I}}(\mathbf{z},\mathrm{I}) \simeq \sum_{\mathrm{k=1}}^{\mathrm{K}} \tilde{\alpha}_\mathrm{k}\mathrm{f_N}\left(\mathrm{z},\mathrm{I}\middle|\tilde{\boldsymbol{\mu}}_\mathrm{k},\tilde{\boldsymbol{\Sigma}}_\mathrm{k}\right) = \sum_{\mathrm{k=1}}^{\mathrm{K}} \tilde{\alpha}_\mathrm{k}\mathrm{f_N}\left(\mathrm{I}\middle|\tilde{\mu}_{\mathrm{I,k}},\tilde{\sigma}^2{}_{\mathrm{I,k}}\right)\mathrm{f_N}\left(\mathrm{z}\middle|\tilde{\boldsymbol{\mu}}_{\mathrm{z,k}},\tilde{\boldsymbol{\Sigma}}_{\mathrm{z,k}}\right) \tag{18}$$

Using the marginalized distribution with respect to I, the conditional PDF of response given I is derived as

$$\mathrm{f_{\mathbf{z},I}}(\mathbf{z}|\mathrm{I}) = \frac{\mathrm{f_{z,I}}(\mathbf{z},\mathrm{I})}{\mathrm{f_I}(\mathrm{I})} = \sum_{\mathrm{k=1}}^{\mathrm{K}} \alpha_\mathrm{k}^*(\mathrm{I})\mathrm{f_N}\left(\mathrm{z}\middle|\tilde{\boldsymbol{\mu}}_{\mathrm{z,k}},\tilde{\boldsymbol{\Sigma}}_{\mathrm{z,k}}\right) \tag{19}$$

where

$$\alpha_\mathrm{k}^*(\mathrm{I}) = \frac{\tilde{\alpha}_\mathrm{k}\mathrm{f_k}\left(\mathrm{I}\middle|\tilde{\mu}_{\mathrm{I,k}},\tilde{\sigma}^2{}_{\mathrm{I,k}}\right)}{\sum_{\mathrm{n=1}}^{\mathrm{K}}\tilde{\alpha}_\mathrm{n}\mathrm{f_n}\left(\mathrm{I}\middle|\tilde{\mu}_{\mathrm{I,n}},\tilde{\sigma}^2{}_{\mathrm{I,n}}\right)} \tag{20}$$

quantifies the contribution of the k-th component given the intensity scale I. The conditional distribution is reduced back to the Gaussian mixture approximation with the dimension of $\boldsymbol{z}$. Note that, in Eq. (19), the parameter related to the augmented dimension only affects the contribution factor $\alpha_k^*(I)$, and the parameters of each Gaussian distribution component do not change over the intensity. The ELS identified from intensity-augmented PDF is termed as the universal ELS, owing to the following properties:

- The structural properties and base locations of the universal equivalent linear oscillators are invariant to the scaling of excitations. Therefore, this ELS needs to be identified only once for

fragility analysis.

- The relative rate of occurrence or contribution between the oscillators changes for different intensities. This can be re-evaluated by simple calculation of Eq. (20), once the mixture parameters are determined.

In general, it is difficult to know the exact shape of the temporal-average and intensity-augmented PDF. Therefore, the most practical choice is to approximate it by discretized result of nonlinear dynamic simulations. In particular, to obtain samples of the intensity-augmented PDF, one could first generate an intensity measure of the ground motion, and perform nonlinear dynamic simulations, by generating artificial ground motion time history that fits to the intensity. An enough number of samples can be obtained by repeating the procedure.

6 Numerical example

To demonstrate GM-ELM, we consider a hysteretic *oscillator with an expression*

$$\mathrm{m}\ddot{\mathrm{X}}(\mathrm{t}) + \mathrm{c}\dot{\mathrm{X}}(\mathrm{t}) + \mathrm{k}_0[\alpha \mathrm{X}(\mathrm{t}) + (1-\alpha)\mathrm{Y}(\mathrm{t})] = -\mathrm{m}\ddot{\mathrm{U}}_\mathrm{g}(\mathrm{t}) \tag{21}$$

where $\ddot{\mathrm{X}}(\mathrm{t})$, $\dot{\mathrm{X}}(\mathrm{t})$, *and* $\mathrm{X}(\mathrm{t})$ *respectively denote the acceleration, velocity and* displacement *of the oscillator, and* m, c *and* k_0 *are the mass, damping and initial stiffness. The parameter* $\alpha = 0.1$ *represents the ratio of post- to pre-yield stiffness. The hysteretic response term* $\mathrm{Y}(\mathrm{t})$ *follows the Bouc-Wen hysteresis model (Wen, 1980), i.e.*

$$\dot{\mathrm{Y}}(\mathrm{t}) = -\gamma\left|\dot{\mathrm{X}}(\mathrm{t})\right||\mathrm{Y}(\mathrm{t})|^{\bar{\mathrm{n}}-1}\mathrm{Y}(\mathrm{t}) - \eta|\mathrm{Y}(\mathrm{t})|^{\bar{\mathrm{n}}}\dot{\mathrm{X}}(\mathrm{t}) + \mathrm{A}\dot{\mathrm{X}}(\mathrm{t}) \tag{22}$$

in which the shape parameters are set as $\gamma = \eta = 1/(2u_y^{\bar{n}})$ where the yielding displacement is $u_y = 0.024m$. The value of the other parameters are $\bar{n} = 3$ and $A = 1$. The initial natural period is 0.2s, and damping ratio is 0.1. The ground motion time history is modeled as a nonstationary process represented by an evolutionary PSD, i.e. $S_g(\omega,t) = \left|A_g(\omega,t)\right|^2 S_o$ in which S_o is the intensity of an underlying white-noise, with the following modulating functions (Rezaeian et al., 2008)

$$\mathrm{A}_\mathrm{g}(\omega,\mathrm{t}) = \mathrm{q}(\mathrm{t})\Phi_\mathrm{g}(\omega|\mathrm{t}) \tag{23}$$

where $q(t)$ is the time-modulating function and $\Phi_g(\omega|t)$ is the frequency-modulating function that depends on time.

$$\Phi_\mathrm{g}(\omega|\mathrm{t})^2 = \frac{\omega_\mathrm{f}(\mathrm{t})^4 + 4\zeta_\mathrm{f}(\mathrm{t})^2\omega_\mathrm{f}(\mathrm{t})^2\omega^2}{(\omega_\mathrm{f}(\mathrm{t})^2 - \omega^2)^2 + 4\zeta_\mathrm{f}(\mathrm{t})^2\omega_\mathrm{f}(\mathrm{t})^2\omega^2} \tag{24a}$$

$$\mathrm{q}(\mathrm{t};\boldsymbol{\alpha}) = \alpha_1 \mathrm{t}^{\alpha_2 - 1}\exp(-\alpha_3 \mathrm{t}) \tag{24b}$$

for which the parameters are chosen as $\omega_f(t) = 22.37 - 0.44(t - 22.59)$ in the unit of rad/s and $\zeta_f(t) = 0.22$. The unit of t is seconds. For $q(t)$, the gamma modulating function is used with the parameters of $\boldsymbol{\alpha} = \{\alpha_1, \alpha_2, \alpha_3\} = \{1.2 \times 10^{-10}, 11.6,\ 0.47\}$. Detailed discussion about choice of the parameters and derivation of relations are available in Rezaeian et al. (2008) and Rezaeian and Der Kiureghian (2010). The strong motion duration is estimated as 20s.

Figure 2 shows the mean up-crossing rates and first-passage probabilities obtained by the temporal-average and intensity-augmented (tri-variate) GM-ELM analysis. A total of 600 different IM values are sampled from uniform distribution $IM \sim U[0, 3.3]$, and the corresponding 600 ground

accelerograms are generated to obtain the samples of $\{z, \dot{z}, IM\}$ through nonlinear dynamic analysis. A total of 196 Gaussian components are used to fit the 3-dimensional intensity-augmented PDF. To get reference MCS results, 5×10^4 runs of dynamic analysis are performed for each intensity level. For the comparison purpose, the results of original GM-ELM analysis using equivalent stationary excitation are also presented. The stationary strong motion duration is defined as the time segment in which the intensity of the excitation peaks exceeds a half of the maximum peak intensity, and the corresponding equivalent stationary PSD is the temporal average of PSD throughout the duration (Duan and Chen, 1999). From the results, one can confirm that equivalent stationary response could highly underestimate the failure probability, therefore it is necessary to assess nonstationary responses.

Figure 3 shows the results of the fragility analysis of nonstationary ground excitations for comparison with TELM (with total 510 runs of dynamic analysis) and MCS results. For the nonstationary TELM analysis, the approximation method proposed in Broccardo (2014), so called "evolutionary TELM" is adopted. However, it should be noted that further investigation and development of the nonstationary TELM are currently underway. Therefore, we performed TELM analysis based on the general procedure discussed in Broccardo (2014) as follows. First, we identified the base tail-ELS from stationary white-noise excitation. Next, the identified ELS is converted into nonstationary evolutionary tail-ELS using the modulating function. Finally, the sampling algorithm in Au and Beck (2001) is employed to evaluate the first passage probability. It is confirmed that the combined application of temporal-average and intensity-augmented GM-ELM accurately evaluate the fragilities for nonstationary excitations.

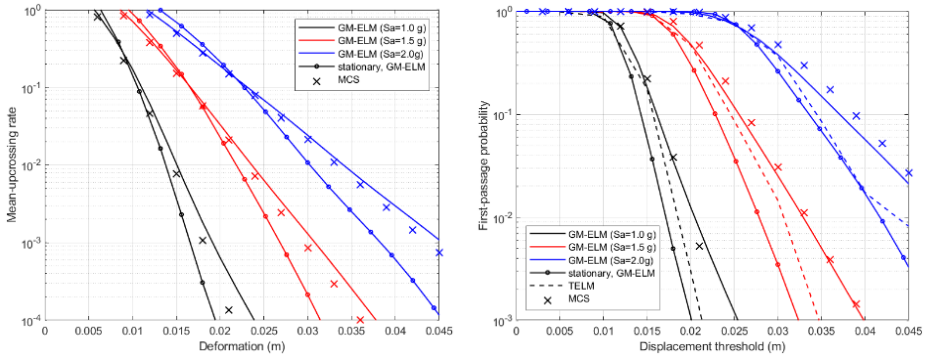

Figure 2 Mean up-crossing rates (left) and first-passage probabilities (right) obtained by temporal-average GM-ELM, equivalent stationary GM-ELM, TELM and MCS

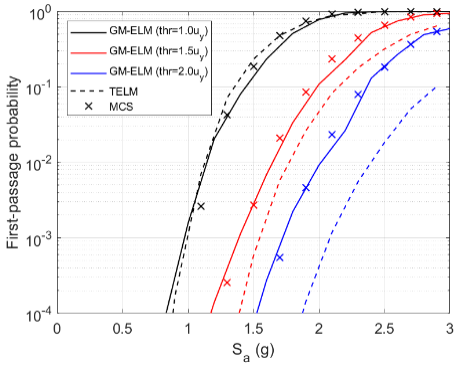

Figure 3. Fragility curves by GM-ELM, TELM and MCS

7 Conclusions

This paper presents a review on the state-of-art development of a stochastic dynamic analysis approach, termed Gaussian mixture based equivalent linearization method (GM-ELM). This new linearization method was initially proposed in attempt to identify an equivalent linear system (ELS) that could preserve the whole shape of the instantaneous probability distribution of a stationary nonlinear response. Using GM-ELM, the arbitrary non-Gaussian nonlinear response is decomposed as a collection of multiple Gaussian linear responses. Therefore, once ELS is identified by Gaussian mixture fitting scheme and structural parameter optimizations, complicated nonlinear responses could be estimated as a combination of the results of linear random vibration analysis. These results include instantaneous failure probability, mean up-crossing rates, first-passage probability, and mean peak response by response spectrum analysis. After introducing basic concept of GM-ELM, three major developments were made: (1) optimization of equivalent damping values, (2) embracement of the non-stationary excitations, and (3) identification of universally equivalent linear system. These further developments respectively allow us to increase the estimation accuracy, employ realistic, i.e. nonstationary stochastic ground motion models, and re-use the identified ELS to obtain nonlinear response subjected to a range of excitation intensities. The encouraging results of the numerical example confirm merits of applying GM-ELM to earthquake engineering problems.

Further research is underway to identify temporal-average and intensity-augmented probability density function more efficiently, in place of brute force sampling approach. In addition, to overcome the inaccuracy of using Poisson assumption in computing first passage probabilities by GM-ELM, a new method is being developed to account for temporal correlations between the passage events, especially when the narrow-band responses are of interest.

8 References

Atalik, T. Selcuk, and Senol Utku. 1976. "Stochastic linearization of multi-degree-of-freedom non-linear systems." *Earthquake Engineering & Structural Dynamics* 4, no.4: 411-420.

Armen Der Kiureghian. 2005. “First- and second-order reliability methods.” In *Engineering design reliability handbook,* edited by E. Nikolaidis, D.M. Ghi-ocel, S. Singhal, chapter 14. Boca Raton: CRC Press.

Broccardo, Marco, “Further development of the tail-equivalent linearization method for nonlinear stochastic dynamics” (PhD diss., UC Berkeley, 2014).

Cacciola, Pierfrancesco, P. Colajanni, and G. Muscolino. 2004. "Combination of modal responses consistent with seismic input representation.” *Journal of Structural Engineering* 130, no.1: 47-55.

Chen, Wai-Fah, and Lian Duan. *Bridge engineering handbook, Second Edition: Seismic Design*. Boca Raton: CRC press, 1999.

Casciati, Fabio, Lucia Faravelli, and Abraham M. Hasofer. 1993. "A new philosophy for stochastic equivalent linearization." *Probabilistic engineering mechanics* 8, no.3-4: 179-185.

Fujimura, Kazuya, and Armen Der Kiureghian. 2007. "Tail-equivalent linearization method for nonlinear random vibration." *Probabilistic Engineering Mechanics* 22, no.1: 63-76.

Lutes, Loren D., and Shahram Sarkani. *Random vibrations: analysis of structural and mechanical systems*. Butterworth-Heinemann: Elsevier, 2004.

McLachlan, Geoffrey, and David Peel. *Finite mixture models*. New York: Wiley, 2000.

Rezaeian, Sanaz, Armen Der Kiureghian, Yousef Bozorgnia. "Stochastic ground motion model with time-varying intensity, frequency and bandwidth characteristics". In Proceeding of 14th World Conference on Earthquake Engineering (14WCEE), Beijing, China, 2008.

Rezaeian, Sanaz, and Armen Der Kiureghian. 2010. "Simulation of synthetic ground motions for specified earthquake and site characteristics." *Earthquake Engineering & Structural Dynamics* 39, no.10: 1155-1180.

Rubinstein, Reuven Y., and Benjamin Melamed. *Modern simulation and modeling. Vol. 7*. New York: Wiley, 1998.

Soong, Tsu T., and Mircea Grigoriu. "Random vibration of mechanical and structural systems." New Jersey: P T R Prentice-Hall, 1993.

Wang, Ziqi, and Junho Song. 2017. "Equivalent linearization method using Gaussian mixture (GM-ELM) for nonlinear random vibration analysis." *Structural Safety* 64: 9-19.

Wen, Yi-Kwei. 1980. "Equivalent linearization for hysteretic systems under random excitation." *Journal of Applied Mechanics (ASME)* 47: 150-154.

Yi, Sang-ri, Ziqi Wang, and Junho Song. 2018. "Bivariate Gaussian mixture–based equivalent linearization method for stochastic seismic analysis of nonlinear structures." *Earthquake Engineering & Structural Dynamics* 47, no.3: 678-696.

Yi, Sang-ri, Ziqi Wang, and Junho Song. 2019. "Gaussian mixture–based equivalent linearization method (GM-ELM) for fragility analysis of structures under nonstationary excitations." *Earthquake Engineering & Structural Dynamics* 48, no.10: 1195-1214.

Zembaty, Zbigniew. 1988. "A note on non-stationary stochastic response and strong motion duration." *Earthquake engineering & structural dynamics* 16, no.8: 1189-1200.

A NEW PDEM-CONSISTENT FUNCTIONAL PERSPECTIVE TO UNCERTAINTY QUANTIFICATION OF STRUCTURAL SYSTEMS INVOLVING UNCERTAIN PARAMETERS

Jianbing Chen

Professor, Tongji University, China

A NEW PDEM-CONSISTENT FUNCTIONAL PERSPECTIVE TO UNCERTAINTY QUANTIFICATION OF STRUCTURAL SYSTEMS INVOLVING UNCERTAIN PARAMETERS

Jianbing Chen[1], Zhiqiang Wan[1,2]
[1]State Key Laboratory of Disaster Reduction in Civil Engineering, College of Civil Engineering, Tongji University, Shanghai, China
E-mail: chenjb@tongji.edu.cn
[2]The Institute for Risk and Reliability, Leibniz Universität Hannover, Hannover, Germany
E-mail: wanzhiqiang@tongji.edu.cn

Abstract:Great challenges still exist in the uncertainty quantification (UQ) and propagationof real-world complex structural systems, where uncertainties are invetibly involved, say in material or geometric parameters. Generally, due to the prohibitive computational efforts in the existing methods, besides the stochastic response analysis and reliability, difficulties exist in many aspests, including: (1) quantification of simultaneous aleotory and epistemic uncertainties; (2)global sensitivity of quantity of interest in terms of basic parameters random in nature; and (3) life-cycle reliability and reliability updating due to data accumulation and source randomness updating. The probability density evolution method (PDEM) provides an efficient solution strategy for stochatic response and reliability evluation of engineering structures. In the present paper, the new advances by advocating a novel PDEM-based functional perspective to uncertainty quantification of structuers involving random parameters are outlined. The basic idea of the new functional perspective is introduced, and then the extensions of applications to resolve the above existing difficult problems are exemplied. Problems to be further studied are also discussed.

***Keywords*:** Uncertainty quantification,Probability density evolution method (PDEM), Functional analysis, Global sensivitiy, Change of probability measure

1 Introduction

Rapid developments have been achieved in the refined analysis of engineering structures or systems due to the advances of fundamental theory, computational technologies and facilities. Nonetheless, great challenges still exist in uncertainty quantification (UQ) ofstructures/systems inevitably involving uncertainties in modeling, geometric and material properties. In general, for real-world problems, there are, more or less, two types of uncertainties, i.e., the aleatory uncertainty (objectively existing) and the epistemic uncertainty (subjectively caused due to lack of knowledge/information) (Ang & Tang 2007, Der Kiureghian&Ditlevsen 2009). Generally, UQ is involved with three parts (Roy & Oberkampf 2011, Soize 2017, Chen & Wan 2019): (1) uncertainty modelling, (2) uncertainty propagation and (3) uncertainty decision-making.Among them, the second part, i.e., the uncertainty propagation (UP), has been the most challenging one.Great endeavors have been devoted to this problem, leading to a variety of methods, including the crude Monte Carlo simulation (MCS, Nie&Ellingwood 2000) and its improvements (Au & Beck 2001), the random perturbation method (Kleiber& Hien 1992), and the polynomial chaos expansion (PCE, Ghanem & Spanos 1990), etc. In the past nearly 20 years, based on the principle of preservation of probability, Li & Chen (2009) developedthe probability density evolution method (PDEM), where the state variables in the generalized density evolution equation (GDEE) are completely decoupled. This equation explicitly reveals that the change of the physical state drives the evolution of probability density of the quantity of interest (QoI), i.e., the propagation of uncertainty is driven by the underlying physical law.The PDEM has been

applied in various fields, including civil engineering, mechanical engineering, and marine engineering, etc. Recently, on the basis of PDEM, a new functional perspective to the stochastic mechanics of systems involving random parameters was proposed. This provides new insights into resolving a series of difficult problems, including the quantification of simultaneous aleatory and epistemic uncertainties, the rational definition and computationally friendly global sensitivity index, and the life-cycle reliability evaluation of structures exhibiting material deterioration and reliability updating due to updating of data from monitoring systems. These new advances are reviewed and exemplified in the present paper. Problems to be further studied are also outlined.

2 Probability density evolution method (PDEM)

For clarity, the probability density evolution method (PDEM) is firstly revisited here.

2.1 Basic theory of PDEM

Without loss of generality, consider a stochastic dynamical system as follows

$$\dot{\mathbf{Z}} = \mathbf{G}(\mathbf{Z}, \boldsymbol{\Theta}, t),\ \mathbf{Z}(0) = \mathbf{z}_0 \tag{1}$$

where $\mathbf{Z} = (Z_1, \cdots, Z_m)^{\mathrm{T}}$ denotes an s-dimensional state vector and $\boldsymbol{\Theta} = (\Theta_1, \cdots, \Theta_s)^{\mathrm{T}}$ is an s-dimensional source random vector with known probability density function (PDF) $p_{\boldsymbol{\Theta}}(\boldsymbol{\theta})$, characterizing the embedded uncertainties in the model. The vector of functions $\mathbf{G} = (G_1, \cdots, G_m)^{\mathrm{T}}$ represents the rule of changing of physical states with the initial condition $\mathbf{z}_0 = (\mathbf{z}_1^{(0)}, \cdots, \mathbf{z}_m^{(0)})^{\mathrm{T}}$ at time instant $t = 0$.

If no new random factors arise nor existing random factors vanish, then the augmented stochastic dynamical system $(\mathbf{Z}(t), \boldsymbol{\Theta})^{\mathrm{T}}$ is probability preserved (Li & Chen 2009, Chen & Li 2009), and there is

$$\frac{\partial p_{\mathbf{Z}\boldsymbol{\Theta}}(\boldsymbol{z}, \boldsymbol{\theta}, t)}{\partial t} + \sum_{\ell=1}^{m} \dot{Z}_\ell(\boldsymbol{\theta}, t) \frac{\partial p_{\mathbf{Z}\boldsymbol{\Theta}}(\boldsymbol{z}, \boldsymbol{\theta}, t)}{\partial z_\ell} = 0 \tag{2}$$

where $p_{\mathbf{Z}\boldsymbol{\Theta}}(\boldsymbol{z}, \boldsymbol{\theta}, t)$ stands for the joint probability density function of $(\mathbf{Z}(t), \boldsymbol{\Theta})^{\mathrm{T}}$ and $\dot{Z}_\ell$ is the ℓ-th velocity of the state $\mathbf{Z}$. Eq. (2) is called the generalized density evolution equation (GDEE).

Remark 1: When the quantity of interest (QoI) is only in one dimension, the GDEE defined in Eq. (2)reduces to

$$\frac{\partial p_{Z\boldsymbol{\Theta}}(z, \boldsymbol{\theta}, t)}{\partial t} = -\dot{Z}(\boldsymbol{\theta}, t) \frac{\partial p_{Z\boldsymbol{\Theta}}(z, \boldsymbol{\theta}, t)}{\partial z} \tag{3}$$

with the initial condition

$$p_{Z\boldsymbol{\Theta}}(z, \boldsymbol{\theta}, t)|_{t=0} = \delta(z - z_0)\, p_{\boldsymbol{\Theta}}(\boldsymbol{\theta}) \tag{4}$$

where z_0 is the deterministic value of $Z(t)$.The PDF of QoI can then be obtained by

$$p_Z(z,t) = \int_{\Omega_\Theta} p_{Z\Theta}(z,\boldsymbol{\theta},t)\,\mathrm{d}\boldsymbol{\theta} \tag{5}$$

where Ω_Θ is the distribution domain of $\boldsymbol{\Theta}$.

Clearly,Eq. (3)indicates that the transition of joint PDF of the Qoland the source randomness is driven by the change of physical states of system, i.e., the generalized speed $\dot{Z}(\boldsymbol{\theta},t)$ (Li et al 2012). In other words, the GDEE reveals the basic laws in the uncertainty propagation of arbitrary stochastic dynamical systems: the uncertainty of inputs propagates on the path of the change of physical states that admitting restrictive physical laws.

2.2 Numerical algorithm of PDEM

To solve the GDEE defined in Eq. (2) (or in Eq. (3) for simplicity), one can firstly integrate on both sides of Eq.(3) in terms of $\boldsymbol{\Theta}$ over any arbitrary partitioned sub-domain Ω_q, resulting in (Li et al 2012)

$$\frac{\partial p_Z^{(q)}(z,t)}{\partial t} + \int_{\Omega_q} \dot{Z}(\boldsymbol{\theta},t)\frac{\partial p_{Z\Theta}(z,\boldsymbol{\theta},t)}{\partial z}\mathrm{d}\boldsymbol{\theta} = 0 \text{ for } q = 1,\cdots,n_{\mathrm{sel}} \tag{6}$$

where Ω_q is the q-th subset of Ω_Θ satisfying $\Omega_i \bigcap \Omega_j = \varnothing$ for $\forall\ i \neq j$ and $\cup_{q=1}^{n_{\mathrm{sel}}}\Omega_q = \Omega_\Theta$, and n_{sel} is the number of partition, and $p_Z^{(q)}(z,t) = \int_{\Omega_q} p_{Z\Theta}(z,\boldsymbol{\theta},t)\mathrm{d}\boldsymbol{\theta}$.Besides, it is obvious that

$$P_q = \int_{-\infty}^{\infty} p_Z^{(q)}(z,t)\mathrm{d}z = \int_{\Omega_q} p_\Theta(\boldsymbol{\theta})\mathrm{d}\boldsymbol{\theta} \text{ for } q = 1,\cdots,n_{\mathrm{sel}} \text{ and } \sum_{q=1}^{n_{\mathrm{sel}}} P_q = 1 \tag{7}$$

which ensures the compatibility of probability, and P_q is called the assigned probability (Chen et al 2009).Once Eq. (6) is solved, the PDF of QoI can be obtained by

$$p_Z(z,t) = \sum_{q=1}^{n_{\mathrm{sel}}} p_Z^{(q)}(z,t) \tag{8}$$

Remark 2: There are two pathways (Li et al 2012) to decouple the second term in Eq. (6):

(1) Warily pick one representative point in each subset, i.e., $\boldsymbol{\theta}_q \in \Omega_q$, and let $\dot{Z}(\boldsymbol{\theta},t) := \dot{Z}(\boldsymbol{\theta}_q,t)$, then Eq. (6)becomes (point evolution GDEE)

$$\frac{\partial p_Z^{(q)}(z,t)}{\partial t} + \dot{Z}(\boldsymbol{\theta}_q,t)\frac{\partial p_Z^{(q)}(z,t)}{\partial z} = 0 \text{ for } q = 1,\cdots,n_{\mathrm{sel}} \tag{9}$$

which is a typical hyperbolic partial differential equation that can be easily solved. To achieve the error estimate of this point-evolution basedalgorithm for GDEE in Eq. (9), a GF-discrepancy minimized strategy was suggested and the extended Koksma-Hlawka inequality was established (Chen & Zhang 2013; Chen et al 2016), where the upper and lower boundaries of error estimation have beenproved (Chen & Chan 2019).

(2) Another choice is to obtain the ensemble average of the second term, which leads to (ensemble-evolution GDEE)

$$\frac{\partial p_Z^{(q)}(z,t)}{\partial t} + \mathbb{E}_q\left[\dot{Z}(\boldsymbol{\theta},t)\right]\frac{\partial p_Z^{(q)}(z,t)}{\partial z} = 0 \text{ for } q = 1, \cdots, n_{\text{sel}} \tag{10}$$

where $\mathbb{E}_q\left[\dot{Z}(\boldsymbol{\theta},t)\right] = \frac{1}{P_q}\int_{\Omega_q} \dot{Z}(\boldsymbol{\theta},t)\, p_{\boldsymbol{\Theta}}(\boldsymbol{\theta})\mathrm{d}\boldsymbol{\theta}$ stands for the mean value of $\dot{Z}(\boldsymbol{\theta},t)$ over the q-th subset Ω_q. Related works can be found in Chen & Yuan (2014) with the equivalent probability flux, Jiang & Li (2017a, 2017b) with the Kriging-based surrogate model, Tao & Li (2017) with the ensemble velocities, Li & Sun (2016) and Wang & Li (2019) with the reproducing kernel particle method, etc.

The numerical algorithm of PDEM for solving the GDEE include the following steps:

Step 1. Point selection. Determine n_{sel} representative points from the probability-assigned space $\Omega_{\boldsymbol{\Theta}}$, i.e., $\mathcal{M} = \{\boldsymbol{\theta}_q\}_{q=1}^{n_{\text{sel}}}$. This can be done with the GF-discrepancy minimized strategy (Chen et al 2016; Chen and Chan 2019), but other strategies of point selection are feasible as well.

Step 2. Model evaluation. The generalized velocities $\mathcal{V} = \left\{\dot{Z}(\boldsymbol{\theta}_q,t)\right\}_{q=1}^{n_{\text{sel}}}$ are calculated and stored together with the point set $\mathcal{M} = \{\boldsymbol{\theta}_q\}_{q=1}^{n_{\text{sel}}}$.

Step 3. Solving the GDEE in either point-evolution based algorithm(9)or ensemble-evolution based algorithm(10). The finite difference method with total variation diminishing (TVD) scheme is suggested herein to solve the GDEE (Li & Chen 2009), but one still has the flexibility of solving the GDEE, e.g., by a Galerkin-based finite element formulation (Papadopoulos &Kalogeris 2016).

Generally, the number of representative points, i.e., n_{sel} is around $100 \sim 500$ for practical problems, see Zhou et al (2016), Jiang & Li (2017b), andTao et al (2018), etc.

2.3 A PDEM-consistent functional perspective of stochastic mechanics/ dynamics

Most engineering systems are well-posed systems such that the solution of dynamical problem is existing, unique and changing continuously with the initial conditions and parameters. Thus, the stochastic dynamical system defined in Eq. (1) can be reformulated as

$$\mathbf{Z}(t) = \mathcal{G}(\boldsymbol{\Theta},t) = \mathcal{G}(t) \circ \boldsymbol{\Theta} \tag{11}$$

where the initial condition $\mathbf{z}_0$ is omitted without inducing confusion, the function $\mathcal{G}(\cdot)$admits the physical laws embedded in Eq. (1), and $\circ$means the action of an operator on a function. With a given PDF of $\boldsymbol{\Theta}$ by $p_{\boldsymbol{\Theta}}(\boldsymbol{\theta})$, the PDF of the QoI $\mathbf{Z}$by $p_{\mathbf{Z}}(\boldsymbol{z})$ can be determined by the rule of change of random variable(s) (Grigoriu 2002)

$$p_{\mathbf{Z}}(\boldsymbol{z},t) = \psi_{\mathcal{G}}(p_{\boldsymbol{\Theta}}(\boldsymbol{\theta}),t) = \psi_{\mathcal{G}}(t) \circ p_{\boldsymbol{\Theta}}(\boldsymbol{\theta}) \tag{12}$$

where $\psi_{\mathcal{G}}(t)$ is an operator determined by $\mathcal{G}(\cdot)$ and essentially the Frobenius-Perron operator (Bobrowski 2005).

Remark 3: Eq. (12) reveals that it is apparent that the propagation of uncertainty is governed

by the embeddedphysical laws, which can also be clearly seen in the GDEE defined in Eqs. (2), where the operator $\psi_{\mathcal{G}}(t)$ is explicitly defined by the partial derivatives with respect to the time t and the QoI, the embedded physical mechanics are manifestly displayed in the form of the generalied velocities of the QoI.

In other words, with certain input parameters, i.e., $\boldsymbol{\Theta}$ is deterministic, we can obtain the QoI $\mathbf{Z}$ by solving Eq. (11) with the operator $\mathcal{G}(\cdot)$; but when the inputs are uncertain, e.g., defined by a probability model $p_{\boldsymbol{\Theta}}(\boldsymbol{\theta})$, one canobtain a corresponding uncertain QoI $\mathbf{Z}$ characterized by $p_{\mathbf{Z}}(\boldsymbol{z})$ via solving Eq. (12)with the operator $\psi_{\mathcal{G}}(t)$ .In particular, in the framework of PDEM involving Eqs.(3)-(5), it is noted that the input information $p_{\boldsymbol{\Theta}}(\boldsymbol{\theta})$ enters the information flow of PDEM in Eq.(4) via the initial conditions, the GDEE (3) and Eq.(5) serve as the implementation of operator in Eq. (12), and the PDF of QoI is output in Eq.(5). In this sense, the functional perspective is completely consistent with the PDEM, but provides new insights.

Remark 4: Eq. (12)makes iteasy to answer what essentially drives the propagation of uncertainty. Moreover, such a functional perspective to theuncertainty quantification provides new possibilities in resolving some difficult problems, including, e.g,

(1) the quantification of simultaneous aleatory and epistemic uncertainty;

(2) high-efficient life-cycle reliability evalution and updating based on new available data; and

(3) new concept and high-efficient computation of global sensitivity index.

More details will be discussed together with numerical examples in the following section.

3 New Extensions of Applications of PDEM

The PDEM has been applied in various fields such as civil engineering, mechanical engineering, marine engineering etc. Due to the insights provided from the new PDEM-consistent functional perspective, new solutions can be provided for some difficult problems in uncertainty quantification of systems involving uncertain parameters. In this section, such extensions will be exemplified.

3.1 A probabilistically consistent framework on UQ of simultaneous aleatory and epistemic uncertainties

In most real engineering issues, there are two types of uncertainties, i.e., the aleatory uncertainty and the epistemic uncertainty. In general, aleatory uncertainty can be well characterized with a certain PDF or CDF in the frameworkof probability theory, while epistemic uncertainty can be represented by p-boxes, i.e., amounts of candidate PDFs or CDFs (Beeret al 2013; Wei et al 2019).This leads to a problem that the original input PDFin Eq.(12) is not deterministic. In this case, the change of probability measure can be incorporated into the PDEM in a natural way, which is called the PDEM-COM method (Chen & Wan 2019).

To be clear, consider a 3-span 10-storey reinforced concrete structure subjected to the El Centro earthquake (in east-west direction),with the compressive strength of concrete being random variables involving both aleatory and epistemic uncertainties (Chen & Wan 2019), as shown in Figure 1(a). Herein, before updating by new available data, the compressive strength of concrete follows normal distribution with the mean value 30MPa and standard derivation

6MPa, but after updating it is regarded to followormal distribution with the mean value 27MPa and standard derivation 4.05MPa.The question arises that if a round PDEM is performed based on the input PDF before updating and then new data comes to update the input PDF, then is a completely new round of PDEMneeded to update the output PDF of QoI? The answer is no, because the embedded physical evaluations have been performed, i.e., the information to determine operator in Eq.(12)has been obtained in the PDEM, and this information can be reused directly in the round of PDEM in terms of the updated input PDF. Therefore, only the assigned probability of the representative points shall be updated, which is essentially the implementation of change of probability measure by the Radon-Nikodym derivative (Chen and Wan 2019). Because the most time-consuming part, the physical evaluation, in PDEMis shared, the efficiency is considerably improved. For the present example, the results, consisting of the 1st and 2nd moments of the QoI and the CDFs of the QoI, are all summarized in Figure 1(b) and 1(c) and a zoom-in difference of Figure 1(b) is present in Figure 1(d) as well, whichdemonstrate again the accuracy as well as the efficiency of the PDEM-COM proposed in Chen & Wan (2019).

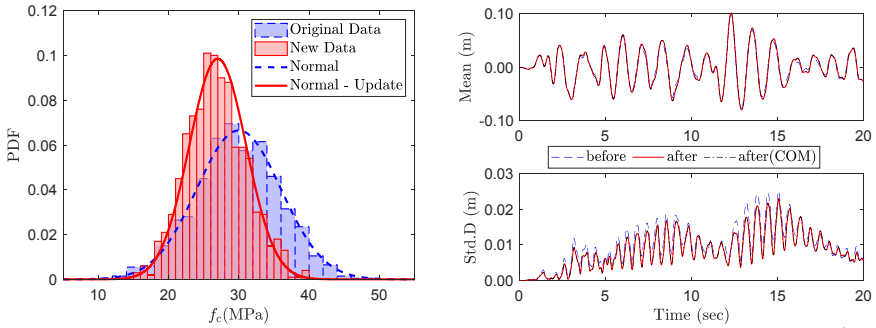

(a) Distributions of the compressive strength due to epistemic uncertainty (b) 1st and 2nd moments of the QoI

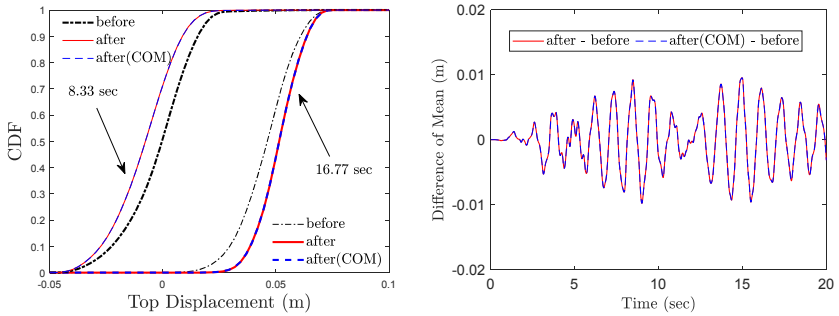

(c) CDFs of QoI due to epistemic uncertainty (d) A zoom-in difference of the mean value of the QoI

Figure 1. A compatible framework on UQ of both aleatory and epistemic uncertainties with PDEM

3.2 Global sensitivity analysis of systems involving random parameters

Global sensitivity is of great importance when the basic parameters are random variables rather than deterministic variables. Based on the above PDEM-consistent functional perspective, an innovative Fréchet derivative-based global sensitivity index can be defined. Specifically, if the input PDF is parameterized, i.e., by its first two or four moments, the Fréchet derivative becomes (Chen et al 2019)

$$\lim_{\|\Delta\boldsymbol{\zeta}\|\to 0}\frac{\|\psi_{\mathcal{G}}(p_{\boldsymbol{\Theta}}(\boldsymbol{\theta};\boldsymbol{\zeta}+\Delta\boldsymbol{\zeta}))-\psi_{\mathcal{G}}(p_{\boldsymbol{\Theta}}(\boldsymbol{\theta};\boldsymbol{\zeta}))-\mathfrak{F}_{\psi}\Delta\boldsymbol{\zeta}\|}{\|\Delta\boldsymbol{\zeta}\|}=0$$
$$\Rightarrow \mathfrak{F}_{\psi}=\frac{\partial\mathcal{F}(\boldsymbol{z};\boldsymbol{\zeta})}{\partial\boldsymbol{\zeta}} \text{ and } \mathcal{F}(\boldsymbol{z};\boldsymbol{\zeta})=\psi_{\mathcal{G}}\circ p_{\boldsymbol{\Theta}}(\boldsymbol{\theta};\boldsymbol{\zeta}) \tag{13}$$

where $\mathfrak{F}_{\psi}$ is the global sensitivity, and $\boldsymbol{\zeta}$ is the distribution parameters of $p_{\boldsymbol{\Theta}}(\boldsymbol{\theta})$. The global sensitivity index defined in Eq. (13) can not only show the importance measure of input variables, but also providethe importance direction (Chen et al 2019). For clarity, the following example is studied. Consider a function with two probability models

$$(a)\ X_a=\Theta_1+\Theta_2 \text{ and } (b)\ X_b=\Theta_3+\Theta_4 \tag{14}$$

where the inputs Θ_1 and Θ_2, Θ_3 and Θ_4 are set to be independent. The subscripts "a" and "b" denote the Case a and Case b, respectively. In Case a, Θ_1 and Θ_2 are exponentially distributed with the mean values 1 and 1/2, and in Case b Θ_3 and Θ_4 are normally distributed with mean values 1 and 1/2, and variances 1 and 1/4, respectively.

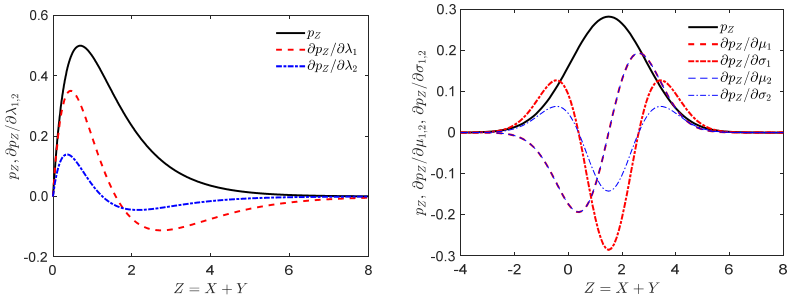

(a) Case a: basic distribution parameters are $\lambda_1=1$ and $\lambda_2=2$ (b) Case b: basic distribution parameters are $\mu_1=\sigma_1=1$ and $\mu_2=\sigma_2=1/2$

Figure 2. Global sensitivity analysis based on Fréchet derivative.

The Fréchet derivative-based sensitivity index can be generated by Eq. (13) and plotted in Figure 2. It is found that, even for the same function, the global sensitivity in terms of basic random variables behaves in different ways: in Case a, the sensitivity in terms of the mean value of Θ_1 is greater than that of Θ_2. However, in Case b, there is no great difference found in the Fréchet derivative-based sensitivity index in terms of the mean values. Instead, the Fréchet derivative-based sensitivity index in terms of the variance tells that Θ_3 is more sensitive than Θ_4. This is apparently clear since the Fréchet derivative-based sensitivity index defined in Eq. (13) is an operator with respect to both the physical equations and the probability models.

3.3 Life cycle reliability analysis and real-time reliability updating with data

Generally, due to the environmental action/erosion, the property of materials will deteriorate, and thus the reliability of structures in service is time-variant. This problem is usually much

more time-consuming compared to the reliability evaluation of structures without deterioration. Combined with the new PDEM-consistent functional perspective, the material deterioration can be converted to a problem involving random material property with time-variant PDF (Wan et al2020), i.e., the operator in Eq.(12)is time-invariant, but the input PDF in Eq.(12) is time-variant. This means that the physical evaluation to determine the operator in Eq.(12) is time-invariant, thus the structural analysis for the structure without material deterioration can be reused, and consequently the efficiency can be improved considerably.

As an example, consider a 13-storey high-rise frame-shear wall structure subjected to gravity load and lateral load. The property of structure will be of deterioration due to the degradation of construction materials, e.g., the strength of concrete, $f_c = f_{c,0}(1-8\times10^7 t^3)$, where $f_{c,0}$~$N(30,3^2)$ MPa. The assessment of probability density evolution contour is plottedin Figure 3(a) with PDFs at arbitrary two time instants shown in Figure 3(b). It is seen that the results of the proposed PDEM-COM agree well with those by direct PDEM. However, the efficiency of PDEM-COM is greatly improved because only one round of embedded physical equation evaluations is performed.

Also, it is noted that such deterioration of materials can be reflected and updated by data, e.g., collected from the structural health monitoring systems. By the proposed method, once the input PDF is updated by data, then the COM can be incorporated to update the reliability in high efficiency. This makes it possible to update real-timethe reliability of a structure in service online according to the updating of data from the monitoring systems.

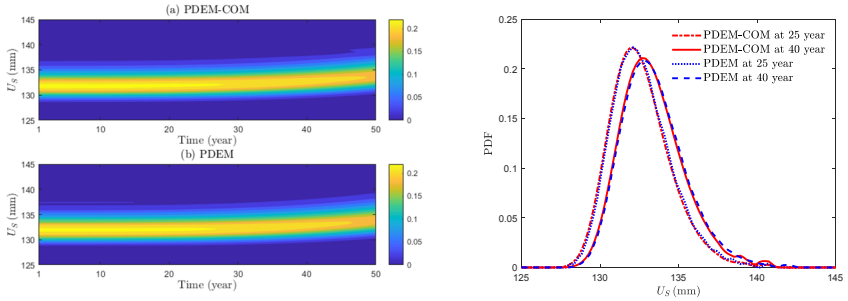

(a) Contours of PDF of the QoI(b) PDFs of the QoI at two time instants

Figure 3. Life cycle reliability analysis by PDEM-COM

4 Conclusions

In the present paper, the advances of PDEM related tothe newfunctional perspective to stochastic mechanics of systems involving random parameters are outlined. In this point of view, the PDF of output of the quantity of interest is the results of the operator acting on the input PDF characterizing the source randomness, whereas the operator is determined by the underlying physical law. In this sense, the PDEM is an implementation of this functional perspective, which provides new insights into resolving a series of difficult problems in uncertainty quantification of engineering structures/systems involving random parameters, including: (1) high-efficient and probabilistically consistent quantification of simultaneous aleatory and epistemic uncertainties; (2) rational definition and high-efficient computation of global sensitivity index for the systems involving random parameters; and (3) the life-cycle reliability evaluation of structures exhibiting material deterioration and high-efficient reliability prediction due to updating of data from monitoring systems.These problems can be tackled by

incorporating the change of probability measure (COM) to the PDEM.The above advances are exemplified in the paper.There are problems to be further studied, e.g., more robust numerical algorithm for the change of probability measure when the distribution parameters change in a large degree, the extension from uncertainties of parameters to model uncertainty, etc.

5 Acknowledgement

Financial supports from the National Natural Science Foundation of China (NSFC Grant Nos. 51725804, 51538010 and 11761131014), DFG Grant No. 392113882 and the NSFC-Guangdong Province Joint Project (Grant No. U1711264) are gratefully appreciated.

6 References

Alfredo H.-S. Ang and Wilson Tang. *Probability Concepts in Engineering: Emphasis on Applications to Civil and Environmental Engineering*. Hoboken: John Wiley & Sons, 2007.

Siu-Kui Au and James Beck,"Estimation of small failure probabilities in high dimensions by subset simulation," *Probabilistic Engineering Mechanics*, 16(2001): 263-277.

Michael Beer, Scott Ferson and VladikKreinovich, "Imprecise probabilities in engineering analyses," *Mechanical Systems and Signal Processing,* 37(2013): 4-29.

Adam Bobrowski. *Functional Analysis for Probability and Stochastic Processes: An Introduction*. London: Cambridge University Press, 2005.

Jianbing Chen and Jianpeng Chan, "Error estimate of point selection in uncertainty quantification of nonlinear structures involving multiple nonuniformly distributed parameters," *International Journal for Numerical Methods in Engineering*, 118(2019): 536-560.

Jianbing Chen, Roger Ghanem and Jie Li, "Partition of the probability-assigned space in probability density evolution analysis of nonlinear stochastic structures," *Probabilistic Engineering Mechanics*, 24(2009): 27-42.

Jianbing Chen and Jie Li, "A note on the principle of preservation of probability and probability density evolution equation," *Probabilistic Engineering Mechanics* 24(2009): 51-59.

Jianbing Chen and Zhiqiang Wan, "A compatible probabilistic framework for quantification of simultaneous aleatory and epistemic uncertainty of basic parameters of structures by synthesizing the change of measure and change of random variables," *Structural Safety*, 78(2019): 76-87.

Jianbing Chen, Zhiqiang Wan and Michael Beer, "A global sensitivity index based on Fréchet derivative and its efficient numerical analysis," (2019, under review).

Jianbing Chen, Junyi Yang and Jie Li, "A GF-discrepancy for point selection in stochastic seismic response analysis of structures with uncertain parameters," *Structural Safety*, 59(2016): 20-31.

Jianbing Chen and Shurong Yuan, "PDEM-based dimension-reduction of FPK equation for additively excited hysteretic nonlinear systems," *Probabilistic Engineering Mechanics*, 38(2014): 111-118.

Jianbing Chen and Shenghan Zhang,"Improving point selection in cubature by a new discrepancy,"*SIAM Journal on Scientific Computing*, 35(5)(2013): A2121-A2149.

Armen Der Kiureghian and Ove Ditlevsen, "Aleatory or epistemic? Dose it matter?," *Structural Safety*, 31(2009): 105-112.

Roger Ghanem and Pol Spanos, "Polynomial Chaos in Stochastic Finite Elements," *Journal of Applied Mechanics*, 57(1990): 197-202.

Zhongming Jiang and Jie Li, "High dimensional structural reliability with dimension reduction," Structural Safety, 69(2017a): 35-46.

Zhongming Jiang and Jie Li, "A new reliability method combining Kriging and probability density evolution method", *International Journal of Structural Stability and Dynamics*, 17(2017b): 1750113.

Michael Kleiber and Tran Duong Hien. *The Stochastic Finite Element Method: Basic Perturbation Technique and Computer Implementation*. Chichester: Wiley, 1992.

Jie Li and Jianbing Chen. *Stochastic Dynamics of Structures*. Singapore: John Wiley & Sons, 2009.

Jie Li, Jianbing Chen, Weiling Sun and Yongbo Peng, "Advances of the probability density evolution method for nonlinear stochastic systems," *Probabilistic Engineering Mechanics*, 28(2012): 132-142.

Jie Li and Weiling Sun, "The refined algorithm of generalized density evolution equation based on reproducing kernel particle method," *Chinese Journal of Computational Mechanics*, 33(2016): 543-548+587 (Chinese)

Mircea Grigoriu. *Stochastic Calculus: Applications in Science and Engineering*. New York: Springer Science + Business Media, 2002.

JinsuoNie and BruceEllingwood, "Directional methods for structural reliability analysis," *Structural Safety*, 22(2000): 233-249.

Vissarion Papadopoulos, IoannisKalogeris, "A Galerkin-based formulation of the probability density evolution method for general stochastic finite element systems," *Computational Mechanics*, 57(2016): 701-716.

Christopher Roy and William Oberkampf, "A compatible framework for verification, validation, and uncertainty quantification in scientific computing," *Computer Methods in Applied Mechanics and Engineering*, 200(2011): 2131-2144.

Christian Soize. *Uncertainty Quantification: An Accelerated Course with Advanced Applications in Computational Engineering*. Switzerland: Springer Nature, 2017.

Weifeng Tao and Jie Li, "An ensemble evolution numerical method for solving generalized density evolution equation," *Probabilistic Engineering Mechanics*, 48(2017): 1-11.

Weifeng Tao, Biswajit Basu, Jie Li,"Reliability analysis of active tendon-controlled wind turbines by a computationally efficient wavelet-based probability density evolution method," *Structural Control Health Monitoring*, 25(2018): e2078.

Zhiqiang Wan, Jianbing Chen, Jie Li and Alfredo H.-S. Ang, "An efficient new PDEM-COM based approach for time-variant reliability assessment of structures with monotonically deteriorating materials," *Structural Safety*, 82(2020): 101878.

Dan Wang and Jie Li, "A reproducing kernel particle method for solving generalized probability density evolution equation in stochastic dynamic analysis," *Computational Mechanics*,

https://doi.org/10.1007/s00466-019-01785-1

Pengfei Wei, Jingwen Song and Sifeng bi et al,"Non-intrusive stochastic analysis with parameterized imprecise probability models: I. Performance estimation," *Mechanical Systems and Signal Processing*, 124(2019): 349-368.

Hao Zhou, Jie Li and Xiaodan Ren, "Multiscale stochastic structural analysis toward reliability assessment for large complex reinforced concrete structures," *International Journal for Multiscale Computational Engineering*, 14(2016): 303-321.

Organized Sessions

STRUCTURAL MONITORING OF PASSIVE CONTROL OF VIBRATION STRUCTURE

Tsutomu Ochiai[1], Takahisa Enomoto[2] and Tetsushi Inubushi[3]
[1]Department of Architecture and Building Engineering, Kanagawa University, Kanagawa, Japan
E-mail: ochiai@kanagawa-u.ac.jp
[2]Department of Architecture and Building Engineering, Kanagawa University, Kanagawa, Japan
E-mail: enomot01@kanagawa-u.ac.jp
[3]Faculty of Architecture, Kindai University, Osaka, Japan
E-mail: inubushi@arch.kindai.ac.jp

Abstract: Kanagawa University, which is a low-rise steel structure, conducts structural health monitoring. In structural health monitoring, strong earthquake motions are observed on the ground and building. In this paper, the transfer function obtained from observation records was examined. At the completion of the building, we always conduct microtremors and shaker experiments. The results of microtremors and shaker experiments were almost the same. The natural frequency in the X direction was 2.4 to 2.5 Hz. The natural frequency in the Y direction was 2.6 to 2.7 Hz. Monitoring has been conducted for 5 years. We have organized 15 earthquakes with tremendous vibration in 5 years. In earthquakes where the maximum acceleration is large in the X direction, the natural frequency tends to be slightly lower. However, such a trend could not be confirmed in the Y direction. We will continue to observe and proceed with further analysis.

Keywords: Structural Health Monitoring, Observation of Strong Earthquake Motion, Primary Natural Frequency,Passive Control of Vibration Structures, secular change

1 Introduction

After the 1995 South Hyogo Prefecture Earthquake , the number of strong earthquake motion observation sites has rapidly increased in Japan, and strong earthquake motion observation is today conducted at a density unmatched in the world. For example, there are NIED and Yokohama City. Moreover, although not matching the extent of ground observations , there has been a steady increase in strong earthquake motion observation focussing on buildings, especially on high-rises. Lastly, although limited in scope, as part of business continuity plans, etc., corporations use the results of building observation records for structural health monitoring to diagnose the actual performance and soundness of their buildings, Ogawa et al (2009).

The Kanagawa University Yokohama Campus Building 3 ("Building 3") was completed in March 2014. Structural monitoring of Building 3 occurs through displacement meters installed on accelerometers and buckling-restrained braces. In addition, in order to grasp the vibration characteristics of the building, microtremor measurements and shaker experimentation were conducted immediately after the completion of the building in January 2015, Inubushi et al (2018), Enomoto et al (2015), Enomoto et al (2016).

In this paper, we outline the observation system, summarize the analysis results of microtremors and shaker experimentation, and with special attention to the primary natural frequency of the building compile a list of results of the strong earthquake motion observations during the fiscal years 2015 to 2019.

2 Outline of the Building and the Structural Monitoring System

2.1 Outline of the building

Building 3 has four floors above ground and two floors below ground. However, since for the purposes of structural design, the building is situated above ground, its structural design reflects five floors above and one floor below ground.

Laterally the structure has atriums on each floor, albeit almost oblong. Vertically, in its top-most section the structure has pillars erected on beams, again almost oblong. The short side of the building (X) has basically a span of 2.8 m while the long side (Y) has a wide span of over 10 m in order to secure a large space as a lecture room. Moreover, although the building is a damage-controlled structure using buckling-restrained braces, its design is static and the building considered earthquake-resistant braced, Yokohama City Architectural Joint Design Office (2014), and Yokohama Structural Design (2011).

- Main structure: Steel frame, partially reinforced concrete
- Foundation structure: Spread foundation (Foundation ground: Mudstone layer with N value of 60 or more)
- Number of floors: Four floors above ground, two floors below ground (eave height 20.45 m)
- Total floor area: 11,480 m^2
- Building area: 2,200 m^2

2.2 Outline of the structural monitoring system

As structural monitoring system, we have conducted seismic observation with accelerometers and displacement observation of the buckling-restrained braces in the building and surrounding ground. In the following, we outline primarily seismic observation.

The earthquake observation system for this building comprises accelerometers installed in three locations of the building (on the 4th floor, 1st floor, and B2 floor) and in two locations in the ground at distances of several tens of meters (ground surface, excluding embankment, at engineering infrastructure depth). Figure 1 shows the locations of the accelerometers in the building. Each accelerometer has three components, two for bi-directional lateral (X, Y) operation and one for vertical operation, with records taken when the trigger level (1 gal) is exceeded at the engineering base position. Observation records are stored on a server and currently collected manually.

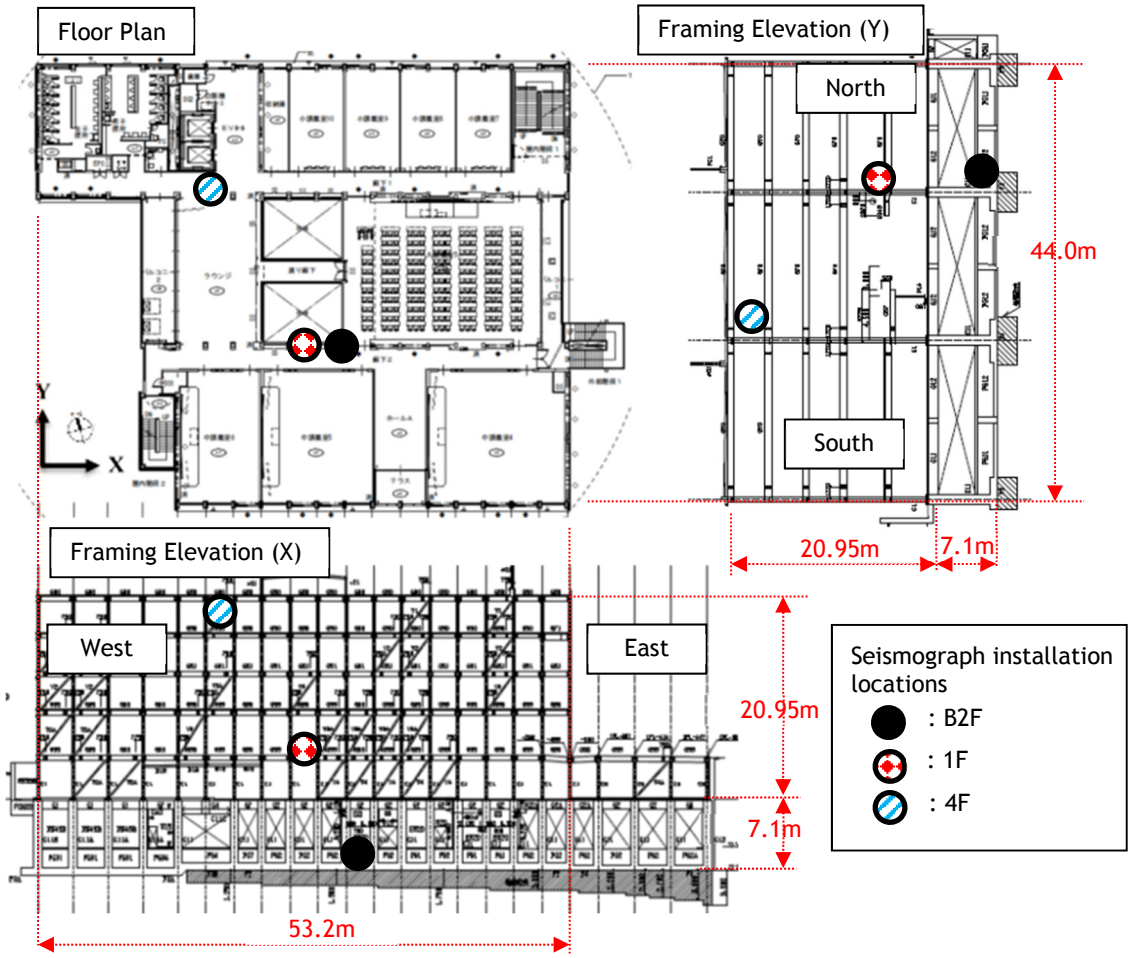

Figure1. Seismograph installation locations

3 Microtremor Measurement and Shaker Experimentation

For microtremor measurements, microtremor meters were installed at the approximate centers of the R and B1 floors of the building. The X-direction and Y-direction transfer function (R floor / B1 floor) was calculated from the Fourier spectrum of the measurement records. The obtained transfer function is shown in Figure 2. The peak frequencies of the transfer function were 2.52 Hz in the X direction and 2.74 Hz in the Y direction, thus slightly higher in the Y direction.

For the shaker experimentation, a small-sized shaker with a linear motor was used by Aoki *et al.* (2007) and Wen *et al.* (2007) In the experimentation, the shaker was installed almost at the center of gravity on the R floor of the building with oscillation one-directionally each in the X and Y directions. Measurements were taken at four points on the R floor. Figure 2 shows the resonance curve of the shaker experimentation. The peak of the resonance curve was 2.38 Hz in the X direction and 2.64 Hz in the Y direction, thus slightly higher in the Y direction like in the microtremor measurement. The peak of more than 3 Hz in the X direction is conceivably due to the torsional component.

With the peak frequency of the transfer function and the peak of the resonance curve respectively

as the primary natural frequencies of the building, the primary natural frequencies are shown in Figure 2. The results of microtremor measurements and shaker experimentation are generally consistent. There are several possible causes for the slightly higher frequency in the Y direction, and conceivably one of them is that the overall dimensions measure about 53 m in the X direction and a somewhat shorter 44 m in the Y direction.

Notably, a calculation with the natural period calculation formula of a general S structure (T = 0.02 x H) yields T = 0.409s (2.44 Hz), which is largely consistent with the measured value.

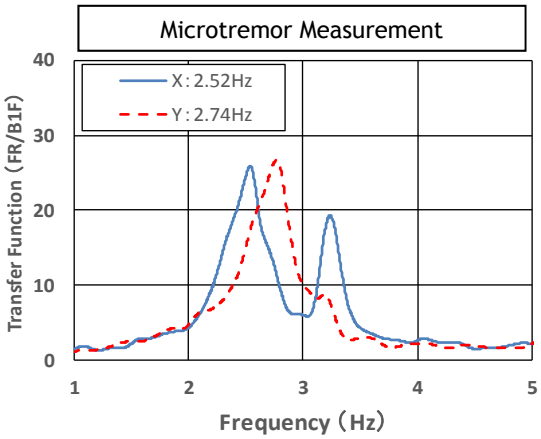

Primary natural frequencies
(Primary natural periods in the bottom

	Microtremo Measuremen	Shake Experimentatio
X	2.52H (0.40)	2.38H (0.42)
Y	2.74H (0.36)	2.64H (0.38)

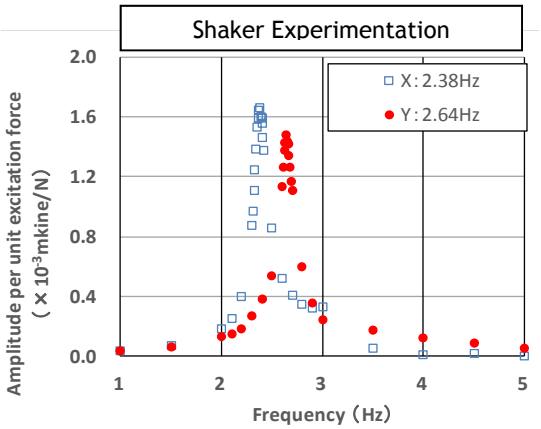

Figure2. Result of Microtremor Measurement and Shaker Experimentation

4 Structural Health Monitoring

4.1 Tareget earthquakes

As mentioned above, as structural monitoring, Building 3 has been subject to strong earthquake motion observation and buckling-restrained braces displacement observation. In the following, we focus on the primary natural frequency of the building obtained from the transfer function of the strong earthquake motion observation records and consider its secular change.

The target period ran from March 2015 (the start of the observation) until August 2019. The target earthquakes comprised 15 earthquakes with a measured seismic intensity of 2.5 or more at K-NET

Yokohama (KNG002), which is located relatively close to Kanagawa University where the target building stands. K-NET Yokohama (KNG002) is a strong Motion observation point by the country. Table 1 lists the target earthquake motions and observation records, and Figure 3 shows the epicenter locations.

Among the target earthquakes, only the epicenter of the No. 2 earthquake is located off the western coast of the Ogasawara Islands in the south. This earthquake, at a depth of 682 km, differs somewhat from the others, which are distributed in a well-balanced manner to surround the target location from the north side to the south side. With epicenters mainly at depths from 10 to 60 km, these earthquakes occurred mainly in shallow strata.

As an example, Figure 4 shows the transient waveform of the earthquake of May 25, 2015. It is apparent that the vibration characteristics differ in the X and Y directions.

Table1. List of target earthquakes

No.	data	soruce region	depth km	M_J	PGA (gal) 4F/1F	
					X	Y
1	2015/5/25	Saitama North	56	5.5	71.6/26.8	36.8/16.9
2	2015/5/30	Ogasawara Islands West	682	8.1	4.3/1.8	6.7/2.6
3	2015/9/12	Tokyo Bay	57	5.2	59.1/46.9	86.3/35.7
4	2016/2/5	Kanagawa West	26	4.6	16.3/30.8	22.4/30.3
5	2016/5/16	Ibaraki South	42	5.5	32.3/19.0	21.9/12.8
6	2016/7/17	Ibaraki South	42	5.0	14.2/11.0	35.7/11.4
7	2016/7/19	Chiba North	33	5.2	26.9/6.8	41.6/10.9
8	2016/11/22	Fukushima East	25	7.4	15.3/7.0	17.4/6.1
9	2016/12/28	Ibaraki North	11	6.3	11.7/4.1	14.3/4.5
10	2017/8/10	Chiba Northeast	64	5.0	13.1/11.9	24.4/18.1
11	2018/1/6	Tokyo Bay	71	4.7	36.5/25.5	26.6/22.4
12	2018/7/7	Chiba East	57	6.0	29.7/11.9	28.4/10.7
13	2019/1/18	Ibaraki South	54	5.3	14.0/5.3	14.3/4.6
14	2019/6/24	Chiba Southeast	61	5.2	22.6/21.0	45.1/21.5
15	2019/8/4	Fukushima East	50	6.2	18.8/6.2	17.1/5.9

※Red：PGA is large earthquake

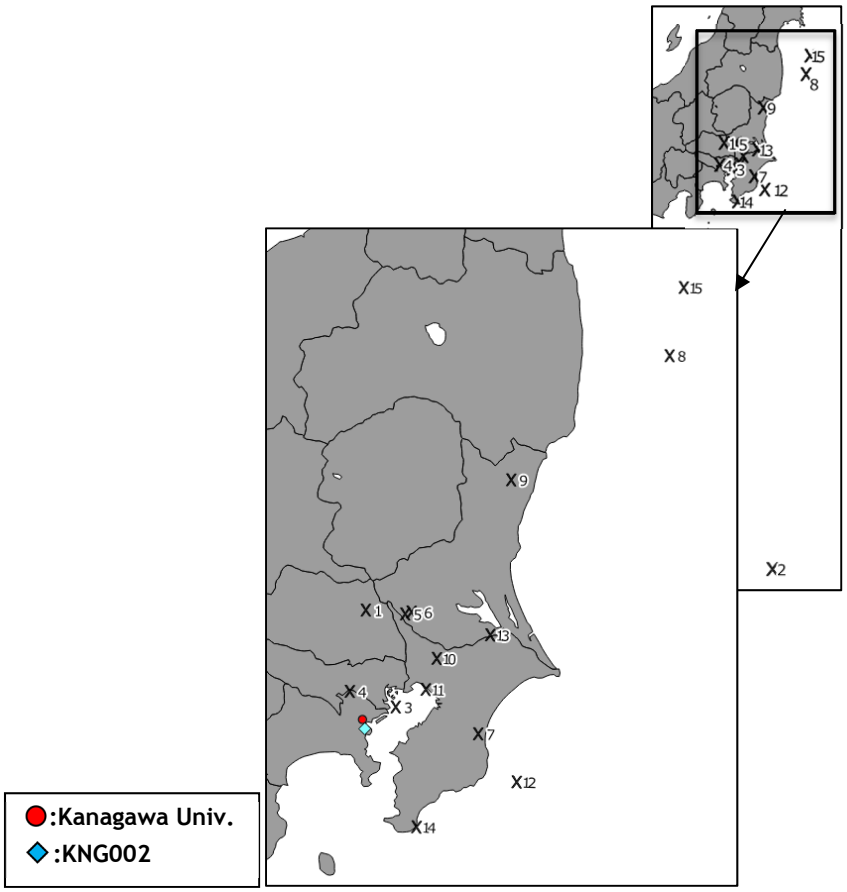

Figure3. Epicenter distribution of the target earthquakes

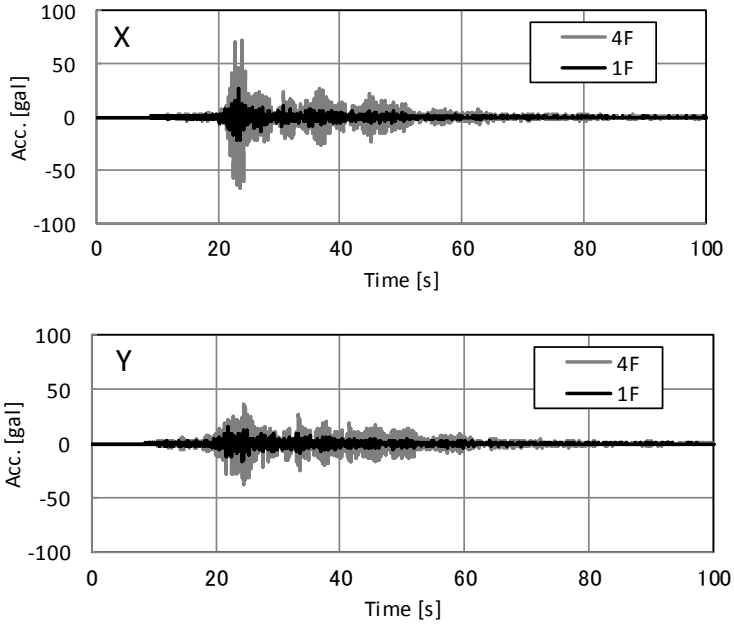

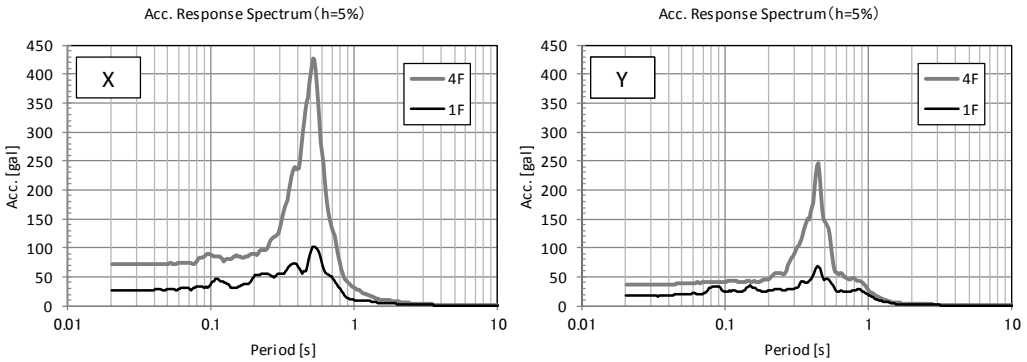

Figure 4. Transient waveform of the earthquake of May 25, 2015

4.2 Primary natural frequency

Figures 5 show the superposition of transfer functions for each earthquake record. Earthquakes with maximum acceleration (earthquakes with a maximum acceleration of 4F exceeding 20 gal in both directions) are shown in red.

In the X direction, when the maximum acceleration is large, the natural frequency tends to be slightly smaller (cycle prolongation). However, this tendency is not apparent in the Y direction.

Figures 6 show the relationship between primary natural frequency and 4F maximum acceleration. They also show the approximate curves and correlation coefficients. As described above, when the maximum acceleration is large, the natural frequency tends to be small. Variation in the X direction is low overall and the correlation coefficient of 0.84 tells of a relatively strong correlation between the two. As seen in the spectrum, for the Y direction the overall variation is somewhat higher, and the correlation is weak at a coefficient of 0.55.

We plan to conduct further analysis of the differences in the characteristics of the X and Y directions.

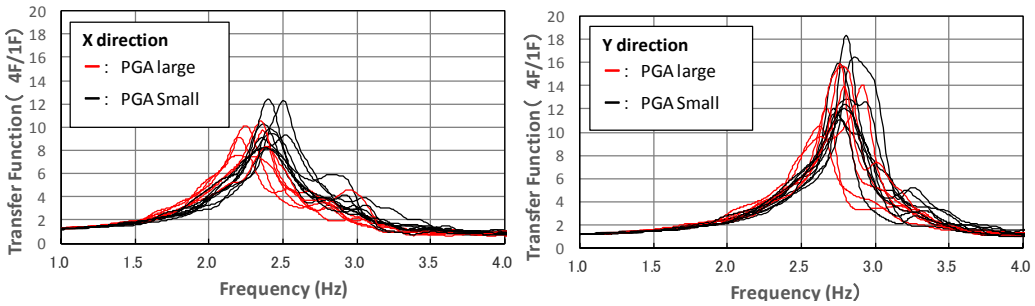

Figure 5. Transfer function (4F/1F)

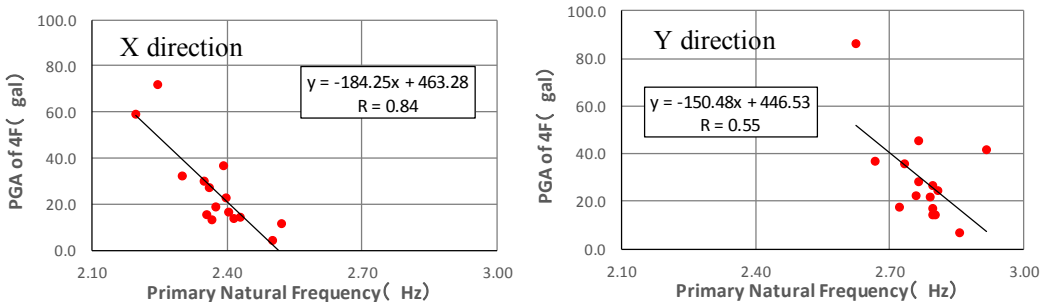

Figure 6. Peak Acceleration and primary natural frequency

4.3 Time-dependent change in Primary natural frequency

Figure 7 shows changes in the primary natural frequency over time from the start of observation until present. As described above, although there is some variation in the magnitude of acceleration, the variation extent is small overall. Given that there has been almost no change in the natural frequency since immediately after construction completion, it is assumed that the soundness of the building remains intact.

For the future, we plan to continue observation and proceed with analyses focusing on questions such as the differences between changes due to external factors such as seismic motion and changes due to aging.

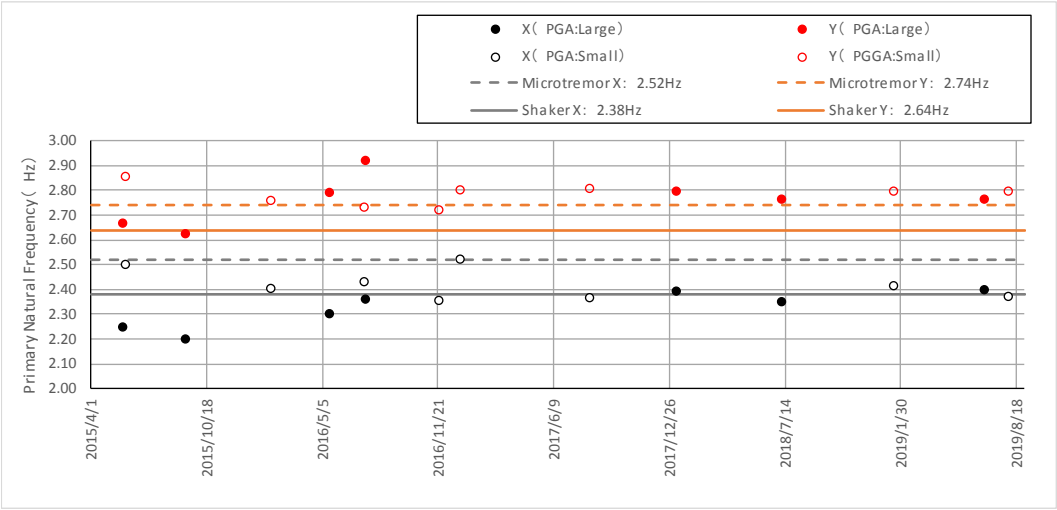

Figure 7. Time-dependent change of primary natural frequency

5 Summry

At Kanagawa University Building 3, we examined building vibration characteristics by microtremor measurement and shaker experimentation. The primary natural frequency data obtained by microtremor measurement and shaker experimentation was largely consistent.

The transfer function obtained from strong earthquake motion observation records evidenced time-dependent change in the primary natural frequency of the building. In the X direction, data showed that the natural frequency decreased when the maximum acceleration was large, and

that the correlation was strong. However, while a similar tendency was observed also in the Y direction, the correlation was weak. We will continue to analyze the differences in vibration characteristics between the X and Y directions. Also, at present, five years after construction completion, secular change is small and conceivably the soundness of the building remains intact.

In the future, based on the results of these analyses, we will focus on extracting indicators that can be used for structural health monitoring.

Notably, while this analysis treats only primary natural frequency, in the future we would like to examine also changes in attenuation characteristics.

6 References

Aoki Tamotsu, et al.: Study on Estimation of Vibration Characteristics of Structures Using Small-Size Shakers - Part 1. Development and Performance Evaluation of Shakers Using Linear Motors -, Summaries of technical papers of annual meeting (Kyushu), Architectural Institute of Japan, August 2007

Enomoto Takahisa, et al.: Shaker Experimentation on Building 3 of Kanagawa University Yokohama Campus, Summaries of technical papers of annual meeting (Kanto), Architectural Institute of Japan, September 2015

Enomoto Takahisa, et al.: Vibration Characteristics Evaluation of Building 3 of Kanagawa University Yokohama Campus Based on Earthquake Observation Records, Summaries of technical papers of annual meeting (Kyushu), Architectural Institute of Japan, August 2016

Inubushi Tetsushi, et al.: Vibration Characteristics Evaluation of Low-rise Steel Structure at Kanagawa University, 16th European conference on Earthquake Engineering, June 2018

National Research Institute for Earth Science and Disaster Resilience (NIED), “Strong-motion Seismograph Network s (K-NET, KiK-net),” Reading date: October 23, 2019, http://www.kyoshin.bosai.go.jp/kyoshin/

Ogawa Shuichi, et al.: Development of Prototype System for Structural Health Monitoring Aimed at Practical Application, Journal of Japan Association for Earthquake Engineering, Vol. 9, Issue 5, 2009

Wen Yongkui et al.: Study on the Estimation of Vibration Characteristics of Structures by Using Small-Size Shakers - Part 2. Estimation Results of Building Vibration Characteristics by Shaker Experimentation -, Summaries of technical papers of annual meeting (Kyushu), Architectural Institute of Japan, August 2007

Yokohama City: Yokohama City High-Density Strong-Motion Seismograph Network

Yokohama City Architectural Joint Design Office: Kanagawa University Yokohama Campus (tentative name) New Building 3, Completion Drawing s, March 2014

Yokohama Structural Design: Kanagawa University Yokohama Campus (tentative name) New Building 3, New Construction, Structural Calculation Documentation, October 2011

COLLISION EXPERIMENT AND SIMULATION ANALYSIS OF BASE-ISOLATED BUILDING MODEL TO RIGID RETAINING WALL BY SMALL SHAKING TABLE TEST

Takumi Horikago[1],Tetsushi Inubushi[2], Yuji Miyamonto[3] , Dong Ha Kim[4] ,
Ayaka Sato[5] ,Shohei Kubo[6]
[1] Majoring Archtecture, Department of Engineering, KanagawaUniversity,
r2015014449zy@jindai.jp, Japan
[2] Lecturer, Faculity of Archtecture, kindai University, inubushi@arch.kindai.ac.jp, Japan
[3] Professor, Graduate School of Engineering, Osaka University, miyamoto@arch.eng.osaka-u.ac.jp, Japan
[4] Graduate School of Engineering, OsakaUniversity, kim_dongha@arch.eng.osaka-u.ac.jp, Japan
[5] Graduate Student, Graduate school of Engineering, Osaka University,
sato_ayaka@arch.eng.osaka-u.ac.jp, Japan
[6] Graduate Student, Graduate school of Engineering, Osaka University,
kubo_syohei@arch.eng.osaka-u.ac.jp, Japan

Abstract: When the earthquake that is much greater than predictionoccur, base-isolated buildings have possibility to collide withthe surrounding retaining wall. Because ofthe isolator, the human life and the facility in the building may be protected, but the damage of the building is unclearunder the present conditions.By the previous researches, the building response for the collision to the retaining wall is being elucidated, but could not evaluate the building damage because the past studies do not have any damage in the building. Therefore we performed theexperiment that the base-isolated building model collide to the rigid retaining wall using the small shaking table. We confirmed the difference of the building response by changing the building stiffness and the input wave. After that, we performed numerical analysis about some experiment cases. We compared between the experiment results and analysis results, and verified the validity of the damage evaluation.

Keywords: Collision to Retaining Wall, Base-Isolated Building, Simulation Analysis,System Identification, Shaking Table Test

1 Introduction

In this chapter, I explain a process and problems of the spread of the isolated building. And I speak the purpose of this study.

1.1 Background

After South Hyogo earthquake generated in Japan in 1995, the isolated buildingswere evaluated as for high seismic performance. After that it spread a lot for function maintenance and the property maintenance of the building at the time of the disaster.For example, the hospital which adopted theisolation continued maintaining a hospital function just after an earthquake by the Tohoku district Pacific earthquake of March, 2011. In addition, in the Kumamoto earthquake of April, 2016, it is confirmed that many isolated buildings maintained a function. On the other hand, it is a fact that the isolation story displacement of the single amplitude 45cm to greatly exceed design displacement in a certain a building is confirmed in Kumamoto.

In Japan, the outbreak of the earthquake including the Nankai trough earthquake more than the current design levels is predicted in the future, and the possibility that the collision to a retaining wall happens is felt uneasy about when theisolated building suffered from it.The permission of the collision is considered as one of the measures to a retaining wall collision. The tendency to responce by the retaining wall collision was becoming clear by a study of the past, but the building was almost no damage. Therefore I cannot perform the inspection about the building damage enough. In addition, it becomes the present conditions that we cannot judge the risk of the retaining wall collision because the examination by the analysis is insufficient.

1.2 Purpose

Therefore we perform an experiment using the three stories isolated building made of steel in this study. It collides as a parameter and experiments on the biggest amplitude of the input wave and a proof stress of superstructure and performs the response by the collision and examination for the damage.

2 Experiment outline

I explain the isolated building model which I used in a retaining wall collision experiment. In addition, I speak it about metering equipments and the input waves.

2.1 Isolated building model

I show the plan of model which I used for this experiment in Figure 1. All the building is made of metal, and each storyis 162mm in height, superstructure is 536mm in height, total weight are approximately 40 kg(each story mass inTable1). The base-isolated story isinstalledin a notch of 1F and the simple mechanism using the springs (k=1.08N/mm) and the linear mortion rails, and isolation period is approximately 1.2 seconds. I use the column is 25mm in width and two kinds of thickness t=1.0, 2.3mm.It becomes the structure that the damage produces only on columns by using one kind thickness in all story, and integrating a floor and a beam. In addition, I show the specifications that were similar by three straight lines by the pulling test result of column steel materials in Table 2. The yield base Shear coefficient of the superstructure becomes 0.26, 1.75 from this resultrespectively. Theretaining wall is iron to reproduce the ideal rigid retaining wall andthickness of 16mm, 74mm in height. The linear mortion rails and the retaining walls are attached on a steel plate attached to theshaking table.

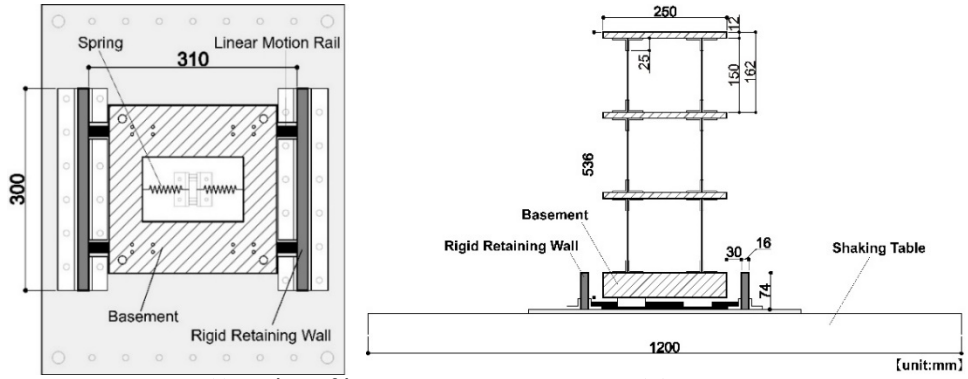

(i) plan of bacement (ii) section

Figure1. plan of model

Table1. mass of each story [kg]Table2physical property of column

	t=1.0mm	t=2.3mm
RF	6.78	6.85
3F	6.79	6.94
2F	6.79	6.94
1F (Basement)	19.3	19.3
Total	39.6	40.1

		t=1.0mm	t=2.3mm
Modulus of elasticity E_0 [N/mm^2]		2.33×10^5	2.38×10^5
First break point	σ_1 [N/mm^2]	97.54	131.5
	ε_1 [$\times10^{-6}$]	419.3	552.5
Second break point	σ_2 [N/mm^2]	158.7	202.8
	ε_2 [$\times10^{-6}$]	1078	1013

2.2 Measurement

In this study, I measured the horizontal acceleration of each story, the relative horizontal displacement with the vibration table and the axis strain of each story column. I perform the strain measurement on the both sides of the top and bottom at a position of 35mm from the column end. I swow the plot plan of measuring instruments in Figure 2.

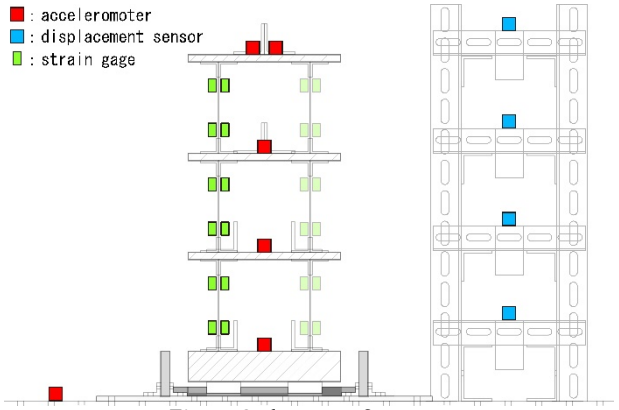

Figure2. layout of sensor

2.3 Input wave

The inputs are the observation wave of EW direction in the Kik-net Mashiki at the 2016 Kumamoto earthquake and the 1.5Hz sine wave. I show each wave in Figure 3. In addition, I convert 2 waves to velocity reponse spectrum in Figure 4. The dumping constant sets on this occasion with 2%.The Mashiki wave is changed with maximum verocity (10cm/s, 15cm/s) and the sine wave is chaned with maximum acceleration (125cm/s^2, 150cm/s^2). We shake the vibration table with 1 horizontal direction.

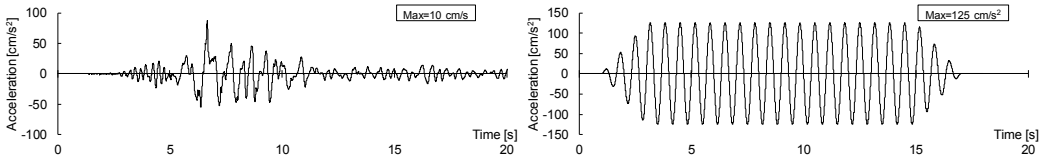

(i) Mashiki wave (ii) sinewave

Figure3. input wave pattern

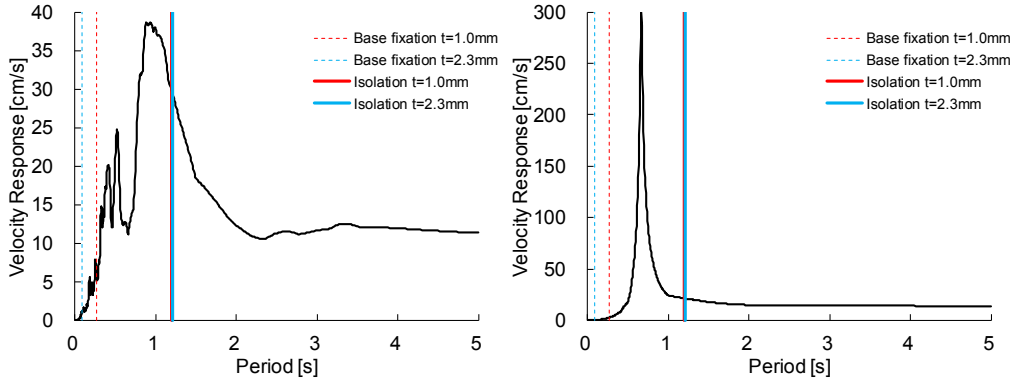

(i) Mashiki wave (ii) sinewave

Figure 4. velocity reponse spectrum

3 Result of experiment

Here, I show the result of the acceleration and the strain observed by a retaining wall collision experiment. In addition, I show vibration properties and restoring force characteristics of isolated story by the non-collision.

3.1 Response and damage of building

I show the 1F acceleration wave pattern of the case which produced a collision by each input in Figure 5.In a figure, the dashed lines are 5500cm/s^2 which is a measurement limit. In addition,I match each phase for comparisons and extract 2seconds including the first collision. The acceleration more than 5500cm/s^2 occurs in 1F because of a collision. Four times of collisions occurred in each column thickness by the Mashiki wave, but slide at the fourth collision time.In the sine wave, 40 times of collisions occurred in t=1.0mm and 42 times in t=2.3mm. As this cause,it is thought that the story rigidity of the superstructure decreases by column thickness becoming light and the energies consumed by the strain increased.Next,I show each floor wave ofcolumn axis strain pattern of each input of the big damage to Figure 6.The dashed lines in a figure express yieldstrain ε_y (1,078*10^{-6} or 1,013*10^{-6}).A big strain occurs as the lower floor,1Fof biggest strain reached 1,072*10^{-6} and produced the damage in Mashiki wave.Finally , I show maximum distribution of the acceleration and strain in Figure 7.By the acceleration, it is amplified by the non-collision gently as the upper story but the acceleration occurs more than 5500cm/s^2 in 1Fat the time of the collision and the acceleration of each story becomes big, too.In addition, the strain damages no layer by the non-collision, but when it collided, columnsare damaged with 1 and 2 stories and know what a remaining strain produces.

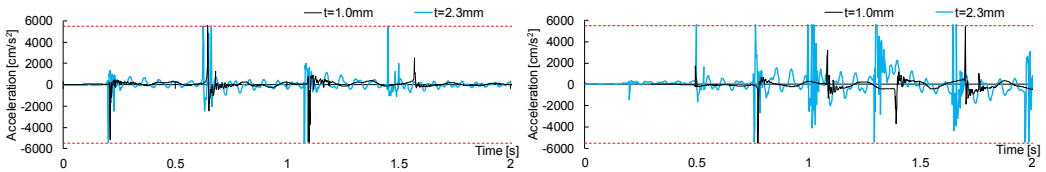

(i) Mashiki wave (15cm/s) (ii) sine wave (150 cm/s^2)

Figure5. accelerationof 1F in collision

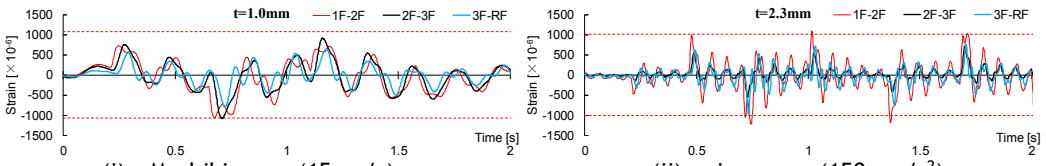

(i) Mashiki wave (15cm/s) (ii) sine wave (150 cm/s^2)

Figure 6. strain of each story in collision

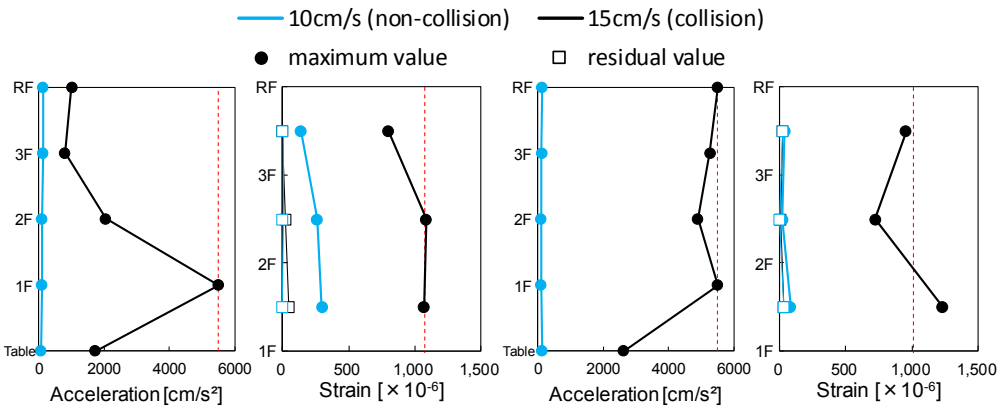

(a) acceleration (b) strain (a) acceleration (b) strain

(i) Mashiki wave (ii) sine wave

Figure 7. maximum value distribution

3.2 Building vibration properties and restoring force characteristics of isolationstory

Initially, I show transmission function (RF/1F) calculated from the acceleration response every thickness inFigure 8.Clear peaks can confirm either result expetc the collision of t=2.3mm. An amplification rate and natural frequency become small when they collide in both cases.The retaining wall collision make column plasticity and it is thought that the change of the vibration characteristic occurred because both become small. Next, I identified 1-3 natural frequency and the damping constant of the with a transmission function that did not produce a collision by the curve fitting of the theory transmission function. I show a part of the result in Figure 9.I can confirm a high quarity with eachpeak, butt=2.3mm has a little difference between observation and theory.In addition, I show restoring force characteristics of isolated story at the time of the non-collision in Figure 10.I found the isolated story shear power of the vertical axis from the friendship of the inertial force that multiplied acceleration by the mass of each story.I can confirm a tendency of the bilinear generally and the second rigidity becomes about half of installed spring.

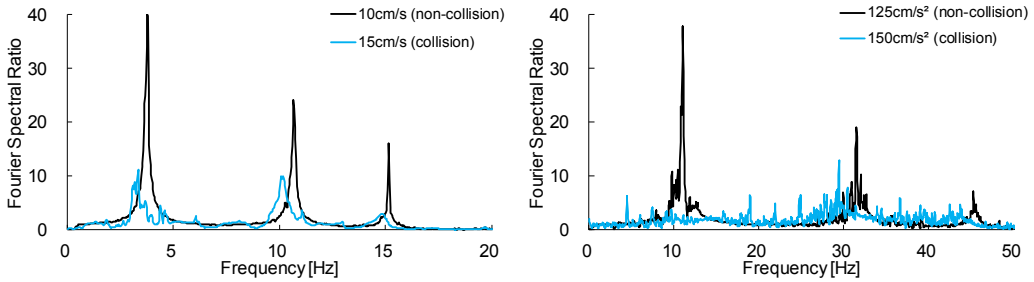

(i) t=1.0mm in Mashiki wave (ii) t=2.3mm in sine wave

Figure 8. transmission function (RF/1F)

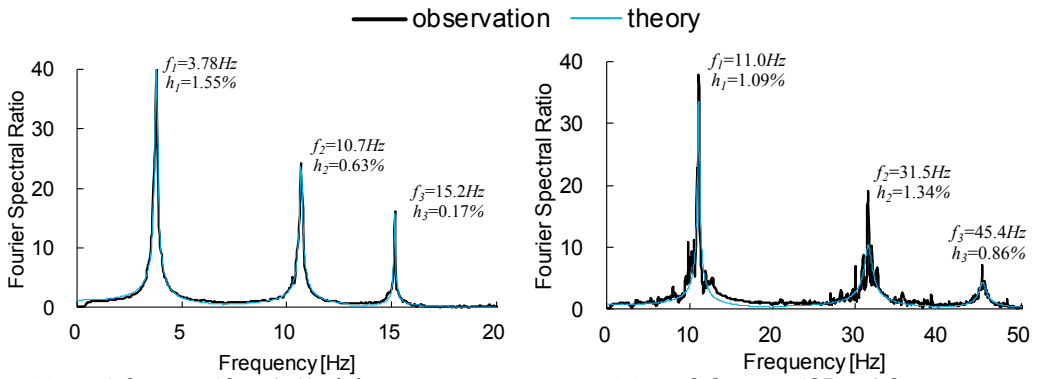

(i) t=1.0mm in 10cm/s Mashiki wave (ii) t=2.3mm in 125cm/s2 sine wave

Figure 9. result of system identification

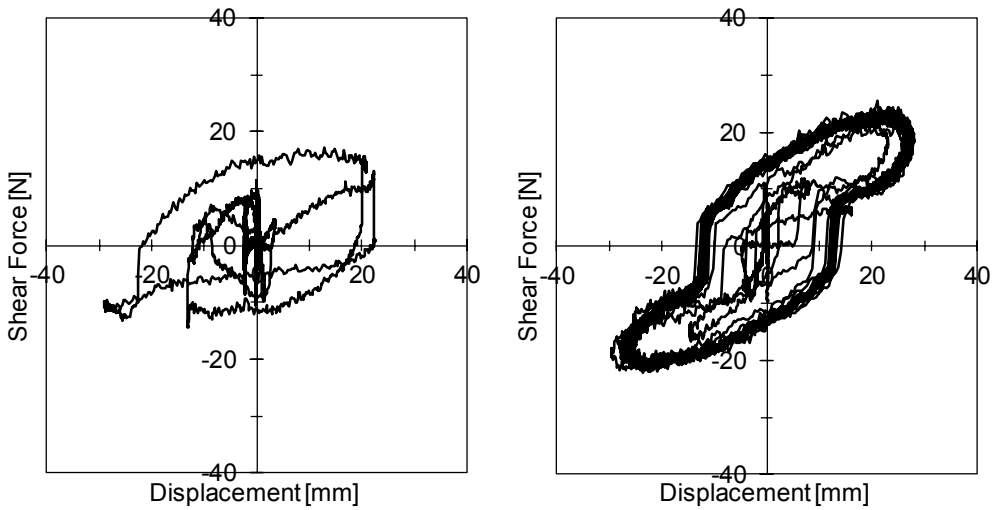

(i) t=1.0mm in 10cm/s Mashiki wave (ii) t=2.3mm in 125cm/s2 sine wave

Figure 10. restoring force characteristics of isolated story

4 Simulation analysis

In this chapter, I explain setting of the analysis. After that, Icompare the analysis and the experiment andconfirmvalidityoftheanalysis.

4.1 Analysis model

I show an analysis model in Figure 11. The beam is rigid, the column is a fiber element and the restoring force characteristics of each segment assumed a pulling test result similar normal tri linear(Table 2). The isolated story assumed bilinear from restoring force characteristics (Figure 10) of the isolated story of the experiment and reproduced by installing a dashpot.I set time increments with 1/200000 seconds for analysis and the beta in the bata method of New-mark is 0.25. Mainly, I explain two cases about the 150cm/s^2 sine wave in each column thickness.

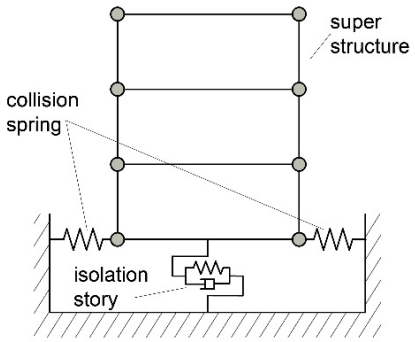

Figure 11. analysis model

4.2 Result of analysis

Firstly I show the non-collision restoring force characteristics of isolated story in t=1.0mm in the Figure 12. The displacement of the 80% degree of the experiment appears by the analysis and it is slightly small, but can reproduce the characteristic like the experiment generally. Nex, show 1F acceleration wave pattern and a strain wave pattern in 150cm/s^2 which produced a retaining wall collision on each column thickness successively Figure 13. I displayed it by the acceleration only in 5500cm/s^2 which was the measurement limit of the experiment, but the acceleration that was much bigger produced it.In addition, I grew big by the analysis than an interval at the collision time by the experiment. By the strain, I showed a value bigger than an experiment by the analysis generally. Particularly, because a big strain occurs in t=1.0mm, the result that a building collapsed like an experiment in the first story was provided. Finally I show the distributions of the maximum of the acceleration and maximum and remaining level of the strain in each story in 125cm/s^2 which did not collide to retaining wall and 150cm/s^2 which collided in both column thickness to Figure 14. But I change the very big value by acceleration of the analysis with 5500cm/s2 which was a measurement limit. The red dashed line expresses a measurement limit (5500cm/s^2) or a yield strainin a figure. By the acceleration, the analysis was smaller than experimental value, but was able to almost reproduce the tendency of the experiment. However, big acceleration occurred by the collision of t=1.0mm in each floors.On the other hand, thenalysis showed a big result by the strain, but the tendency of the experiment was able to reappear.Particularly, I was able to reproduce it with high precision with the case of the non-collision of t=1.0mm.It became the big evaluation with the case which collided and was damaged in all stories.

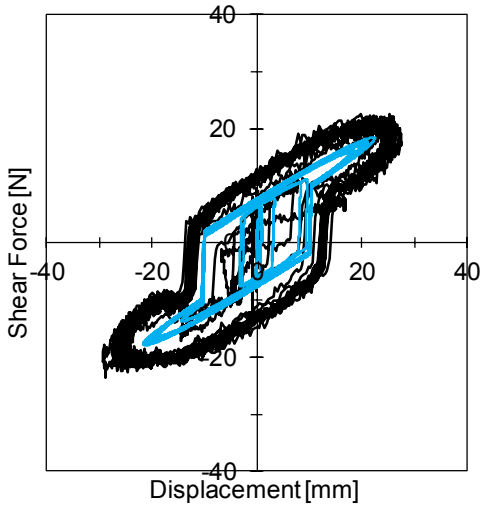

Figure 12. restoring force characteristics

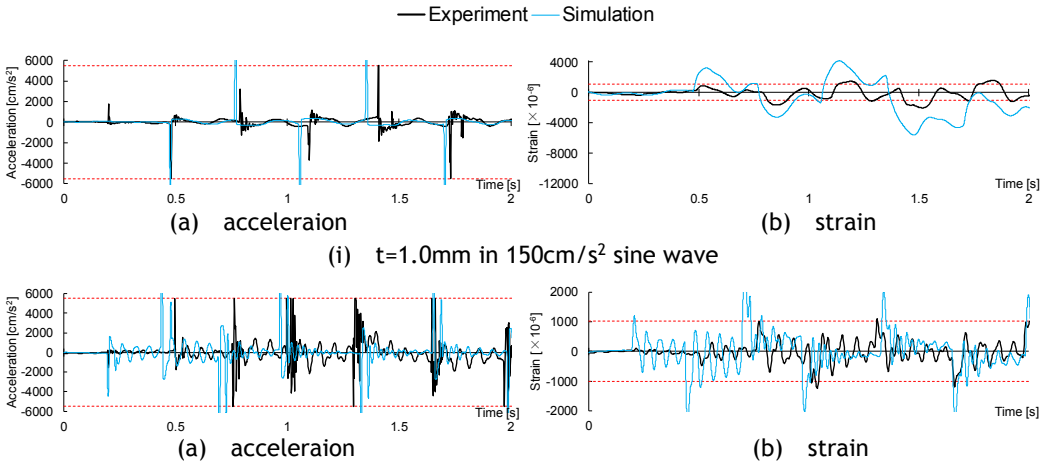

(a) acceleraion (b) strain

(i) t=1.0mm in 150cm/s^2 sine wave

(a) acceleraion (b) strain

(ii) t=2.3mm in 150cm/s^2 sine wave

Figure 13. wave pattern

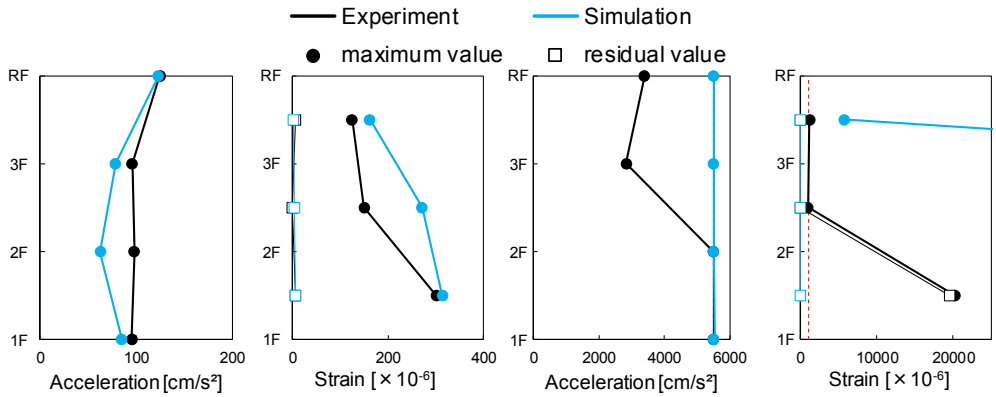

(a) acceleration (b) strain (a) acceleration (b) strain

(i) sine wave in t=1.0mm (125 cm/s^2) (ii) sine wave in t=1.0mm (150 cm/s^2)

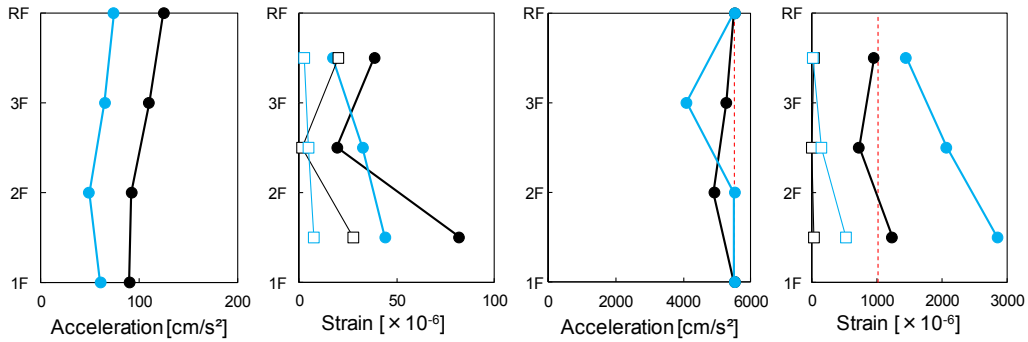

(a) acceleration (b) strain (a) acceleration (b) strain

(i) sine wave in t=2.3mm (125 cm/s^2) (ii) sine wave in t=2.3mm (150 cm/s^2)

Figure 14. maximum value distributionin experiment and analysis

5 Conclusion

In this study, I do the collision experiment and the simulation analysis to confirm the tendency of building response and damage. This study provided the following knowledges.

(i) A big acceleration occurs in 1F by the retaining wall collision and a big residual strain occurs as the lower stories.

(ii) The outbreak time was behind with the strain of each story as the upper story.

(iii) Because acolumn became plasticity by a collision, a natural frequency and the amplification ratio became small, and vibration properties changed.

(iv) By the analysis, I did a smaller evaluation by anaccelerationand bigger by a strain.

(v) I was able to reproduce the tendency of the result of experiment by the maximum value response.

(vi) I could almost reproduce a laboratory finding in numerical analysis.

6 References

Eiji Sato and others, “Development of Innovative Base-Isolation Systems based on E-Defense Full-scale ShakeTable Experiments Part 1-8,” Collection of Architectural Institute of Japan meeting arts and sciences lecture summaries, Aug., 2013

Goro Miwada and others, “Experiments of Collision to Retaining Wall with Real-Scale Base-Isolated Building,”Obayashi Corporation institute of technology report, No.74, 2010

Kazuhiko Kasai and others, “Evaluation rule for vibration period, damping, and mode vector of buildings tested by a shake table with inevitable rocking motions,“ J. Struct. Constr. Eng., AIJ, Vol. 76, No. 670, 2031-2040, Dec., 2011

SEISMIC RESILIENCE ASSESSMENT ON STEEL BRACED-FRAME

Fang-Wen GE[1] and Yan-Gang ZHAO[2]
[1]Department of Architecture, Kanagawa University, 3-27-1 Rokkakubashi, Yokohama, Japan
[1]E-mail: gefangwen@outlook.com
[2]Department of Architecture, Kanagawa University, 3-27-1 Rokkakubashi, Yokohama, Japan
[2]E-mail: zhao@kanagawa-u.ac.jp

Abstract: The concept of seismic resilience, i.e., the capability of the object to maintain a level of functionality after an earthquake and recover to the original state as soon as possible, has been widely accepted in structure engineering field over the past two decades. As the current situation in Japan, although research on this topic has been focused gradually, most of the studies still remain on the theoretical and application stage. Furthermore, for earthquake-prone countries like Japan, although steel braced-frames have usually been applied as a fundamental structural type to resist the seismic force, the role of braces on improving seismic resilience of steel frames has not been investigated. In this paper, a methodology based on a proposed conceptualization framework to conduct seismic resilience assessment suitable for single buildings is summarized. And following this procedure, seismic resilience assessment on two analytical steel frame models with and without braces are performed. Finally, by comparing the two calculated seismic resilience indices, braces are confirmed quantitatively as effective structural members that can enhance seismic resilience of main structures.

Keywords: seismic resilience assessment, loss function, recovery function, fragility analysis, steel frame

1 Introduction

Currently, the concept of resilience is widely applied in field of materials, ecological or transportation systems, etc. In structure engineering, a conceptualization framework to measure seismic resilience is firstly presented in 2003 (Bruneau et al. 2003). Following this work, Chang(Chang et al. 2004) contributed a resilienc …e evaluation method that relates the expected loss and the post-disaster recovery rate to seismic performance. Bruneau(Bruneau et al. 2007) proposed a quantitative assessment framework by associating resilience, probability function, and fragility in a single integrated approach for the first time and perform it in the case of acute care facilities. Then Cimellaro (Cimellaro et al. 2010) defined a unified term as seismic resilience index that can be evaluated quantitatively based on this framework. This enhanced framework was subsequently revised and applied in many seismic resilience evaluation studies. (Bocchini et al. 2012; Dong et al. 2015; Biondini et al. 2015; Tirca et al. 2016, etc.)

In Japan, research on seismic resilience has made rapid progress in the past decade (Hukuda 2014; Furuta et al. 2016; Takewaki 2014; Takewaki 2017). Although the correlated research increased following the establishment of the High Resilience Structural System Subcommittee in 2007, most of the studies still remain on the theoretical and application stage. There are few studies on quantitative seismic resilience assessment for single structures and it is not clear the contribution of braces on improving seismic resilience. Therefore, in this study, in order to promote the research from conceptualization to practical stage and make the quantification assessment possible, seismic resilience on analytical steel frame models with and without braces are evaluated and the enhancement of braces on seismic resilience of the main

structures will be quantitatively confirmed.

2 Seismic resilience assessment method

2.1 Seismic resilience index

In structural engineering, seismic resilience of the single building can be defined as the ability of the building to maintain a certain functionality and recover even if an earthquake occurs. Fig. 1 shows a conceptual diagram of seismic resilience representing the disaster-response capability measured by the functionality changes. The horizontal and vertical axes represent time and functionality of the objective building, respectively.

Quantification of seismic resilience has been measured by various methods. In this paper, seismic resilience assessment on specific single structures is performed using the seismic resilience index (Cimellaro et al. 2010) as shown in Eq. (1).

$$R = \int_{t_0}^{t_1} \left(1 - Q(t)\right) dt \tag{1}$$

where

$$Q(t) = 1 - L \times \left[H(t - t_0) - H(t - t_1) \right] \times f_{REC} \tag{2}$$

where Q(t) is the performance function representing functionality changes over time; t_0 is the occurrence time of earthquake event; t_1 is the end time of recovery; H(.) is the Heaviside step function; L is the loss function and f_{REC} is the recovery function.

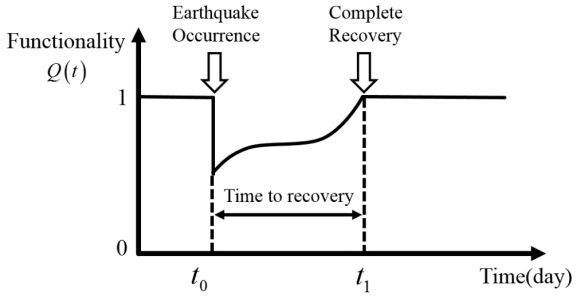

Fig. 1 Conceptual diagram of seismic resilience

2.2 Loss function

As shown in Eq. (2), loss function L in performance function is necessary for quantifying seismic resilience index. Cause single buildings were the analytical object, only the direct economic losses, which can be expressed as the ratio of the building repair cost and the rebuilding cost as shown in Eq. (3) is considered in this study.

$$L = \sum_{j=1}^{4} \frac{C_{s,j}}{I_s} \times \prod_{i=1}^{T_i} \frac{(1+\delta_i)}{(1+r_i)} \times P_j \tag{3}$$

where j is the performance limit state; C_{sj}/I_s is the structural loss ratio (C_{sj} is the building repair cost and I_s is the rebuilding cost); r_i and δ_i are the annual discount rate and annual depreciation rate, respectively; T_i is the elapsed years since the earthquake event occurred and

P_j is the total failure probability.

2.3 Fragility analysis

In seismic reliability analysis, total failure probability P_j as shown in Eq. (4) can be obtained combining fragility curves P_f (I) and the occurrence probability of earthquake intensity p(I) calculated from hazard curves H(I) as shown in Eq. (5).

$$P_j = \sum_{I=0}^{n} P_f(I)\, p(I) \tag{4}$$

$$p(I) = \Delta\left(1 - H(I)\right) \tag{5}$$

where I is the seismic intensity measure and used as peak ground velocity (PGV) in this paper.
Total failure probability can be expressed as a conditional probability with respect to seismic intensity measure, which can be represented by fragility curves as shown in Eq. (6).

$$P_f(I) = \Pr ob\left[DM > Ds \mid I\right] \tag{6}$$

where DM is the maximal interstory drift ratio, and Ds is the prescribed threshold of the interstory drift ratio for each performance limit state.
In this study, numerical simulation using linear regression in log-space is adopted for generating fragility curves (Zentner et al. 2017). Firstly, this method requires *N* input-output pairs (I_i, DM_i) from nonlinear time history analysis. In general, *DM* is often assumed to be a lognormal random variable as Eq. (7).

$$DM = aI^b\varepsilon \tag{7}$$

where is the lognormal random variable with a median of 1 and logarithmic standard deviation of ; a and b are the parameters which can be determined by linear regression in log-space.
Then, *Ds* can also be defined in the same form using the median of *DM*, i.e., A_m, as shown in Eq. (8).

$$Ds = aA_m^b \tag{8}$$

From Eq. (8), A_m can be expressed as follows:

$$A_m = \exp\left[\frac{\ln(Ds/a)}{b}\right] \tag{9}$$

Using the definition of safety factor as shown in Eq. (10), fragility curves can be expressed as Eq. (11).

$$Z = \frac{Ds}{DM} \tag{10}$$

$$P_f(I) = \Pr ob\left[Z < 1 \mid I\right] = \Pr ob\left[\ln Z < 0 \mid I\right] \tag{11}$$

$$\ln Z = \ln Ds - \ln DM = b\ln A_m - b\ln I - \ln\varepsilon \tag{12}$$

where lnZ as shown in Eq. (12) is normal distributed.

Finally, using the mean (Eq. 13) and standard deviation (Eq. 14) of lnZ, fragility curves can be expressed as Eq. (15) with the normal cumulative distribution function.

$$\mu_{\ln Z} = b\ln A_m - b\ln I \tag{13}$$

$$\sigma_{\ln Z} = \sigma \tag{14}$$

$$P_f(I) = \Phi\left(-\frac{\mu_{\ln Z}}{\sigma_{\ln Z}}\right) = \Phi\left(\frac{\ln I - \ln A_m}{\sigma / b}\right) \tag{15}$$

2.4 Recovery function

Another important part of seismic resilience assessment is the recovery process modeling. After an earthquake, modeling for this stage is very complicated because it is affected by various external factors. Although many studies have been conducted, three simplified recovery models representing different recovery paths as shown in Eq. (16) to (18) are often applied for the sake of simplicity. (Cimellaro et al. 2010; Bocchini et al. 2012 and Kafali et al. 2005)

$$f_{REC1} = 1 - \frac{t - t_0}{t_1 - t_0} \tag{16}$$

$$f_{REC2} = \exp\left[-\ln 200 \times \frac{t - t_0}{t_1 - t_0}\right] \tag{17}$$

$$f_{REC3} = \frac{1}{2}\left\{1 + \cos\left[\pi \times \frac{t - t_0}{t_1 - t_0}\right]\right\} \tag{18}$$

In summary, the flowchart of seismic resilience assessment suitable for single structures is concluded in Fig. 2.

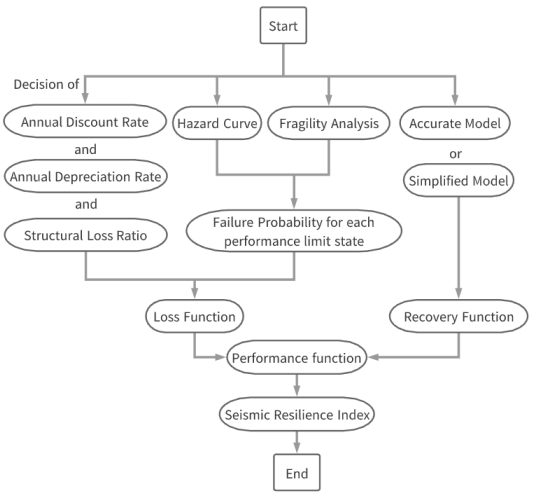

Fig. 2 Flowchart for seismic resilience assessment on single structures

3 Assessment example

3.1. Analytical models

To quantitatively evaluate the effect of braces on seismic resilience of main structures, a 5-story 3-span steel bare-frame and a 5-story 3-span steel braced-frame with braces as shown in Fig. 3 are set as the analytical models. Two models are set as the same dimensions, member yield stress as 235N / mm^2, except of the arrangement of braces. The story weight for two models are set as 39kN/m of the beam and distributed evenly to all nodes. The columns are square steel pipe and the beams are H-shaped steel. Table 1 shows the detailed information.

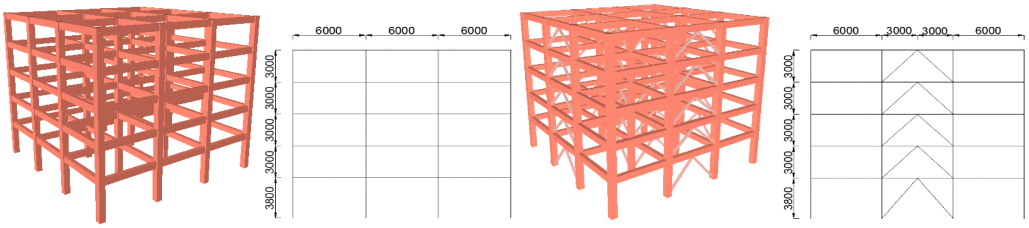

(a) Model 1 (b) Model 2

Fig. 3 Analysis models (mm)

Table 1 Detailed structural member dimensions (mm)

Story	Column	Beam	Brace
1	400×400×11	390×300×9×14	12×70
2	350×350×11	360×300×9×14	12×60
3	350×350×9	340×250×9×14	12×45
4	350×350×8	300×200×9×14	12×32
5	250×250×6	240×170×7×11	9×25

3.2 Loss Function

3.2.1 Result of the fragility curves from nonlinear time history analysis

In this study, *Ds* of the steel structures for each performance limit state determined by literature (JSCA, 2018; GB/T 18208.4, 2005) are listed in Table 2, with the correlated structural loss ratio C_{sj}/ I_s.

Table 2 Threshold of performance limit state and corresponding structural loss ratio

Performance Limit State	Threshold *Ds*	Structural Loss Ratio
None	1/200	5%
Slight	1/150	15%
Moderate	1/100	45%
Extensive	1/75	85%

In order to obtain *DM*, nonlinear time history analysis is performed. The properties considered are 205 kN/mm^2 for Young's modulus, bilinear model for restoring force characteristic, 1/50 of the initial stiffness for the secondary stiffness and 2% for the damping ratio of the fundamental period. 10 simulated earthquake motions conforming to the response spectrum for rare earthquake motions design stipulated by Building Standards Law of Japan are adjusted to 8 phases from the PGV of 10 kine to 150 kine as input waves. The velocity time histories of the

input earthquakes motions are shown in Fig.4. As the result of nonlinear time history analysis, Fig. 5 shows the relationships between PGV of the input ground motions and *DM* of the analytical models. And Fig. 6 shows the generated fragility curves of the two models by numerical simulation using linear regression in log-space. From the results, it can be seen that braces can suppress the failure probability for each performance limit state of the main structure effectively.

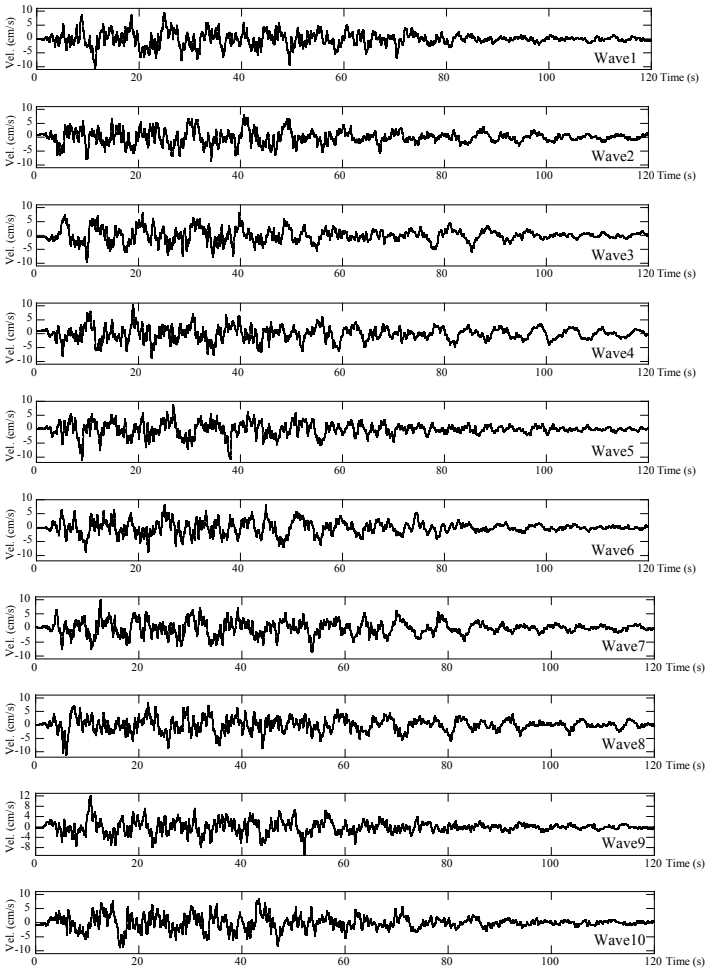

Fig. 4 Velocity time history of input earthquake motions

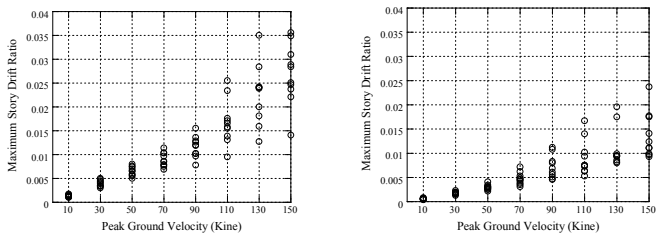

(a) Model 1 (b) Model 2

Fig. 5 Nonlinear time history analysis results

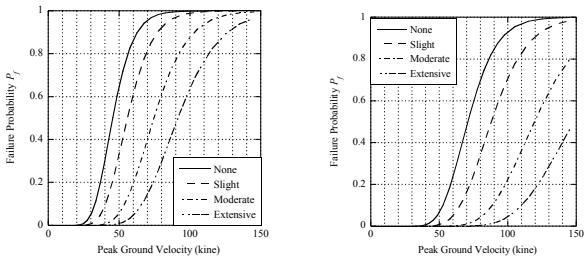

(a) Model 1 (b) Model 2

Fig. 6 Fragility Curves

3.2.2 Total failure probability

In this study, Tokyo, Kumamoto, Hiroshima, and Osaka are selected for assessment. Hazard curves (J-SHIS) with calculated $p(I)$ of the selected cities are shown in Fig. 7. Then based on the generated fragility curves in Fig. 6, the total failure probability P_f are calculated by Eq. (4) and summarized in Table 3.

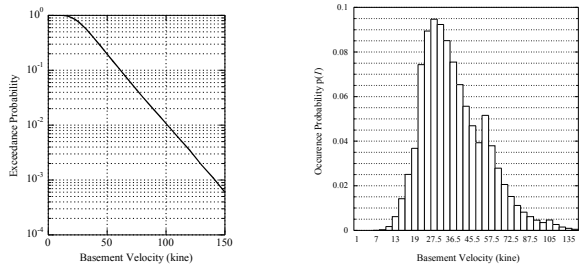

(a) Tokyo

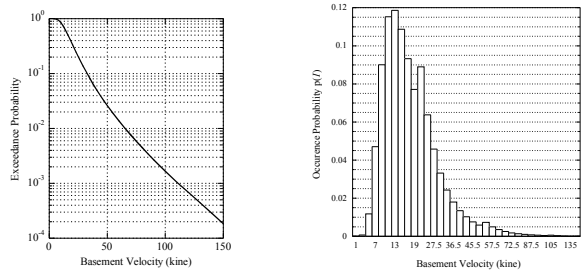

(b) Kumamoto

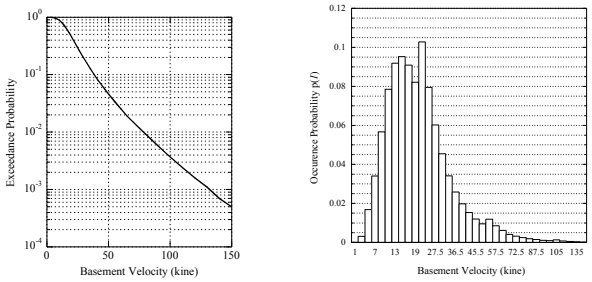

(c) Hiroshima

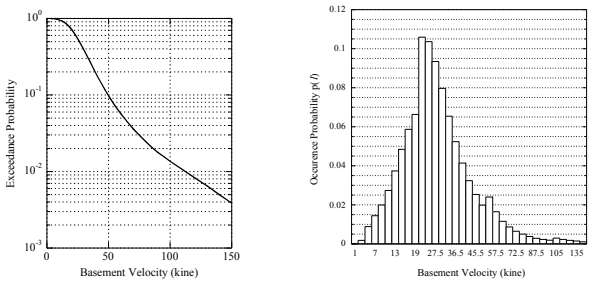

(d) Osaka

Fig. 7 Hazard curves and the calculated probability of the earthquake intensity for selected seismic zones

Table 3 Total failure probability for each performance limit state

City	Model	Total Failure Probability P_j			
		None	Slight	Moderate	Extensive
Tokyo	1	0.2918	0.1723	0.0678	0.0302
	2	0.0775	0.0332	0.0076	0.0020
Kumamoto	1	0.0476	0.0248	0.0090	0.0040
	2	0.0102	0.0044	0.0011	0.0003
Hiroshima	1	0.0767	0.0422	0.0165	0.0077
	2	0.0187	0.0085	0.0022	0.0006
Osaka	1	0.1564	0.0879	0.0361	0.0184
	2	0.0406	0.0200	0.0064	0.0022

Direct economic losses are calculated with the assumptions of r_i and $_i$ of 4% and 1%, and T_i of 1 year. Fig. 8 shows the results. It can be seen that although for the same model, L varies with the changing seismic regions, it can be reduced by nearly 85% using the arrangement of braces.

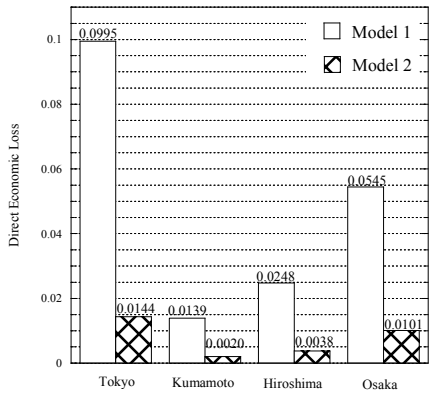

Fig. 8 Comparison of the direct economic loss between two models in different seismic regions

3.3 Recovery Function

In seismic resilience assessment, modeling of the recovery process is a very important part. Even for the same analytical object, calculated seismic resilience index will be various with the different selected recovery model. In practice, it is desirable to set a propriate recovery model

consistent with the objective building. However, it is complicated to model this process because of the uncertainties existed. Cause the purpose of this paper is to clarify the role of braces in seismic resilience, for the sake of simplicity, an exponential recovery model as shown in Eq. (17) is adopted with the recovery time of 30, 90 and 180 days into three damage levels (PD materials, AIJ, 2019).

3.4 Assessment result

Using the calculated results of *L* with the assumption of exponential recovery process under the three damage levels, the performance curves and the calculated seismic resilience indices of the two analytical models are shown in Fig. 9. It can be seen from the result that seismic resilience indices of the steel braced-frame model are greater than that of other one regardless of the seismic regions and the recovery time under the same assumption of recovery process. Therefore, braces are confirmed quantitatively as effective seismic control members to improve the seismic resilience of main structures.

4 Conclusions

In this paper, a methodology for conducting seismic resilience assessment suitable to be applied in assessing single buildings is summarized. Furthermore, this framework is performed on two steel frame models with and without braces. Finally, by comparing the calculated seismic resilience indices, the role of braces effecting seismic resilience on main structures are quantitatively evaluated. Conclusions are summarized as follows:

(1) Although the expected direct economic losses caused by earthquake show variation with assumptions of seismic regions, all of them can be reduced around 85% by the arrangement of braces.

(2) In an assessment example, seismic resilience indices of the two steel frame models are calculated under the same assumption of a simplified exponential recovery process considering three recovery times. Although modelling of the recovery process will affect the seismic resilience, it can be still seen that the braced-frame model shows a better seismic resilience performance than the bare one. Thus, braces are proved quantitatively as effective structural members which can enhance the seismic resilience of the main structure.

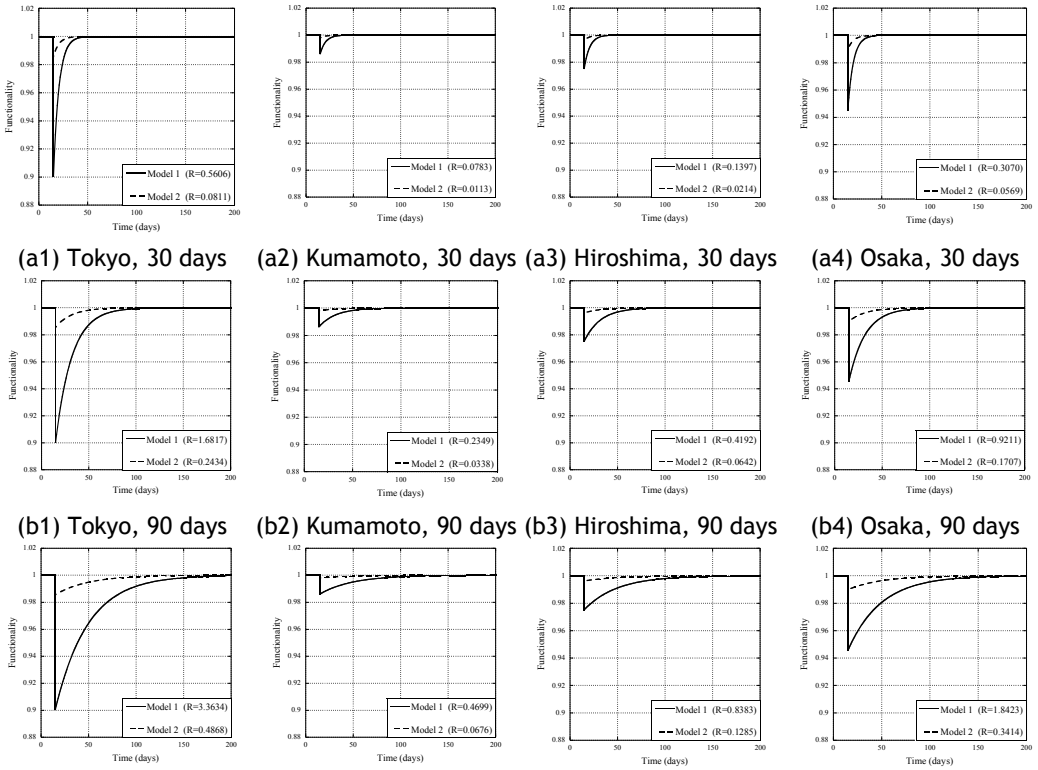

(a1) Tokyo, 30 days (a2) Kumamoto, 30 days (a3) Hiroshima, 30 days (a4) Osaka, 30 days

(b1) Tokyo, 90 days (b2) Kumamoto, 90 days (b3) Hiroshima, 90 days (b4) Osaka, 90 days

(c1) Tokyo, 180 days (c2) Kumamoto, 180 days (c3) Hiroshima, 180 days (c4) Osaka, 180 days

Fig. 9 Comparisons of the performance curves under the exponential recovery process

5 References

Biondini F., Camnasio E. and Titi A.: "Seismic resilience of concrete structures under corrosion", *Earthquake Engineering& Structural Dynamics*, Vol. 44: 14 (2015): 2445-2466

Bocchini P., Decò A. and Frangopol D. M.: "Probabilistic functionality recovery model for resilience analysis", In Bridge Maintenance, Safety, Management, Resilience and Sustainability, -Biondini & Frangopol (Eds), CRC Press, Taylor and Francis: UK (2012): 1920-1927

Bruneau M. and Reihorn A.: "Exploring the concept of seismic resilience for acute care facilities", *Earthquake Spectra*, Vol. 23, No. 1 (2007): 41-62, 2007. 2

Bruneau M., Chang S. E., Eguchi R. T., Lee G. C., O' Rourke T. D., Reinhorn A. M., Shinozuka M., Tierney K., Wallace W. A. and von Winterfeldt D.: "A framework to quantitatively assess and enhance the seismic resilience of communities", *Earthquake Spectra*, Vol. 19, No. 4 (2003): 733-752

Chang S. E. and Shinozuka M., "Measuring improvements in the disaster resilience of communities", *Earthquake Spectra*, Vol. 20, No. 3 (2004): 739-755

Cimellaro G.P., Reihorn A. M. and Bruneau M., "Framework for analytical quantification of disaster resilience", *Engineering Structures*, Vol. 32 (2010): 3639-3649

Dong Y. and Frangopol D. M., "Risk and resilience assessment of bridges under mainshock and

aftershocks incorporating uncertainties", *Engineering Structures*, Vol. 83 (2015): 198-208

Furuta K. and Kanno T., "Birth and prospect of resilience engineering", *Systems, Control and Information*, Vol. 60, No. 1 (2016): 3-8 (in Japanese)

GB/T 18208.4-2005, Post-earthquake field works- Part 4 Assessment of direct loss[S], Beijing: Seismological Press, 2005 (in Chinese)

Hukuda R., "Structural resilience -Keyword for disaster mitigation-", *Concrete Journal*, Vol. 53, No. 1 (2014): 92-96 (in Japanese)

Japan Structural Consultants Association, The guide to safe buildings JSCA performance-based seismic design, 2018. 3 (in Japanese)

Kafali C. and Grigoriu M., "Rehabilitation decision analysis", Proc. Ninth Int. Conf. on Structural Safety and Reliability (ICOSSAR), ISO Press, Netherlands

"Japan Seismic Hazard Information Station", http://www.j-shis.bosai.go.jp/

Special Research Committee on Evaluation of Resilience and BCP Index: Proposing seismic resilience index for BCP decision, Panel Discussion Materials of Annual Meeting, AIJ

Takewaki I., "Toward higer building resilience as a new measure for earthquake resistance", *Journal of Architecture and Building Science*, Vol. 129, No. 1663 (2014): 3 (in Japanese)

Takewaki I., "Summary of the panel discussion on structural design for resilient and safer buildings", *Journal of Architecture and Building Science*, Vol. 132, No. 1702 (2017): 36-37 (in Japanese)

Tirca L., Serban O., Lin L., Wang M. and Lin N., "Improving the seismic resilience of existing braced-frame office buildings", *Journal of Structure Engineering*, Vol. 142 (2016): 1-14

Zentner I., Gündel M. and Bonfils N., "Fragility analysis methods: Review of existing approaches and application", *Nuclear Engineering and design*, Vol. 323 (2017): 245-258

STUDY ON CONFINEMENT PATH OF FRP-CONFINED CONCRETE COLUMN

Jian-ming Li[1], Yan-gang Zhao[1,2], Siqi Lin[2]
[1] Department of Architecture and Building Engineering, Kanagawa University, Kanagawa 2218686, Japan
[2] Key Laboratory of Urban Security and Disaster Engineering of Ministry of Education, Beijing University of Technology, Beijing 100124, China
Correspondence e-mail address: ljm2604330@gmail.com

Abstract: Previous research has indicated that the compressive strengths of the concrete were obviously affected by the confinement paths of confined concrete in circular concrete-filled steel tube (CFST) short columns that withstands axial compression. However, investigation into the confinement paths on the compressive strengths of confined concrete in axially loaded circular fiber reinforced polymer (FRP) confined concrete columns has been still limited. The purpose of this paper is to investigate the confinement paths of confined concrete and their corresponding effects on the compressive strengths of confined concrete in axially loaded circular FRP-confined concrete columns. An experimental program with a total of 32 specimens was carried out, and the detailed parameters that include the concrete strength and layers of FRP were investigated. The results suggested that the confinement paths of confined concrete in axially loaded circular FRP-confined concrete columns were significantly affected by the column parameters, and had no lateral stage which were different from those in circular CFST short columns. Based on the test results, a compressive strength model incorporating the confinement path effects is optimized and good performance was found in comparison with the experimental results.

Keywords: Confinement path, Compressive strength, Fiber reinforced polymer (FRP) confined concrete column, Compressive strength model.

1 Introduction

Fiber Reinforced Polymer (FRP) confined concrete columns has been widely studied by many researchers, due to their excellent mechanical properties. The compressive strength models of confined concrete in FRP-confined concrete columns is a primary parameter to determine the axial bearing capacity of FRP-confined concrete column. So far, the existing compressive strength models of confined concrete such as models of Richard and Mander are mainly developed based on the experimental tests of actively confined concrete. However, when a FRP-confined concrete column is axially compressed, the lateral confining stress of the concrete increases with the increase of compressive stress, but it's not constant as actively confined concrete. The relationship between the lateral stress and compressive stress of confined concrete is defined as confinement path. Till now, only the confinement path of CFT columns has been investigated [1], but investigation of confinement path of the FRP-confined concrete columns has not been found.

The purpose of this paper is to investigate the confinement paths of axially loaded FRP-confined concrete column, and its effect on the compressive strength of concrete.
There are many types of FRP columns, e.g., Aramid fiber columns, Carbon fiber columns and Glass fiber columns, among which Carbon fiber is the most commonly used one in practical construction. The ultimate capacity is the primary concern in practical engineering, which can be given by:

$$f_{cc} = f_c + k\sigma_{ru} \tag{1}$$

Where f_{cc} is the ultimate strength of the confined column; f_c is the compressive strength of unconfined concrete; σ_{ru} is the lateral stress provided by the constraint material, k is the confinement factor, for which a value of 2.0-4.1 was generally adopted, respectively.
Eq. (1) suggests that well predicting its compressive strength of confined concrete is important to predict the ultimate strength of the confined columns. Compressive strength models of confined concrete developed based on the experimental tests of actively confined concrete are widely adopted in the researches of the confined columns.

For actively confined concrete, specimens were subjected to a constant hydrostatic lateral pressure. However, when a confined column is compressed axially, the lateral stress of the concrete is not constant but increases with the compressive stress. The relationship between the lateral stress and compressive stress of confined concrete is known as confinement path. The different confinement path between the actively confined concrete and concrete in passively confined column may results in a different confinement effect of the two types of concrete, leading to a different compressive strength. Thus, modelling the concrete in passively confined columns by using the models of actively confined concrete is doubtful.

The confinement paths studied in these studies are shown in Fig.1. It should be noted that the confinement paths shown in Fig.1 (a) and (b) are generally adopted in the test of actively confined concrete and are also investigated.

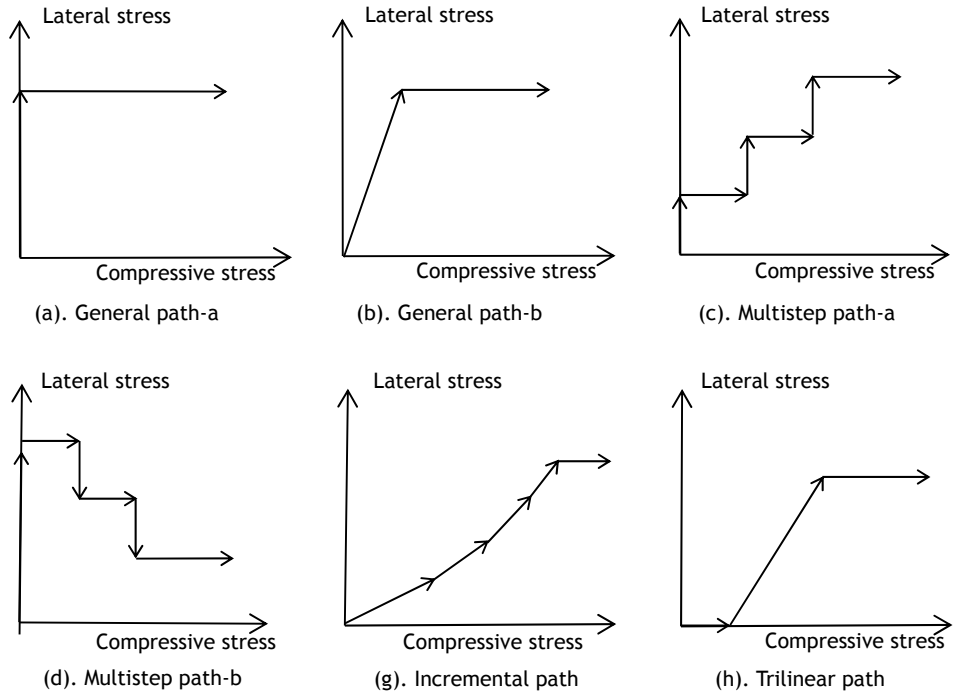

Fig.1 .Confinement paths in previous studies

Previous research has indicated that the compressive strengths of the concrete were obviously affected by the confinement paths of confined concrete in circular concrete-filled steel tube (CFST) short columns that withstands axial compression [1,2]. However, investigation into the

confinement paths on the compressive strengths of confined concrete in axially loaded circular fiber reinforced polymer (FRP) confined concrete columns has been still limited.

2 Experimental summary

Experimental tests with a total of 18 specimens, including 1 layer, 2 layers and 3 layers FRP-confined concrete specimens, respectively, were conducted to investigate confinement path of axially loaded FRP-confined concrete column, and its effect on the compressive strength of concrete.

3 Evaluation methods of confinement paths and corresponding effects

A confinement path is defined as the relationship between the lateral and axial stresses of concrete by previous studies [1,2] . Several typical confinement paths are given in Fig. 2.

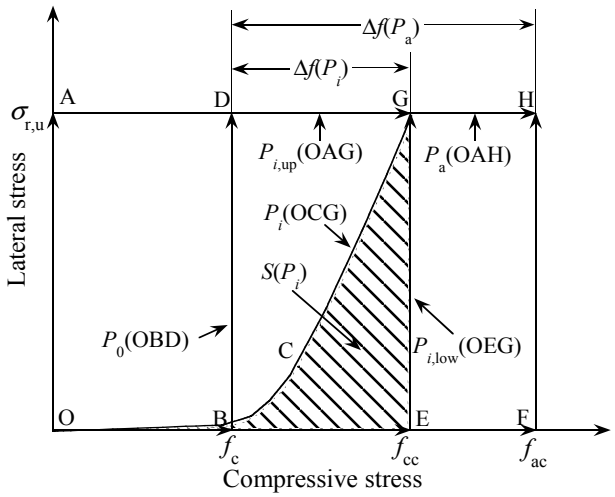

Fig.2. Typical confinement path of concrete

(1). Path P_0: There is no lateral stress before axial stress reaching the compressive strength of plain concrete f_c. Although lateral stress is applied, no increase of compressive strength is achieved. Therefore, Path P_0 could be considered as the confinement path of plain concrete.

(2). Path P_a: A certain significant lateral stress is applied from the very beginning of axial loading. Such confinement path is generally adopted in the test of actively-confined concrete. Concrete would be well confined under confinement path P_a, thus the compressive strength will be significantly increased compared with plain concrete, which is indicated by$\Delta f(P_a)$ in the figure.

(3). Path P_i: Lateral stress is quite small at the initial stage, and then become larger with increasing axial stress at the later stage. Such confinement path is generally achieved in actual confined concrete structures, e.g. reinforced concrete, concrete-filled steel tube and FRP-confined concrete which belong to passively-confined concrete. The increased compressive strength is indicated by$\Delta f(P_i)$.

Based on Ref. [1],$\Delta f(P_i)$ is generally found less than$\Delta f(P_a)$ despite paths *Pi* and *P*a having a same ultimate lateral stress. This could be attributed to the different confinement paths of paths P_i

and P_a. Therefore, the confinement effects can't simply be evaluated via the ultimate lateral stress.

Thus, to investigate the confinement path of confined concrete and its effect upon the compressive strength, two evaluation indices are used [1], They are lateral stress domination index and an effect index λ, respectively.

Firstly, the dominance degree of the lateral stress in a stress path P_i is characterized by a lateral stress domination index, which was defined as:

$$SI(P_i) = \frac{S(P_i)}{S(P_{i,up})} \tag{2}$$

where $S(Pi)$ is the area enclosed by path Pi and its lower boundary path $P_{i,\text{low}}$ (OEG). Correspondingly, $S(P_{i,\text{up}})$ is the area enclosed by path $P_{i,\text{up}}$ (OAG) and the lower boundary path $P_{i,\text{low}}$. It should be noted that a higher value of SI means the lateral stress is more significant.

Secondly, to predict the effect of stress path upon the compressive strength of confined concrete, an effect index was defined as:

$$\lambda(P_i) = \frac{\Delta f(P_i(OCG), \sigma_{r,u})}{\Delta f(P_a, \sigma_{r,u})} \tag{3}$$

Where $\Delta f(P_i(\text{OCG}), \sigma_{r,u})$ is the increased strength of the concrete under stress path P_i, namely $\Delta f(P_i(\text{OCG}), \sigma_{r,u}) = f_{cc} - f_c$, where f_{cc} is the compressive strength of confined concrete, f_c is the strength of plain concrete, respectively. $\Delta f(P_a, \sigma_{r,u})$ Was given in the previous studies[1], is given as $2.2 f_c^{0.3} \sigma_{ru}^{0.81}$.

In Eq. (3), $\lambda(P_i)$ =1.0 means the influence of path P_i(OCG) on the increased strength is completely the same with that of path P_a. In other words, $\lambda(P_i)$ =1.0 means the compressive strength of the confined concrete is independent of confinement paths. On the contrary, $\lambda(P_i) \neq 1.0$ means the influence of path P_i(OCG) on the increased strength differs from that of path P_a. That is, the compressive strength of confined concrete is path-dependent.
In summary, the effect index $\lambda(P_i)$ can be calculated by:

$$\lambda(P_i) = \frac{f_{cc} - f_c}{2.2 f_c^{0.3} \sigma_{ru}^{0.81}} \tag{4}$$

4 Confinement paths and ultimate lateral stress

To obtain the confinement path, the axial stress and lateral stress at each loading step should be known. The axial stress of FRP-confined concrete column can be determined by dividing the axial load by the sectional area of concrete:

$$f_{z,i} = \frac{N_i}{A_c} \tag{5}$$

The lateral stress can be determined by:

$$\sigma_{r,i} = \frac{2 f_{frp} n t}{D} = \frac{2 E_f \varepsilon_{h,i} n t_f}{D} \tag{6}$$

where f_{frp} is FRP material tensile strength in the hoop direction; E_f is the elastic modulus of FRP material; $\varepsilon_{h,r}$ is the hoop strain at i-th loading step measured from the strain gauge; t_f is the thickness of FRP sheet; n is the layers of FRP applied; D is the diameter of core concrete; N_i is the axial load at i-th loading step read from the testing equipment; A_c is the sectional area of core concrete.

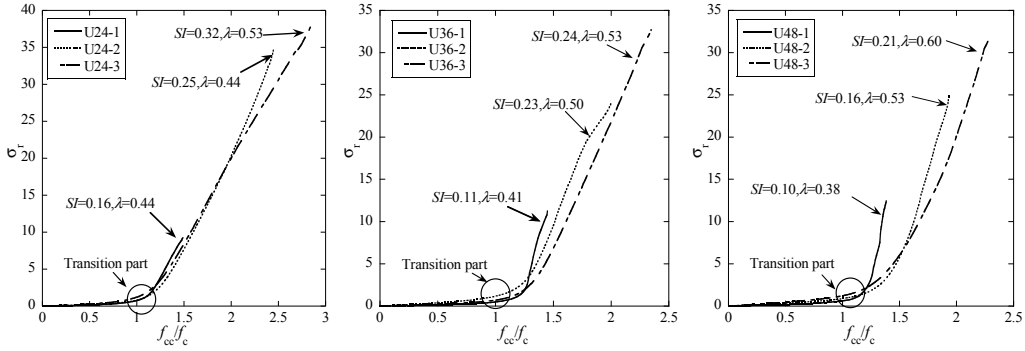

Fig.3. Confinement paths of FRP-confined concrete

The confinement paths of the concrete for the specimens UC24, UC36, UC48 are given in Fig.2. It can be found that confinement path has a transition part. Before the transition part, the lateral stress is quite insignificant because the microcrack of concrete hardly develops and lateral expansion is in significant at this stage. With the increase of axial stress, the microcracks of concrete starts to develop quickly, leading to significant lateral expansion of concrete and thus the increase of lateral stress.

5 Confinement path effects on compressive strength of concrete

In this section, the confinement path effects upon the compressive strength of confined concrete are discussed. Fig.3 shows the relationship between lateral stress domination index *SI* and f_y/f_c ratio; *SI* and D/t ratio, it can be seen that, *SI* increases as f_y/f_c ratio increases, and decreases as D/t ratio increases, that is, the *SI* is influenced by column parameters.

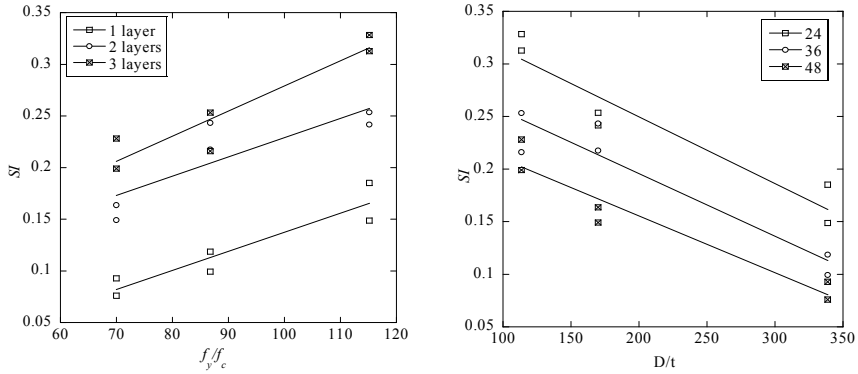

Fig.4. Lateral stress domination index SI corresponding fy/fc ratio and D/t ratio

Fig.4 shows the relationship between effect index λ and lateral stress domination index *SI* in the present and previous researches, λ was increase with *SI* initially, and then remain a constant of roughly unity after *SI* exceeding about 0.5. That is, for the confinement path with a small *SI*, its effect on the compressive strength is significant, while for the confinement path with a *SI*

exceeding about 0.5, its effect on compressive strength can be neglected. Based on the results, the relationship between effect index and lateral stress domination index can be predicted by:

$$\lambda = \begin{cases} 1.69SI^{0.77} & ,0 \leqslant SI < 0.5 \\ 1 & ,SI \geqslant 0.5 \end{cases} \tag{7}$$

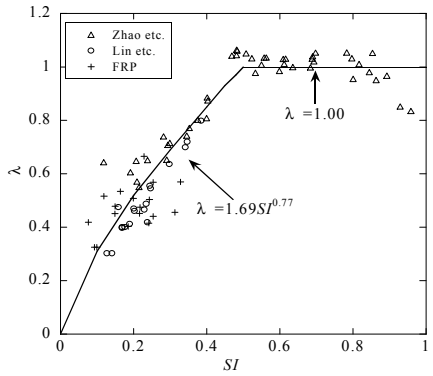

Fig. 5. The relationship between the SI and

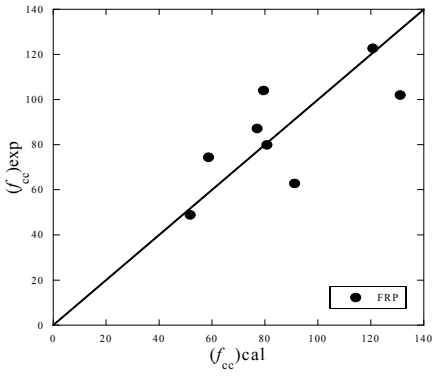

Fig. 6. Preformance of the proposed model

According to Eq. (1-7), the compressive strength model of confined concrete in FRP-confined concrete column incorporating the effect of the confinement path can be determined by:

$$f_{cc} = f_c + 2.2\lambda f_c^{0.3} {\sigma_{ru}}^{0.81} \tag{8}$$

where λ is the effect index of confinement path, obtained by Eq.7.

Fig.6 shows the performance of the proposed model by comparison with the experimental results. According to the Fig.6 we can know the proposed model is good performance was found in comparison with the experimental results.

6 Conclusions

Confinement path and its effect of FRP-confined concrete column are investigated and the compressive strength model of confined concrete is proposed in this paper.

7 References

Zhao Yan-Gang, Lin Siqi, Zhao-Hui Lu, Saito Takasuke, He Liusheng. Loading paths of confined concrete in circular concrete loaded CFT stub columns subjected to axial compression. Engineering Structures 2018;156: 21–31.

Siqi Lin, Yan-Gang Zhao. Liusheng He, Stress paths of confined concrete in axially loaded circular concrete-filled steel tube stub columns. Engineering Structures 2018; 173:1019–1028.

I.A.E.M. Shehata, L.A.V. Carneiro and L.C.D. Shehata, Strength of short concrete columns confined with CFRP sheets, Materials and Structure, Vol. 35, January-February 2002, pp 50-58.

Guoqiang Li. Experimental study of FRP confined concrete cylinders. Engineering Structures 28 (2006) 1001-1008.

T. Jiang, J.G. Teng, Analysis-oriented stress–strain models for FRP–confined concrete. Engineering Structures 29 (2007) 2968-2986.

F. Ansari, Q. Li, High-strength concrete subjected to triaxial compression, ACI Mater J 1998; 95:747–755.

J. Xie, A.E. Elwi, J.G. Macgregor, Mechanical properties of three high-strength concretes containing silica fume, ACI Mater J 1995; 92: 135–145.

I. Imran, S.J. Pantazopoulou, Experimental study of plain concrete under triaxial stress, ACI Mater J 1996; 93: 589–601.

RELIABILITY ANALYSIS OF TOTAL CONSTRUCTION DURATION BASED ON CUBIC NORMAL DISTRIBUTION

LU REN[1], YAN-GANG ZHAO[2]
[1] Department of Architecture, Kanagawa University, Yokohama, Japan
E-mail: Sylvia7910422@gmail.com
[2] Department of Architecture, Kanagawa University, Yokohama, Japan
E-mail: zhao@kanagawa-u.ac.jp

Abstract: In recent years, the combination of Building Information Modeling (BIM) technology and the Project Management and Review Technology (PERT) has been widely applied to the optimization of construction schedule. Construction schedule control is one important part of the management of construction schedule. Therefore, the reliability analysis of total construction duration is necessary for construction companies. Most of the existing studies on the reliability analysis of the total construction duration prepared by PERT assumed that the total construction duration is subject to a normal distribution. However, in actual projects, the distributions of the total construction duration are usually unknown. To address this issue, a flexible distribution was utilized to represent the distribution of the total construction duration. In the proposed method, the cubic normal distribution which determined by its first four moments (mean, standard deviation, skewness and kurtosis) was adopted to fit the distribution of the total construction duration. After obtaining its cubic normal distribution, a more rational reliability analysis of the total construction duration was conducted. Through a practical engineering case, it is proved that the proposed method is more accurate and efficient.

Keywords: Reliability analysis, Cubic normal distribution, Total construction duration

1 Introduction

Building Information Modeling (BIM) is a recognized advanced technology that enhances the effectiveness and efficiency of projects in the construction, engineering and construction industries(Tsai et al. 2014, 189–199). For the project, the total construction duration is directly linked to the cost, so that the evaluation of the reliability of it is particularly important for the entire project. PERT is one of the most commonly and classically used tools in project management of construction schedule plan since it appearance in 1959 (Malcolm et al. 1959, 646–669). PERT assumed that the total construction duration is subject to a normal distribution to evaluate its reliability(S. Mubarak. 2005). However, the distribution of the total construction duration is actually uncertain. Therefore, the reliability prediction result given by PERT is not reasonable. This paper utilized cubic normal distribution to represent the distribution of the total construction duration. The proposed method is as follows: firstly, building the BIM model of the project and integrating the original construction duration with BIM model; secondly, formulating the reliability model of total construction duration; thirdly, using cubic normal distribution (determined by its first four moments, mean, standard deviation, skewness and kurtosis) to fit the distribution of the total construction duration and conducting the reliability analysis of it. After obtaining its four parameter distribution, a more rational reliability analysis of the total construction duration was conducted. Through case analysis, it is proved that this method is more accurate and efficient.

2 Formulating the reliability model of total construction duration

Based on the existing design information, establish a BIM model, integrate it with construction schedules. The project duration has its own specific calculation principles and methods, usually obtained using PERT. The PERT model in this paper was developed using assumptions similarly to the traditional PERT method, as follows:

1. The probability of the duration of the activity is using the beta distribution to represent, which can be determined using three times estimate: the most optimistic time a, the most pessimistic time b and the most probable time m. The optimistic time a and pessimistic time b represent the extreme values of the probability distribution (ie 0 and 100%), the most likely time is m. Studies have shown that the duration of many construction activities can be expressed in terms of beta distribution (AbouRizk et al., 1994).

The beta distribution is defined over the (0,1) interval, through the affine transformation Y= a + (b − a) X allows the beta distribution to be defined in any finite interval (a, b). The original PERT obtains the calculation formula of the mean and variance of the construction duration by assuming the parameters of the beta distribution p=4, q=4. However, in practice this assumption does not necessarily hold. Therefore, in order to select a more reasonable beta distribution assumed that the probability of m is k times of the probability of a and b. Then let $pq=k^2$ and y_0=m, so that by solving the equations $pq=k^2$ and (p-1)/(p+q-2)=(m-a)/(b-a), the values of p and q can be obtained.

2. The activities in the network path are not correlated, the total construction duration is determined by the key route of the project, which takes the longest time, as shown in Figure 1.

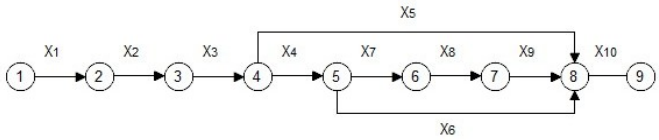

Figure 1. The arrow diagram

The performance function G of construction duration is:

$$G(\mathrm{X}) = T_M - \sum_{i=1}^{n} x_{\mathrm{i}} \tag{1}$$

where T_M indicates the prescribed total planned duration, x_{i} represents each sub-item of the critical path.

The formulas for calculating the first four moments of the total construction duration are:

$$\mu_{\mathrm{G}} = \sum_{i=1}^{n} \mu_{\mathrm{i}} \tag{2}$$

$$\sigma_{G}^{2} = \sum_{i=1}^{n} \sigma_{i}^{2} \tag{3}$$

$$\alpha_{3G}\sigma_{G}^{3} = \sum_{\mathrm{i}=1}^{n} \alpha_{3i}\sigma_{i}^{3} \tag{4}$$

$$\alpha_{4G}\sigma_{G}^{4} = \sum_{\mathrm{i}=1}^{n} \alpha_{4i}\sigma_{i}^{4} + 6\sum_{\mathrm{i}=1}^{n-1}\sum_{\mathrm{j}>\mathrm{i}}^{n} \sigma_{i}^{2}\sigma_{j}^{2} \tag{5}$$

The reliability analysis of the first four moments of the total construction period is carried out by using the cubic normal distribution.

3 Reliability analysis of total construction duration model

In the existing model that the distributions of random variables in construction schedule are assumed to follow normal distribution. It is inappropriate to use normal distribution to deal with the random variables in construction schedule, cause the distributions of random variables are generally unknown, and in most cases, they do not obey normal distributions. While it is easy to obtain their first four moments so that the cubic normal distribution is used in this study, which has a single expression and can more effectively fit the histograms of available data than normal distribution (Zhao YG, Lu ZH. 2008, 263-280).

For a random variable G, if its first four moments mean (μ_G), standard deviation (σ_G), skewness (a_G), and kurtosis (a_{4G}) are known, the standardized random variable G_s can be expressed by the cubic normal transformation: G_s = (G-μ_G) / σ_G, as follows (Fleishman AI. 1978, 521–32):

$$G_s = S_u(u, \mathbf{M}) = a_1 + a_2 u + a_3 u^2 + a_4 u^3 \tag{6}$$

in which, G_s is a standardized random variable, with the skewness and kurtosis are the same as those of G, $\mathbf{M}$ is a vector denoting the first four moments of G, $S_u(u)$ is a third-order polynomial of u, Φ and ϕ are the cumulative distribution function (CDF) and probability density function (PDF) of a standard normal random variable u; a_1, a_2, a_3 and a_4 are coefficients up to the first four moments of the left side of Eq. (6) and it is equal to those of the right side(Zhao YG et al. 2018, 186–99). Therefore, the inverse function of the relationship between standard normal variable u and the standardized variable G_s can then be expressed as

$$u = S^{-1}(G_s, \mathbf{M}) \tag{7}$$

where the S^{-1} denotes inverse function of S and the explicit expression of u are summarized in Table 1 (Zhao YG, Lu ZH. 2008, 263-280). The parameters p, q, Δ, θ, J_1^*, J_2^* and J_0 of Table 1 can be given as follows:

$$p = \frac{3b - a^2}{9} \tag{8}$$

$$q = \frac{a^2}{27} - \frac{ab}{6} - \frac{a}{2} - \frac{G_s}{2a_4}, \Delta = \sqrt{p^3 + q^2} \tag{9}$$

$$\theta = \arccos\left[-q / (\sqrt{-p})^3\right] \tag{10}$$

$$J_1^* = \sigma_G a_4 (-2|p|^{3/2} + 2q + G_s / a_4) + \mu_G \tag{11a}$$

$$J_2^* = \sigma_G a_4 (2|p|^{3/2} + 2q + G_s / a_4) + \mu_G \tag{11b}$$

$$J_0 = -(a_2^2 / 4a_3 + a_3)\delta_G + \mu_G \tag{12}$$

where parameters a and b are respectively defined as $a = a_3/a_4$ and b= a_2/a_4. It can be seen from Table 1 that there are six types in the cubic normal distribution, including unbounded

distributions (Types I and VI), unilaterally bounded distributions (Types II, III, and V), and a bounded distribution (Type IV).

Table 1 Expressions of *u*

Parameters			*u*	Range of *G*	Type
$p \geq 0$			$-p/\sqrt[3]{\Delta-p}+\sqrt[3]{\Delta-p}-a/3$	$(-\infty,\infty)$	Ⅰ
$p<0$	$a_4>0$	$\alpha_{3G}\geq 0$	$2\sqrt{-p}\cos(\theta/3)-\mathrm{a}/3$	$J_1^*<G<J_2^*$	Ⅱ
		$\alpha_{3G}<0$	$-p/\sqrt[3]{\Delta-p}+\sqrt[3]{\Delta-p}-a/3$	$G\geq J_2^*$	
			$-p/\sqrt{\Delta-p}+\sqrt{\Delta-p}-a/3$	$G\leq J_1^*$	Ⅲ
			$-p/\sqrt{-p}\cos[(\theta-\pi)/3]-a/3$	$J_1^*<G<J_2^*$	
	$a_4<0$		$-p/\sqrt{-p}\cos[(\theta+\pi)/3]-a/3$	$J_1^*\leq G\leq J_2^*$	Ⅳ
	$a_4=0$	$\alpha_{3G}>0$	$\sqrt{1/4+(a_3/a_2)^2+a_3G_s/a_2}-1/2$	$G\geq J_0$	Ⅴ
		$\alpha_{3G}<0$	$\sqrt{1/4+(a_3/a_2)^2+a_3G_s/a_2}-1/2$	$G\leq J_0$	
		$\alpha_{3G}=0$	G_s	$(-\infty,\infty)$	Ⅵ

According to Eq. (6) the CDF and PDF are expressed as (Rackwitz R, Fiessler B. 1978, 489–94):

$$F(G)=\Phi(u) \tag{13}$$

$$f(G)=\frac{\phi(u)}{\sigma_G(3a_4u^2+2a_3u+a_2)} \tag{14}$$

Substituting Eq. (6) with an explicit expression listed in Table. 1 into Eq. (13), one obtains that

$$F_{G_s}(G_s)=\Phi(u)=\Phi[S^{-1}(G_s,\mathbf{M})] \tag{15}$$

Therefore, the probability of failure can be expressed as

$$P_F=F_{G_s}(\frac{0-\mu_G}{\sigma_G})=\Phi[S^{-1}(\frac{0-\mu_G}{\sigma_G},\mathbf{M})] \tag{16}$$

4 Example

Build the BIM model of the project, showing in Figure 2. Integrate the construction schedule information with BIM model. Take a simple but representative part of the project as an example. The prescribed total planned duration of this construction stage is T_M =40 days.

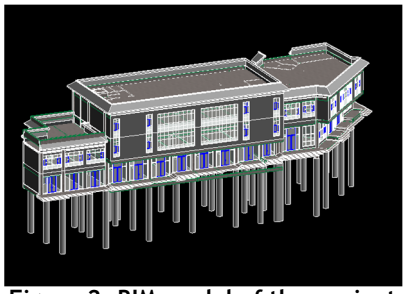

Figure 2. BIM model of the project

It is known that the key path of a sub-item project consists of four parts. The three times estimates data of each part given by the expert is showing in Table 4-1.

Table 4-1 Three time estimates of each part

Symbol	Duration / d		
	a	m	b
x_1	6	8	14
x_2	5	6	13
x_3	6	8	20
x_4	3	4	11

The performance function *G* of construction duration is:

$$G(\mathrm{X}) = T_M - \sum_{i=1}^{n} x_{\mathrm{i}} = 40 - \sum_{i=1}^{n} x_{\mathrm{i}}$$

Let k =1.5, then the shape parameters p and q of each sub item can be obtained. And the first four moments of each part of the project can be calculated according to the definition, as shown in Table 4-2.

Table 4-2 First four moments of each sub-item

	μ	σ^2	a_3	a_4
x_1	10.4852	2.1594	0.2214	2.1041
x_2	7.88	3.5747	0.4644	2.2887
x_3	11.2243	11.1782	0.4069	2.2341
x_4	5.88	3.5746	0.3290	2.28870

According to the formula 2-5, the first four moments of the total construction schedule are obtained.

Table 4-3 The first four moments of the data andcoefficients of the cubic normal distribution

First four moments		Coefficients of the cubic normal distribution	
μ_G	4.52449	a_1	0.0516
σ_G	4.15886	a_2	1.0662
a_{3G}	-0.2676	a_3	-0.0516
a_{4G}	2.6402	a_4	-0.0234

Based on the three times estimation of the sub-projects, the simulation of function performance *G* was carried out using the Monte Carlo method. The number of times is 10000, and the probability distribution histogram of the total construction duration is obtained, as presented in Figure 3.

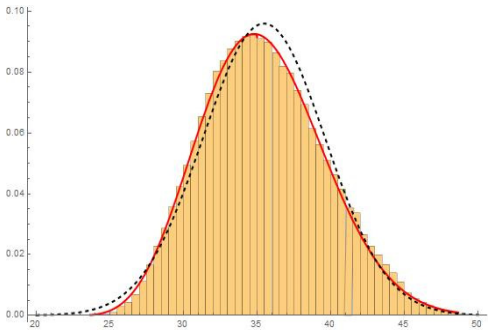

Figure 3 Comparison between normal distribution and cubic ormal distribution in fitting statistical data

Figure 3 is along with the fitted PDF of the normal distribution, whose mean value and standard deviation are equal to those of the three times estimates data, and the fitted PDF of the cubic normal distribution whose first four moments of *G* and coefficients are shown in Table 4-3. It can be seen from Figure 3 that the cubic normal distribution fits the histogram much better than the normal distribution. According to the cubic normal distribution, the corresponding failure probability of 40 days of the total construction duration is 0.149. It shows that the planned total duration of 40 days is reliable.

5 Conclusions

This new computing model combined with PERT and cubic normal distribution takes advantage of several methods proposed since the original PERT was introduced. A real project was analyzed by comparing cubic normal distribution and normal distribution with Monte Carlo simulation which illustrated that the use of this new proposed model can enable more accurate reliability analysis of the total construction duration for the projects.

6 Reference

AbouRizk, S. M., Halpin, D. W., and Wilson, J. R. “Fitting beta distributions based on sample data.” *Journal Construction Engineering Management*, 120.2 (1994), 288–305.

Fleishman AI. A method for simulating non-normal distributions. *Psychometrika*, 43.4 (1978), 521–32.

Malcolm, D. G., Roseboom, J. H., Clark, C. E., and Fazar, W. “Application of a technique for research and development program evaluation.” *Operations. Research*, 7.5(1959), 646–669.

Rackwitz R, Fiessler B. Structural reliability under combined load sequence. *Computer Structure*, 9.5(1978.), 489–94.

S. Mubarak. *Construction Project Scheduling and Control*, Pearson/ Prentice Hall, New Jersey. 2005.

Tsai, M. H., S. C. Kang, and S. H. Hsieh. “Lessons Learnt from Customization of a BIM Tool for a Design-Build Company.” *Journal of the Chinese Institute of Engineers* 37.2(2014): 189–199.

Zhao YG, Lu ZH. Cubic normal distribution and its significance structural reliability. *Structural Engineering and Mechanics*, 28.3(2008.3), 263-280.

Zhao YG, Zhang XY, Lu ZH. Complete monotonic expression of the Fourth-Moment normal transformation for structural reliability. *Computer Structure*, 196(2018), 186–99.

International Symposium on Reliability of Multi-disciplinary Engineering Systems under Uncertainty (ISRMES2019), 8-11 December 2019, Taipei
Chen, S. S. & Ang, Alfredo. H-S. (Editors)

SIMULATION OF DISTRIBUTED GEOTECHNICAL HAZARDS ON A DRUM CENTRIFUGE

Wenjun Lu[1], Limin Zhang[1,2]
[1]The Hong Kong University of Science and Technology, Hong Kong, China
[2]HKUST Shenzhen Research Institute, Shenzhen, China
E-mail: wenjunlu@connect.ust.hk (W. Lu), cezhangl@ust.hk (L. M. Zhang)

Abstract: A class of distributed hazards is difficult to simulate on a beam centrifuge, such as long-distance landslides, debris flows, and hillslope and coastal erosion. A drum centrifuge, with the advantage of much longer model channel and smaller boundary effects than those of a beam centrifuge, is an alternative and a more suitable tool for studying such distributed geotechnical hazards. A modular drum centrifuge equipped with a 3D robot will be installed in the Hong Kong University of Science and Technology. The drum centrifuge will have a maximum centrifugal acceleration of 250 g and a model channel 0.7 m in width and 6.91 m in length. The 3D robot is capable of forming various models in-flight as it can serve as a sand rainer, soil pourer or model profiler. A fluid circulation system will be developed to trigger a soil slide or initiate bed erosion or a debris flow within the drum channel. A compact high-speed image capture system using a high-speed camera and particle image velocimetry (PIV) techniques, and an array of sensors will be installed to capture the flow velocity along the long drum channel.

Keywords: centrifuge modelling; drum centrifuge; 3D robot; fluid circulation system; instrument system; geotechnical hazard.

1 Introduction

Centrifuge modelling has been widely used in many geotechnical investigations because of the advantage of identical stress level realized by the centrifugal force (Schofield 1980, Zhang and Wong 2007, Ng et al. 2015). However, a class of distributed hazards has emerged, such as natural terrain landslides and debris flows (Zhang et al. 2014, Chen et al. 2015), dam breaching (Chang et al. 2010), and aging of slopes (Cheung and Tang 2003). These issues involve removal and long-distance movement of sediment at kilometre scale, which cannot be simulated properly on a beam centrifuge due to the limited length of the model container. Therefore, a drum centrifuge, with the advantage of a much longer model channel and smaller boundary effects than those of a beam centrifuge, has become an alternative and a more suitable approach for studying the aforementioned problems (Springman et al. 2001, Wang et al. 2014). A modular drum centrifuge facility with a 3D robot has been designed and will be installed in the Hong Kong University of Science and Technology (HKUST) for investigating the distributed geotechnical hazards. This paper provides a brief introduction to the technical specifications and structural details of the drum centrifuge facility, the three-dimensional robot, the data acquisition system, and the model packages designed for simulating different long-distance geotechnical hazards.

2 Drum centrifuge

The HKUST drum centrifuge include a drum centrifuge facility, a three-dimensional robot, an instrumentation system and a data acquisition system.

2.1 Drum centrifuge facility

A modular drum centrifuge will be acquired from Thomas Broadbent and Sons Limited, UK, due to its flexible modular structure, high performance, and affordability. The drum is fabricated with carbon manganese steel with a robust protective paint coating. As shown in Figure 1, the inner diameter of the model channel is 2.2 m, and the depth and width of the channel are 0.4 m and 0.7 m respectively. The drum centrifuge will be able to produce a radial acceleration of up to 250 g on a test payload of 3480 kg, corresponding to a maximum speed of 450 rotations per minute and a capacity of 870 g-ton. These figures make the centrifuge the largest of its kind in the world. The base platform will be supplied with twin concentric shafts, a controller, a tool table, and two independent Ethernet-based 32-channel data acquisition systems. In the future, it is possible to add the capability of spinning both 30 g-ton beam and 2 g-ton permeameter test environments, which will further augment the modelling power.

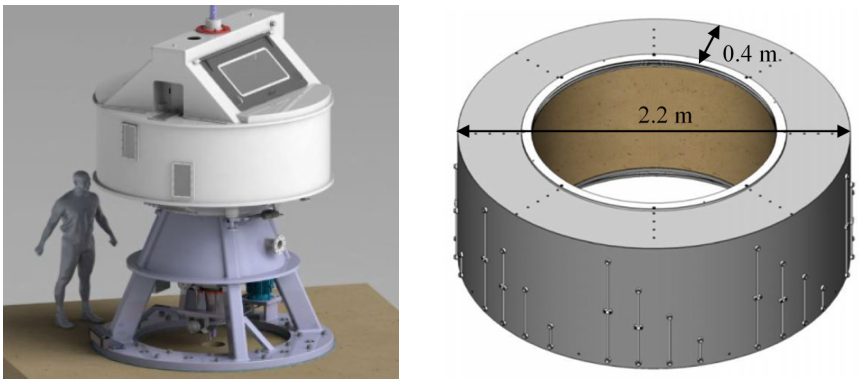

(a) Three-dimensional diagram (b) Model channel

Figure 1. Drum centrifuge facility

2.2 Three-dimensional robot

Most geotechnical structures are subject to combined vertical (V), horizontal (H) and moment (M) loadings, and the bearing capacity envelope can be described by a three-dimensional ellipsoid (e.g. Cassidy et al. 2002). Hence a multi-axis loading device is essential for foundation-related studies. A unique three-dimensional (3D) robot will be attached to the tool table on this new drum centrifuge to allow 3D movement and load application at any position in the model in flight. A 2D actuator will be installed on the tool table. In combination with the tool table rotary actuator integrated into the twin concentric shaft system on the basic centrifuge, this will allow fully controllable 3D positioning and load application throughout the whole of the model in the drum channel. The 2D loading actuator will be designed to move at velocities of 0-5 mm/s, with a load capacity of ±5 kN.

The versatile 3D capability of the unique loading actuator and the twin-shaft system form the basis of various in-flight model formation tools:

- Sand rainer: This only needs a feed pipe and a level mechanism to amplify the y-axis motion of the actuator to achieve the higher y-axis velocities needed for uniform distribution.
- Soil pourer: This is similar to the sand rainer, but a different feed pipe is needed to suit the different flow characteristics.

- Model profiler: The actuator can achieve the motions required for profiling the surface of the model.

2.3 Instrumentation system

Two instrumentation systems will be developed to instrument the drum channel to enable capturing the debris flow, bed erosion and sediment transport processes in the channel: (a) a compact high-speed image capture system using a high-speed camera and particle image velocimetry (PIV) techniques, and (2) an array of photoconductive sensors and Doppler velocimeters to capture the distribution of flow velocity along the long drum channel. The high-speed camera will allow the dynamic failure process and the fluid-soil bed interface behaviour be captured (Stanier et al. 2014). PIV (White et al. 2003, Take 2015) will be a versatile and efficient tool for measuring the movement, velocity and strain fields of a soil model. Photoconductive sensors and Doppler velocimeters will be used particularly for fluid dynamics applications.

2.4 Data acquisition

Two independent Ethernet-based 32-channel data acquisition systems, Drum DAS and Tool Table DAS, will be equipped at the base platform. The Drum DAS will comprise a 32 channel, medium speed, high gravity windows based data acquisition system with on-board digitization, networked acquisition and control. The Tool Table DAS will be a duplicate of the Drum DAS, with the exception that the Tool Table DAS will utilize a Fibre Optic Rotary Joint for the LAN interface. The Drum DAS, due to the presence of the brake and clutch assembly of the Twin Concentric Shaft Drive, will utilize a wireless 150 MN/S interface for the LAS connection. The Tool Table DAS will be required due the Table to circumnavigate the drum wall periphery many times during the test sequence, hence the Tool Table DAS requirement to retrieve data independent of the drum DAS.

3 Geotechnical hazards simulation

In order to simulate distributed geotechnical hazards such as rain-induced long-distance landslides, soil erosion, long-distance debris flows, and sediment transport, a fluid circulation system has been designed. For the sake of space-saving and convenient operation, 1/6 length of the drum model channel will be used as a fluid storage tank. The fluid storage tank will be sealed by a top cover and two rigid baffles. The inlet on the top cover will be connected to an air pump whereas the outlet will be linked to a fluid box through a pipeline. The operation of the air pump will be operated through a remote controller.

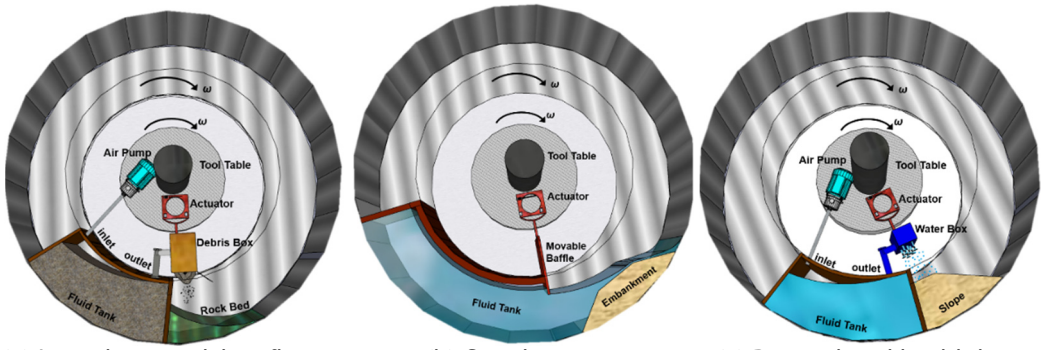

(a) Long-distance debris flows (b) Costal erosion (c) Rain-induced landslides

Figure 2. Model packages for geotechnical hazards simulation

3.1 Long-distance debris flows

Debris flows can be reproduced using the fluid circulation system and a debris box. A rigid rock bed is fixed in the channel before the test. After the drum centrifuge spins to the design speed, the compressed air pump will be used to drive the debris flow material from the fluid tank into the debris box, releasing the debris flow from a design height over the rockbed to reproduce the movement of the debris flow. Photoconductive sensors, Doppler velocimetry sensors, and high-speed cameras will be employed to monitor the complete process of debris flow. Details are shown in Figure 2(a).

3.2 Coastal erosion

The overtopping and erosion of coastal and estuary embankments can be simulated using the fluid tank and a movable baffle controlled by an actuator. An embankment model is pre-installed into the model channel. After the drum centrifuge rotates to the design speed, the movable baffle will be uplifted by the actuator to let the fluid to flow into the reservoir behind the embankment. The baffle will keep moving upward until water overtops the embankment. Pore pressure sensors inside the embankment will be used to measure the change of pore pressure inside the embankment. A schematic diagram is shown in Figure 2(b).

3.3 Rain-induced landslides

Rainfall-induced landslides can be simulated with the fluid circulation system and an artificial raining device that are installed at the end of the fluid box. After the drum centrifuge speed reaches the design rotation speed, the air pump will be turned on at the remote controller, pressuring the water from the fluid tank into the fluid box. As a result, water will be sprayed to the pre-constructed slope model to trigger landslides. The sliding process can be monitored by PIV during the experiment. High-speed cameras are employed to monitor the landslide process for PIV analysis. Pore pressure sensors are installed inside the slope to measure the change of pore pressure inside the slope. A schematic diagram is shown in Figure 2(c).

4 Summary

A brief introduction to the HKUST drum centrifuge facility is provided in this paper. The fluid circulation system and different model packages are presented for simulating distributed geotechnical hazards, particularly long-distance debris flows, coastal erosion and rain-induced long-distance landslides.

5 Acknowledgement

The drum centrifuge facility is supported by the Research Grants Council of the Hong Kong SAR (Grant No. C6021-17EF) and the HKUST. The research on simulating distributed geohazards is also supported by the Science and Technology Plan of Shenzhen (Project No. 20180428170335970).

6 References

Cassidy M.J., Byrne B.W. and Houlsby G.T. 2002. “Modelling the behaviour of circular footings under combined loading on loose carbonate sand.” *Geotechnique* 52(10): 705 – 712.

Chang D.S. and Zhang L.M. 2010. "Simulation of the erosion process of landslide dams due to overtopping considering variations in soil erodibility along depth." *Nat. Haz. and Earth Sys. Sci.* 10(4): 933-946

Chen H.X. and Zhang L.M. 2015. "EDDA: integrated simulation of debris flow erosion, deposition and property changes." *Geoscientific Model Development Discuss.* 7: 7267-7316

Cheung R.W.M. and Tang W.H. 2003. "Reliability of deteriorating slopes." *Journal of Geotechnical and Geoenvironmental Engineering* 131(5): 589-597.

Ng, C.W.W., Shi C., Gunawan A., Laloui L., and Liu H.L. 2015. "Centrifuge modelling of heating effects on energy pile performance in saturated sand." *Canadian Geotechnical Journal* 52(8): 1045-1057.

Schofield A.N. 1980. "Cambridge geotechnical centrifuge operations." *Geotechnique* 30: 227-268.

Springman S.M., Laue J., Boyle R., White J., and Zweidler A. 2001. "The ETH Zurich geotechnical drum centrifuge." *Int. Journal of Physical Modelling in Geotechnics* 1: 59-70.

Stanier S.A., Breen J., and White D.J. 2014. "A compact high-speed image capture system for a drum centrifuge." *Proc. Physical Modelling in Geotechnics (Gaudin & White, eds)*, Taylor & Francis Group, London, 241-246.

Take W.A. 2015. "Thirty-Sixth Canadian Geotechnical Colloquium: Advances in visualization of geotechnical processes through digital image correlation." *Canadian Geotech. J.* 52(9): 1199-1220.

White D.J., Take W.A., and Bolton M.D. 2003. "Soil deformation measurement using particle image velocimetry (PIV) and photogrammetry." *Géotechnique* 53(7): 619-631.

Wang Z., Chen Z., and Luan M. 2014. "Generation of progressive wave in a drum centrifuge." *Proc. Physical Modelling in Geotechnics (Gaudin & White, eds)*, Taylor & Francis Group, London, 235-240.

Zhang L.M. and Wong. Eric Y.W. 2007. "Centrifuge modelling of large diameter bored pile groups with defects." *J. Geotech. Geoenviron. Eng.* 133(9): 1091-1101.

Zhang S., Zhang L.M. and Chen H.X. 2014. "Relationships among three repeated large-scale debris flows at the Pubugou Ravine in the Wenchuan earthquake zone." *Canadian Geotech. J.* 51(9): 951-965.

International Symposium on Reliability of Multi-disciplinary Engineering Systems under Uncertainty (ISRMES2019), 8-11 December 2019, Taipei
Chen, S. S. & Ang, Alfredo. H-S. (Editors)

FLOOD AND ITS IMPACT ON URBAN SYSTEMS UNDER EXTREME RAINSTORMS: A CASE STUDY IN HONG KONG

Jian He1, Yejia Qiang[2]
[1]HKUST Shenzhen Research Institute, Shenzhen, China
[2]The Hong Kong University of Science and Technology, Hong Kong, China
E-mail: jhebl@connect.ust.hk (J. He), yqiang@connect.ust.hk (Y.J. Qiang)

Abstract: Hong Kong is a densely populated metropolis. It is faced with increasing intensity of rainstorm due to climate change. To enhance the resilience of the city, it is important to analyze the impact of flood resulted from extreme rainstorms on the city. In this study, flooding induced by an extreme rainstorm is simulated for Kowloon, Hong Kong. The urban settings, namely, building and drainage system are incorporated into the flood simulation model. To illustrate the effectiveness of drainage system in reducing the flood, flood simulation is also carried out for the case without the drainage system. The impact of flood on major roads and MTR (Mass Transit Railway) stations is investigated. The results show that the study area would be severely flooded with 16 MTR stations and more than 60 major roads affected by the flood if the drainage system did not work, while the drainage system could effectively reduce the number of affected major roads and MTR stations. The results also suggest that although current drainage system in Kowloon is capable of preventing severe flooding, some low-lying areas are still prone to flood hazard and more measures should be taken to deal with the flooding in those areas.

***Keywords*:** flood, urban systems, extreme rainstorm, drainage system.

1 Introduction

Urban floods caused by intensive rainstorms are common hazards for modern metropolis, especially under global warming. The complicated urban environment makes the flood processes different from that in the rural environment, and urban floods can affect multiple urban systems, as shown in Figure 1. Hong Kong is one of the most densely populated cities in the world. The city has built up an advanced storm water treatment system to address the challenge caused by intensive rainstorm. However, whether the system is capable of dealling with extreme rainstorms considering the climate change remains unknown.

For urban flood research, characterization of urban environment is always an issue. Researchers have attempted to construct models for urban flood modelling considering the influences of urban features. For example, Wang et al. (2018) tried to capture building layouts and roads with multiple sources of terrain data, and simplified the urban drainage capacity with reduction of rainfall as well as increase of infiltration. Bertsch et al. (2017) modelled the urban drainage capacity with synthetic storm drain networks to make up for the lack or incomplete knowledge of actual drainage networks. In this paper, a coupled flooding model (overland flow and storm drain flow) is built to investigate the impact of extreme rainstorms on the urban infrastructures of Kowloon, Hong Kong.

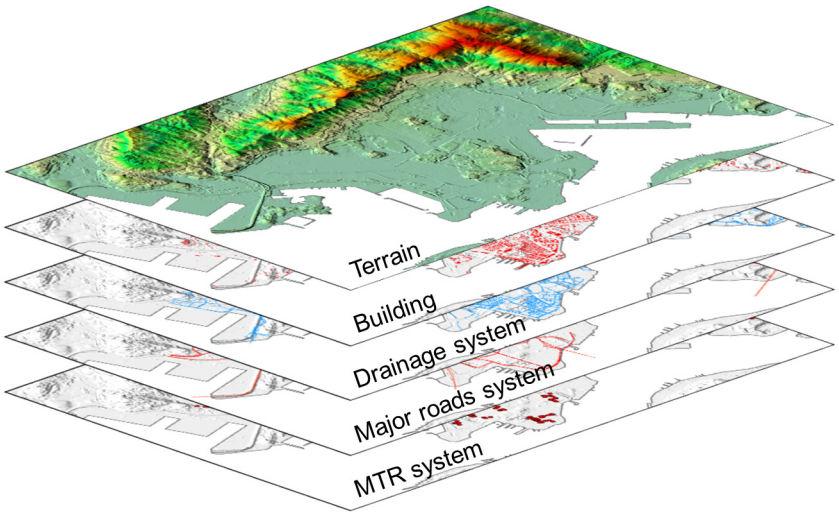

Figure 1. Urban systems

2 Methodology

Flood simulation is carried out based on a cell-based system, where the fluid in each cell has eight potential flow directions, namely, four cardinal directions and four intercardinal directions. For each direction, the flow is governed by depth-averaged one dimensional continuity and momentum equations:

$$\frac{\partial h}{\partial t}+\frac{V\partial h}{\partial t}=i-j \tag{1}$$

$$\frac{\partial h}{\partial x}+\frac{V}{g}\frac{\partial V}{\partial x}+\frac{1}{g}\frac{\partial V}{\partial t}+S_f=S_0 \tag{2}$$

where h is the flow depth; V is the depth-averaged velocity in x direction; i is the excessive rainfall intensity; j is the depth of water flowing into the drainage system; S_f is a friction coefficient based on Manning's equation and S_0 is the bed slope.

Buildings have great influence on the flow process. In this study, the buildings in a cell are characterized by an area reduction factor and width reduction factors. The area reduction factor affects the storage of water in a cell. While the width reduction factors control the width of a boundary that allows water exchange. The Green-Ampt model is adopted to simulate infiltration.

The flow in the drainage system is governed by the one dimensional Saint Venant equations:

$$\frac{\partial A}{\partial t}+\frac{\partial Q}{\partial x}=0 \tag{3}$$

$$\frac{\partial Q}{\partial t}+\frac{\partial (Q^2/A)}{\partial x}+gA\frac{\partial H}{\partial x}+gAS_f+gAh_L=0 \tag{4}$$

where A is the cross-sectional area of the pile; Q is the discharge; H is the hydraulic head of water in the pipe; S_f is the friction slope of the pipe; h_L is the local energy loss per unit length of the pipe.

The abovementioned floodplain and pipe network flow governing equations can be solved using FLO-2D (FLO-2D Software Inc., 2018), a two-dimensional flood routing model. Based on the flow depth in each cell, the influence of flood on facilities or services in a cell can be analyzed. In this study, major roads and MTR systems are considered. The cells through which roads pass and cells which contain MTR stations are considered in the impact analysis. A road is regarded out of service if the water depth in any cell it passes through exceeds a threshold value. For a MTR station, if the water depth in any cell in which its entrances are located exceeds a threshold value, the station is regarded to be difficult to access and considered affected.

3 Study area

Kowloon is located in a subtropical monsoon climate zone, with an average annual total rainfall of 2398.5 mm (1981-2010), measured at Hong Kong Observatory (HKO). This area is prone to heavy rainstorms in summer. According to a report from HKO, the most severe rainstorm since 1884 brought 841.2 mm rainfall to Kowloon within 2 days. This hazardous event caused severe flooding and triggered multiple landslides, which resulted in major interruption in transportation, communication, food and water supply in many places of the city. Kowloon is one of the most densely populated area in Hong Kong, with over 2.2 million residents in an area of about 47 km^2, namely, over 30% population in about 4% area of Hong Kong. The transportation system in Kowloon is well developed, with 27 MTR stations and more than 80 major roads. Due to its highly urbanized environment, there used to be lots of low-lying areas prone to flooding hazard in this area. After decades of efforts in flood prevention projects, the number of flooding blackspots in Kowloon has been reduced to one as reported by Drainage Services Department of HKSAR. However, the annual total rainfall recorded at HKO and the annual number of heavy rain days have been increasing at rates of 37mm/decade and 0.2 days/decade since 1947. Hong Kong is likely to experience more severe rainfall in the future considering climate change. A report published by Geotechnical Engineering Office of HKSAR estimates that the 24-hour probable maximum precipitation (PMP) in Kowloon is 1187.6 mm. In this study, a rainstorm lasting for 2 days with the 24-hour rolling maximum rainfall amount up to 80% of PMP is considered, as shown in Figure 2. The 24-hour rolling maximum rainfall amount is 950 mm and the total rainfall amount is 1014.3 mm.

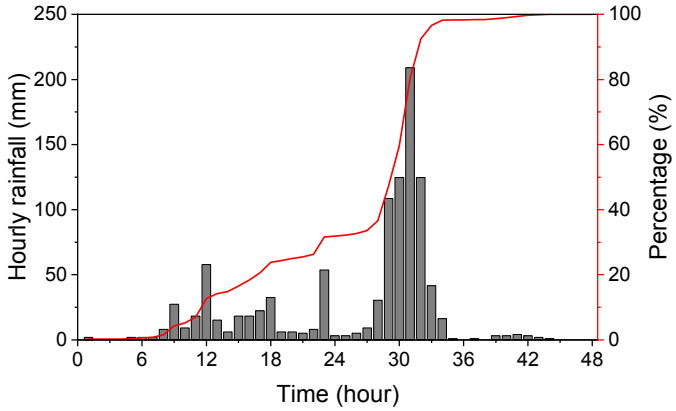

Figure 2. Hourly rainfall and cumulative distribution of the extreme rainstorm

4 Results and conclusions

The maximum flow depth during the design rainstorm is shown in Figure 3. Most reclaimed areas,

especially western Kowloon, are severely flooded due to their relatively low-lying terrain. The drainage system can effectively reduce the maximum flow depth. However, some low-lying places would be still severely flooded under the extreme rainstorm with current drainage system. Major roads and MTR stations are regarded as affected if the water depth exceeds 0.5 m. The number of affected major roads and MTR stations is shown in Figure 4. If there were no drainage system, 16 MTR stations and more than 60 major roads could be affected. While with the current drainage system, the impact of flood on major roads and MTR stations is reduced to a certain extend. However, the number of major roads affected is still significant, indicating that more measures are needed to further mitigate the influence of flood to the major roads system.

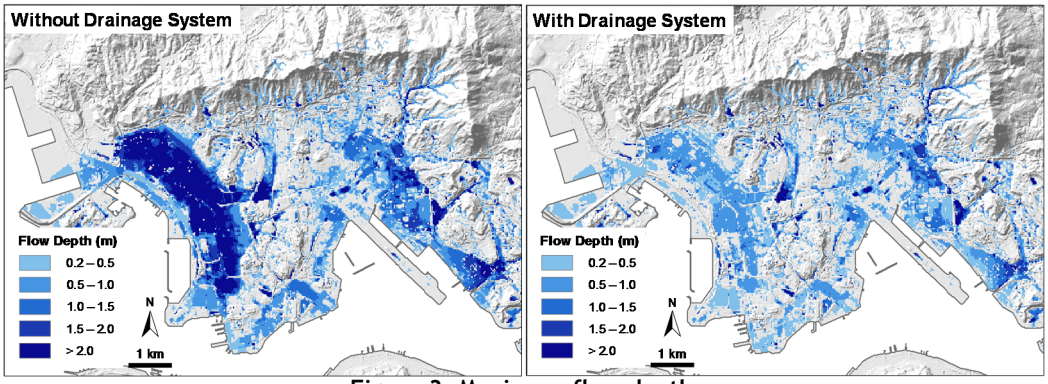

Figure 3. Maximum flow depth

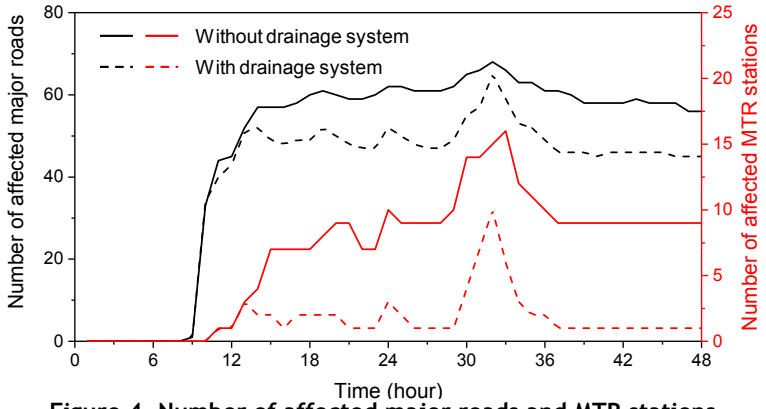

Figure 4. Number of affected major roads and MTR stations

5 Acknowledgement

This research is substantially supported by the Science and Technology Plan of Shenzhen (Project No. 20180428170335970) and the Research Grants Council of the Hong Kong SAR Government (Grant No. 16206217).

6 References

AECOM Asia Company Limited, and Lin, Bingzhang. 24-hour Probable Maximum Precipitation Updating Study (GEO Report No. 314). Hong Kong: HKSAR, 2015.

Bertsch, Robert, Vassilis Glenis, and Chris Kilsby. “Urban Flood Simulation Using Synthetic Storm Drain Networks.” Water 9 (2017): 925.

FLO-2D Software Inc. (2015) FLO-2D, Nutrioso, Arizona, USA.

Hong Kong Observatory. "Climate Change in Hong Kong." Accessed October 1, 2019. https://www.hko.gov.hk/climate_change/obs_hk_rainfall_e.htm

Wang, Yuntao, Albert S. Chen, Guangtao Fu, Slobodan Djordjević, Chi Zhang, and Dragan A. Savić. "An Integrated Framework for High-Resolution Urban Flood Modelling Considering Multiple Information Sources and Urban Features." Environmental Modelling & Software 107 (2018): 85–95.

NATURAL TERRAIN LANDSLIDE RISK TO POPULATION UNDER EXTREMESTORMS

T. Abimbola Owolabi[1] and Limin Zhang[2]
[1,2]Department of Civil and Environmental Engineering,
Hong Kong University of Science and Technology, Hong Kong.
[1]E-mail: taowolabi@connect.ust.hk
[2]E-mail: cezhangl@ust.hk

Abstract: Many landslides can occur during a severe storm and cause unexpected consequences. Landslides in Hong Kong interact intensely with human activities in densely populated areas. This paper quantifies the elements at risk in terms of buildings and population in the buildings. The approach includes producing landslide and risk maps and quantifying the numbers of buildings of all types and exposed individuals affected by the landslides under two rainstorm scenarios of 29% and 85% Probable Maximum Precipitation (PMP). The number of persons at risk inside each building was based on estimation of number of floors, number of flats and the average number of people living in a flat in Hong Kong during the time of the event. Within the high prone areas of the western parts of Hong Kong Island, the dispersal rate of the landslides varies depending on the terrain of the area. The north-eastern part with relatively even terrain will experience fewer landslides. For the storm with a rainfall intensity of 85% PMP, the most affected buildings and population are in the residential buildings, Among the least affected buildings and population are hospitals, community and church buildings. Only one residential building is affected under the storm scenario of 29% PMP. The outcome of this study is useful for future risk assessment and management.

Keywords: Landslides, extreme storms, element at risk, climate change.

1 Introduction

Landslides are one of the major hazards which involve movements of grounds, rocks and debris, and may lead to social and economic devastation. Landslides commonly occur due to climate and geological reasons. Landslide risk assessment is a decision tool that gives important information for risk mitigation. There are some uncertainties; nevertheless, decisions will have to be made under uncertainty. Therefore, decision makers need some informed judgements about the nature and extent of the uncertainty (Lee, 2015). The triggering factors may be extreme storm events, strong earthquakes, high groundwater levels, gully under cutting, snow avalanche, construction and human activity.

Many landslides can occur during a severe storm and cause unexpected consequences. In a storm, many hazards can occur at a time and interact with each other to give cascading effects. Landslides in Hong Kong interact intensely with human activities in densely populated area in Hong Kong (Wong, 2014). Intensive work has been done by previous researchers on landslide risk assessment (e.g., Nadim et al., 2006; Zhang et al., 2012; Corominas et al., 2014; Lacasse et al., 2008; Lee and Jones, 2004; Glade et al., 2005; GEO 2006; Guzzetti et al., 2005; Fell et al., 2008; Van Westen et al., 2008), but limited studies have quantified risk of landslide under large storms.

2 Description of the study area

This study focuses on Hong Kong Island which covers an area of 78.59 km^2 with a population of 1,289,500 and a population density of 16,390/km^2. A prompt risk analysis for the western part of

Hong Kong Island by Zhang et al. (2016) reveals that the slopes in the catchment are rather steep, ranging from 0 to 73° and more than 60% of the terrain has slope angles larger than 15°. The natural terrain covers over 60 % of the total land area of Hong Kong Island.

3 Shallow landslides

As the rainwater infiltrates into the soil, changes in pore water pressure and seepage force occur, leading to significant build-up of pore water pressure. Also, where there is an impervious layer underlying a layer of soil, infiltrated water tends to pool in the boundary of these two layers. Eventually this leads to loss in shear strength due to decrease in soil suction or build-up of pore water pressure (Zhang et al., 2011; Fourie et al., 1999; Fredlund and Rahardjo, 1993).

Some methods can be used to estimate the occurrence of landslides, such as empirical methods built on event-based landslide inventories, site investigation, analysis of remote sensing data (aerial photos and satellite images), and numerical simulations. The approach used in this study is numerical simulation (Zhang et al., 2017). The intensity and magnitudes of extreme storms are characterized by the Probable Maximum Precipitation (PMP)

The landslide results under storms scenarios with rainfall intensities of 29% PMP, and 85% PMP are presented in Fig. 1, where the occurrence of landslides under the two storms is depicted. At 85% PMP, the number of landslides and the risk they pose on buildings and population are far greater than those under 29% PMP.

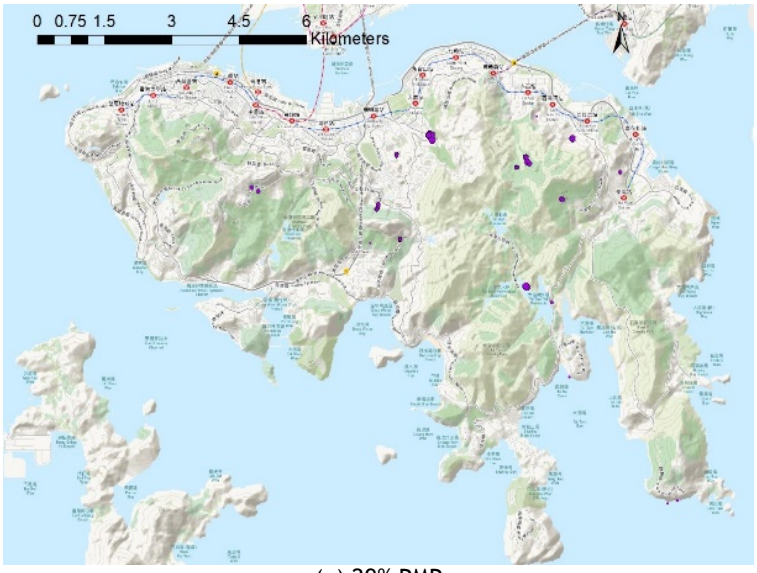

(a) 29% PMP

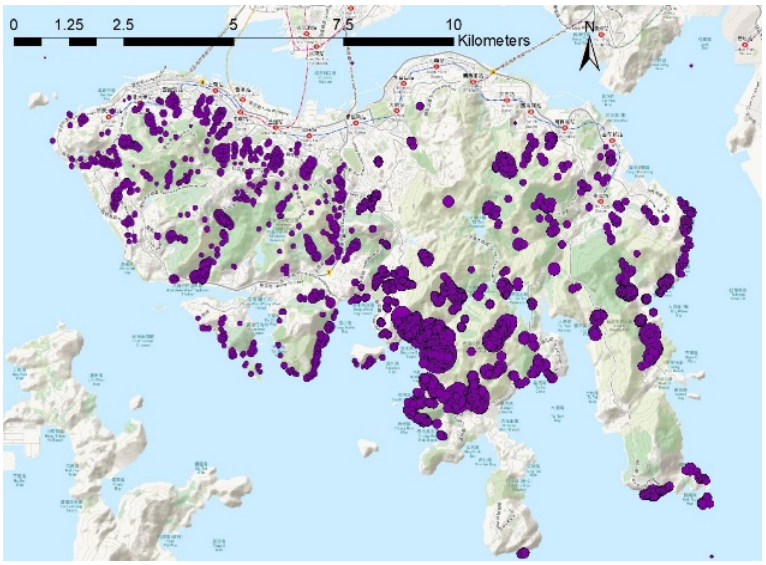

(b) 85% PMP

Figure 1. Landslide maps over Hong Kong Island under storms with intensities of 29% and 85% PMP.

4 Elements at risk

The elements at risk are those exposed to or affected by the landslide. In this study, building data records were used first as a database for the elements affected by the numerous landslides triggered by the two different scenario events, second to calculate the number of elements at risk, and third to estimate the population at risk. The types of buildings considered were residential buildings, schools, hospitals, commercial centres, temples, factories, community centres, government buildings and church buildings. The number of persons at risk inside each building was based on estimation of number of floors, number of flats and the average number of people living in a flat in Hong Kong during the time of the event. The number of floors was calculated using the building height and floor height.

The population at risk (PAR) can be expressed as:

$$PAR = N_b N_f N_{ave} \quad (1)$$

where N_b is the number buildings N_f is the number of occupied flats and N_{ave} is the average number of persons per occupied flat in Hong Kong.

5 Distribution of buildings and population affected by landslides

For the storm with rainfall intensities of 85% PMP, the highest affected buildings and population is in the residential buildings. Among the least affected buildings and population are hospitals, community and church buildings. Only one residential building is affected under the storm scenario of 29% PMP (Fig 2).

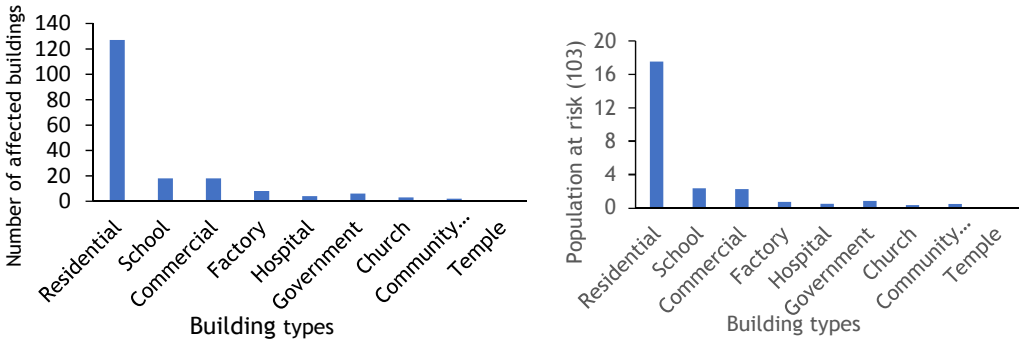

(a) 85% PMP

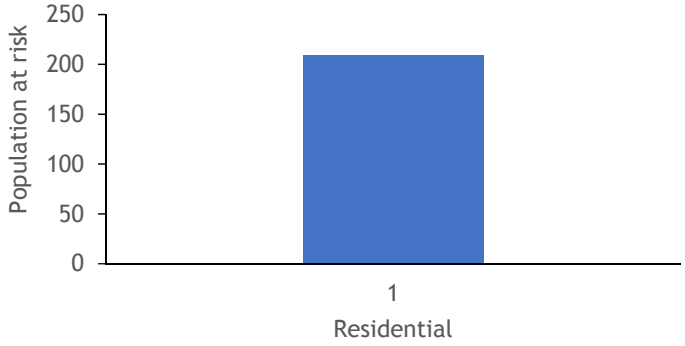

(b) 29%PMP

Figure 2. Number of buildings and population at risk under storms of 85% and 29% PMP.

6 Conclusions

The buildings and storm-triggered landslides were analyzed with respect to their spatial locations in a GIS environment in order to quantify the number of people at risk inside each building. The western and southern parts of Hong Kong Island are more prone to landslides with higher risk due to the steeper terrain, while the north-eastern part with relatively even terrain will experience fewer landslides. Even within the high prone areas of the western part of Hong Kong Island, the dispersal rate of the landslides varies depending on the terrain of the area. A significant number of residential buildings may be affected under high-intensity storms.

7 Acknowledgment

The authors wish to acknowledge the support from the Research Grants Council of the Hong Kong SAR (No. C6012-15G and No. 16206217).

8 References

Corominas J, Van Westen C, Frattini P, Cascini L, Malet JP, Fotopoulou S, Smith JT (2014). Recommendations for the quantitative analysis of landslide risk. *Bulletin of Engineering Geology and the Environment* 73(2): 209–263.

Fell R, Corominas J, Bonnard C, Cascini L, Leroi E, Savage WZ (2008). Guidelines for landslide susceptibility, hazard and risk zoning for land use planning. *Engineering Geology* 102: 85–98.

Fourie AB, Rowe D, Blight GE (1999). The effect of infiltration on the stability of the slopes of a dry ash dump. *Geotechnique* 49(1):1–13.

Fredlund DG, Rahardjo H (1993). Soil mechanics for unsaturated soils. Wiley, New York, NY, USA.

GEO (2006). Assessment of landslide risk in natural hillsides in Hong Kong. Report No. 191. Hong Kong Geotechnical Engineering Office, Hong Kong, p 117.

Glade T, Anderson M, Crozier MJ (2005). Landslide hazard and risk. Wiley, Chichester, p 802.

Guzzetti F, Galli M, Reichenbach P, Ardizzone F, Cardinali M (2005). Landslide hazard assessment in the Collazzone area, Umbria, Central Italy. *Natural Hazards Earth System Science*s 6: 115–131.

Lacasse S, Eidsvig U, Nadim F, Hoeg K, Blikra LH (2008). Event tree analysis of Aknes rock slide hazard. *Proceedings of the 4th Canadian Conference on Geohazards: From Causes to Management*. Presse de l'Université Laval, Québec, 594 p.

Lee EM (2015). Landslide risk assessment: the challenge of communicating uncertainty to decision-makers. https://doi.org/10.1144/qjegh2015-066.

Lee EM, Jones DK (2004). Landslide risk assessment. Thomas Telford Publishing, London, p 454.

Nadim F, Kjekstad O, Peduzzi P, Herold C, Jaedicke C (2006). Global landslide and avalanche hotspots, Landslides 3: 159–173.

Van Westen CJ, Castellanos E, Kuriakose, SL (2008). Spatial data for landslide susceptibility, hazard, and vulnerability assessment: an overview. *Engineering Geology* 102(3): 112–131.

Wong HN (2014). Is landslide risk quantifiable and manageable? Geotechnical Safety and Risk IV; *Proceeding 4th International Symposium on Geotechnics Safety and Risk,* Taylor and Francis Group, London, 101-111.

Zhang LL, Zhang J, Zhang LM, Tang WH (2011). Stability analysis of rainfall-induced slope failure: a review. *Geotechnical Engineering, Proceedings of the Institution of Civil Engineers* 164(5): 299-316.

Zhang, LM, Chen, HX, Gao L (2016). Prompt assessment of multi-hazard landslide risks. In Huang HW, Li J, Chen JB (eds), Keynote Lecture, *Proc. 6th Asian-Pacific symposium on structural reliability and its applications* (APSSRA6), 28-30 May 2016, Shanghai, China. Tongji University Press, Shanghai, 77-87.

Zhang LM, Gao L, Zhou SY, Cheung RW, Lacasse S (2017). Stress testing framework for managing landslide risks under extreme storms. Keynote Lecture, *4th World Landslide Forum (*WLF4), Ljubljana, Slovenia, 29 May - 2 Jun 2017. Springer International Publishing AG 2017, M. Mikoš et al. (eds.), pp. 17-32.

Zhang S, Zhang LM, Peng M, Zhang LL, Zhao HF, Chen HX (2012). Assessment of risks of loose landslide deposits formed by the 2008 Wenchuan earthquake. *Natural Hazards and Earth System Sciences*, 12(5): 1381-1392.

International Symposium on Reliability of Multi-disciplinary Engineering Systems under Uncertainty (ISRMES2019), 8-11 December 2019, Taipei
Chen, S. S. & Ang, Alfredo. H-S. (Editors)

DEVELOPMENT OF RELIABILITY-BASED LIMIT STATE DESIGN CODE OF UNDERGROUND RC BOX FOR ELECTRIC POWER LINES

Sang-Hyo Kim[1], Sang-Kyun Woo[2], Juhwan Shin[1], Dae-Yoon Kim[1], Oneil Han[1]
[1]Department of Civil and Environmental Engineering, Yonsei University, Seoul, Korea
E-mail: sanghyo@yonsei.ac.kr
[2]KEPCO Research Institute, Daejeon, Korea
E-mail: skwoo96@kepco.co.kr
[3]Korean Engineering Consultants Corporation , Seoul, Korea
E-mail: shinjh@kecc.co.kr

Abstract: The underground RC box-type culverts are widely adopted for the electric power lines especially in the urban area along the traffic roads in Korea. It is currently designed according to a design code, which is based mainly on the american ACI 318 code and some items adopted from those for underground culverts in AASHTO specification. Since the ACI 318 code is developed mainly for the building structures, it does not provide the proper design rules for the structures under the vertical and horizontal earth pressures. Currently, the load combinations adopted in the Korean practice are based on those in ACI 318 and are modified to include the terms with the earth pressures. This study is aimed to develop the limit state load combinations, and design loads and resistances for the underground RC boxes, considering the general design and construction practice in Korea. The typical configuration of the underground power line boxes has a width of 2.6-4.5m and a height of 2.6-3.5m. The depth of earth fill over the buried box is 1-6m, sometimes increases up to 8m or higher. The major loadings to be included are the traffic load, vertical and horizontal earth pressure, ground water pressure, and dead load. The probabilistic load models are being developed and the probabilistic characteristics of resistances of RC boxes are being evaluated based on the construction geometric errors collected from the various construction fields of the buried RC boxes as well as the tolerances allowed in the construction practices. The varying characteristics of the concrete strength are also included based on the field data. The experimental loading tests are being performed to figure out the effects of the various construction errors, such as cover depth, rebar placement, concrete properties, etc.

Keywords: Underground RC Box, Electric Power Line, Limit State Design Code, Probabilistic Load Model, Probabilistic Resistance Model, Construction Error

1 Current design practices in Korea

The Design Code for Underground RC Box Power Lines(URCPL) is the most widely adopted in Korea in current practice, which is proposed by Korea Electric Power Corporation in 2008. Recently, the Korean government has proposed the Design Code for Multi-purpose Underground RC Box(MURC; MOLIT, 2016), which adopts most parts of the regulations in ACI318-14.

The first major load combination in URCPL2008 is:

$$\overline{\mathrm{U}} = 1.4(D + H_v) + 1.7L \tag{1}$$

, in which the dead load(D) can be increased 10% when the dead load is dominant, that is, the combination may become:

$$\overline{U} = 1.54D + 1.4H_v + 1.7L \quad (2)$$

,in which H_v is the vertical earth pressure and L is the live(traffic) load. The second major load combination in URCPL2008 is:

$$\overline{U} = 1.4(D + H_v) + 1.7L + 1.8H_h \quad (3)$$

, in which the dead load can be also increased 10%:

$$\overline{U} = 1.54D + 1.4H_v + 1.7L + 1.8H_h \quad (4)$$

, in which H_h is the horizontal earth pressure. The third one is the load combination, in which the horizontal load effects are significant:

$$\overline{U} = 0.9(D + H_v) + 1.7L + 1.8H_h \quad (5)$$

or when the live load is not present:

$$\overline{U} = 0.9(D + H_v) + 1.8H_h \quad (6)$$

In MURC2016 code, there are two major load combinations:

$$\overline{U} = 1.4(D + H_v) \quad (7)$$

$$\overline{U} = 1.2D + 1.6L + 1.6\alpha_H H_v + 1.6H_h \quad (8)$$

, in which α_h is the modification factor with various earth fill depth(h), from 1.0 for h ≤ 2m, to 0.875 for h > 7m. These load combinations are same as the equations in ACI318-14 except the load parts related to earth pressure.

There are some other load combinations including other loads, such as E(earthquake load), F(underground water pressure), etc. For the underground RC boxes in Korea the seismic load effects are not much dominant generally.

The resistance factors for RC members proposed in URCPL2008 are:

0.85 for flexure resistance

0.80 for shear resistance

In MURC2016,

0.85 for tension controlled sections

0.75 for shear resistance

, whereas in ACI318-14, the strength reduction factors are:

0.90 for tension controlled sections

0.75 for shear resistance

The major resistance behavior in the underground RC boxes is the flexure limit state in both slab and wall.

2 Typical sections for underground RC boxes for power lines

There are various sections adopted for underground power line boxes. However, the most boxes have an outer width ranging 2.6-4.5m (inner width: 2.2-3.8m), and an outer height ranging 2.6-3.5m(inner height: 2.0-2.2m). The most thicknesses of both wall and slab range 240-450mm, depending on the earthfill depth and span width.

3 Development of probabilistic resistance models of RC slab and wall

To select the reliability-based resistance factors (strength reduction factors), the probabilistic resistance model should be generated, considering the local characteristics, such as the dimensions of structural members (thickness, reinforcement ratio, cover depth of slab and wall) adopted in underground power lines, concrete properties, rebar properties, construction site errors, etc. The following works are now being performed: 1) literature survey, 2) field data survey on the in-service power line boxes, 3) field data collection from the on-going construction sites for power lines, 4) experimental load tests with various specimens, such as flexure test with slabs, both closing moment and opening moment loading test with various corner joint specimens with or without haunch, and full-scale RC box loading test, etc. 5) simulation process for the member resistance with the probabilistic models of basic design variables, such as dimensions, concrete peroperties, rebar properties, in which the random charateristics involved in the realistic member resistance will be reflected based on the experimental loading test results. This part will be explained in the accompanying paper in details.

4 Development of probabilistic models of loads acting on underground RC boxes

The major loadings in the underground RC boxes may be the dead load, earth load (vertical and horizontal), and traffic live load. The underground water pressure may be important, however the randomness related to the water pressure may be neglected, as long as the ground water level is determined reasonably. The traffic load related parts will be discussed in the accompanying paper. The earth load related part will be introduced in another accompanying paper in this session.

The basic data for the cured plain concrete weight are being collected when the cylinder modules are made for the concrete compression strength test. The nominal design unit weight of reinforced concrete is ranging from 24.5 kN/m^3(MURC2016) to 25.0 kN/m^3 (URCPL2008) in Korean codes. For the plain concrete, from 23.0 kN/m^3 (MURC2016) to 23.5 kN/m^3 (URCPL2008). In most codes, the reinforced concrete weight is generally 1.5 kN/m^3 heavier than the plain concrete. In Eurocode, the normal weight concrete is suggested to be 24.0 kN/m^3 and additional 1 kN/m^3 for normal percentage of reinforcing.

The statistical review on the field data cllected by our survey team gives the mean of 21.7 kN/m^3 and the standard deviation of 0.35 kN/m^3, so far. Therefore, the nominal value of 23.0 kN/m^3 is the statistical value of mean + 3.7SD, and 23.5 kN/m^3 is the value of mean + 5.2SD. Both values are quite reasonable. The nominal weight, 24 kN/m^3, suggested in Eurocode for plain concrete may be a little high. However, the nominal weight, 25 kN/m^3, for the normal reinforced concrete may be reasonable.

5 Investigation on load factors for maxumum and minimum load effects

The design codes provide the maximum load factors to consider the underestimating situation, whereas the minimum load factors to overcome the overestimating situation, which may generate more unfavourable design results. Table 1 summarizes both the maximum and minimum load factors suggested for the dead load in the current design codes. The different maximum load factors, such as 1.54 and 1.05 in URCPL2008, are applied to the different load combinations. Table 2 contains the maximum and minimum load factors for the earth pressure, which may be more important than the dead loads. The minimum load factors in the horizontal earth pressure in modern LRFD design formats are working as the concept of the so-called half earth pressure condition in the allowable design formats. Therefore, the minimum load factors should be able to consider the very unusual low earth pressure situation, that is, the chance that the horizontal earth pressure can drop upto 50% of normal design pressure without considering any safety margin. However, the LRFD load factors for minimum conditions are selected as halves of the maximum load factors. That is, 0.90 to 1.80, 0.80 to 1.60. The probabilistic safety margins attained with those minimum load factors are explained in Figure 1. The minimum load factors suggested in Canadian Highway Bridge Design Code is 0.65, which is much smaller than those in AASHTO, 0.90. However, it should be considered that the maximum in Canada is only 1.25. The minimum load factors should be adjusted downward to consider the unusual low horizontal earth pressure, such as the half of the normal pressure in the traditional allowable design codes.

It should be noticed in URCPL2008 that the Eq.1 does not contain the term of the horizontal earth pressure of Eq.2. The only difference between Eq.1 and Eq.2 is the omission of 1.8 H_h in Eq.2. Therefore, the design check with Eq.1 may have the effect, unintentionally, to consider a very low situation of the horizontal earth pressure, which may leads to very conservative results.

Table 1. Dead load factors

		Dead load factors			
Design Code for Underground RC Box Power Lines (URCPL) 2008		1.54	1.05	0.90	
KCI Code 2012		1.40	1.20	0.90	
Design Code for Multi-purpose Underground RC Box (MURC) 2016		1.40	1.20	0.90	
Canadian Highway Bridge Design Code			1.25	0.90	
AASHTO LRFD	DC		1.25	0.90	
	DW	1.50			0.65

Table 2. Vertical and horizontal earth pressure factors

		Vertical Earth Pressure factors			Horizontal Earth Pressure factors			
Design Code for Underground RC Box Power Lines (URCPL) 2008		1.40		0.90	1.80		0.90	
KCI Code 2012		$1.6\,\alpha_H$ (1.6~1.4)	1.20	0.90	1.60	1.00	0.80	0.50
Design Code for Multi-purpose Underground RC Box (MURC) 2016		$1.6\,\alpha_H$ (1.6~1.4)	1.20	0.90	1.60	1.00	0.80	0.50
Canadian Highway Bridge Design Code	Current		1.25	0.80		1.25		0.65
	Recommended	1.40		0.80		1.25		0.65
AASHTO LRFD			1.30	0.90	Active	1.50	0.90	
					At-Rest	1.35	0.90	

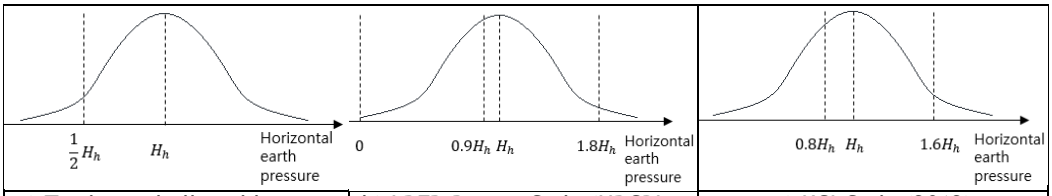

a) Traditional allowable design code | b) LRFD Design Code (URCPL 2008) | c) KCI Code (2012)

Figure 2. Probabilistic safety margins attained with minimum load factors

6 Future process

The current design codes, mainly URCPL2008 and MURC2016, will be calibrated to select the target reliability levels for the major load combinations. The various load factors and resistance factors adopted in the current practices will be evaluated in the calibration works.

The first step in the development of reliability-based limit states for the underground RC boxes, may be the selection of the major load combinations. The second step is to select the proper resistance factors, in which the current strength reduction factors may be maintained not to make the practical design engineers confused. In addition, a reasonable construction tolerance guideline may be provided, on which the probabilistic resistance models adopted in calibration works may be based. In this procedure it should be decided how to treat the unusual statistical data collected from the construction sites. The third step is to select the proper ranges of the combined loads, which requires the evaluation of the load effects in the various design cases. The fourth step is to select the sets of optimum load factors for major load combinations, based on the selected target reliability levels. The final stage is to design and compare many example cases based on both the proposed design rules and the current rules.

7 Acknowledgement

This research program was funded by Korea Electric Power Corporation Research Institute (KEPCO-RI) of Korea, and its kind support is gratefully acknowledged. This work was also supported by the Korea Institute of Energy Technology Evaluation and Planning (KETEP) and the Ministry of Trade, Industry & Energy (MOTIE) of the Republic of Korea (No. 20174030201480).

8 References

AASHTO LRFD Bridge Design Specification, American Assosiation of State Highway and Transportaion Officials, Washington D.C., 2016.

Alfredo H.S. Ang and Wilson H. Tang. *Probability Concepts in Engineering: Emphasis on Applications to Civil and Environmental Engineering*, Hoboken: Wiley, 2007.

Andrzej S. Nowak. *National Cooperative Highway Research Program Report 368: Calibration of LRFD Bridge Design Code*, Washington, D.C.: National Academy Press, 1999.

Bruce Ellingwood, Theodore V. Galambos, James G. MacGregor and C. Allin Cornell. *Development of a Probability Based Load Criterion for American National Standard A58: Building Code Requirements for Minimum Design Loads in Buildings and Other Structures*, US. Department of Commerce, 1980.

Building *Code Requirements for Structural Concrete (ACI 318-14)*, American Concrete Institute, 2014.

Canadian *Highway Bridge Design Code (CHBDC)*, Canadian Standards Assosiation, 2016.

Design *Code for Multi-purpose Underground RC Box (MURC)*, Korean Ministry of Land, Infrastructure and Transport, 2016.

Design *Code for Underground RC Box Power Lines (URCPL)*, Korea Electric Power Corporation, 2008.

Korea *Concrete Institute Code (KCI)*, Korea Concrete Institute, 2012.

International Symposium on Reliability of Multi-disciplinary Engineering Systems under Uncertainty (ISRMES2019), 8-11 December 2019, Taipei
Chen, S. S. & Ang, Alfredo. H-S. (Editors)

PROBABILISTIC RESISTANCE MODELS FOR FLEXURAL MEMBERS OF UNDERGROUND RC BOXES CONSIDERING CONSTRUCTION ERRORS AND TOLERANCES

Dae-Yoon Kim[1], Tuguldur Boldoo[1], Kijung Kim[2], Inyeop Chu[3], Sang-Hyo Kim[1]
[1]Department of Civil and Environmental Engineering, Yonsei University, Seoul, Korea
E-mail: daeyoon@yonsei.ac.kr
[2]CENITS Corporation, Seoul, Korea
E-mail: kijung_kim@hanmail.net
[3]KEPCO Research Institute, Daejeon, Korea
E-mail: chu.inyeop@kepco.co.kr

Abstract: The underground RC boxes are constructed in a limited working space of the excavated ground environment. Therefore, the quality control may not be proper in the construction process, such as concrete form work, rebar assembly, concrete cast and curing, etc. Since the section dimensions are not large, the minor errors may cause some serious consequences. The depths of slabs and thicknesses of walls, which are the major structural members of RC boxes, are about 240-400mm in the typical box sections. In the general construction practice some geometric tolerances are allowed. However, it has been found that the construction errors are often beyond the allowable tolerances due to the unusual work environments of the buried RC boxes. The concrete quality may not be achieved as in the normal sites. Experimental loading tests are being performed with various models, such as simple one way slabs, coner joint specimens with or without haunch between upper slab and wall, full box specimens. In addition, the field data on the construction errors have been collected to understand the general trend of geometric errors, in a systematic procedure from various construction sites of underground box culverts as well as the existing electric power line boxes. The probabilistic models of the basic design variables, such as the section dimension, effective depth of rebar, steel area, concrete strength, rebar strength, etc., are developed based on the field/rab data and the reference models adopted in previous studies. The Monte Carlo simulations will be performed to figure out the probabilistic characteristics of the flexural resistances of slab and wall members of RC box, based on the probabilistic models of basic design variables. The sensitivity analysis will be performed to evaluate the effects of the tolerance levels allowed in the general practice. Based on this study the proper and practical tolerances may be proposed.

Keywords: RC Box Culvert, Probabilistic Resistance Model, Construction Error, Allowable Tolerance, Monte Carlo Simulation

1 Development of construction error models

The most significant construction errors at the sites of underground powerline RC boxes are found to be member dimension errors, such as the thicknesses of both slab and wall, effective depth and cover depth of rebars, concrete properties, rebar properties, etc.

2 Concrete strength survey

The compressive strength of 27MPa concrete is generally adopted in the underground RC boxes for power lines. The compressive strength data of in-site concrete are being collected in 3 systems mainly. First, the cylinder test specimens (D100xH200mm) are made at the selected construction sites for power lines(Fig.1 and 2a). The slab type specimens (W1,000xL1,000xT200mm) are also made(Fig.2b). All specimens are cured under site condition

for 14 days. Then all specimens are transported to the test laboratory. The compressive strength is tested on 14 days and 28 days. The slab type specimen is tested through the non-destructive test method, Schmitt hammer test, on 28 days first. Then 3 cylinder cores with diameter of 100mm are made to be tested per each slab type specimen. Second way to collect the concrete strength data is to make the strength test specimens at the laboratory when the experimental member specimens for the loading test(Fig.3), such as the one-way slab specimens, the coner joint specimens, and the full-scale box-type specimens, in which the mixed concrete is provided through the ready mixed concrete carriers. Third way is to collect the strength data by evaluating the compressive strength through the nondestructive Schmitt hammer test on the in-service RC boxes. These data are calibrated with the results obtained through the slab type specimens mentioned above.

Figure 1. Construction site

a) Cylinder type specimens

b) Slab type specimens

Figure 2. Cylinder type and slab type specimens

a) Corner joint specimen

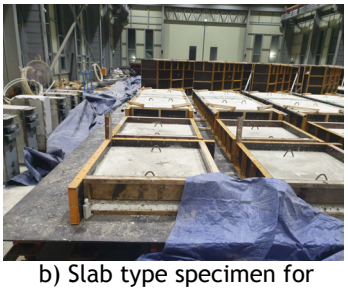

b) Slab type specimen for concrete strength

c) Cyliner type specimen for concrete strength

Figure 3. Lab view and specimens

3 Construction error survey

The major construction errors in the underground RC boxes are the dimension errors related to the member thickness and the placement of rebars. The tolerance allowed in current practice for slab and wall thickness at sites are summarized in Table 1. The tolerances for the cover depth are summarized in Table 2. The construction error on the rebar location, such as the effective depth, is a fuction of the thickness error and cover depth error.

Table 1. Tolerance for slab thickness

KCI 2012 (ACI 318-14)	ACI 117-10	Eurocode2 (BS EN13670-2009)	Korean Highway Design Code 2015
– Effective depth d – ± 10mm (200mm) ---------- ± 13mm	– Section depth – suspended slab – 6.4 mm Slab on ground Average of 4 measurements: -9.5mm Individual measurement : -19.1mm	– Section dimension – (Class 1) ± 10mm / (Class 2) ± 5mm (150mm) ---------- (200mm) ± 11mm / ± 6mm (300mm) ± 13mm / ± 8mm Linear interpolation / Linear interpolation (400mm) ± 15mm / ± 10mm Linear interpolation / Linear interpolation (2,500mm) ---------- ± 30mm / ± 30mm	N/A · Highway bridge construction practice (2013) – Slab deck depth: + 20mm ~ – 10 mm – Section dimensions of column and beam: Min{±2% of section dimensions; ±30mm}
ACI 117-10 : Specification for Tolerances for Concrete Construction and Materials · Based on Eurocode2 Table A.1 Reduced deviations			

Table 2. Tolerance for cover depth

KCI 2012 (ACI 318-14)	ACI 117-10	Eurocode2 (BS EN13670-2009)	Korean Highway Bridge Code 2015
– Effective depth d – – 10mm (200mm) ---------- – 13mm · –7mm to the outer concrete form · Not exceeding $-\frac{1}{3}$ of minimum cover depth	– Thickness – – 9.5mm (300mm) ---------- – 12.7mm · Not exceeding $-\frac{1}{3}$ of required cover depth	– Effective depth: rebar placement – (Class 1) ± 10mm / (Class 2) ± 5mm (150mm) ---------- (200mm) ± 11mm / ± 6mm (300mm) ± 13mm / ± 8mm regression / regression (400mm) ± 15mm / ± 10mm regression / regression (2,500mm) ---------- ± 25mm / ± 20mm · Cover depth: minimum +10mm · Structure on ground: Max. '+' tolerance=15mm	N/A

The field data on the construction errors are being collected from the construction sites for underground RC boxes. Figure 4 and Figure 5 show the construction error measurements at sites. The cover depth data are being collected also from the in-service power line boxes, using the rebar detector.

a) slab thickness / cover depth

b) wall thickness / cover depth

Figure 4. Measurements on thickness and cover depth

a) rebar spacing

b) cover depth / rebar location

Figure 5. Measurements of rebar placement

4 Flexural experimental test with slabs

27 slab specimens have been tested. The specimens have various thickness, rebar ratio, and cover depth, but have the same width(1,000mm) and length(3,000mm). The specimens have been loaded under 4 points loading method until the concrete in the compressive zone was crushed. The load-deflection, rebar strains, and concrete strains are measured. Table 3 provides the design variables of the test specimens with the typical section. The section is shown in Fig.6. 9 more slab specimens are made with 400mm thickness, which will be tested in the near future.

Table 3. Experimental specimens in slab type

Unit: mm

Type / Dimension	A	B	C	D	E	F-	SH	SI	SJ
c′	80	60	80	80	60	80	3	3	3
a	160	180	175	130	130	125	80	80	80
c	60	60	45	60	60	35	260	280	290
h	300	300	300	270	250	240	60	40	30
d[=c′ +a]	240	240	255	210	190	205	400	400	400
rebar[ratio]	H16 [0.0066]	H16 [0.0066]	H16 [0.0062]	H16 [0.0076]	H16 [0.0084]	H16 [0.0078]	340	360	370
	H19 [0.0096]	–	H19 [0.0090]	–	–	–	H19 [0.0067]	H19 [0.0064]	H19 [0.0062]

Figure 6 shows the set-up for the loading on the slab specimen. Figure 7 contains the load-deflection and some load-strains of upper rebar, lower rebar, and concrete at top compressive zone. In the figures, the loadings related to the nominal flexure capacities for both the section with both upper/lower rebars and lower rebars only, are marked. At the final stage it is found that the upper rebars are in tensile yield condition. The ultimate strain values at the top concrete are found to exceed 0.003(nominal design value) very much, upto 0.005.

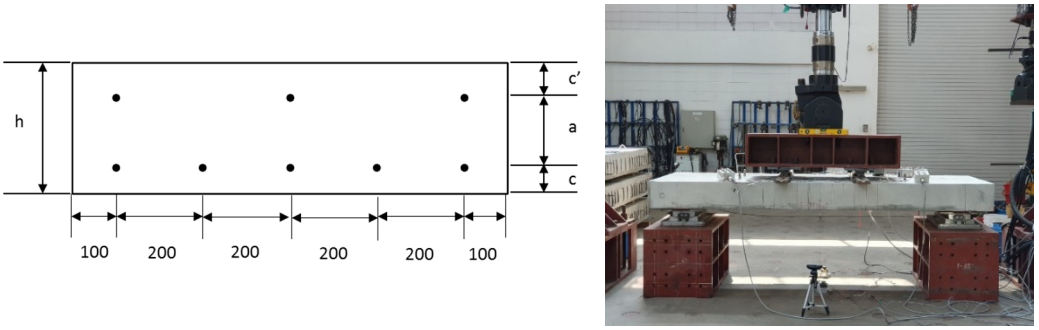

a) section view b) test set-up

Figure 6. Loading test set-up

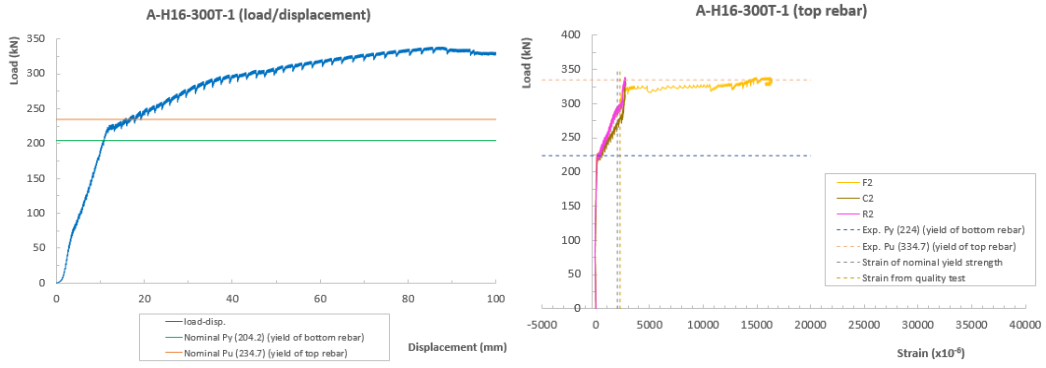

a) A-H16-300T-1 (load/displacement) b) A-H16-300T-1 (top rebar)

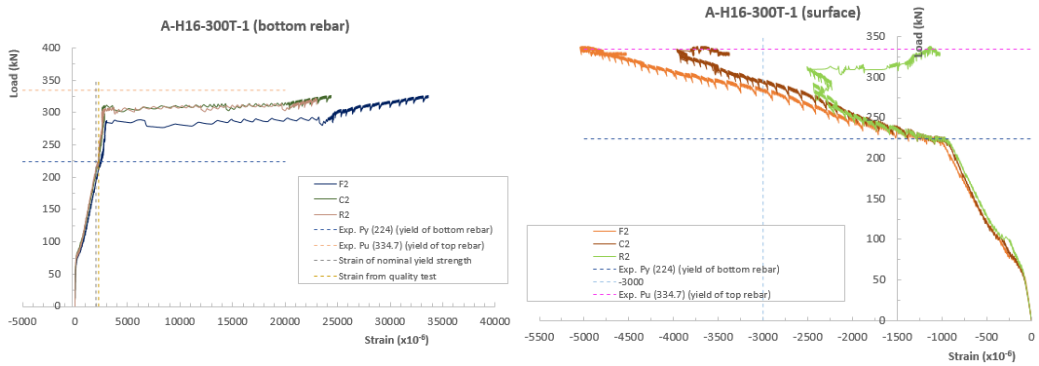

c) A-H16-300T-1 (bottom rebar) d) A-H16-300T-1 (surface concrete)

Figure 7. Experimental results

Table 4 contains the experimental results of some specimens, in which the nominal values are calculated with the design values of the design variables, and the modified values are evaluated with the real(constructed) values of the design variables for thickness and cover depth(effective rebar depth).

As shown in Figure 8, it is found that the ultimate moment capacity is related to the cover depth, especially the ultimate moment resistance of the slab becomes quite low when the cover depth is quite shallow, such as less than 40mm. Figure 8 shows the increasing trend of the normalized moment capacity with the increasing cover depth, in the figure the normalized flexural moment resistance is plotted with respect to a fuction of the clear cover depth and rebar diameter, $C_c/\sqrt{D}$. The regression line of the normalized values varies from 1.18 to 1.41, about 20% increament. This means that the ultimate flexural moment capacity can be reduced about 20% when the tensile rebars in the flexural members do not occupy the proper cover depth. The improper shallow cover depth may cause may not provide the proper bonding development functions on the tensile rebars.

Table 4. Nominal moment capacity and experimental results

Specimen	Analytical				Experimental	
	nominal P_n [kN]	revised P_d [kN · m]	nominal M_n [kN · m]	revised M_n [kN · m]	yield P_y [kN]	ultimate P_u [kN]
A-H16-1	234.70	234.74	105.59	105.63	224.00	334.70
A-H19-1	326.00	332.22	146.71	149.46	321.70	425.50
B-H16-1	224.10	219.74	100.83	98.88	224.10	324.20
C-H16-1	247.90	243.83	111.55	109.73	234.00	328.90
C-H19-1	345.10	339.27	155.31	152.67	322.40	419.60
D-H16-1	208.20	208.79	93.68	93.96	194.50	298.30
E-H16-1	179.90	176.22	80.97	79.30	171.90	247.50
F-H16-1	203.80	208.17	91.69	93.68	184.10	262.30

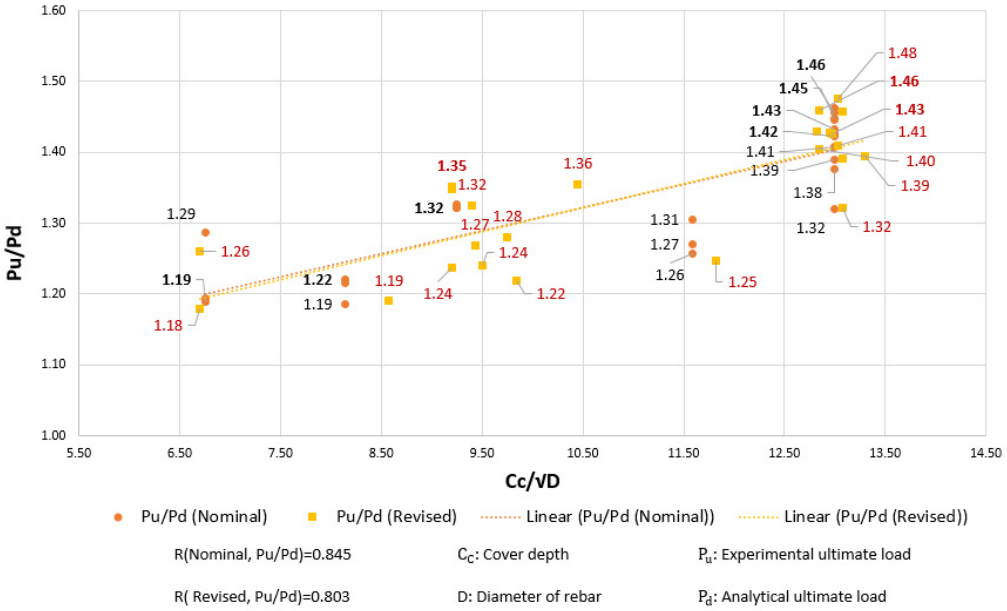

Figure 8. Normalized ultimate moment capacity and cover depth

Table 5 summarizes the statistical results of the normalized ultimate flexural resistances of the slab members, in which the nominal clear cover depth(design value) with the measured clear cover depth and the nominal thickness(design value) with the measured thickness are included. The first column of Pu/Pd(Modi I) contains the results, which have been normalized with the nominal flexural resistance, calculated with the measured C_c and t. The statistical average and cov are evaluated in two groups with different cover depths, such as measured C_c < 50.0mm, and 50.0mm ≤ C_c. The average of the shallow cover depth group is 1.272, wheras the average of the normal cover depth group is 1.404, about 13% higher. The cov of the normal cover depth group is about 10% smaller than the shallow cover depth group. The cov increases very much when the cover depth factor is ignored.

The second column of Pu/Pd(Modi II) contains the normalized values with the nominal flexural resistance, calculated considering the measured f_{ck} from the cylinders, the yield strength of rebar obtained through the tensile test(450Mpa for H16, 452MPa for H19), and the ultimate concrete strains measured in the loading experiments of the slab specimens, in addition to the measured t and C_c. The bias factor is found to be reduced: from 1.338 to 1.183 for the whole group. The cov is almost same: from 0.068 to 0.070. All results will be updated with the future additional data.

Table 5. Statistical evalutation results

	Cc design (mm)	Cc Measured (mm)	t design (mm)	t Measured (mm)	Pu/Pd (Modi I)			Pu/Pd (Modi II)		
F-H16-3	27.0	26.8	240.0	241.0	1.180	Average 1.272 COV 0.049	Average 1.338 COV 0.068	1.045	Average 1.123 COV 0.048	Average 1.183 COV 0.070
F-H16-1	27.0	26.8	240.0	243.0	1.260			1.116		
F-H16-2	27.0	34.3	240.0	245.0	1.190			1.054		
C-H16-2	37.0	36.8	300.0	296.0	1.351			1.191		
C-H16-1	37.0	36.8	300.0	297.0	1.349			1.189		
C-H16-3	37.0	37.6	300.0	300.0	1.324			1.168		
C-H19-1	35.5	40.1	300.0	300.0	1.237			1.091		
C-H19-2	35.5	41.1	300.0	297.0	1.269			1.120		
C-H19-3	35.5	41.4	300.0	296.0	1.242			1.096		
E-H16-2	52.0	41.8	250.0	250.0	1.356			1.200		
A-H19-1	50.5	42.5	300.0	298.0	1.281			1.130		
A-H19-2	50.5	42.9	300.0	302.0	1.219			1.076		
D-H16-1	52.0	51.3	270.0	270.0	1.429	Average 1.404 COV 0.045		1.258	Average 1.244 COV 0.047	
E-H16-1	52.0	51.4	250.0	247.0	1.404			1.243		
D-H16-3	52.0	51.4	270.0	270.0	1.459			1.284		
A-H19-3	50.5	51.5	300.0	302.0	1.247			1.100		
B-H16-2	52.0	51.8	300.0	302.0	1.428			1.271		
A-H16-1	52.0	51.9	300.0	300.0	1.426			1.269		
A-H16-2	52.0	52.1	300.0	300.0	1.409			1.254		
B-H16-1	52.0	52.1	300.0	297.0	1.475			1.313		
E-H16-3	52.0	52.3	250.0	250.0	1.321			1.170		
B-H16-3	52.0	52.3	300.0	300.0	1.458			1.297		
A-H16-3	52.0	52.3	300.0	300.0	1.392			1.239		
D-H16-2	52.0	53.2	270.0	274.0	1.395			1.228		

5 Simulation of flexural resistance based on probabilistic design variables

The probabilistic models of the major design variables will be developed based on the available models and collected data(construction site, laboratory, in-service powerline boxes, etc.) in this study. The probabilistic artificial data of the flexural resistance will be generated through Monte Carlo simulation with the procedure to calculate the nominal flexural resistance. The biasness explained in Chap.5(Modi. II) should be considered.

6 Acknowledgement

This research program was funded by Korea Electric Power Corporation Research Institute (KEPCO-RI) of Korea, and its kind support is gratefully acknowledged. This work was also supported by the Korea Institute of Energy Technology Evaluation and Planning (KETEP) and the Ministry of Trade, Industry & Energy (MOTIE) of the Republic of Korea (No. 20174030201480).

7 References

Alfredo H.S. Ang and Wilson H. Tang. *Probability Concepts in Engineering: Emphasis on Applications to Civil and Environmental Engineering*, Hoboken: Wiley, 2007.

Eurocode 2: Design of Concrete Structures, British Standard, 2008.

Korea Concrete Institute Code (KCI), Korea Concrete Institute, 2012.

Korean Highway Bridge Code, Korean Ministry of Land, Infrastructure and Transport, 2016.

Specification for Tolerances for Concrete Construction and Materials (ACI 117-10) and comentary, American Concrete Institute, 2010.

International Symposium on Reliability of Multi-disciplinary Engineering Systems under Uncertainty (ISRMES2019), 8-11 December 2019, Taipei
Chen, S. S. & Ang, Alfredo. H-S. (Editors)

TRAFFIC LOAD MODEL FOR LIMIT STATE DESIGN OF UNDERGROUND RC BOXES

Dae-Yoon Kim[1], Tuguldur Boldoo[1], Gi-Yong Kang[2], Sang-Hyo Kim1, Kwangkyu Yang[3]
[1]Department of Civil and Environmental Engineering, Yonsei University, Seoul, Korea
E-mail: sanghyo@yonsei.ac.kr
[2]KEPCO Research Institute, Daejeon, Korea
E-mail: giyong.kang@kepco.co.kr
[3]CENITS Corporation INC, Seoul, Korea
E-mail: vndn0715@naver.com

Abstract: Most underground power line RC boxes are constructed with the shallow earth fills due to the construction cost, mainly with 1-3m depth. The traffic load may become one of major design loads. The traffic load effects distributed on the underground RC boxes are evaluated in terms of the equivalent uniform load with two formations: the first is that one design truck(KL-510) adopted in the Korean Highway Design Code(2015) is loaded and the second is that two design trucks are loaded side-by-side together. The equivalent uniformly distributed load(EUDL) is the uniform load, which generates the same load effect on the structural member as the real non-uniform loadings caused by the multiple truck wheels. The load dispersion of the wheel loads through the earth fill is modeled with typical 1:2 model, and other dispersion models are compared to verify the effects. The probabilistic characteristics of the traffic load will be generated based on the local traffic models and the influence lines. The influence lines are developed by calculating the EUDL under the loading condition of a single design truck and the other truck on the adjacent traffic lane assumed to be located with various headway distances, such as 1m to 6m. The probabilistic gross weight models of the heavy vehicles are adopted, which are based on the local data in Korea. The heavy vehicle composition model and the effect of consecutive running of heavy vehicles will be considered.

***Keywords*:** Underground RC Box, Design Traffic Load, EUDL, Probabilistic Truck Weight Model, Consecutive Running Model

1 Current design live loads for underground boxes

Table 1 contains the current design live loads adopted widely in Korea, the first is URCPL2008(Design Code for Underground RC Box Power Lines) developed by Korea Electric Power Corporation, 2008. The second is MURC2016(Design Code for Multi-purpose Underground RC Box) proposed by Korean Government(MOLIT). The third one is the design loads proposed by JSCE in Standard Specifications for Tunneling 2016-Open Cut Construction Boxes. The design live loads required in the current URCPL2008 are quite higher than both MURC2016 and JSCE. The impact factor of 0.3 is proposed to be same for all earth depths in URCPL2008, which may be very conservative. AASHTO Specification adopts since 1998, 0.195 for earth fill of 1.0m, 0.127 for 1.5m, 0.059 for 2.0m, and no impact is considered for over 2.4m depth. The design load values of JSCE contain the impact effects for the earth fills shallower than 3m.

Table 1. Current design live loads for underground structures

(Unit: kN/m^2)

Earth fill depth (m)		1.0 (1.2)	1.5	2.0	2.5	3.0	3.5	4.0	4.5	5.0	~7.0	8.0	9.0	10.0	11.0~
URCPL 2008		←	←	51.0	39.0	21.0	17.0	15.0	→	→	→	15.0	12.0	11.0	10.0
MURC 2016	Section 1. (B_0=2.64m)	36.0 (30.0)	25.0	18.0	14.0	11.0	10.0	→	→	→	→	→	→	→	→
	Section 3. (B_0=3.52m)	33.0 (30.0)	24.0	18.0	14.0	11.0	10.0	→	→	→	→	→	→	→	→
	Section 5. (B_0=4.48m)	33.0 (27.5)	24.0	18.0	14.0	10.0	10.0	→	→	→	→	→	→	→	→
JSCE 2016		40.0	28.5	20.5	15.0	12.0	11.5	10.5	10.0	→	→	→	→	→	→

2 Evaluation of truck wheel load dispersion through earth fills

Figure 1 shows the design trucks adopted in Korea for the highway facilities. The first one is the traditional one, which has been modified from HS20 of AASHTO, 33% heavier, that is, the total weight is 432kN. The second one has been developed recently when the LRFD Design Specification was adopted in Korea, the total weight is 510kN, however, the final load effects on structural members may be not much changed from the traditional design truck.
In this study KL510 design truck is adopted to evauate the live load effects on the underground RC boxes.

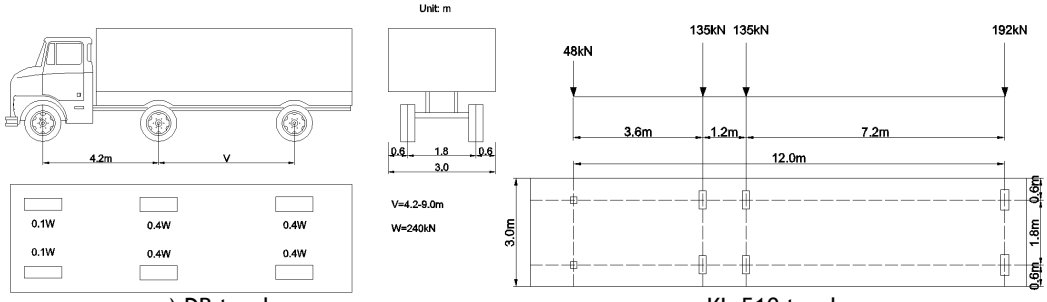

a) DB truck KL-510 truck

Figure 1. Design trucks in Korean Codes

Figure 2 is the dispersion model(1:2) adopted in this study. When the fill material is better, 1.15:2 model can be adopted. However, 1:2 model is a conservative model. Figure 3 is an example of the wheel load effects on the underground box with 2m earth fill for the set of 4-67.5kN wheels of KL-510. The EUDL(equivalent uniformly distributed load) is calculated, which generates the same bending moment effect on the slab of RC box with the non-uniform dipersion loads given in Figure 3.

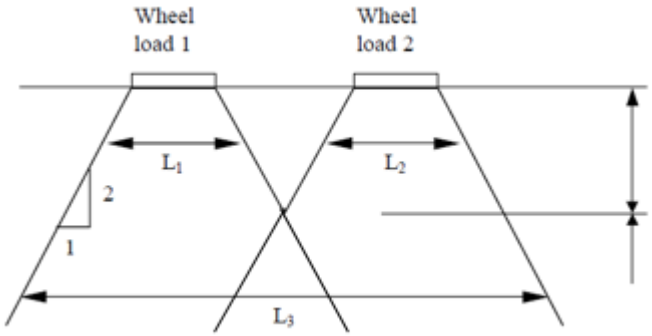

Figure 2. Dispersion of wheel loads through fill (lateral and longitudinal)

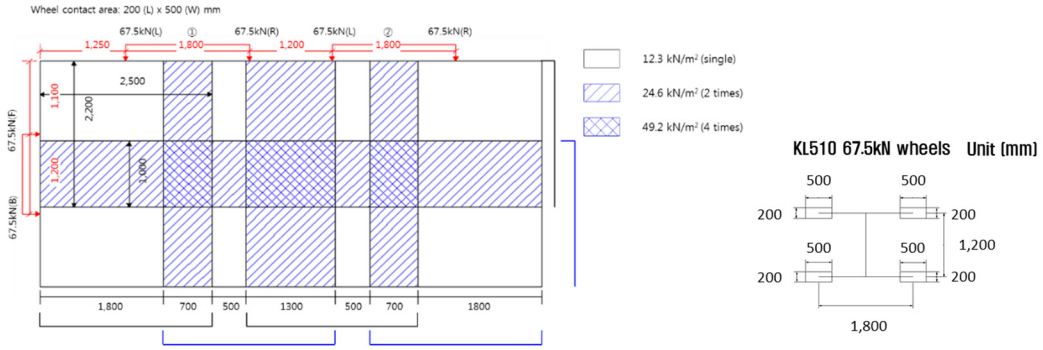

Figure 3. Dispersion of 4-67.5kN wheels of KL-510

Two different directions of underground box line with respect to the traffic flow are considered, one is th case that the traffic flow follows the direction of the underground box line and the other is the case that the traffic flow crosses perpendicularly the underground box line. Figure 4 shows the results of EUDL's for 2 different outer width boxes(2,640mm and 4,480mm). Both results of the single presence and two adjacent presence(3.0m apart from center to center of two KL-510's) are compared. The current design loads are also plotted together. For the shallow earth fills upto 3.0m it is found that the design loads proposed in the current Power Line Box Design Code(URCPL2008) are much larger than even EUDL's of two truck presence very close. The multiple presence factor of 0.90 for 2 trucks is considered. It is found that EUDL decreases with the increasing width of boxes.

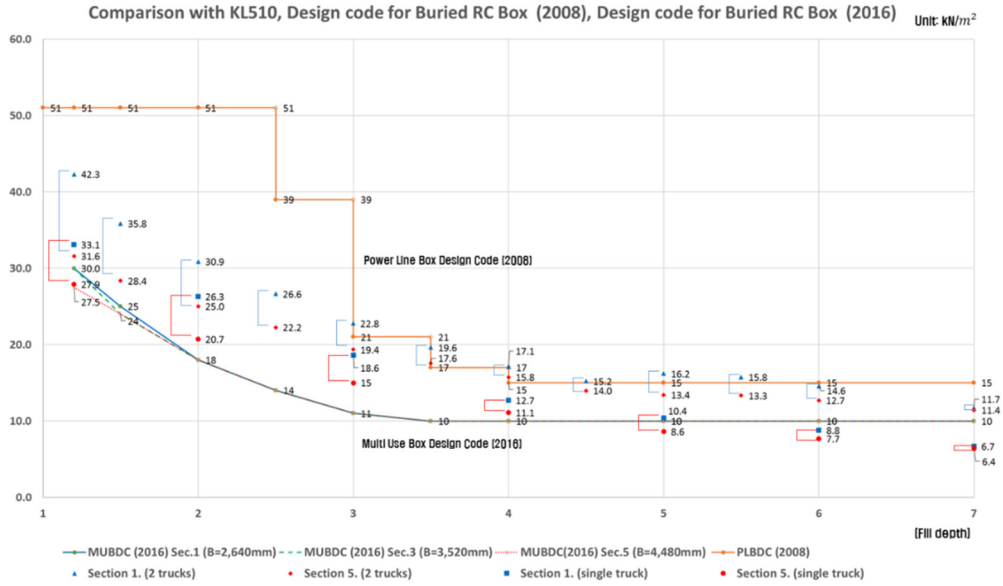

Figure 4. EUDL due to KL-510 and current design loads

3 Effect of headway between two trucks on adjacent traffic lanes

When two trucks running on the adjacent lanes are apart with a headway(the distance between the head of one truck and another truck head on the adjacent lane), the resulting load effect may decrease from the case of a side-by-side. The headway effects are evaluated, in which two trucks are assumed to run on the paths 3.0m apart to obtain conservative results. Figure 5

contains some example influence lines: a) Section 1- earth fill depth 1.2m, b) Section 5- earth fill depth 1.2m, c) Section 1- 4.0m d) Section 5- 4.0m, e) Section 1- 6.0m, f) Section 5- 6.0m, in which the section 1 has an outer width of 2.640m and the section 5 is 4.480m wide. The headway distance of 0.0m means two trucks are loaded side-by-side on the adjacent lanes. And the maximum EUDL is selected among all the possible cases with the same headway distance, including the traffic flow direction, the underground box direction, the headway direction(forward, backward), etc. In the simulation one truck is located at the position, where the EUDL becomes maximum. Then the other truck is assumed to move on the adjacent traffic lane with the preassigned headway distance and the maximum EUDL is obtained and plotted. It is found that the effect of the adjacent truck can be ignored when the headway is longer than the earth fill depth.

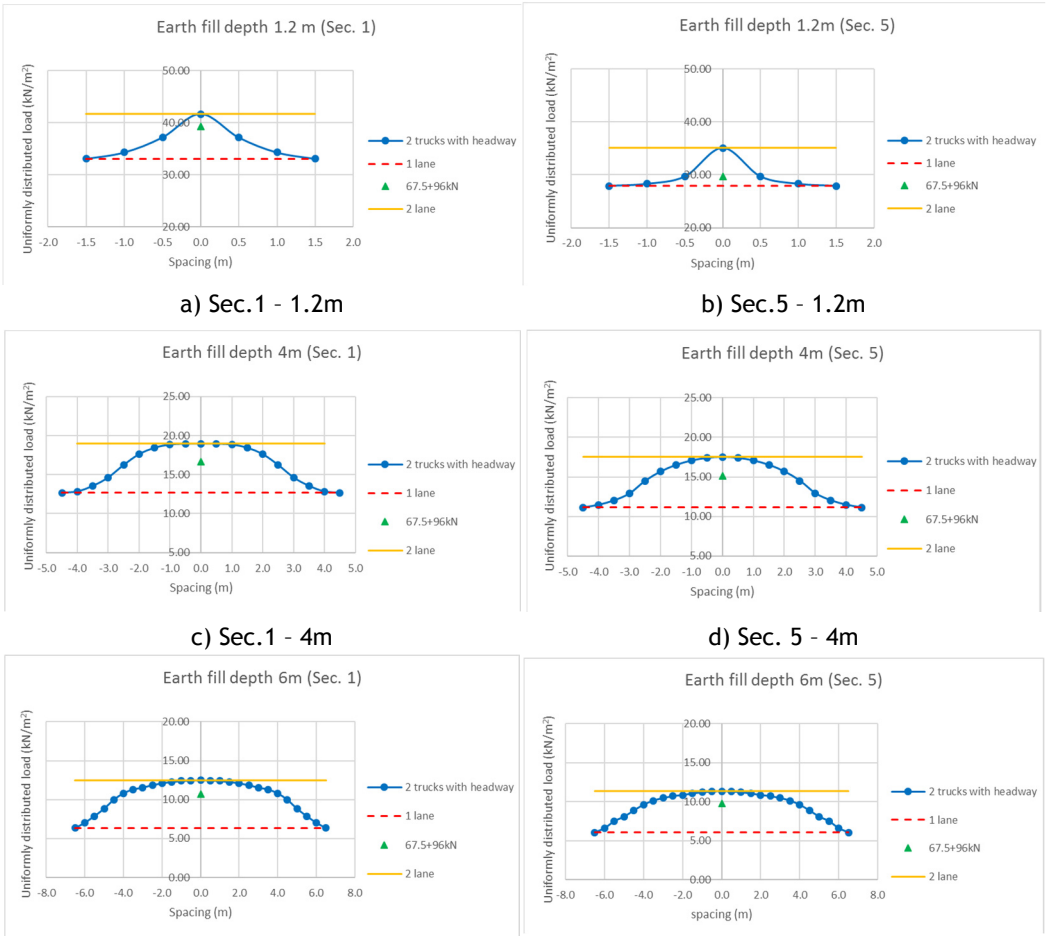

a) Sec.1 – 1.2m

b) Sec.5 – 1.2m

c) Sec.1 – 4m

d) Sec. 5 – 4m

e) Sec.1 – 6m

f) Sec.5 – 6m

Figure 5. Influence lines of adjacent trucks with headway distance

4 Simulation of traffic load effects on underground RC boxes

The traffic load effect will be simulated using the various traffic models, such as the traffic composition model, vehicle weight model, wheel load distribution model, wheel load dispersion(influence) model, etc. The traffic flow will be generated based on the vehicle type

composition models for the selected road traffic condition(mainly daily traffic volume and heavy vehicle volume), in which 5 vehicle types(P, B, T, TT, ST) are classified, in which P-passenger car, B-bus, T-light truck, TT-truck with tandom wheel, and ST-heavy truck with either trailor type or semi-trailor type. The vehicle weights will be simulated based on the local vehicle gross weight model for each vehicle type. Then the wheel loads will be distributed from the generated vehicle gross weight. Finally the load effect EUDL will be calculated using the influence lines shown in Figure 5. The maximum value during the predefined interval, such as daily maximum, weekly maximum, monthly maximum, etc., will be selected and the extreme value analysis will be performed to generate the probabilistic live load effect models.

As shown in the influence lines in Figure 5, the effect of the truck on the adjacent traffic lane can be ignored when the headway distance is longer than the fill depth. Therefore, the simulation will be performed in two different traffic condition, such as a congested condition and normal running condition. In the congested condition, the vehicles are assumed to run with a very close distance, such as 2.0m between two consecutive vehicles on the same traffic lane, bumper-to-bumper distance. The vehicles in the normal traffic condition are assumed to run in a normal speed, such as 40-60 km/hr, this means that the distance between two consecutive vehicles on one lane will be longer than 4-6m. In the normal traffic condition, the bumper-to-bumper distance is assumed to keep 4.0m. The total daily traffic volume will be divided with a predefined ratio depending on the total volume, such as a higher congested volume ratio will be assumed when the total traffic volume increases.

The distance between the rear axles of two consecutive heavy trucks on the same traffic lane will be quite long and the combined effect can be ignored, even for the congested traffic condition.

5 Acknowledgement

This research program was funded by Korea Electric Power Corporation Research Institute (KEPCO-RI) of Korea, and its kind support is gratefully acknowledged. This work was also supported by the Korea Institute of Energy Technology Evaluation and Planning (KETEP) and the Ministry of Trade, Industry & Energy (MOTIE) of the Republic of Korea (No. 20174030201480).

6 References

Alfredo H.S. Ang and Wilson H. Tang. *Probability Concepts in Engineering Planning and Design: Volume II-Decision, Risk and Reliability*, Hoboken: Wiley, 1990.

Design Code for Underground RC Box Power Lines (URCPL), Korea Eelctric Power Corporation, 2008.

Design Code for Multi-purpose Underground RC Box (MURC), Korean Ministry of Land, Infrastructure and Transport, 2016.

Sang-Hyo Kim, Won-Ho Heo, Dong-Woo You and Jaegu Choi. *Vehicle Loads for Assessing the Required Load Capacity Considering the Traffic Environment*, Applied Sciences 7 (4): 365, 2017.

Standard Specifications for Tunneling-Open Cut Construction Boxes, Japan Society of Civil Engineers, 2016.

CENTRIFIGE TESTS TO ACCESS VARIABILITY OF THE VERTICAL AND LATERAL EARTH PRESSURES ACTING ON UNDERGROUND REINFORCED CONCRETE BOXES

Sang Inn Woo[1],Dongwook Kim[2], Sang-Kyun Woo[3],Sang-Hyo Kim[4]
[1]Department of Civil and Environmental Engineering, Hannam University, Daejoen, Korea
E-mail: sanginnwoo@gmail.com
[2]Department of Civil and Environmental Engineering, Incheon National University, Incheon, Korea
E-mail: dwkim@inu.ac.kr
[3]KEPCO Research Institute, Daejeon, Korea
E-mail: skwoo96@kepco.co.kr
[4]Department of Civil and Environmental Engineering, Yonsei University, Seoul, Korea
E-mail: sanghyo@yonsei.ac.kr

Abstract: This paper shows the experimental study focusing on the variability of the vertical and lateral earth pressure acting on the underground reinforced concrete box structures based on multiple centrifuge tests. For the centrifuge tests, a well-graded soil was applied for a model ground. The model ground was built up using a funnel type sand raining system to avoid the material segregation during sand raining. The model underground box has multiple stress measuring points along the top and sides to check the variability of the earth pressure. A centrifuge tests consisted of three stages (initial loading, loading, and unloading) consisting of multiple steps with a constant gravitational acceleration. The centrifuge test results show that both vertical and lateral earth pressures have great variability. Based on the centrifuge test data, this paper presents the mean and coefficient of variance of the soil-structure interaction coefficient and lateral earth pressure coefficient for the vertical and lateral earth pressure, respectively.

Keywords: Centrifuge test, underground box structures, sand, earth pressure, variability

1 Introduction

In South Korea, underground reinforce concrete (RC) boxes have been frequently used for the underground power lines. For the limit state design of the underground RC boxes, one of the important steps is to define and access the variability of loads acting on the RC box structures. One of dead loads acting the underground RC box structures is earth pressure transmitted from ground. Soil, one of particulate materials, naturally has great variability in the earth pressure because of uncertainties in the particle structure (where the inter-particle forces transfer), soil properties, and environmental factors such as ground water. In these backgrounds, the present study experimentally assesses the variability of the vertical and lateral earth pressure using multiple centrifuge tests.For the underground box structures, Oshati, Valsangkar, and Schriver (2012) and Abuhajar, Newson, and Naggar (2017)conducted centrifuge tests to assess the earth pressure acting on the boxes.Oshati, Valsangkar, and Schriver (2012) performed centrifuge tests for underground box structures with great soil cover depth (over 50 m)under positive projection and induced trench conditions; however, for power lines, soil cover depth for the box structures in South Korea is typically 2 to 4 m, which is much smaller than Oshati, Valsangkar, and Schriver (2012). Abuhajar, Newson, and Naggar (2017)performed centrifuge tests to check the change of the vertical and lateral stress acting on the box structures when a strip footing was newly installed over the model ground that consisted of uniform sand. For the box structure without the footing, they conducted only one centrifuge test which is not enough to estimate variability

of the earth pressure.Based on these backgrounds, this study focuses on multiple centrifuge tests for the underground box structure with multiple pressure measurement points. Based on the centrifuge tests on the vertical and lateral earth pressure, this study presents statistics for the soil-structure interaction coefficient F_e for the vertical earth pressure and lateral earth pressure coefficient K for the lateral earth pressure.

2 Centrifuge test

In South Korea, excavated (residual) soil has been typically reused to bury the underground box structure; therefore, this study builds up a model ground for centrifuge tests using a well-graded soil ground. Figure 1 shows (a) size distribution curve and (b) photo of the sand used to build model grounds in the centrifuge tests in this study.To make up the well-graded sand,this study mixed multiple uniform sands (No. 5 to 8 sand in Figure 1). The average size D_{50} of particles is 0.4 mm and the coefficient of uniformity C_U and curvature C_C are 4.09 and 1.18, respectively. After performing the standard compaction test results for the well-graded sand, the maximum dry unit weight and optimum moisture contents were found as 1.66 t/m^3 and 5%, respectively.

For uniform sands, the traditional sand raining system canbe adopted to build a model ground without worry about the material segregation; however, for the well-graded sand, it may induce the material segregation during unconstraint free falling (Fretti, Lo Presti, and Pedroni 1995); thus, this study developed a funnel sand raining system based on Fretti, Lo Presti, and Pedroni (1995).Figure 2 shows the developed funnel sand raining system. The system consists of the sand container, flexible tube, sieve, rigid pipe, guide system, and soil chamber as shown in Figure 2. In the system, sand particles in the upper soil container naturally move down through the flexible tube to the sieve. At the sieve, the particles deposits depending on the size of the sieve; the smaller size sieve allows the more deposition of the particles. After passing the sieve, the particles fall freely to the soil chamber inside the rigid pipe. To form a model ground in the chamber uniformly, using the guide system (Figure 2), the rigid pipe travels across the soil chamber. With the funnel sand raining system and well-graded sand, the present study formed the model ground with dry unit weight as 1.64 t/m^3 corresponds to about 99% of the relative compaction.

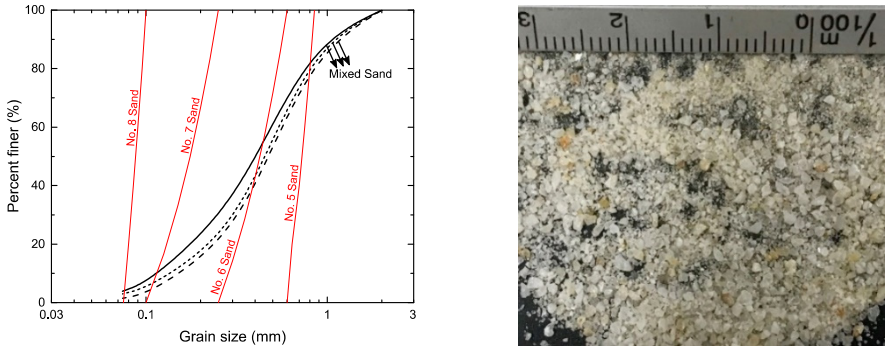

(a) (b)

Figure 1. (a) photo, (b) size distribution curve, and (c) compaction curve of the well-graded (mixed) sand used in this study

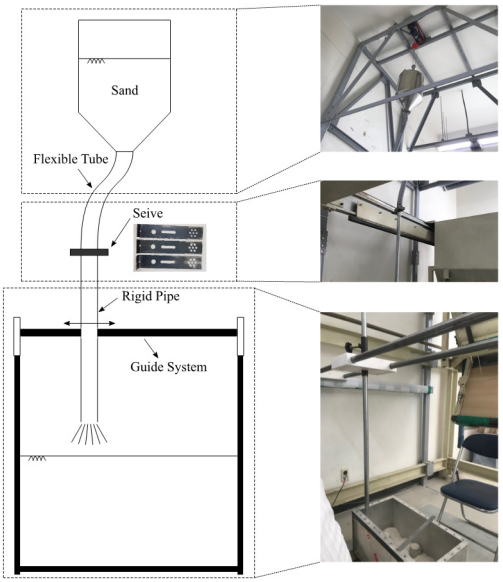

Figure 2. Sand raining system used in this study

Figure 3 shows (a) photo and (b) schematic diagram of the model box structure used in this study. The model box structure consists of aluminum and has three pressure measurement points on each side (Figure 3(a)). The width and height of the model box structure are 5.2 and 5.6 cm, respectively. Under the 50g condition, the corresponding width of height of the box structure are 2.6 and 2.8 m, which are generally accepted dimensions of underground RC boxes for the power lines in South Korea.As shown in Figure 3(b), the soil depth under the box structure locates was 20 cm (= 10 m under 50g) and the soil cover depth H_s over the box structure was adjusted as 4, 8, and 12 cm (= 2, 4, and 6 m under 50g, respectively) to consider the effect of the soil cover depth.

Table **1** lists centrifuge tests performed in this study. In this study, to check the variability of vertical and lateral earth pressures acting on the box structure, each experimental case was performed multiple times with identical conditions. For Case 1 (H_s = 4 cm), total three tests were performed including a preliminary test. For Cases 2 and 4 (H_s = 8 and 12 cm, respectively), this study performed total two tests under same conditions.

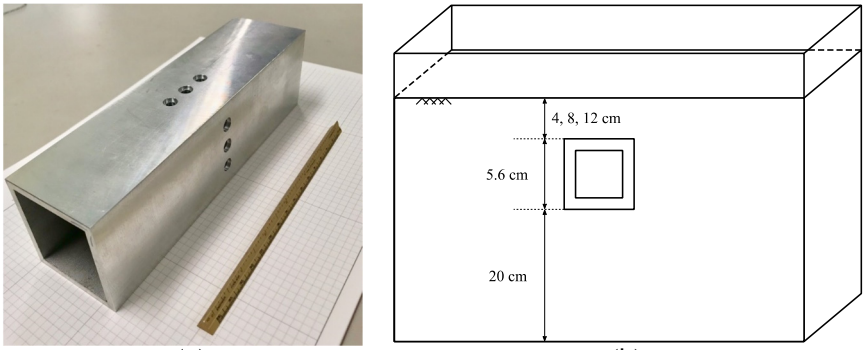

(a) (b)

Figure 3. (a) photo of the model box structure and (b) schematic diagram of the model box structure inside the model ground

Table 1 Centrifuge tests

No.	RC Box Structure		Soil Cover	Model Ground
	Width W_b	Height H_b	Depth H_s	
Case 1			4.0 cm @ 1g 2.0 m @ 50g	
Case 2	5.2 cm @ 1g 2.6 m @ 50 g	5.6 cm @ 1g 2.8 m @ 50 g	8.0 cm @ 1g 4.0 m @ 50g	Drywell-graded sand Relative compaction R_c> 95%
Case 3			12.0 cm @ 1g 6.0 m @ 50g	

Figure 4 illustrates the loading scenario applied in the centrifuge tests in this study.Initially, the gravitational acceleration applied to the model ground increases in steps of 20g up to 100g to stabilize the model ground. After the initial stabilization, the gravitational acceleration decreases to 1g. In the subsequent loading stage, the gravitational acceleration increases from 1g to 50g with 10g steps; each loading step sustained at least ten minutes to measure stabilized earth pressures at each sensor. In the unloading stage following the loading stage, the gravitational acceleration decreases from 50g to 1g with 10g steps which maintained five minutes.

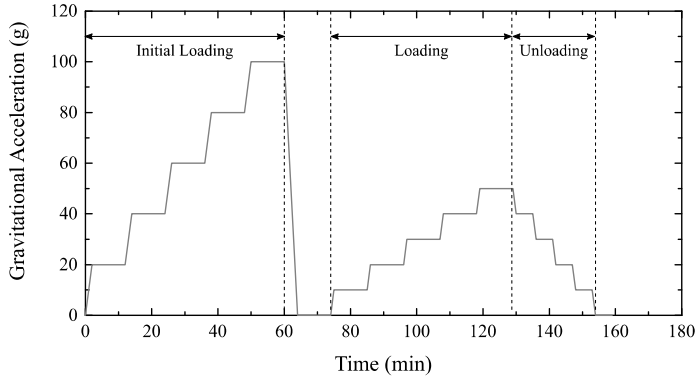

Figure 4 Loading senario applied for the centrifuge tests in this study

3 Results and discussions

3.1 Vertical earth pressure

Figure 5plots measured vertical stress values acting on the culvert versus theoretical overburden pressure for each step in Case 1, 2, and 3. It also show the vertical stress using the soil-structure interaction coefficient F_e (= 1.15 in this study) recommended byAASHTO (2010). First, Figure 5 show the considerable variability of the vertical earth pressure acting on the box structure. Second, the measured stress values are generally greater than the AASHTO recommended pressure as well as the theoretical overburden pressure. Third, the bandwidth of the measured stress increases rapidly at the low level of vertical stress; however, after 50 kPa, its size does not change.

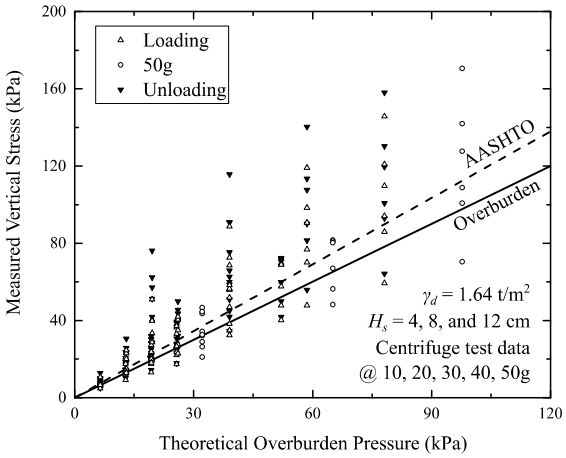

Figure 5. Measured vertical earth pressure versus theoretical overburden pressure with AASHTO recommendation vertical pressure

Figure 6 plots histograms of the soil-structure interaction coefficient F_e for (a) all test data and (b) test data only for 50g stage. In this study, the soil-structure interaction coefficient F_e was calculated by:

$$F_e = \frac{\sigma_{v,measured}}{\sigma_{v,overburden}} \tag{1}$$

where $\sigma_{v,measured}$ is a vertical stress value measured in this study and $\sigma_{v,overburden}$ is a theoretically calculated overburden pressure using the soil cover depth and unit weight of soil. Using all data of each loading and unloading step (Figure 6(a)), mean value of F_e is 1.365, which is greater than 1.15 (AASHTO recommended value); and COV (Coefficient of Variation) of F_e is calculated as 0.359. The shape of the distribution of F_e is similar to the lognormal distribution. In Figure 6(b), for test data under 50g conditions (where the corresponding dimensions of the RC box structure matches the typical sizes of underground RC box structures for power lines in South Korea), the mean value of F_e is 1.113, which is very closed to the AASHTO recommended value (= 1.15) and COV is found as 0.253. Using only 50g data, the shape of the distribution of F_e is more closded to the normal distirubiton than the lognormal distribution.

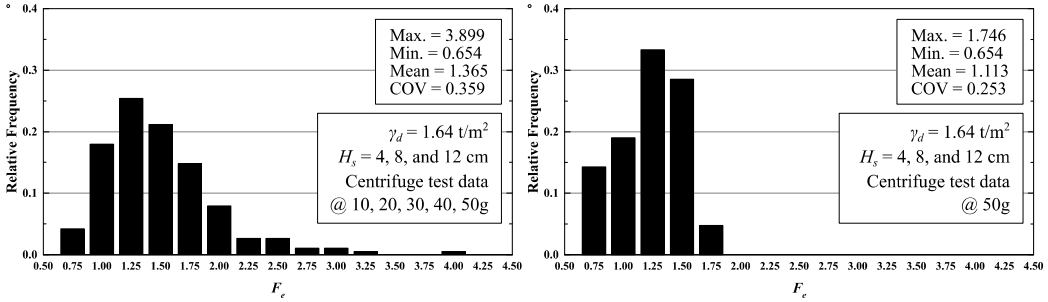

Figure 6. Distribution of soil-structure interaction coefficient Fe measured in the centrifuge tests

3.2 Lateral earth pressure

Figure 7plots measured lateral stress values acting on the side of the box structure versus

theoretical overburden pressure for each step in Case 1, 2, and 3. It also show the lateral stress line calculated using lateral earth pressure coefficients *K* = 0.2, 0.3, 0.4, 0.5, and 0.6 as references; in Figure 7, the typical range of the lateral earth pressure coefficient *K* is 0.2 to 0.6.Figure 7 shows that the variability of the lateral earth pressure is greater than the vertical earth pressure. It also implies that the bandwidth of the measured stress increases with the soil cover depth unlike the vertical stress.

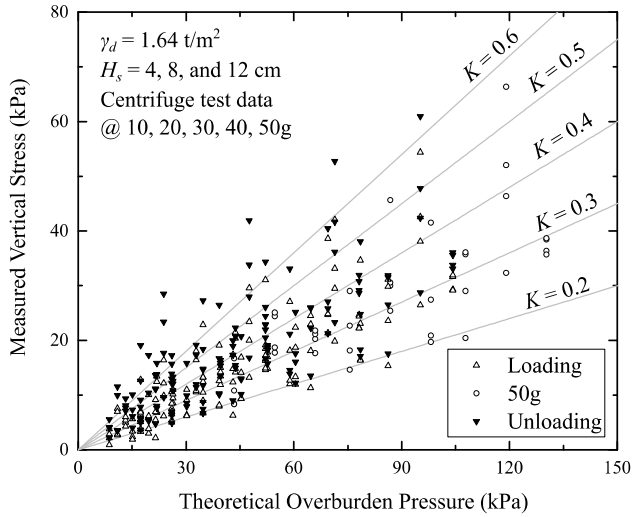

Figure 7. Measured lateral earth pressure versus theoretical overburden pressure

Figure 8 plots histograms of the lateral earth pressure coefficient *K* for (a) all test data and (b) test data only for 50g stage. In this study, the soil-structure interaction coefficient *K* was calculated by:

$$K = \frac{\sigma_{h,measured}}{\sigma_{v,overburden}} \tag{2}$$

where $\sigma_{h,measured}$ is a lateral stress value measured in this study and $\sigma_{v,overburden}$ is a theoretically calculated overburden pressure using the soil cover depth and unit weight of soil. Using all data of each loading and unloading step (Figure 8(a)), mean and COV of *K* are 0.384 and 0.427, respectively. The shape of the distribution of *K* is similar to the lognormal distribution. In Figure 8(b), for test data under 50g conditions, the mean value of *K* is 0.319 and COV is found as 0.286. Using only 50g data, the shape of the distribution of F_e is also closded to the lognormal distribution.

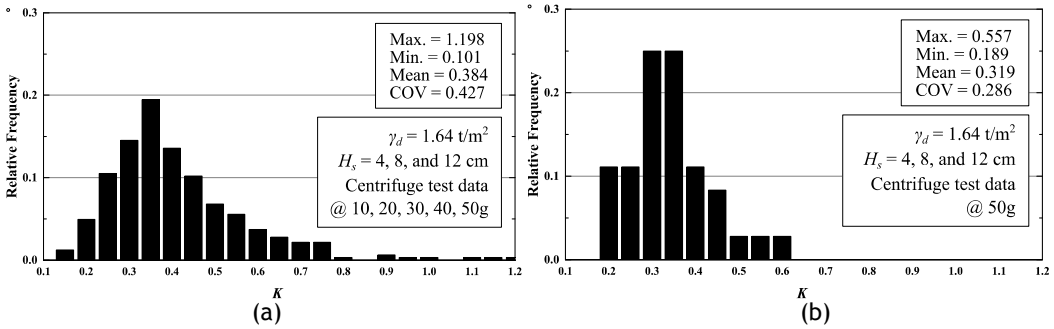

Figure 8. Distribution of lateral earch pressure coefficient K measured in the centrifuge tests

4 Summary and Conclusions

This study accesses the variability of the vertical and lateral earth pressure acting on the underground reinforced concrete box structures, typically used for the underground power lines in South Korea by performing multiple centrifuge tests. For the centrifuge tests, this study relied on a well-graded soil (which is typically used to burying the underground box structure) for the model ground. To build up the model ground using the well-graded soil, the present research adopted a funnel type sand raining system to avoid the material segregation during sand raining. The model underground box has three stress measuring points along the top and each side to check the variability of the earth pressure. A centrifuge tests consisted of three stages (initial loading, loading, and unloading) and each stage has multiple steps where gravitational acceleration was sustained. The centrifuge test results imply that both vertical and lateral earth pressures have great variability. For the vertical earth pressure acting on the top of the box structures, using all test data (loading and unloading steps), mean and COV values of the soil-structure interaction coefficient F_e are 1.365 (greater than AASHTO recommended value) and 0.359, respectively. For test data under 50g conditions, the mean and COV values of F_e is 1.113 (closed to the AASHTO recommended value) and 0.253, respectively. For the lateral earth pressure acting on the sides of the box structures, mean and COV of the lateral earth pressure coefficient K are 0.384 and 0.427, respectively. For test data under 50g conditions, the mean value of K is 0.319 and COV is found as 0.286.

5 Acknowledgement

This research program was funded by Korea Electric Power Corporation Research Institute (KEPCO-RI) of Korea, and its kind support is gratefully acknowledged.

6 References

AASHTO. 2010. “AASHTO Standard Specifications for Highway Bridges.” Washington, DC.

Abuhajar, Osama, Tim Newson, and Hesham El Naggar. 2017. “Centrifuge Modeling of Surface Foundation Effects on Buried Box Culverts Modélisation de Centrifugeuse Des Effets de Fondation de Surface Sur Dalots Enterrés.” In *The 19th International Conference on Soil Mechanics and Geotechnical Engineering*, 881–84. Seoul.

Fretti, C, DCF Lo Presti, and S Pedroni. 1995. “A Pluvial Deposition Method to Reconstitute Well-Graded Sand Specimens.” *1Geotechnical Testing Journal* 18 (2): 292–98. https://doi.org/10.1520/GTJ10330J.

Oshati, OS, AJ Valsangkar, and AB Schriver. 2012. “Earth Pressures Exerted on an Induced Trench Cast-in-Place Double-Cell Rectanglular Box Culvert.Pdf.” *Canadian Geotechnical Journal* 49: 1267–84.

International Symposium on Reliability of Multi-disciplinary Engineering Systems under Uncertainty (ISRMES2019), 8-11 December 2019, Taipei
Chen, S. S. & Ang, Alfredo. H-S. (Editors)

PROBABILISTIC APPROACH FOR ROTATIONAL STIFFNESS OF WEDGE JOINT CONNECTING VERTICAL AND HORIZONTAL MEMBERS OF TEMPORARY STEEL SUPPORTS

Jeong-Hun Won[1], Ye Ji Na[2], Nam-Gwon Jang[3], Seung Hyeon Shin[4]
[1]Department of Safety Engineering, Chungbuk National University, Cheongju, Korea
E-mail: jhwon@chungbuk.ac.kr
[2] Department of Disaster Prevention Engineering, Chungbuk National University, Cheongju, Korea
E-mail: layj1019@hanmail.net
[3]Department of Safety Engineering, Chungbuk National University, Cheongju, Korea
E-mail: 93kjng@gmail.com
[4]Department of Safety Engineering, Chungbuk National University, Cheongju, Korea
E-mail: shshin0317@naver.com

Abstract: The nonlinear rotational stiffness of wedge joints, which were used widely to connect vertical and horizontal members of temporary steel system supports,wasinvestigated experimentally. To predict exact behaviors of system supports, the estimation of the rotational stiffness of the jointsshould be firstly estimated. And, it is need to estimate the nonlinear stiffness of joints reflecting the characteristics of reused members, which were generally utilized. Experimental tests were conducted for both new product members and reused members in order to assess the normality of the measured data. The joint type used in this study is a wedge joint used widely for easy installation and dismantling. Results show that the nonlinear stiffness could be modelled by trilinear model. The initial rotational stiffness decreased with continued use of the joint. The lower limit of the 95% confidence interval of the initial rotational stiffness was 20.688 kNm/rad, and the upper limit was 24.262 kNm/rad.

Keywords: Rotational stiffness, wedge joint, system support, experimental test.

1 Introduction

A steel system support is widely used to resist the concrete loads during the casting the concretesince it provideseasy installation and dismantlement than conventional supports. In the system support, vertical, horizontal, and bracing members are installed at regular intervals by connecting joints such as wedge joints. However, the rotational stiffness of the jointsdoesnot considered in the design stage. As the boundary condition of the joint between vertical and horizontal members is assumed to be a simple hinge in design standards and the safety of a structure is considered to depend on its elastic behavior within the allowable stress range, there are limitations on accurately predicting the ultimate behavior of systemsupports.

Even though the performance of system supports is based on new products, both new and reused products are used on construction sites. To reflect the reused characteristics of system supports, probabilistic studies should be conducted. Unfortuately, it is difficult to find such researchesin South Korea. Therefore, this study examined the probablistic value of the rotational stiffness of wedge joints by experiments reflecting the characteristics of reused members.Based on the results, the 95% confidence intervals of the initial rotational stiffness of wedge-type joints were determined by conducting a probabilistic analysis.

2 Experimental test

The specimen consisted of one vertical member, one horizontal member, and a joint at which a pin at the end of the horizontal member was inserted into a ring attached to the vertical member to connect the two members. To reflect the reuse characteristics of temporary structures, the vertical and horizontal members that had been used before were prepared. Even though specimens must be prepared based on the reused number, it is practically difficult to find members with usage history since the history of temporary materials was not managed. Therefore, specimens were selected randomly by purchasing products made by the same manufacturer from a large leasing company, based on the period of use.

Eleven sets of products used for one year, eleven sets of products used for four years, and eleven sets of products used for seven years were purchased. In addition, thirteen sets of new members were prepared to compare and analyze changes of rotational stiffness of the joint. The material properties of specimens are shown in Table 1. The test was performed in the cantilever state as shown in Figure 1.

Table 1. Material properties

Classification	Vertical member	Horizontal member
Steel grade	SGH 490	STK 400
Yield strength (MPa)	365	235
Length (mm)	432	1,468
Diameter (mm) / Thickness (mm)	60.5 x 2.6	42.7 x 2.2

The load was applied at a rate of 10 mm per minute using a universal testing machine (UTM) with a capacity of 200 kN. To prevent the occurrence of out-of-plane motion, a guide was installed behind the loading point. In addition, a guide made of steel was placed around the joint to prevent accidents caused by debris.

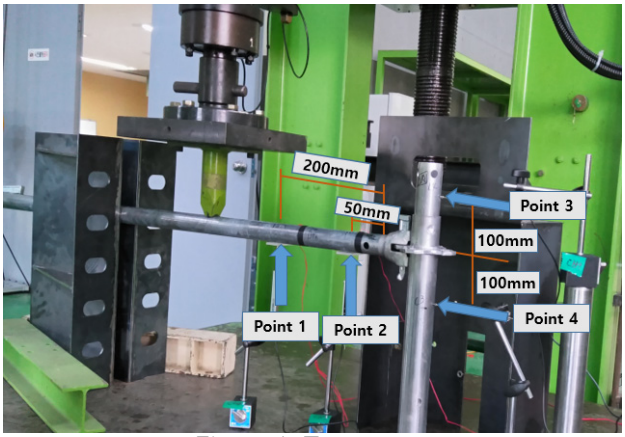

Figure 1. Test set-up

3 Results

The rotation angle as a function of the load was calculated using the measured displacement and equation (1).

$$\theta = tan^{-1}\left(\frac{\Delta_1-\Delta_2}{d_{1-2}}\right) - tan^{-1}\left(\frac{\Delta_3-\Delta_4}{d_3+d_4}\right) \quad (1)$$

where$\Delta_1$is the displacement of point 1, Δ_2 is the displacement ofpoint 2, Δ_3 is the displacement ofpoint 3, and Δ_4 is the displacement ofpoint 4. $d_{1\text{-}2}$ is the distance betweenpoint 1 andpoint 2, $d_3$is the distance between point 3 and the joint, and d_4 is the distance betweenpoint 4 and the joint (see Figure1).

Figure2 shows the moment-rotation curves of specimens and the slope of the moment-rotation curves represents the rotational stiffness of wedge joint.It is found that the specimens with new members exhibited the highest initial rotational stiffness and they generally exhibitedhigher moment capacity than the reused specimens. As the reuse period increased, the moment-rotation curveswere found to be lower.

The trilinear model was adopted to analyze the rotational stiffness of the wedge joint by averaging the results for the new and reused specimens. The proposed trilinear model was shown in Figure 3. The initial rotational stiffness was 22.475 kNm/rad, the second interval was 4.705 kNm/rad, and the third interval was 1.577 kNm/rad. The new and reused specimens was compared with the average values. The initial rotational stiffness of the wedge joint decreased as the reuse period increased. For the specimens with a 1-year reuse period, the initial rotational stiffness was 89.5% level compared to that of the new specimens. And, the specimens with a 4-yearand 7-year reuse period show 80.7% and 68% initial rotational stiffness compared to new specimens.

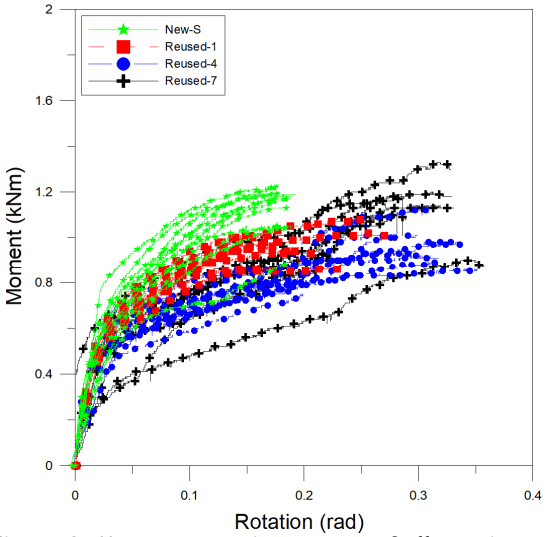

Figure 2. Moment-rotation curves of all specimens

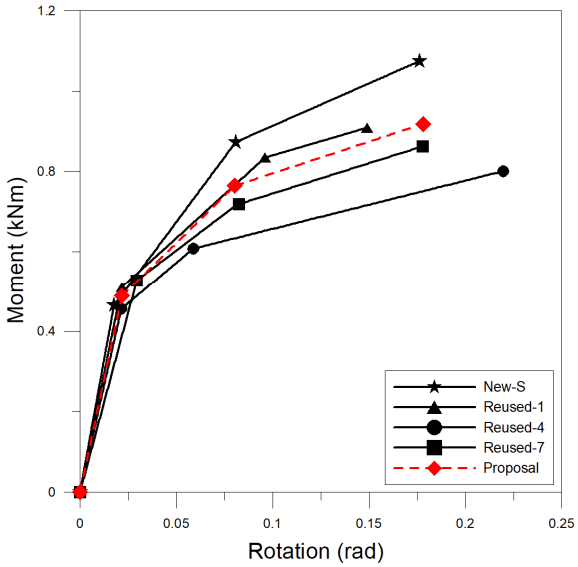

Figure 3. Proposed trilinear moment-rotation model

To estimate probabilistic value, a statistical analysis was conducted using the data for all the news and reused specimens.Since the significance probabilities obtained from the Kolmogorov-Smirnov and Shapiro-Wilk tests were higher than the significance level of 0.05, the initial rotational stiffness values were found to be normally distributed. Figure4represents the normality graph of the estimated initial rotational stiffness. The lower and upper limits of the 95% confidence interval of the initial rotational stiffness were20.688 kNm/rad and 24.262 kNm/rad, respectively.

4 Conclusions

In this study, the experimental tests were performed to estimate the nonlinear rotational stiffness of wedge jointsconsidering the characteristics of new and reused members. From results, it is found that the rotational stiffness of the joint could be described by a trilinear model.The rotational stiffnesseswas22.475 kNm/rad for the first range, 4.705 kNm/rad for the second range, and 1.577 kNm/rad for the third range. A probabilistic analysis shows that the lower and upper limits of the 95% confidence interval of the initial rotational stiffness (first range in the trilinear model)were20.688 kNm/rad and s 24.262 kNm/rad,respectively.

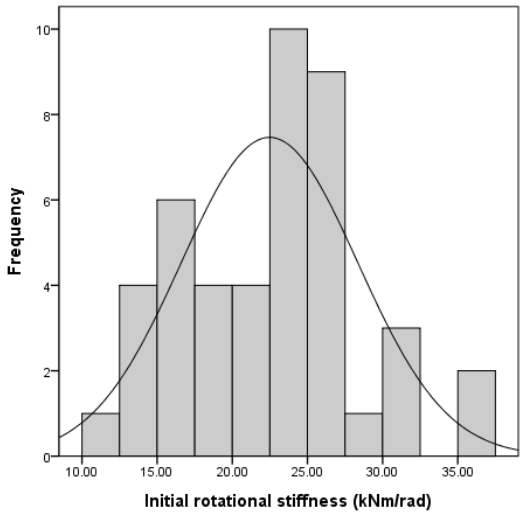

Figure4. Frequency distribution and normal distribution curve of initial rotational stiffness data

5 Acknowledgement

This research program was funded by Korea Electric Power Corporation Research Institute (KEPCO-RI) of Korea, and its kind support is gratefully acknowledged.

6 References

Błazik-Borowa E., Szer J., Borowa A., Robak A., Pieńko M.,"Modelling of load-displacement curves obtained from scaffold components tests,"*Bulletin of the Polish Academy of Sciences. Technical Sciences*67(2019): 317–327.

Sakurai S., Ellingwood BR., Kushiyama S.,"Probabilistic study of the behaviour of steel frames with partially restrained connections",*Engineering Structures*23(2001): 1410-1417.

Zhang H., Chandrangsu T., Rasmussen KJR.,"Probabilistic study of the strength of steel scaffold systems,"*Structural Safety*32(2010): 393-401.

Zhu QX., Wan YC., Zhang QL.,"Rotational stiffness test and calculation model of steel scaffolds' coupler connections,"*Journal of Shandong Jianzhu University*5(2010): 007.

OPTIMAL DECISION-MAKING ON PIPELINE SIZES OF WATER NETWORKS UNDER SEISMIC CONDITIONS

Sungsik Yoon[1], Young-Joo Lee[2], Hyung-Jo Jung[3]
[1,3]Department of Civil and Environmental Engineering, Korea Advanced Institute of Science and Technology, 291 Daehak-ro, Yuseong-gu, Daejeon 34141, Republic of Korea
E-mail: yss3366@kaist.ac.kr, hjung@kaist.ac.kr
[2]School of Urban and Environmental Engineering, Ulsan National Institute of Science and Technology, 50 UNIST-gil, Eonyang-eup, Ulju-gun, Ulsan 44919, Republic of Korea
E-mail: ylee@unist.ac.kr

Abstract: *I*n this study, an optimal decision-making model on pipeline sizes of a water transmission network has been proposed. The purpose of the optimal decision-making model is to maximize seismic performance with limited construction cost. The proposed model estimates network performance using spatially correlated seismic attenuation law, determination of the failure status of the network component, and numerical modeling of water networks. For this purpose, MATLAB code has also been developed to enable EPANET analysis using pressure-based analysis and numerical modeling of network systems. To verify the proposed model, an actual urban water network has been adopted, taking into account the location and magnitude of the historical earthquake. In addition, two performance indices were introduced to assess network performance. The numerical results show that the optimized network model increased system serviceability and node serviceability by 9.9% and 11%, respectively, and the average node pressure of the network increased 3.6m over the existing model.

Keywords: Optimal decision making, pipeline size distribution, urban water networks, genetic algorithm, seismic risk assessment

1 Introduction

The water supply network serves to meet the needs of commercial facilities, industrial facilities and residents by supplying drinking water from water treatment plants to water storage tanks through complex pipeline systems. Therefore, damage to the water supply system can lead to disruption of residential activities, as well as economic damage to commercial and industrial facilities. For this reason, it is critical to maintaining supply performance in large, unplanned events such as natural disasters, random component failures, and excessive demands. In particular, because lifeline facilities are concentrated throughout the city, extreme events such as earthquakes can cause social disruption both directly and indirectly throughout the city.

2 Network optimization model

2.1 Ground motion prediction equation

If the location and magnitude of the input seismic motion are determined, various ground motions can occur, depending on soil conditions, wave propagation paths and site characteristics. For a simple mathematical representation of complex wave phenomena, the ground motion prediction equation (GMPE) has been adopted with various intensity measurements such as peak ground acceleration (PGA), peak ground velocity (PGV), and peak ground deformation (PGD). In this study, the PGV seismic attenuation law proposed by Wang

and Takada (2005) and the PGA seismic attenuation law proposed by Kawashima et al. (1984) has been adopted to predict the ground motion of each network components:

$$log\left(\overline{PGV_j}\right) = 0.725M_i + 0.00318H - 0.519 - 1.318\,log\left(R_{ij} + 0.334e^{0.653M_i}\right) \quad (1)$$

$$\overline{PGA_j} = 403.8 \text{ x } 10^{0.265M_i} \text{ x } (R_{ij} + 30)^{-1.218} \quad (2)$$

where $\overline{PGV_j}$ and $\overline{PGA_j}$ are the mean values of the peak ground velocity and acceleration at the j-th location, M_i is the earthquake magnitude at the i-th source, H is the length of the focal depth, and R_{ij} represents the distance between source i and site j.

2.2 Failure probability calculation

According to Hazus-MH (FEMA 2003), the water facility is classified into five damage states, and the probability of failure is represented by two parameters of the lognormal distribution: the median and the log-normal standard deviation. Unlike other water utilities, the vulnerabilities of buried pipelines have been reported to be more sensitive to PGV and PGD than to PGA (FEMA 2003). PGV is a suitable parameter for buried pipeline damage due to seismic propagation, and PGD predicts the effects of liquefaction, landslides and ground settlement. The proposed model does not take into account the effect of PGD, and only the effect of a strong ground motion (PGV and PGA) was considered. The following equation shows the PGV-repair rate relation proposed by O'Rourke and Ayala (1993):

$$Repair\ rate\ (RR_i) = C_1 0.0001(PGV_i)^{2.25} \quad (3)$$

$$P_{breakage,i} = 1 - e^{-RR_i L_i} \quad (4)$$

where PGV_i represents the intensity measure (maximum ground velocity) at the i-th pipeline, and C_1 represents the modified factor for the repair rate according to the pipeline diameter

2.3 Hydraulic simulation

For the numerical modeling of the pipeline, the broad approach proposed by Hwang, Lin, and Shinozuka (1998) is adopted. In hydraulic simulations, the discharge flow due to leaks and breaks in the pipeline can be represented using the emitter function. For detailed description of hydraulic simulation, Yoon, Lee and Jung (2019) proposed a numerical modelling and numerical model methodology of water network facilities.

2.4 Pipeline construction data

The buried pipelines and facilities of the A-City water supply network are managed by the Ministry of Environment of Korea government (Ministry of Environment 2016). According to the data provided by the Ministry of Environment, the cost of construction of each facility is classified by its diameter and buried environments. In particular, this document presents the costs for material and construction, depending on the standard pipeline sizes and on site (soil, asphalt, concrete) conditions.

3 Numerical example

To demonstrate the network optimization model, an actual water transmission network of A-city in South Korea was chosen as the benchmark water network. The geographic information

system (GIS) information and operational data for the A-city water network were provided by the A-city waterworks headquarters, and the EPANET input file was reconstructed based on the data provided. The A-City water network provides 3.26× 105 m3/day of water to 23 water storage tanks through 17 pumping facilities from two water treatment plants for 1.15 million residents. The entire network consists of 259 nodes (water treatment plants and storage tanks), 265 links (pipelines), and 17 pumping plants, with a total pipeline length of approximately 140.6 km (Yoon, Lee, and Jung 2019).

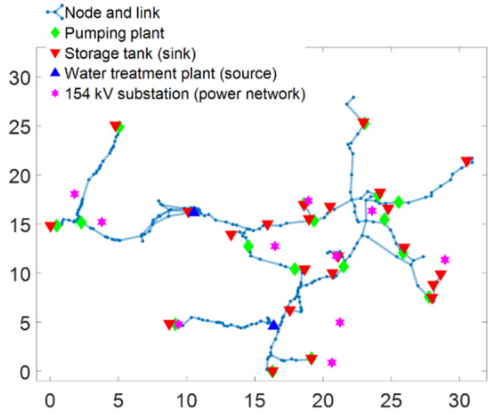

Figure 1. Construction of network map of urban water system in A-city (Yoon, Lee, and Jung 2019)

The construction budget was considered in the range of 152-192 billion Korean won, and to evaluate the construction cost needed for optimal pipeline diameter distribution, numerical analysis was conducted at intervals of 5 billion Korean won. The range of construction budget was determined by considering the cost of existing network (163.3 billion Korean won), and the cost of existing pipelines increased as the size of the pipeline increased by one size (182.6 billion Korean won). Figure 2 shows the change in S_S as the construction cost of the pipeline increases. For the existing water network, S_S was 0.5697, increasing by about 1.5% when the size of the pipeline was increased by one size (Yoon, Lee, and Jung 2019).

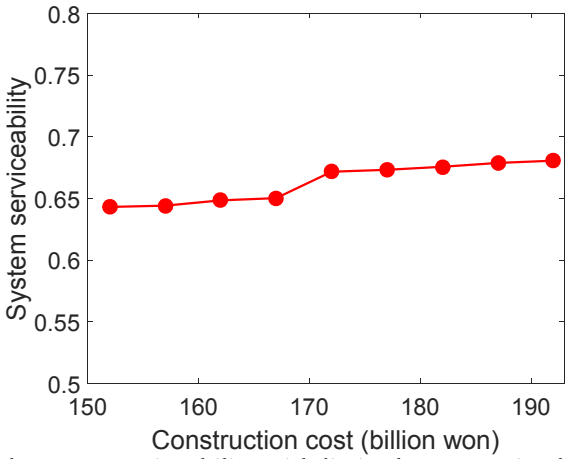

Figure 2. Optimized system serviceability with limited construction budgets (Yoon, Lee, and Jung 2019)

4 Conclusions

In this study, a comprehensive network model for the optimal system design of water transmission network has been proposed under seismic conditions. Compared to existing pipeline designs, S_S was found to perform significantly better in the optimal design. In addition, the network performance decreased with elapsed times and interdependency.

Acknowledgments

This work was supported by the Korea Institute of Energy Technology Evaluation and Planning (KETEP) Grant funded by the Korean Government (MOTIE) (No. 20181510102410)

6 References

FEMA. *Multi-Hazard Loss Estimation Methodology Earthquake Model, HAZUS-MH MR3 Technical Manual*. United States Department of Homeland Security, Federal Emergency Management Agency, Washington, DC, 2003.

Hwang H., Lin H., and Shinozuka M., "Seismic performance assessment of water delivery systems" *Journal of Infrastructure Systems* 4(3) (1998): 118-125.

Kawashima K., Aizawa K., and Takahashi K., "Attenuation of peak ground motion and absolute acceleration response spectra" *Proceedings Eighth World Conference on Earthquake Engineering* (1984): pp. 257-264.

Ministry of Environment. *Estimation standard for operation and construction cost of waterworks facility*. Republic of Korea, 2016.

O'Rourke M. and Ayala G., "Pipeline damage due to wave propagation" *J Geotech Eng* 119 (1993): 1490-1498

Wang M. and Takada T., "Macrospatial correlation model of seismic ground motions" *Earthq. Spectra* 21(4) (2005): 1137-1156.

Yoon S., Lee Y., and Jung H., "Flow-based Optimal System Design of Urban Water Transmission Network under Seismic Conditions," *Water Resources Management* (2019) (under review)

BAYESIAN NETWORK FOR STRUCTURES SUBJECTED TO SEQUENCE OF MAIN AND AFTERSHOCKS

Changuk Mun[1], Junho Song[2]
[1]Dept. of Civil and Environmental Engineering, Seoul National University, Seoul, Korea
E-mail: changwook80@snu.ac.kr
[2]Dept. of Civil and Environmental Engineering, Seoul National University, Seoul, Korea
E-mail: junhosong@snu.ac.kr

Abstract: For probabilistic prediction and inference regarding structures under complex hazard of main and aftershocks, this paper proposes a new Bayesian Network (BN) framework. First, causal relationships between factors affecting a sequence of main and aftershocks are modeled by a BN. To incorporate the properties of ground motions of main and aftershocks into the BN, artificial ground motions are generated using a stochastic model describing the characteristics of main and aftershocks and their relationships. Since the damage caused by the main-shock load affects the aftershock performance of the structure, the sub-networks describing main and aftershocks are interconnected through the nodes representing the structure. To this end, nonlinear dynamic analysis is performed using generated sequences of main and aftershocks. Based on these results, a comprehensive probabilistic model is constructed using the Matrix-based Bayesian network (MBN) for efficient BN modelling. The proposed BN model can update aftershock fragility by probabilistic inference when new information about the sequential event is observed. The proposed BN framework is expected to support decision making process after the aftermath of a main shock as demonstrated by numerical examples.

Keywords: Bayesian network, Matrix-based Bayesian network, Main shock, Aftershock, Probabilistic inference, Fragility

1 Introduction

Since strong earthquakes are often accompanied by aftershocks, the seismic risk assessment for upcoming aftershocks is essential for decision making regarding disaster risk management and evacuation from damaged building. Such seismic risk anaylsis requires a probabilistic approach because earthquake events and seismic behavior of structures have significant uncertainties. In particular, the fragility, i.e. the conditional failure probability given the value of seismic intensity measure (IM) is often evaluated to quantify the risk of aftershocks as well as main shock.

In the literature, fragility for aftershocks is evaluated using elaborate structural models and prescribed limit states (Ryu et al., 2011; Shin et al., 2014; Zhai et al., 2014). Since fragility evaluation often uses a set of selected ground motions, the fragility estimate is valid only for the seismic hazard represented by the selected ground motions. It is also noted that ground motions are usually scaled to perform Incremental Dynamic Analysis (IDA) (Vamvatsikos and Cornell, 2002) or Multiple Stripe Analysis (MSA) (Baker, 2015). The scaling is performed in terms of a specific IM, e.g. peak ground acceleration (PGA), spectral acceleration (Sa), so the set of selected ground motions might not represent possible ground motions at a site of interest.

Earthquake events have many uncertainties and complex relationships, so a comprehensive probabilistic model is needed for systematic treatment of the uncertainties. In this regard, Bayesian network (BN) is considered a powerful tool, which is especially useful for decision making after a disaster. A stochastic ground motion model by Rezaeian and Der Kiureghian

(2008) is reconstructed as a BN model in this study to reflect mechanisms of main and aftershocks. Besides, the relationships between the seismology of main and aftershocks and the stochastic model (Rezaeian and Der Kiureghian, 2010; Hu et al., 2018) are incorporated into the BN model. Lastly, structural responses to main and aftershocks are modeled with the damage under main shock considered.

The constructed BN model allows us to evaluate the fragility of the structure under aftershocks. By the BN-based probabilistic inference, the aftershock fragility can be estimated for any level of intensity of the main shock. By considering the statistical dependence between main and aftershocks, and effect of the main shock damage on performance of structure under aftershock, the risk of the complex hazard can be evaluated more accurately. This probabilistic inference can facilitate decision-making process after main shock event. Furthermore, the information about main shock can update the aftershock fragility and thus helps us cope with upcoming aftershocks more effectively.

The rest of this paper is organized as follows: Section 2 first provides a brief introduction of the BN and the stochastic model of ground motions. Section 4 presents the new BN framework proposed for probabilistic modeling of a sequence of main and aftershocks and estimating the fragility of structures. Section 4 shows the results of fragility estimation using a numerical example. Finally, Section 5 provides a summary and concluding remarks.

2 Backgrounds

2.1 Bayesian Network (BN)

Bayesian Network (BN) is one of the widely used probabilistic models (Koller and Friedman, 2009), which facilitates efficient quantification of the joint distribution for many random variables (r.v.'s). In a BN model, the dependency of r.v.'s is modeled using a directed acyclic graph while nodes and arcs represent r.v.'s and their statistical dependencies respectively. See Figure 1 for a simple example of a BN model. The graph-based structure of a BN provides intuitive modeling and presentation of the causal relationship between r.v.'s. The dependent r.v.'s are termed child nodes while affecting r.v.'s on the other end are called parent nodes. For example, in Figure 1, the child nodes of X_1 are X_2 and X_3, and the parent node of X_2 (or X_3) is X_1. After the development of a graphical model, the conditional distribution needs to be defined for each node. If there is no parent node e.g. X_1, the conditional distribution becomes marginal distribution. The joint distribution of r.v.'s is factorized by conditional distributions of each node based on the conditional independence assumption. This factorization of joint distributions in BN model enables us to construct a probabilistic model for multiple r.v.'s more efficiently. For example, the example BN in Figure 1 describes the joint distribution as follows:

$$\mathrm{P}(\mathrm{X}_1, \mathrm{X}_2, \mathrm{X}_3) = \mathrm{P}(\mathrm{X}_1)\mathrm{P}(\mathrm{X}_2|\mathrm{X}_1)\mathrm{P}(\mathrm{X}_3|\mathrm{X}_1) \quad (1)$$

where $P(X_2|X_1)$ and $P(X_3|X_1)$ are conditional distribution of X_2 given X_1, and that of X_3 given X_1, respectively.

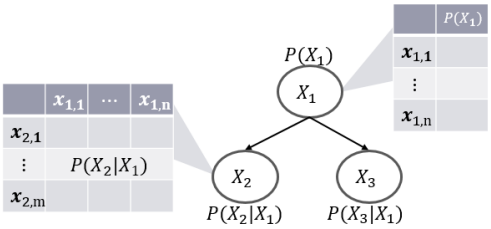

Figure 1. A simple example of Bayesian network

The distribution for the subset of r.v.'s can be derived by the marginalization. In addition, the conditional distribution for a specific condition can be estimated using Baye's rule. For example, the posterior distribution of a r.v. Y when another r.v. X is observed to have a value e is calculated as follows:

$$\mathrm{P(Y|X=e)} = \frac{\mathrm{P(Y,X=e)}}{\mathrm{P(X=e)}} \tag{2}$$

Both denominator and numerator in Eq. 2 can be acquired by the marginalization of the joint distribution on overall r.v.'s. In this way, the distribution of r.v.'s in BN model can be updated more accurately when new information is obtained.

2.2 Stochastic model for generating artificial ground motions

Real ground motions show nonstationary characteristics for its amplitude and frequency contents, that is, the amplitude and frequency contents are varying as the time goes by. As an effort to generate artificial ground motions resembling such characteristics of real ground motions, Rezaeian and Der Kiureghian (2008) proposed a stochastic model of artificial ground motions. In this method, artificial ground motions are generated by two-step transformation of a white noise process. The frequency contents and amplitude of the white noise process are modulated at each transformation. After two transformations of the white noise process $\omega(\tau)$, the random process $x(t)$ is given as

$$x(t) = q(t,\boldsymbol{\alpha})\left\{\frac{1}{\sigma_h(t)}\int_{-\infty}^{t} h[t-\tau,\boldsymbol{\lambda}(\tau)]\omega(\tau)d\tau\right\} \tag{3}$$

where $q(t,\boldsymbol{\alpha})$ is the time-modulating function with parameter $\boldsymbol{\alpha}$, $\sigma_h(t)$ is the standard deviation of the integral process (see below for details), and $h[t-\tau,\boldsymbol{\lambda}(\tau)]$ is the impulse response function (IRF) with time-varying parameters $\boldsymbol{\lambda}(\tau)$, which is determined as the acceleration response of an oscillator, i.e.

$$\begin{aligned} h[t-\tau,\boldsymbol{\lambda}(\tau)] &= \frac{\omega_f(\tau)}{\sqrt{1-\zeta_f^2}}\exp\left[-\zeta\omega_f(\tau)(t-\tau)\right]\sin\left[\omega_f(\tau)\sqrt{1-\zeta_f^2}(t-\tau)\right], \tau \le t \\ &= 0 \text{ otherwise} \end{aligned} \tag{4}$$

where natural frequency $\omega_f(\tau)$ and damping ratio ζ_f are IRF model parameters.

In other words, the first transformation, which is expressed as the integral in Eq. 3, is performed by calculating the acceleration response of an oscillator with natural frequency $\omega_f(\tau)$ and damping ratio ζ_f to a white noise process. The natural frequency $\omega_f(\tau)$ is defined as a linear function of time to describe the varying frequency contents of real ground motions:

$$\omega_f(\tau) = \omega_{mid} + \omega'(\tau - t_{mid}) \tag{5}$$

where t_{mid} denotes the time at the middle of the strong-shaking phase, ω_{mid} is the natural frequency at time t_{mid}, and ω' is the variation of the natural frequency. The transformed process, i.e. the integral in Eq. 3 is normalized by its standard deviation, which is

$$\sigma_h(\tau) = \left[\int_{-\infty}^{t} h[t-\tau, \boldsymbol{\lambda}(\tau)]\omega(\tau)d\tau\right]^{1/2} \tag{6}$$

The second step of the transformation modifies the amplitude of the normalized process by using time-modulating function, which is

$$q(t, \boldsymbol{\alpha}) = \alpha_1 t^{\alpha_2 - 1}\exp(\alpha_3 t) \tag{7}$$

where α_1, α_2, and α_3 are parameters to be prescribed. These parameters determine the shape of the time-modulating function, and can be related to the three physical terms: $\bar{I}_{\mathrm{a}}$, D_{5-95}, and t_{mid} in which $\bar{I}_{\mathrm{a}}$ is the expected Arias intensity defined as

$$\bar{I}_{\mathrm{a}} = E\left[\frac{\pi}{2g}\int_0^{t_n} x^2(t)dt\right] \tag{8}$$

Next, D_{5-95} denotes the effective duration of the motion, which is defined as the time interval between 5 and 95% levels of the expected Arias intensity. Finally, t_{mid} is the time point at which 45% level of the expected Arias intensity is achieved.

Therefore, once the six model parameters ($\bar{I}_{\mathrm{a}}$, D_{5-95}, t_{mid}, ω_{mid}, ω', ζ_f) are determined, consistent random processes can be generated using Eq. 3. Then, an additional post-process is required because $x(t)$ tends to yield a larger response for long period systems when compared to the corresponding real ground motion. As the post process, high-pass filter with parameter ω_c is used, so the final synthetic ground motion $\ddot{z}(t)$ is obtained by solving the following equation of motion:

$$\ddot{z}(t) + 2\omega_c(t)\dot{z}(t) + \omega_c^2 z(t) = x(t) \tag{9}$$

3 BN model of an SDOF system under sequence of main and aftershocks

3.1 BN modeling of the sequence of ground motions

The six parameters ($\bar{I}_{\mathrm{a}}$, D_{5-95}, t_{mid}, ω_{mid}, ω', ζ_f) in the stochastic model can be considered as causes of the statistical properties of the generated ground motions while the IM of the ground motions is one of the *effects* of the causes. This causal relationship can be represented in a BN model as shown in Figure 2. The conditional distribution of IM given the model parameters can be estimated from ground motions simulated for joint states of the model parameters.

Rezaeian and Der Kiureghian (2010) performed a regression analysis to relate the stochastic model parameters with earthquake and site properties using far-field strong motion records. The regression model predicts the six parameters using four input variables: fault type (F), magnitude (M), source-to-site distance (R_{rup}), and site shear-wave velocity (V_{s30}). The regression model includes Gaussian noise that explains intra- and inter-event uncertainty of ground motions. The regression model is incorporated into the BN model as shown in Figure 3 in which the conditional distributions of the model parameters are quantified using the regression model. In this research, the regression model by Rezaeian and Der Kiureghian (2010) is used to

estimate the conditional distribution of model parameters for main shock with the assumption that the strong motion records used for the regression occurred as main shocks.

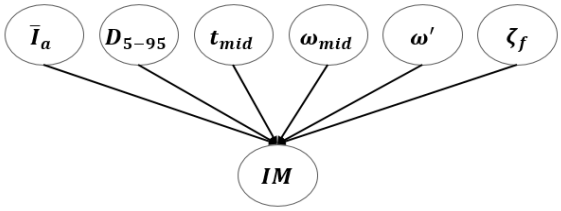

Figure 2. Bayesian network for the stochastic model

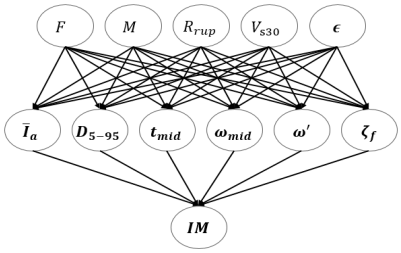

Figure 3. Bayesian network for an earthquake event and stochastic model

For aftershock events, Hu *et al*. (2018) proposed another regression model using aftershock ground motion records. In the process, the Joyner-Boore distance (R_{JB}) was additionally considered as an input variable. The information about fault shape is required to differentiate the two distance measures R_{JB} and R_{rup}, so both are assumed to be the same in this study. Based on the regression model by Hu *et al*. (2018), BN model for aftershocks can be constructed. Furthermore, it is noted that the earthquake and site characteristics of aftershocks depend on those of the main shock. To describe this relationship in BN, this study adopts the branching aftershocks sequence (BASS; Turcotte *et al*., 2007) model, which was also used in Hu *et al*. (2018). Finally, this study proposes the BN model in Figure 4 to describe a sequence of main and aftershocks.

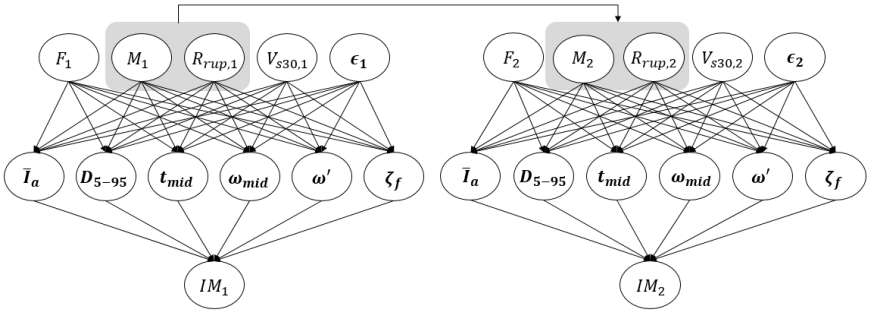

Figure 4. Bayesian network for the sequence of main and aftershocks

3.2 BN modeling of structural system

If structures are not damaged or degraded during the main shock, additional assessment of risk caused by possible aftershocks might not be a critical task because the intensity of aftershock is usually less severe than that of the main shock. However, if there exists some damage under main shock, the fragility for aftershocks will increase and thus upcoming aftershocks can be a fatal disaster. The structural damage can be described in terms of permanent deformation or deterioration of material properties. In order to incorporate these effects in dynamic analysis, this study models the structure by a Bouc-Wen class model, termed Bouc-Wen-Baber-Noori model (Baber and Noori, 1985) which is a modified version that can incorporate degrading behavior, e.g. degradation of stiffness or strength and pinching effect. For simplicity, in this study, stiffness degradation is only considered. The typical hysteresis of this model is shown in Figure 4.

The response of a structural system is determined by the properties of the system as well as ground motion. For example, natural frequency, damping ratio, or hysteresis behavior can be considered. In this study, the stiffness of a single-degree-of-freedom (SDOF) structure is selected as a variable to describe the degradation or damage of a single target structure. In BN, nodes representing the stiffness before main shock (k_1), after main shock (k_2), and after aftershocks (k_3) are introduced as shown in Figure 5. In this BN model, EDP (Engineering Demand Parameters), e.g. peak displacement of the structure, denotes the key seismic response, which is selected to determine whether the structure exceeds the limit state or not. Accordingly, EDP_1 and EDP_2 in the BN denote the structural response to main shock and aftershocks respectively. The conditional distribution of these variables can be estimated by performing dynamic analysis using sequences of main and aftershock ground motions generated from the stochastic models in Section 3.1.

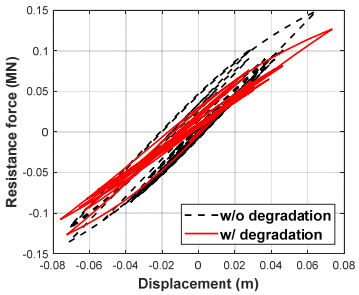

Figure 4. Typical hysteresis of the Bouc-Wen-Baber-Noori model

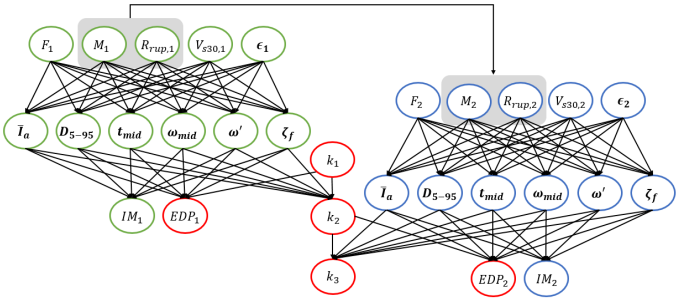

Figure 5. Bayesian network for an SDOF system under main and aftershocks

3.3 Fragility assessment using probabilistic inference

In a conventional fragility analysis approach using selected ground motions, the fragility is given as a function of IM only, but actual failure probability might be significantly affected by other characteristics of the earthquake event and site. In the developed framework, therefore, the fragility is estimated for a specific earthquake scenario and site condition using the BN models. Specifically, the fragility is computed as

$$Fragility = P(EDP \geq EDP_c | IM, F, M, R_{rup}, V_{s30}) \tag{10}$$

where EDP_c is a prescribed threshold value. Once the BN model in Figure 5 is constructed, the fragility in Eq. (10) can be calculated by the probabilistic inference for any value of IM, F, M, R_{rup}, and V_{s30}.

After the discretization of r.v.'s, the conditional distribution of each child node is saved as a table form, which is so-called Conditional Probability Table (CPT). This CPT requires the conditional distribution of a child node to be defined in the entire domain of parent nodes. For example, in this paper, the child nodes of model parameters should be defined in the domain as follows:

$$\Omega(\boldsymbol{X}) = \prod_{i=1}^{6}(ub(x_i) - lb(x_i)) \tag{11}$$

where $ub(x_i)$ and $lb(x_i)$ for $i = 1, \ldots, 6$ denote the upper and lower bounds of the model parameters, i.e. $\bar{I}_a$, D_{5-95}, t_{mid}, ω_{mid}, ω', ζ_f. However, these parameters are actually concentrated in a subdomain of Eq. 11 because of significant correlation between random

variables. These correlations are from the characteristics of real ground motions and reflected by the residual terms in the regression models by Rezaeian and Der Kiureghian (2010) and Hu et al. (2018). To take advantage of the correlation structure for efficient BN modeling, in this research, the Matrix-based Bayesian network (MBN; Byun et al., 2019) is used instead of conventional BN modeling that requires huge CPTs. The MBN manages the information of distribution as a matrix form to facilitate effective and efficient modeling and inference of BN.

4 Numerical example

To demonstrate the proposed BN framework, we investigate an example SDOF system with damping ratio 0.07. The natural period of the structure is randomly sampled from a Gaussian distribution with mean 1.3s and coefficient of variation 0.025. Using randomly selected values of stochastic model parameters, 2,100 main shocks and 1,500 aftershocks are generated to create 2,100×1,500 sequences of ground motions. Next, for each sequence of generated main and aftershocks, dynamic analysis is performed to simulate the effects of stiffness degradation caused by main shock on the seismic performance under aftershocks. In this study, peak ground acceleration (PGA) and peak displacement (D) are considered as IM and EDP respectively. Because PGA depends on the parameters of time-modulating function rather than those of IRF, the dependency on the parameters of IRF is ignored. This is reflected by removing the corresponding arcs in the BN structure as shown in Figure 6.

In general, statistical models require more data when its structure is complex. In a BN model, for example, the conditional distribution of a child node will be defined better if the supporting data is enough for various combinations of the parent node values. Accordingly, a systematic simulation strategy is required for stable performance of BN model. Nevertheless, this is not carefully considered in this paper, which aims to propose the framework. The randomly generated ground motions (2,100 main shock and 1,500 aftershocks) were not enough to cover all model parameters, so the dependency on t_{mid} and ζ_f are not considered in this study. However, in future research, the BN model will be refined through a systematic simulation strategy.

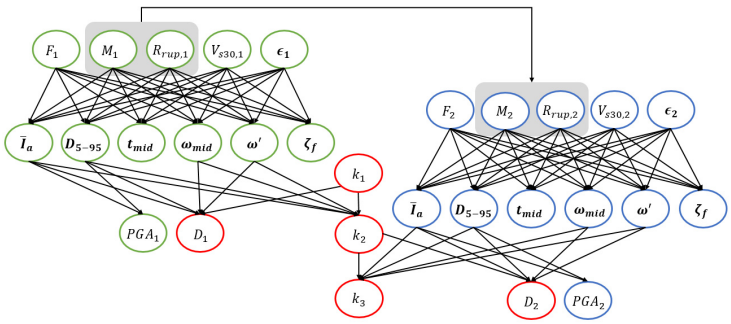

Figure 6. Bayesian network of the SDOF system used for fragility assessment in numerical example

To take into account the structural damage caused by the main shock, the aftershock fragility is conditioned not only the PGA of aftershocks but also that of the main shock. Table 1 summarizes two assumed scenarios of main shocks. The fault type and site shear-wave velocity of the two scenarios are assumed to be the same, but the magnitude and rupture distance of the main shock in Case 2 are assumed to be more dangerous.

The fragility is evaluated by BN inference as shown in Figure 7 and Figure 8. In the figures, PGA_1 and PGA_2 respectively denote the PGAs of the main and aftershocks. In both cases, the aftershock fragility shows larger probability as the PGA of main shock increases. This reflects the effects of the main shock damage on the seismic performance during the aftershock. The variability of the aftershock fragilities is larger in Case 2 than Case 1 because more destructive earthquake event is likely to induce more significant main shock damage and effects. For comparison, Figure 7 and Figure 8 show the fragility for the main shock when $PGA_1 = PGA_2$. The fragility for main shock is not always larger than aftershock fragility, which indicates some damage yields a more dangerous situation for ground motions by aftershocks although it has the same PGA with main shock.

Table 1. Earthquake scenarios of main shocks

	F	M	$R_{rup}\ (km)$	$V_{s30}\ (m/s)$
Case 1	reverse	7	40	760
Case 2	reverse	8	20	760

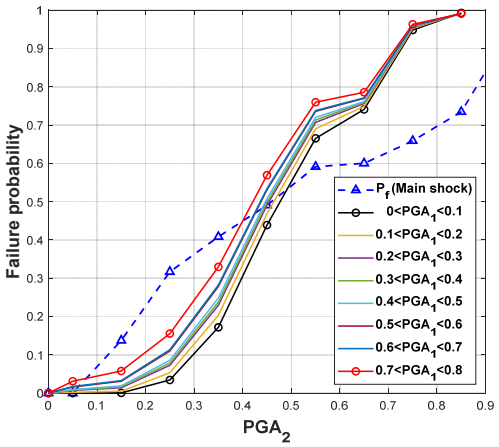

Figure 7. Aftershock fragility in Case 1

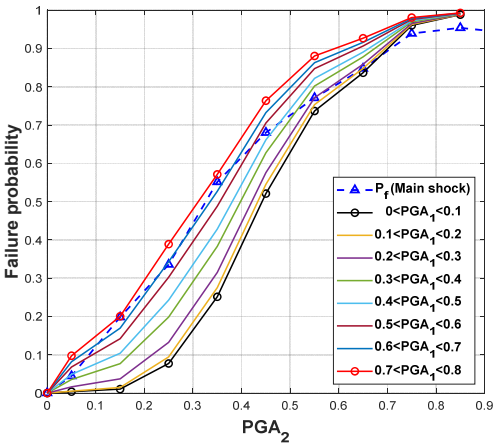

Figure 8. Aftershock fragility in Case 2

5 Conclusions

In this paper, a Bayesian network (BN) model is developed for the sequence of main and aftershocks for the purpose of fragility assessment. Earthquake scenarios of main and aftershocks are modelled by BN for a comprehensive description of their correlations, their dependency on local earthquake hazard, characteristics of ground motions, and aftershock response of structures which has been damaged under main shocks. The relationship between these features is displayed intuitively in the graphical structure. The developed BN model presents a new framework to evaluate the fragility of structures and facilitates updating aftershocks fragility using the information related to the aftermath of main shock.

In order to construct the BN model, artificial ground motions are simulated using the stochastic model. The parameters of the stochastic models constitute the BN model. This representation enables us to encompass a consistent domain of ground motion regardless of the type of IM. In the proposed process, the Matrix-based Bayesian network (MBN) is used for efficient quantification of the BN structure. The numerical examples of the SDOF system are investigated

to show the applicability and capability of the proposed BN framework.

Although the BN model is applicable to general structural systems, a comprehensive study on the construction of BN model has not been considered elaborately for a wider class of problems. Strategies for sampling and discretization of random variables, especially for model parameters, should be further investigated to ensure a desirable level of accuracy. Further development of each component of the model is underway to enhance the performance of the proposed BN methodology, and provide a more accurate evaluation of fragility and post-disaster inference.

6 Acknowledgement

This work is financially supported by Korea Ministry of Land, Infrastructure and Transport (MOLIT) as the Innovative Talent Education Program for Smart City.

7 References

Baber, T., and Noori, M., 1985, "Random vibration of degrading pinching systems." *Journal of Engineering Mechanics* 111, no.8

Baker, J. W., 2015, "Efficient analytical fragility function fitting using dynamic structural analysis." *Earthquake Spectra* 31: 579-599

Byun, J., Zwirglmaier, K., Straub, D., and Song, J., 2019, "Matrix-based Bayesian network for efficient memory storage and flexible inference." *Reliability Engineering and System Safety* 185: 533-545

Hu, S., Gardoni, P., and Xu, L., 2018, "Stochastic procedure for the simulation of synthetic main shock-aftershock ground motion sequences." *Earthquake Engineering and Structural Dynamics* 47: 2275-2296

Koller, D. and Friedman, N., "Probabilistic graphical models: principles and techniques", Cambridge: The MIT Press, 2009

Rezaeian, S. and Der Kiureghian, A., 2008, "A stochastic ground motion model with separable temporal and spectral nonstationarities." *Earthquake Engineering & Structural Dynamics* 37: 1565-1584

Rezaeian, S. and Der Kiureghian, A., 2010, "Simulation of synthetic ground motions for specified earthquake and site characteristics." *Earthquake Engineering & Structural Dynamics* 39: 1155-1180

Ryu, H., Luco, N., Uma, S. R., and Liel, A. B., 2011, "Developing fragilities for mainshock-damaged structures through incremental dynamic analysis." 9th Pacific Conference on Earthquake Engineering, Auckland, New Zealand

Shin, J., Kim, J., and Lee, K., 2014, "Seismic assessment of damaged piloti-type RC building subjected to successive earthquakes." *Earthquake Engineering and Structural Dynamics* 43: 1

Turcotte, D. L., Holliday, J. R., and Rundle, J. B., 2007, "BASS, an alternative to ETAS." *Geophysical Research Letters* 34

Vamvatsikos, D. and Cornell, C. A., 2002, "Incremental dynamic analysis." *Earthquake Engineering & Structural Dynamics* 31: 491-514

Zhai, C., Wen, W., Li, S., Chen, Z., Chang, Z., and Xie, L., 2014, "The damage investigation of inelastic SDOF structure under the mainshock-aftershcok sequence-type ground motions." *Soil Dynamics and Earthquake Engineering* 59: 30-41

A MULTI-HARMONIC BALANCE METHOD FOR DETERMINING STEADY STATE RESPONSE OF HYSTERESIS SYSTEMS ENDOWED WITH FRACTIONAL DERIVATIVES

Fan Kong[1], Zhaoxu Hou[1], Shujin Li[1]
[1]School of Civil Engineering and Architecture, Wuhan University of Technology, 122 LuoshiRoad, Wuhan 430070, Hubei, China

Abstract: A multi-harmonic balance method for steady-state response determination of a Bouc-Wen hysteretic dynamic system subject to harmonic excitation and endowed with fractional derivative element is developed in this paper. The problem may arise in, for example, a base isolated structure with lead-core rubber bearing subject to seismic excitations. Specifically, by relying on the spectral representation for the response and excitation, and utilizing the Galerkin approximation method, the equation of motion in the form of a differential equation endowed with fractional element is transferred into a set of algebraic equations. To solve the algebraic equations, the time/frequency domain alteration with the Fast Fourier Transform (FFT) is introduced to deal with the non-linear hysteresis term. An efficient Levenberg-Marquardt (LM) algorithm is used to seek the solution of the algebraic equations. The system steady-state response calculated by the proposed method are juxtaposed with that obtained by a time domain integration method. Pertinent numerical examples demonstrate the efficiency and the reliability of the proposed method.

Keywords: Multi-harmonic balance, hysteresis system, fractional derivative, Levenberg-Marquardt algorithm, frequency response curve

1 Introduction

Structural component of civil buildings under disastrous external loadings often exhibit nonlinear hysteretic behavior. In fact, this behavior has been often incorporated into certain structural/detail components deliberately to dissipate input earthquake energy and to avoid overall structural collapse. Besides, the hysteretic behavior is utilized in control devices that can be replaced easily after the disastrous ambient excitations, to mitigate the excessive response and to enhance the resilience of the structures. To capture reliably the quantitative features of the hysteretic phenomenon in civil engineering applications, several hysteretic models have been developed, such as the piecewise models (include bilinear model), Ramberg-Osgood model, Jenkins-Iwan model, and the differential models (Bouc-Wen model and its improved version). The preceding hysteretic models provide a force-displacement relationship that are not only depends on the instantaneous state, but also on its past history. A fully understanding on the dynamic behavior of the hysteretic system facilitate the implementation of the model in to engineering applications. In this context, a detailed study on the steady-state of the hysteretic systems subject to periodic harmonic excitation is not only necessary but also the most important to achieve this target. Therefore, several research efforts have been devoted to the steady-state response of the hysteretic system by using the analytical method, step-by-step integration method, equivalent linearization method, and the harmonic balance method; also see (Wong, Ni, and Ko 1994, Wong, Ni, and Lau 1994) for a detailed overview.

Some viscoelastic materials commonly used in engineering structures and control devices exhibit obvious rate/frequency dependent constitutive laws. For instance, the storage and loss modulus of the natural rubber usually depends on loading frequency and they cannot be captured accurately by the classic simple Kelvin and Maxwell model simultaneously(Di Paola, Pirrotta, and Valenza 2011). To fill this gap, combinations of Kelvin and Maxwell units, called Standard Linear

Solid (SLS) models, are often used to better capture the experimental data from the relaxation/creep test. An alternative choice is the fractional calculus. Recently, investigations (Di Paola, Pirrotta, and Valenza 2011, Sasso, Palmieri, and Amodio 2011) indicated that the fractional model uses much less parameters while maintains satisfactory accuracy in viscoelastic modeling compared to the SLS model. A pertinent application of the fractional derivative in mechanical and civil engineering application pertains to the modeling of dampers/isolators to mitigate excessive vibration(Di Matteo et al. 2015, Hwang and Wang 1998, Makris, Dargush, and Constantinou 1993, Xu, Xu, and Hu 2013). Researchers found that some dampers/isolators may not only exhibit a frequency-depended force-displacement relationship, which can be modeled conveniently with fractional elements, but also a nonlinear or even hysteretic behaviors. Therefore, considerable attention has been devoted to the response determination of linear/nonlinear system endowed with fractional element subject to stochastic/deterministic excitations. Specifically, deterministic response of single- or multi- degree-of-freedom (SDOF/MDOF) linear system endowed with fractional elements subject to deterministic excitation can be found by Fourier transform(Suarez and Shokooh 1995), Laplace transform(Bagley and Torvik 1985, Suarez and Shokooh 1995), an eigenvector expansion(Suarez and Shokooh 1997), and numerical methods(Shokooh and Suárez 2016, Singh, Chang, and Nandan 2011). For stochastic of linear systems, the response power spectral density can be determined by an extension of the classic random vibration theory of integer-order linear systems in the Frequency domain(Spanos and Zeldin 1997). Alternatively, in the time domain the response second moment can be determined by a double integral of the impulse response function (Agrawal 2001, Kun, Li, and Jiaxiang 2003). A method base on order-increase of the original system worth attention. This method, initially proposed for deterministic response of linear system with fractional element (Schmidt and Gaul 2006, Yuan and Agrawal 2002), was extended to treat stochastic linear (Di Paola, Failla, and Pirrotta 2012) and zero-memory nonlinear system (Failla and Pirrotta 2012). The steady-state response of a fractional nonlinear system subject to harmonic excitation remains an important area for studying fundamental dynamic behaviors of nonlinear systems. In this regard, investigations have been reported pertaining to the nonlinear systems with zero memory, such as the Duffing and Van der Pol oscillators, using averaging (Duan, Huang, and Liu 2015), linearization (Spanos and Evangelatos 2010), and harmonic balance method (Shen et al. 2016). Similarly, several other efficient methods for stochastic nonlinear system with integer order, such as stochastic averaging method (Huang and Jin 2009, Spanos, Di Matteo, and Pirrotta 2019), statistical linearization (Spanos and Evangelatos 2010), path integral, and so forth, were also extended to determining stochastic response of nonlinear systems endowed with fractional elements (Huang and Jin 2009, Spanos and Evangelatos 2010).

From the preceding literature review, one may know that the nonlinear dynamic behavior of a hysteretic system endowed with fractional elements has not been sufficiently studied yet. A very recent contribution on this aspect was made by Spanos and et al (Spanos, Di Matteo, and Pirrotta 2019). Specifically, an equivalent linearization approach was used to determine the frequency response curve of a general hysteretic system with different order of fractional derivatives. However, due to the limitations of linearization, this approximation method cannot capture the super-resonance of the nonlinear frequency response curve. Therefore, the present paper focus on the steady state response determination of a hysteretic system with fractional element using a multi-harmonic balance method. In particular, the equation of motion endowed with hysteretic model and fractional element is transferred into a least-squares problem, by the Galerkin projection of a time-varying residue on the harmonic basis. The objective function is then minimized by an efficient Levenberg-Marquardt (LM) algorithm to seek optimal unknown response

Fourier coefficient. The accuracy of the proposed frequency-domain method is validated by the time-domain step-by-step integration method. The effect of the fractional order on the hysteresis loop and the frequency response curve is investigated.

2 Mathematical Formulation

Consider a single-degree-of-freedom (SDOF) hysteresis system endowed with fractional elements, whose motion is governed by the differential equation

$$m\ddot{y}(t)+c_q\left({}_0^C D_t^q y\right)(t)+\alpha k y(t)+(1-\alpha)kz(t)=w(t), \tag{1}$$

where a dots over the symbol *y*denotes differentiation with respect to time; *m* and *k* is the mass, fractional damping and stiffness of the dynamic system; $y(t)$ is the system displacement; $z(t)$ is an arbitrarily chosen hysteresis restoring force that depends on the response history; α is a measure of the relative contribution of the hysteretic component $z(t)$; $\omega(t)$ is a sinusoidal excitation; $c_q=2\zeta_0 m\omega_n^{2-q}$ denotes the fractional damping coefficient. Further, $\left({}_0^C D_t^q y\right)(t)$ is an *q* order Caputo fractional derivative defined as

$$\left({}_0^C D_t^q y\right)(t)=\frac{1}{\Gamma(1-q)}\int_0^t \frac{\dot{y}(\tau)}{(t-\tau)^q}ds \tag{2}$$

where $\Gamma(\ )$ is the Gamma function; q is the fractional order.

The Fourier series allows one to expand the periodic excitation $w(t)$ and the response $x(t)$ and $z(t)$ with continuous time parameter in the form of linear combination of sinusoidal functions:

$$y(t)=C_0+\sum_{k=1}^{\infty}\left(C_k\cos\omega_k t+D_k\sin\omega_k t\right), \tag{3}$$

$$z(t)=U_0+\sum_{k=1}^{\infty}\left(U_k\cos\omega_k t+V_k\sin\omega_k t\right), \tag{4}$$

$$w(t)=A_0+\sum_{k=1}^{\infty}\left(A_k\cos\omega_k t+B_k\sin\omega_k t\right), \tag{5}$$

where $\omega_k=k\Delta\omega$ and $\Delta\omega=2\pi/T$ with $T=$ the fundamental period; C_0, U_0 and A_0 are the direct current term; $(C_k D_k)$, (U_k, V_k) and (A_k, B_k) are Fourier series coefficients of $y(t), z(t)$ and $w(t)$,respectively. Taking next Galerkin approximations of the Fourier series shown in Eq. (3) -(5)

$$y\approx C_0+\sum_{k=1}^{N}\left(C_k\cos\omega_k t+D_k\sin\omega_k t\right), \tag{6}$$

$$z\approx U_0+\sum_{k=1}^{N}\left(U_k\cos\omega_k t+V_k\sin\omega_k t\right), \tag{7}$$

$$f\approx A_0+\sum_{k=1}^{N}\left(A_k\cos\omega_k t+B_k\sin\omega_k t\right). \tag{8}$$

Note that the Galerkin approximation of the process equals to the continuous function at discrete time points with a minimum time step $\Delta t = \pi / \omega_\mu$, where ω_μ is the cutoff frequency. Considering the fractional derivative of the harmonic function, i.e.

$$ {}_0^C\mathrm{D}_0^q\left[\cos\omega_k t\right] = \omega_k^q \cos\left(\omega_k t + \frac{\pi}{2}q\right) \tag{9} $$

as well as the integer derivatives of the excitation/response, and substituting Eqs.(6) -(8) and (9) to the equation of motion shown in Eq. (1)leads to

$$ \begin{aligned} &m\sum_{k=1}^{N}\left(-C_k\omega_k^2\cos\omega_k t - D_k\omega_k^2\sin\omega_k t\right) + k\alpha\left[C_0 + \sum_{k=1}^{N}\left(C_k\cos\omega_k t + D_k\sin\omega_k t\right)\right] + \\ &c_q\left\{\frac{C_0}{\Gamma(1-q)t^q} + \sum_{k=1}^{N}C_k\omega_k^q\cos\left(\omega_k t + \frac{\pi}{2}q\right) + D_k\omega_k^q\sin\left(\omega_k t + \frac{\pi}{2}q\right)\right\} + (1-\alpha)k\left[U_0 + \sum_{k=1}^{N}\left(U_k\cos\omega_k t + V_k\sin\omega_k t\right)\right] \\ &= A_0 + \sum_{k=1}^{N}\left(A_k\cos\omega_k t + B_k\sin\omega_k t\right). \end{aligned} \tag{10} $$

Taking next multi-harmonic balance on both sides of Eq.(10), yields

$$ \left(-m\omega_k^2 + k\alpha + c_q\omega_k^q\cos\frac{\pi q}{2}\right)C_k + \omega_k^q c_q\sin\frac{\pi q}{2}D_k + F_k^c + (1-\alpha)kU_k = A_k, \tag{11} $$

$$ -c_q\omega_k^q\sin\frac{\pi q}{2}C_k + \left(-m\omega_k^2 + k\alpha + c_q\omega_k^q\cos\frac{\pi q}{2}\right)D_k + F_k^s + (1-\alpha)kV_k = B_k, \tag{12} $$

$$ k\alpha C_0 + (1-\alpha)kU_0 + F_0^c = A_0, \tag{13} $$

for $k = 1, 2, \cdots, N$, where

$$ F_k^c = \frac{c_q C_0}{\Gamma(1-q)}\frac{2}{T}\int_0^T\frac{1}{t^q}\cos\omega_k t\mathrm{d}t,\ F_k^s = \frac{c_q C_0}{\Gamma(1-q)}\frac{2}{T}\int_0^T\frac{1}{t^q}\sin\omega_k t\mathrm{d}t,\ F_0^c = \frac{c_q C_0}{\Gamma(1-q)}\frac{2}{T}\int_0^T\frac{1}{t^q}\mathrm{d}t. $$

Further manipulating on Eq. (11)-(12) yields an explicit expression between the Fourier coefficient of $z(t)$ and $x(t)$

$$ \frac{1}{k(\alpha-1)}\left(\mathbf{C}_{1,k}\begin{Bmatrix}C_k\\D_k\end{Bmatrix} - \begin{Bmatrix}A_k\\B_k\end{Bmatrix} + \begin{Bmatrix}F_k^c\\F_k^s\end{Bmatrix}\right) = \begin{Bmatrix}U_k\\V_k\end{Bmatrix}, \tag{14} $$

for $(k = 1, 2, \cdots, N)$, where

$$ \mathbf{C}_{1,k} = \begin{bmatrix} -m\omega_k^2 + k\alpha + c_q\omega_k^q\cos\frac{\pi q}{2} & c_q\omega_k^q\sin\frac{\pi q}{2} \\ -c_q\omega_k^q\sin\frac{\pi q}{2} & -m\omega_k^2 + k\alpha + c_q\omega_k^q\cos\frac{\pi q}{2} \end{bmatrix} \tag{15} $$

and the superscript 1 denote "linear". Eqs. (13)-(14) can be further cast into a compact form

$$ \frac{1}{k(\alpha-1)}\left(\mathbf{C}_1\mathbf{C} + \mathbf{F} - \mathbf{A}\right) = \mathbf{U}, \tag{16} $$

where

$$\mathbf{C}_1 = \begin{bmatrix} k\alpha & 0 & \cdots & 0 \\ 0 & \mathbf{C}_{1,1} & 0 & 0 \\ \vdots & \vdots & \ddots & \vdots \\ 0 & 0 & 0 & \mathbf{C}_{1,N} \end{bmatrix}$$

and the vectors are $\mathbf{A} = \left[A_0, A_1, B_1, \cdots A_N, B_N\right]^{\mathrm{T}}$, $\mathbf{C} = \left[C_0, C_1, D_1, \cdots, C_N, D_N\right]^{\mathrm{T}}$, $\mathbf{F} = \left[F_0^c, F_1^c, F_1^s, \cdots, F_N^c, F_N^s\right]^{\mathrm{T}}$, $\mathbf{U} = \left[U_0, U_1, V_1, \cdots, U_N, V_N\right]^{\mathrm{T}}$.

In Eq. (1)the hysteretic force $z(t)$ can be described by an auxiliary differential equation, i.e.,

$$\dot{z}(t) = z_0\left(\dot{y}, z, t\right) \tag{17}$$

that combined with the dynamic equation of motion, fully governs the hysteretic system. In this regard, writing

$$r(t) = \dot{z}(t) - z_0\left(\dot{y}, z, t\right) \tag{18}$$

as the residual time history, and applying the Fourier-Galerkin method again to Eq. (18)and considering (14)leads to

$$\mathbf{P}(\mathbf{C}) = 0 \tag{19}$$

where $\mathbf{P} = \left\{P_0, Q_0, P_1, Q_1, \cdots, P_N, Q_N\right\}^{\mathrm{T}}$ is a vector comprised of Fourier series coefficients of the residual $r(t)$ in terms of the displacement Fourier series $\mathbf{C}$. Previously, Eq. (19)may be treated by the established techniques for solving non-linear algebraic equations, taking Newton's method for instance. However, these techniques, are often quite sensitive to the initial values, leading a disconvergent solution. An efficient alternative procedure to obtain the solutions of Eq.(19) is to consider it as an equivalent least-squares problem

$$\min f(\mathbf{C}) = \left\|\mathbf{P}(\mathbf{C})\right\|^2 = \mathbf{P}^{\mathrm{T}}\mathbf{P} \tag{20}$$

In this regard, the Levenberg-Marquardt (LM) algorithm can be used to seek the least squares solution shown in Eq.(20). Compared to Newton's method, the LM algorithm can circumvent the difficulty caused by the singular Hessian matrices. The iteration solution of the LM algorithm can be written as

$$\mathbf{C}^{(k+1)} = \mathbf{C}^{(k)} - \left\{\mathbf{J}^T\left[\mathbf{C}^{(k)}\right]\mathbf{J}\left[\mathbf{C}^{(k)}\right] + \varphi^{(k)}\mathbf{I}\right\}^{-1}\mathbf{J}\left[\mathbf{C}^{(k)}\right]^T\mathbf{P}\left[\mathbf{C}^{(k)}\right] \tag{21}$$

where the superscript k in a parenthesis denote the k th iteration; $\mathbf{J}$ is the Jacobian's matrix expressed as

$$\mathbf{J}=\frac{\partial \mathbf{P}}{\partial \mathbf{C}}=\begin{bmatrix} \frac{\partial P_0}{\partial C_0} & \frac{\partial P_0}{\partial C_1} & \frac{\partial P_0}{\partial D_1} & \cdots & \frac{\partial P_0}{\partial D_N} \\ \frac{\partial P_1}{\partial C_0} & \frac{\partial P_1}{\partial C_1} & \frac{\partial P_1}{\partial D_1} & \cdots & \frac{\partial P_1}{\partial D_N} \\ \frac{\partial Q_1}{\partial C_0} & \frac{\partial Q_1}{\partial C_1} & \frac{\partial Q_1}{\partial D_1} & \cdots & \frac{\partial Q_1}{\partial D_N} \\ \vdots & \vdots & \vdots & \ddots & \vdots \\ \frac{\partial Q_N}{\partial C_0} & \frac{\partial Q_N}{\partial C_1} & \frac{\partial Q_N}{\partial D_1} & & \frac{\partial P_N}{\partial D_N} \end{bmatrix}; \tag{22}$$

ϕ is the Levenberg-Marquardt parameter; and $\mathbf{I}$ denotes an identity matrix. The entries in Jacobian's matrix shown in Eq. (22)can be obtained by the Fourier series of $\partial r(t)/\partial C_k, \partial r(t)/\partial D_k$ as

$$\frac{\partial r(t)}{\partial C_k}=\frac{\partial r(t)}{\partial \dot{y}}\frac{\partial \dot{y}}{\partial C_k}+\frac{\partial r(t)}{\partial z}\frac{\partial z}{\partial C_k}+\frac{\partial r(t)}{\partial \dot{z}}\frac{\partial \dot{z}}{\partial C_k} \tag{23}$$

$$\frac{\partial r(t)}{\partial D_k}=\frac{\partial r(t)}{\partial \dot{y}}\frac{\partial \dot{y}}{\partial D_k}+\frac{\partial r(t)}{\partial z}\frac{\partial z}{\partial D_k}+\frac{\partial r(t)}{\partial \dot{z}}\frac{\partial \dot{z}}{\partial D_k} \tag{24}$$

where

$$\frac{\partial \dot{y}}{\partial C_k}=-\omega_k \sin \omega_k t \tag{25}$$

$$\frac{\partial \dot{y}}{\partial D_k}=\omega_k \cos \omega_k t \tag{26}$$

$$\begin{bmatrix} \frac{\partial z}{\partial C_k} & \frac{\partial z}{\partial D_k} \\ \frac{\partial \dot{z}}{\partial C_k} & \frac{\partial \dot{z}}{\partial D_k} \end{bmatrix}=\begin{bmatrix} \cos \omega_k t & \sin \omega_k t \\ -\omega_k \sin \omega_k t & \omega_k \cos \omega_k t \end{bmatrix}\begin{bmatrix} \frac{\partial U_k}{\partial C_k} & \frac{\partial U_k}{\partial D_k} \\ \frac{\partial V_k}{\partial C_k} & \frac{\partial V_k}{\partial D_k} \end{bmatrix} \tag{27}$$

and according to Eq. (14)

$$\begin{bmatrix} \frac{\partial U_k}{\partial C_k} & \frac{\partial U_k}{\partial D_k} \\ \frac{\partial V_k}{\partial C_k} & \frac{\partial V_k}{\partial D_k} \end{bmatrix}=\frac{\mathbf{C}_{l,k}}{k(\alpha-1)} \tag{28}$$

Other partial derivatives in Eqs. (23)-(24) depend on the hysteretic model adopted in Eq.(17). For instance, consider herein a Bouc-Wen hysteretic model

$$\dot{z}=\dot{y}\left[A-|z|^n\left(\gamma \operatorname{sgn}(\dot{y})\operatorname{sgn}(z)+\beta\right)\right], \tag{29}$$

where A, β, γ and n are loop parameters that control the shape and magnitude of the hysteresis

loop. These parameters can be adjusted to capture a wide range of hysteresis loops, including softening, hardening and quasi-linear behaviors. Usually, A, γ and n are positive real numbers and β may be a positive or negative real number. In this regard

$$\frac{\partial r}{\partial \dot{z}} = 1 \tag{30}$$

$$\frac{\partial r}{\partial z} = \dot{y}\left|z\right|^{n-1}\left(\gamma \mathrm{sgn}\left(\dot{y}\right) + \beta \mathrm{sgn}\left(z\right)\right) \tag{31}$$

$$\frac{\partial r}{\partial \dot{y}} = -A + \left|z\right|^{n-1} z\left(\gamma \mathrm{sgn}\left(\dot{y}\right) + \beta \mathrm{sgn}\left(z\right)\right) \tag{32}$$

3Numerical examples

Consider a Bouc-Wen hysteric dynamic system endowed with fractional derivative. First, investigate a hysteric dynamic system with softening Bouc-Wen model subject to a sinusoidal excitation. The system parameters are $m = 1, \zeta_0 = 0.1, \omega_n = 1, \gamma = 0.5, \beta = 0.5, n = 1, A = 1, \alpha = 0.1, q = 0.5$, $w(t) = w_0 \sin(\omega t)$ and the sinusoidal excitation parameters are $w_0 = 1$ and $\omega = 1$. Figs.1(a) - Fig.1(b) shows the time histories of the system responses ($y(t)$ and $z(t)$) calculated by the Liemann-Liouville-Newmark (LLN) algorithm in the time domain and the proposed multi-harmonic balance method (MHB) in the frequency domain. Fig. 1(c) further shows the softening hysteresis loops calculated by the two methods in this situation. It seems that all the results obtained by the time history obtained by the LLN method agree well with that obtained by the proposed MHB method, except at the beginning of the time history. This discrepancy is because the frequency-domain method ignores of the initial conditions; in addition, the MHB only obtains the stationary solution of the considered system, while the time-domain method one can consider the instantaneous solution at the beginning of the response induced by the initial conditions.

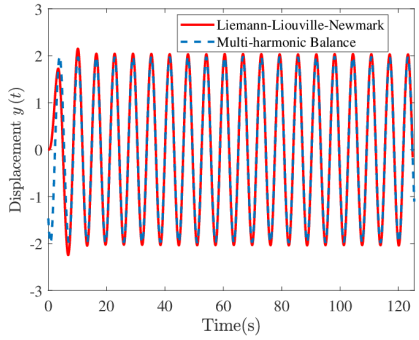

(a)

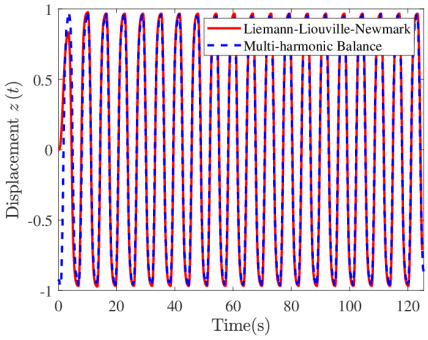

(b)

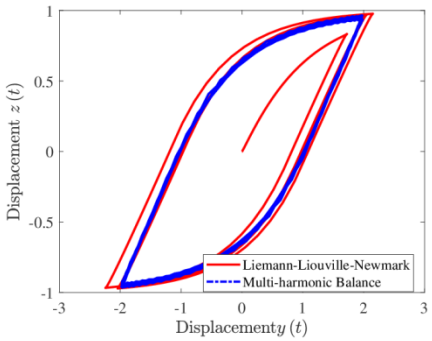

(c)

Fig. 1 Comparison between the Liemann-Liouville-Newmark algorithm and the multi-harmonic balance method in terms of (a) displacement $y(t)$, (b) hysteretic displacement $z(t)$ and (c) hystersis loop

To investigate the effect of fractional orders on the shape/size of the response amplitude and hysteresis loop, consider the system in the last case with the same parameters but with different fractional orders. Fig. 3 show the curves of fractional order q versus the displacement $y(t)$ or $z(t)$ amplitude of the systems with fractional orders $q = 0, 0.2, 0.4, 0.6, 0.8, 1$. It seems that the displacement $y(t)$ decrease significantly, whereas $z(t)$ decreases slightly and remains almost the same with increasing fractional order. Besides, results obtained by the proposed method agrees well with those obtained by the LLN algorithm. Fig. 4 shows different hysteresis loops calculated by the proposed MHB method. One may conclude that the loop becomes smaller while the shape remains the same with increasing fractional order in the present case.

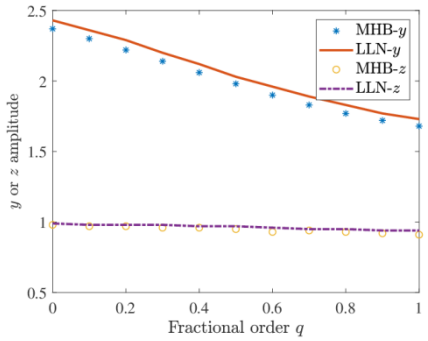

Fig.2 Fractional order versus displacement amplitude

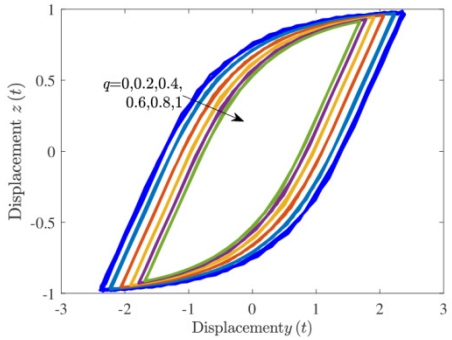

Fig. 3 Hysteretic loop of the softening Bouc-Wen system endowed with different fractional orders

The four-parameter Bouc-Wen model may exhibit different hysteresis loop with different parameters. Various studies, for instance (Ismail, Ikhouane, and Rodellar 2009) and (Wong, Ni, and Ko 1994), suggeste d that the model reduce to a strain-softening formulation when $\beta+\gamma>0$, and to a strain-hardening one when $\beta+\gamma<0$. The hysteretic system may also behavesquasilinearly when $\gamma+\beta=0$. Therefore, Fig. 2 shows the a typical softening hysteresis loop and Fig. 3 shows the size of the loops decreases with increasing fractional orders, when the Bouc-Wen model exihibit softening behavior and the excitation frequency ω is larger than the

resonant frequency. However, this tendency is not the case when the model has a stiffening behavior. Fig. 4 shows the curves of q versus displacement y or z of a hardening Bouc-Wen model with $\gamma = 0.35$ and $\beta = -0.65$. This figure suggest that the hysteretic displacement $z(t)$ increases with increasing fractional order q, whereas the displacement $y(t)$ only increases slightly in the hardening case when the excitation frequency is larger than the resonant frequency. Fig. 5 further shows the loop size of the system with different fractional orders. Contrary to the case of softening case, the loop size remains almost the same in this case. This situation can be clarified in the following frequency-amplitude analysis. In fact, the relationship between the response amplitude and the fractional order q not only depends on the Bouc-Wen model parameters, but also the excitation frequencies.

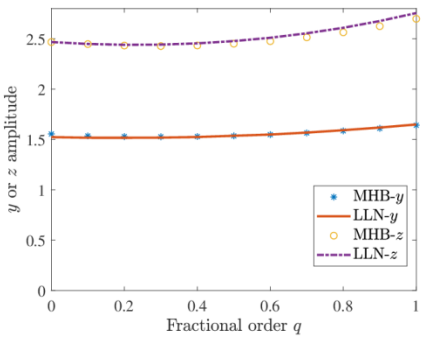

Fig. 4 Fractional order versus displacement amplitude for a hysteretic dynamic system with hardening Bouc-Wen model

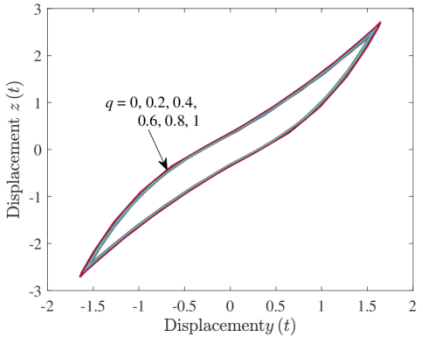

Fig. 5 Hysteretic loop of the hardening Bouc-Wen system endowed with different fractional orders

To make this argument clear, Fig. 6 and Fig. 7 shows the relationship between the excitation frequency and the response amplitude relationship of the softening and hardening Bouc-Wen dynamic system, respectively. Fractional derivative with different factional orders $q = 0.2, 0.4, 0.6$ is presented. It can be concluded that the proposed method captures the super- and the primary- harmonic component of the response with promising accuracy. From Fig. 6 one can conclude that the response amplitude decreases with increasing fractional order when the excitation frequency is larger than the primary resonant frequency; Besides, the response amplitude increase with increasing fractional order when the excitation frequency is smaller than the excitation resonant frequency, A similar conclusion can be draw from the hardening Bouc-Wen case.

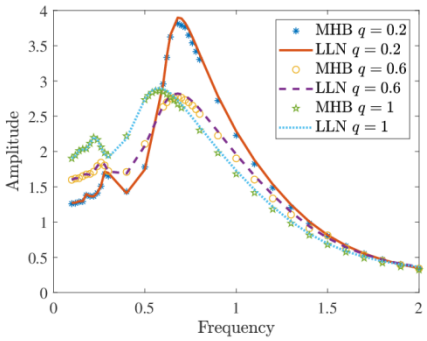

Fig. 6 Steady state response amplitude of a hysteretic system with softening Bouc-Wen model

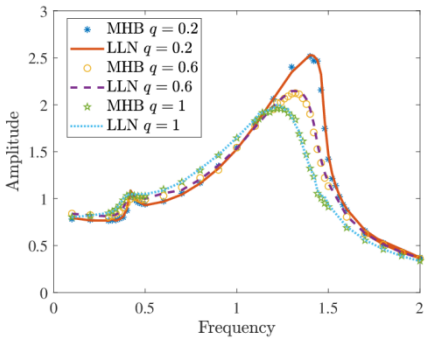

Fig. 7 Steady state response amplitude of a hysteretic system with hardening Bouc-Wen model

4 Concluding Remarks

The steady state dynamic response of a Bouc-Wen hysteretic system endowed with fractional element subject to sinusoidal excitation has been considered in this paper. It has been achieved by a multi-harmonic balance method for determining coefficients of response Fourier series. Specifically, the nonlinear hysteretic differential equation of motion has been transferred into a set of nonlinear algebraic equations. These algebraic equations have been solved by the efficient Levenberg-Marquardt method to obtain the response Fourier series. To validate the proposed frequency domain method, a time-domain integration method has been developed based on discretizing the integral in Liemann-Liouville definition of fractional derivative, the Newmark-β treatment of integer-order derivatives, and the Newton-Raphson iteration of the hysteretic term. The proposed frequency domain method has been found in good agreement with the developed time-domain method in term of stationary time history response, as well as primary- and super-harmonics in the frequency-amplitude curve. Depended on the relative values of the excitation and the resonant frequency, it has been found that the response amplitude has positive/inverse correlation with the fractional order. Clearly, the proposed method has great advantages over the time-domain step-by-step integration method on computational efficiency, numerical stabilities and determining multi-value frequency response curve. The applicability of the methods presented herein, which have been kept at a limited depth, could be implemented by a suite of convenient parameter studies and by considering other versatile hysteretic models.

5 References

Agrawal O. P. "Stochastic analysis of dynamic systems containing fractional derivatives." *Journal of Sound and Vibration* 247 (5) (2001):927-938.

Bagley R. L., and Torvik P. J. "Fractional calculus in the transient analysis of viscoelastically damped structures." *AIAA Journal* 23 (6) (1985):918-925.

Di Matteo A., et al. "Innovative modeling of Tuned Liquid Column Damper motion." *Communications in Nonlinear Science and Numerical Simulation* 23 (1) (2015):229-244.

Di Paola M., et al. "Visco-elastic behavior through fractional calculus: An easier method for best fitting experimental results." *Mechanics of Materials* 43 (12) (2011):799-806.

Di Paola M., et al. "Stationary and non-stationary stochastic response of linear fractional

viscoelastic systems." *Probabilistic Engineering Mechanics* 28 (2012):85-90.

Duan J. S., et al. "Response of a fractional nonlinear system to harmonic excitation by the averaging method." *Open Physics* 13 (1) (2015):177-182.

Failla G., and Pirrotta A. "On the stochastic response of a fractionally-damped Duffing oscillator." *Communications in Nonlinear Science and Numerical Simulation* 17 (12) (2012):5131-5142.

Huang Z. L., and Jin X. L. "Response and stability of a SDOF strongly nonlinear stochastic system with light damping modeled by a fractional derivative." *Journal of Sound and Vibration* 319 (3-5) (2009):1121-1135.

Hwang J. S., and Wang J. C. "Seismic response prediction of HDR bearings using fractional derivative Maxwell model." *Engineering Structures* 20 (9) (1998):849-856.

Ismail M., et al. "The Hysteresis Bouc-Wen Model, a Survey." *Archives of Computational Methods in Engineering* 16 (2) (2009):161-188.

Kun Y., et al. "Stochastic seismic response of structures with added viscoelastic dampers modeled by fractional derivative." *Earthquake Engineering and Engineering Vibration* 2 (1) (2003):133-139.

Makris N., et al. "Dynamic Analysis of Generalized Viscoelastic Fluids." *Journal of Engineering Mechanics* 119 (8) (1993):1663-1679.

Sasso M., et al. "Application of fractional derivative models in linear viscoelastic problems." *Mechanics of Time-Dependent Materials* 15 (4) (2011):367-387.

Schmidt A., and Gaul L. "On a critique of a numerical scheme for the calculation of fractionally damped dynamical systems." *Mechanics Research Communications* 33 (1) (2006):99-107.

Shen Y.-J., et al. "Dynamical analysis of fractional-order nonlinear oscillator by incremental harmonic balance method." *Nonlinear Dynamics* 85 (3) (2016):1457-1467.

Shokooh A., and Suárez L. "A Comparison of Numerical Methods Applied to a Fractional Model of Damping Materials." *Journal of Vibration and Control* 5 (3) (2016):331-354.

Singh M. P., et al. "Algorithms for seismic analysis of MDOF systems with fractional derivatives." *Engineering Structures* 33 (8) (2011):2371-2381.

Spanos P. D., and Zeldin B. A. "Random Vibration of Systems with Frequency-Dependent Parameters or Fractional Derivatives." *Journal of Engineering Mechanics* 123 (3) (1997):290-292.

Spanos P. D., and Evangelatos G. I. "Response of a non-linear system with restoring forces governed by fractional derivatives—Time domain simulation and statistical linearization solution." *Soil Dynamics and Earthquake Engineering* 30 (9) (2010):811-821.

Spanos P. D., et al. "Steady-state dynamic response of various hysteretic systems endowed with fractional derivative elements." *Nonlinear Dynamics* (2019).

Suarez L., and Shokooh A. "Response of Systems With Damping Materials Modeled Using Fractional Calculus." *Applied Mechanics Reviews* 48 (11S) (1995):S118-S126.

Suarez L. E., and Shokooh A. "An Eigenvector Expansion Method for the Solution of Motion Containing Fractional Derivatives." *Journal of Applied Mechanics* 64 (3) (1997):629-635.

Wong C. W., et al. "Steady-State Oscillation of Hysteretic Differential Model. II: Performance Analysis." *Journal of Engineering Mechanics* 120 (11) (1994):2299-2325.

Wong C. W., et al. "Steady-State Oscillation of Hysteretic Differential Model. I: Response Analysis." *Journal of Engineering Mechanics* 120 (11) (1994):2271-2298.

Xu Z. D., et al. "Equivalent fractional Kelvin model and experimental study on viscoelastic damper." *Journal of Vibration and Control* 21 (13) (2013):2536-2552.

Yuan L. X., and Agrawal O. P. "A numerical scheme for dynamic systems containing fractional derivatives." *Journal of Vibration and Acoustics-Transactions of the Asme* 124 (2) (2002):321-324.

A NEW SUPERVISED DIMENSION REDUCTION METHOD FOR HIGH-DIMENSIONAL RELIABILITY PROBLEMS

Zhongming Jiang[1]
[1]College of Engineering and Technology, Southwest University, Chongqing, Chian
E-mail: jiangzm@swu.edu.cn

Abstract: In stochastic dynamic response analysis, high dimensional uncertainty is hard to deal with because "the curse of dimension" will make most surrogate model meth-od and sample method impracticable. Dimension reduction is a newly and promis-ing technology, it can be used in many engineering problems with high dimension issue. In this article, a novel reliability analysis methodology based on a supervised dimension reduction method named "ASK" is introduced to solve high-dimensional reliability problem. This method aims at finding a subspace whose dimensionality is lower than the original input space. In this subspace, the variability of the quantity of interest can be best estimated through doing eigenvalue decomposition to the gradients matrix. By projecting the former high dimensional input to a set of new coordinates, a low dimensional kriging metamodel can be established with an observable improvement of the accuracy and simplicity. Then, we can use PDEM-based method or MCS to perform the system reliability analysis. The result shows that the new method is effective and reliable especially when the dimension of the random variable is high.

Keywords: High-dimension, reliability analysis, dimension reduction, metamodel, PDEM

1 Introduction

Stochastic structure analysis continues getting more attention in the academy and engineering field because the existence of randomness in both external excitation and structural properties is widely recognized by scientists and engineers. In the practical engineering, the randomness in stochastic analysis includes external loads, material properties, member sizes and construction procedures. It naturally lead the uncertainty quantification problem(Chowdhury, Rao, and Prasad 2009) in structure dynamics to be high-dimensional.

There are a crowd of approaches have been developed, such as the Monte Carlo Simulation method(Schuëller, Pradlwarter, and Koutsourelakis 2004) , the random perturbation method(Kleiber and Hien 1992), the orthogonal polynomial expansion method(Ghanem and Spanos 1990) and a family of Probability Density Evolution Method (PDEM)(Li and Chen 2009), etc. However, the cost of performing a reliable reliability analysis increases rapidly as the dimensionality of the randomness increase. By using the probability conservation principle with a new strategy of point selection, the Probability Density Evolution Method (PDEM) established a new method to reach the balance between computational efficiency and accuracy. One way to reduce the computational requirement is employing computationally inexpensive metamodel (e.g., Neural Network(Papadrakakis, Papadopoulos, and Lagaros 1996), Support Vector Machines(Bourinet, Deheeger, and Lemaire 2011), Kriging to substitute the authentic function of quantity of interest (QOI). However, most metamodel method are haunted by "curse of dimensionality" problem where the consumption of building a reliable metamodel rise sharply. Besides, the practicability of metamodel fall off under high-dimensional circumstance because the redundant complexity in high-dimensional metamodel can bring extra modeling error(Vitali 2000).

An new supervised dimension reduction method called Active Subspace(Constantine 2015) is introduced in this research. This method aims at finding a subspace whose dimensionality is lower than the original input space. In this subspace, the variability of the quantity of interest can be best estimated through doing eigenvalue decomposition to the gradients matrix. By projecting the former high dimensional input to a set of new coordinates, a low dimensional kriging metamodel can be established with an observable improvement of the accuracy and simplicity. Then, we can use PDEM-based method or MCS to perform the system reliability analysis.

2 Active subspace combine kriging method

2.1 Active subspace method

Considering a multivariable function with m continuous inputs,

$$h = h(\mathbf{x}),\ \mathbf{x} \in \chi = [-1,1]^m = \mathbb{R}^m \tag{1}$$

with a bounded and continuous probability density function $f : \chi \to \mathbb{R}_+$,where

$$f(\mathbf{x}) > 0,\ \mathbf{x} \in \chi \quad \text{and} \quad f(\mathbf{x}) = 0,\ \mathbf{x} \notin \chi \tag{2}$$

Assume h is a continuous and differentiable function. So that we can get the gradient of h ,

$$\nabla_{\mathbf{x}} h(\mathbf{x}) = \left[\frac{\partial h}{\partial x_1}, \cdots, \frac{\partial h}{\partial x_m} \right]^T \tag{3}$$

Then, a $m \times m$ matrix $\mathbf{G}$ can be subsequently deduced as

$$\mathbf{G} = \int_{\chi} (\nabla_{\mathbf{x}} h)(\nabla_{\mathbf{x}} h)^T f \, \mathrm{d}\mathbf{x} \tag{4}$$

which represents the uncentered covariance of the gradient vector. As $\mathbf{G}$ is a symmetric and positive semidefinite matrix, it admits real eigenvalue decomposition

$$\mathbf{G} = \mathbf{W}\boldsymbol{\Lambda}\mathbf{W}^T, \quad \boldsymbol{\Lambda} = \mathrm{diag}(\lambda_1, ..., \lambda_m), \quad \lambda_1 \geq \cdots \geq \lambda_m \geq 0 \tag{5}$$

Partitioning the eigenvalues and eigenvectors,

$$\boldsymbol{\Lambda} = \begin{bmatrix} \boldsymbol{\Lambda}_1 & \\ & \boldsymbol{\Lambda}_2 \end{bmatrix}, \qquad \mathbf{W} = \begin{bmatrix} \mathbf{W}_1 & \mathbf{W}_2 \end{bmatrix} \tag{6}$$

where $\boldsymbol{\Lambda}_1 = \mathrm{diag}(\lambda_1, ..., \lambda_n)$ is the first (and largest) *n* eigenvalues, $\mathbf{W}_1$ contains the first *n* eigenvectors. Then a new sets of subspace are defined as,

$$\mathbf{y} = \mathbf{W}_1^T \mathbf{x} \ \textit{and} \ \ \mathbf{y} \in \mathbb{R}^n, \quad \mathbf{z} = \mathbf{W}_2^T \mathbf{x} \ \textit{and} \ \ \mathbf{z} \in \mathbb{R}^{m-n} \tag{7}$$

Subspace defined by $\mathbf{W}_1$ is so-called *active subspace*, the variables $\mathbf{y}$ is active variables. In 2010, Russi first used this presentation in his Phd dissertation(Russi 2010).

Compare to the changes caused by the perturbation along the direction $\mathbf{W}_1$, the changes caused by the perturbation with the directions $\mathbf{W}_2$ is sometimes negligible. Whether or not it is negligible depend on how much the eigenvalues in $\boldsymbol{\Lambda}_2$ is relatively smaller than the eigenvalues

in $\mathbf{\Lambda}_1$. When an eigenvalue is negligible, then the corresponding eigenvector implies the existence of a direction from which $h(\mathbf{x})$ looks virtually flat. In words, the magnitude of the eigenvalues define how averagely h changes in response to perturbations of $\mathbf{x}$ with the corresponding eigenvector directions. When there is a large decline between λ_n and λ_{n+1}, then $h(\mathbf{x})$ can be reasonably approximated as a low-dimensional function.

$$h(\mathbf{x}) \approx q(\mathbf{W}_1^T \mathbf{x}) \tag{8}$$

2.2 ASK implementation

2.2.1 Kriging method

As a stochastic approach, kriging method (or Gaussian process approximation) has been intensively investigated(Kaymaz 2005). One of the biggest advantage of kriging method is it not only give the predicted values, but also give the variance of the predict model itself. Because of its robustness and veracity, kriging method was widely used for structural reliability analysis. The numerical Matlab toolbox ooDACE(Lophaven, Nielsen, and Søndergaard 2002) is employed in this work because of its robustness and efficiency.

In the Kriging method, assume the observation of the quantity of interest can be describes as a sum of trend function and a Gaussian process

$$q(\mathbf{x}) = \mathrm{r}(\mathbf{x}) + \mathrm{U}(\mathbf{x}) \tag{9}$$

where $\mathrm{r}(\mathbf{x})$ is a trend function, $\mathrm{U}(\mathbf{x})$ is a zero-mean stationary Gaussian process with variance σ^2. According to different kind of kriging methods, the regression function has different form. In universal kriging, the regression function is defined as

$$\mathrm{r}(\mathbf{x}) = \sum_{i=1}^{p} \alpha_i b_i(\mathrm{x}) \tag{10}$$

in which $b_i(\mathrm{x})$ are $i = 1 \ldots p$ basis functions and α_i is the coefficients. Consider a set of training samples $X = \{\mathbf{x}^1, \ldots, \mathbf{x}^n\}$ in *d* dimension and associated function values $\mathbf{y} = \{y^1, \ldots, y^n\}$. Then, the trend part can be set as $n \times p$ matrix F

$$\boldsymbol{B} = \begin{bmatrix} b_1(\mathbf{x}^1) & \cdots & b_p(\mathbf{x}^1) \\ \vdots & \ddots & \vdots \\ b_1(\mathbf{x}^n) & \cdots & b_p(\mathbf{x}^n) \end{bmatrix} \tag{11}$$

Correspondingly, the stochastic part U is defined by the $n \times n$ correlation matrix\

$$\mathbf{\Phi} = \begin{bmatrix} \phi(\mathbf{x}^1, \mathbf{x}^1) & \cdots & \phi(\mathbf{x}^1, \mathbf{x}^n) \\ \vdots & \ddots & \vdots \\ \phi(\mathbf{x}^n, \mathbf{x}^1) & \cdots & \phi(\mathbf{x}^n, \mathbf{x}^n) \end{bmatrix} \tag{12}$$

where $\phi(\cdot,\cdot)$ is the correlation function. A popular class of stationary correlation functions is defined as

$$\phi(\mathbf{x},\mathbf{x}') = \exp\left(-\sum_{i=1}^{d}\theta_i\left|x_i - x_i'\right|^p\right) \tag{13}$$

Subsequently, the prediction mean and prediction variance of kriging model are derived respectively,

$$u(\mathbf{x}) = \boldsymbol{B}_0\boldsymbol{\alpha} + \boldsymbol{\Phi}_0\boldsymbol{\Phi}^{-1}\cdot(\mathrm{q} - \boldsymbol{B}\boldsymbol{\alpha}) \tag{14}$$

$$s^2(\mathbf{x}) = \sigma^2(1 - \boldsymbol{\Phi}_0\boldsymbol{\Phi}^{-1}\boldsymbol{\Phi}_0^T + \frac{(1 - \boldsymbol{B}^T\boldsymbol{\Phi}^{-1}\boldsymbol{\Phi}_0^T)}{\boldsymbol{B}^T\boldsymbol{\Phi}^{-1}\boldsymbol{B}}) \tag{15}$$

where $\boldsymbol{B}_0 = \left[b_1(\mathbf{x}_0)\ \ b_2(\mathbf{x}_0)\ \cdots\ b_p(\mathbf{x}_0)\right]$ is the model matrix of the testing point $\mathbf{x}$, $\boldsymbol{\alpha} = (\boldsymbol{B}^T\boldsymbol{\Phi}^{-1}\boldsymbol{B})^{-1}\boldsymbol{B}^T\boldsymbol{\Phi}^T\mathbf{q}$ is a $p\times 1$ vector denoting the coefficients of the regression function, and $\boldsymbol{\Phi}_0 = \left[\phi(\mathbf{x},\mathbf{x}^1)\ \cdots\phi(\mathbf{x},\mathbf{x}^n)\right]$ is an $1\times n$ vector of correlations between point $\mathbf{x}$ and the training samples X. The variance σ^2 is given by $\frac{1}{n}(\mathrm{q} - \boldsymbol{B}\boldsymbol{\alpha})^T\boldsymbol{\Phi}^{-1}(\mathrm{q} - \boldsymbol{B}\boldsymbol{\alpha})$.

2.2.2 Probability Density Evolution Method

A muti-degree-of-freedom (MDOF) structure is presented here as a common example

$$\mathbf{M}(\boldsymbol{\Theta})\ddot{\mathbf{Y}} + \mathbf{C}(\boldsymbol{\Theta})\dot{\mathbf{Y}} + \mathbf{f}(\boldsymbol{\Theta},\mathbf{Y}) = \boldsymbol{\Gamma}\mathbf{G}(\boldsymbol{\Theta},t) \tag{16}$$

where $\boldsymbol{\Theta}$ is the high dimensional randomness in which involved the physical properties of structure and external load. $\mathbf{Y}$, $\dot{\mathbf{Y}}$ and $\ddot{\mathbf{Y}}$ are the displacement, velocity and acceleration response of structure, respectively. $\mathbf{M}$ and $\mathbf{C}$ are the matrixes of mass and damping, $\mathbf{f}$ is the structural restoring force, $\mathbf{G}(\boldsymbol{\Theta},t)$ is the loading vector and $\boldsymbol{\Gamma}$ is the loading influence matrix.

In well-posed dynamical system, the solution of Eq. (16) exists uniquely as a function of $\boldsymbol{\Theta}$. Subsequently, the quantity of interest such as strain or deformation at a certain position usually can be determined by the solution of Eq. (16). Then we can make reasonable inferences that the quantity of interest is also a vector of function of $\boldsymbol{\Theta}$

$$\mathbf{Z} = \mathbf{H}(\boldsymbol{\Theta},t),\ \dot{\mathbf{Z}}(t) = \mathbf{h}(\boldsymbol{\Theta},t) \tag{17}$$

where $\mathbf{H} = \left(H_1, H_2, \cdots, H_m\right)^{\mathrm{T}}$, $\mathbf{h} = \left(h_1, h_2, \cdots, h_m\right)^{\mathrm{T}}$, *m* is the number of quantities of interest.

According to the principle of probability conservation(Li and Chen 2009), all the uncertainties involved in the system are contained in the $\boldsymbol{\Theta}$. Therefore, the generalized evolution equation (GDEE) is deduced:

$$\frac{\partial p_{\mathbf{Z}\boldsymbol{\Theta}}(\mathbf{z},\boldsymbol{\theta},t)}{\partial t} + \sum_{j=1}^{m}\dot{Z}_j(\boldsymbol{\theta},t)\frac{\partial p_{\mathbf{Z}\boldsymbol{\Theta}}(\mathbf{z},\boldsymbol{\theta},t)}{\partial z_j} = 0 \tag{18}$$

where $p_{\mathbf{Z}\boldsymbol{\Theta}}(\mathbf{z},\boldsymbol{\theta},t)$ is the joint probability density function (PDF) of $(\mathbf{Z}(t),\boldsymbol{\Theta})$. The corresponding boundary condition for Eq. (18) is

$$p_{\mathbf{Z}\boldsymbol{\Theta}}(\mathbf{z},\boldsymbol{\theta},t)\big|_{t=t_0} = \delta(\mathbf{z} - \mathbf{z}_0)\,p_{\boldsymbol{\Theta}}(\boldsymbol{\theta}) \tag{19}$$

where $\mathbf{z}_0$ is the deterministic initial value, $\delta(\cdot)$ is the Dirac's delta function. By adopting Finite Difference Method (FDM) and representative point method, we can numerically solve Eq. (18) and (19).

For reliability analysis, the first-passage dynamic reliability with single failure criteria is defined as

$$R = \Pr\left\{ Z(\boldsymbol{\Theta}, t) \in \Omega_s,\ \forall t \in [0, T] \right\} \tag{20}$$

in which Ω_s is the safe domain, $[0, T]$ is the duration of time. When there is a boundary condition, Eq. (20) can be rewritten as

$$R = \Pr\left\{ \left| Z(\boldsymbol{\Theta}, t) \right| < z_b,\ \forall t \in [0, T] \right\} \tag{21}$$

Subsequently, the reliability problem in Eq. (21) is transformed to

$$R = \Pr\left\{ W_{\max} < z_b \right\} = \int_{-\infty}^{z_b} p_{W_{\max}}(w) \mathrm{d}w \tag{22}$$

where $p_{W_{ext}}(w)$ is the equivalent extreme value distribution.

2.2.3 ASK implementation

This section summarizes the implementation of the ASK method. The general procedures of the introduced method are illustrated as following:

(i) Select the representative points $\mathbf{x}_i^m,\ i = 1, 2, ..., N_{sel}$ of the *m* dimensional random variable. Perform the simulations to obtain the quantity of interest $\mathbf{Z}(\mathbf{x}_i, t)$ (or $\mathbf{Z}(\mathbf{x}_i)$) and the corresponding equivalent extreme value $W_{\max}(\mathbf{x}_i) = \max_{t \in [0,T]} \left(\left| Z(\mathbf{x}_i, t) \right| \right)$;

(ii) Approximate the gradients $\nabla_{\mathbf{x}} Z(\mathbf{x}) = \left[\frac{\partial Z}{\partial x_1}, \cdots, \frac{\partial Z}{\partial x_m} \right]^T$, compute the matrix $\mathbf{G} = \frac{1}{N_{sel}} \sum_{i=1}^{N_{sel}} \nabla_{\mathrm{x}} Z(x_i) \nabla_{\mathrm{x}} Z(x_i)^T$ and perform eigenvalue decomposition to achieve $\mathbf{W}_1$ in Eq. (6);

(iii) Implement $\mathbf{y} = \mathbf{W}_1^T \mathbf{x},\ \mathbf{y} \in \mathbb{R}^n, \mathbf{x} \in \mathbb{R}^m$ in Eq. (7) to get low dimensional data set $\left(\mathbf{y}_i, W_{\max,\mathrm{i}} \right),\ i = 1, 2, ..., N_{sel}$, then train a kriging metamodel $\tilde{q} = \tilde{q}(\mathbf{y})$ on the dimension-reduced data set;

(iv) Select a new set of enriched representative points $\boldsymbol{\theta}_j^m,\ j = 1, 2, ..., N_{enrich}$ and similarly implement the dimension reduction procedure $\boldsymbol{\beta} = \mathbf{W}_1^T \boldsymbol{\theta},\ \boldsymbol{\beta} \in \mathbb{R}^n, \boldsymbol{\theta} \in \mathbb{R}^m$ on the points. The transformed low dimensional data $\left(\boldsymbol{\beta}_j, \tilde{W}_{\max,\mathrm{j}} \right),\ j = 1, 2, ..., N_{enrich}$ are estimated by the trained kriging metamodel;

(v) Employ PDEM, the desired PDF of equivalent extreme value and the corresponding reliability can be determined consequently.

2.2.4 Numerical example

In this example, a theoretical serial system(Vitali 2000, Schueremans and Van Gemert 2005) is

first studied for verification. The two dimensional random variable $\boldsymbol{x}$ is uniformly distributed on $[-1,1]^2$. The extreme value reliability is defined as

$$R = \Pr\{G(x_1, x_2) > 0\} \tag{23}$$

where

$$G(x_1, x_2) = \min\left\{\begin{array}{c} 0.2 + 0.6(x_1 - x_2)^4 - \dfrac{(x_1 - x_2)}{\sqrt{2}}; \\ 0.2 + 0.6(x_1 - x_2)^4 + \dfrac{(x_1 - x_2)}{\sqrt{2}}; \\ (x_1 - x_2) + \dfrac{5}{\sqrt{2}} - 2.2; (x_2 - x_1) + \dfrac{5}{\sqrt{2}} - 2.2 \end{array}\right\} \tag{24}$$

3D-plot of the function is shown in Figure. 1.

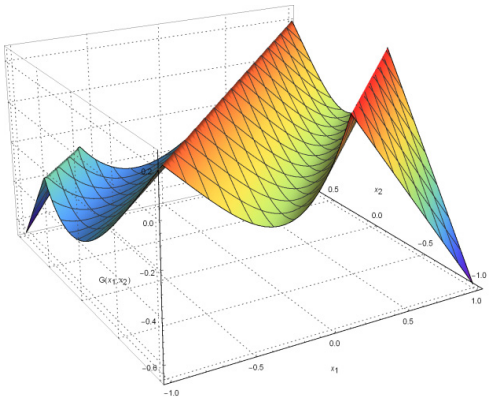

Figure 1: The 3D plot of the function

The number of calls to the function $G(x_1, x_2)$ is 50 for reliability calculation, extra 10000 simulations is used for Monte Carlo Simulation whose result can be treated as a benchmark and 200 simulations are performed to test the quality of metamodel with the histogram of the log of relative error.

50 samples are used to approximate the gradient vector $\nabla_x G$, and a eigenvalue decomposition is performed to achieve the active subspace mapping matrix $\mathbf{W}_1$. Then, a one-dimensional kriging metamodel is built on the dimension reduced 50 samples as presented in Figure .2.

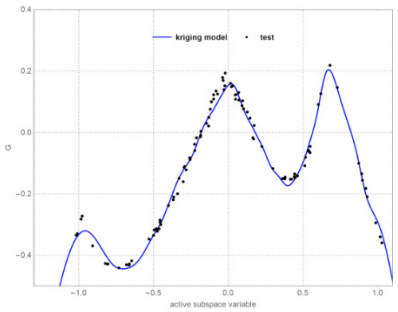

(a) ASK

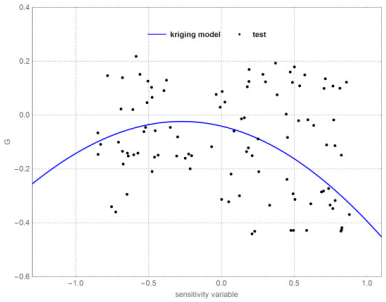

(b) Sensitivity analysis

Figure 2: The plot of the dimension reduced function

The blue line is the kriging prediction and the black dots are the 200 test sample calculated by the original $G(x_1, x_2)$. The low-dimensional data in Figure.2(a) shows a more structured deployment which means the ASK method uncovered the essential one dimensional structure form the high-dimensional appearance. The variance-based sensitivity indices computed by ANOVA decomposition(Pianosi, Sarrazin, and Wagener 2015) are $V_{x_1} = 0.2059$ and $V_{x_2} = 0.5800$, which yields a conclusion that the influence of x_2 is more significant than x_1.

The Figure. 2(b) shows that the global sensitivity analysis cannot reveal the intrinsic low-dimensional structure of the function, therefore the predictive ability of the corresponding kriging metamodel is questionable. Figure.4 is the histograms of logarithm error between the testing samples and prediction samples. The results of the two dimension reduction methods quantitatively confirm the same conclusion draw in Figure. 3.

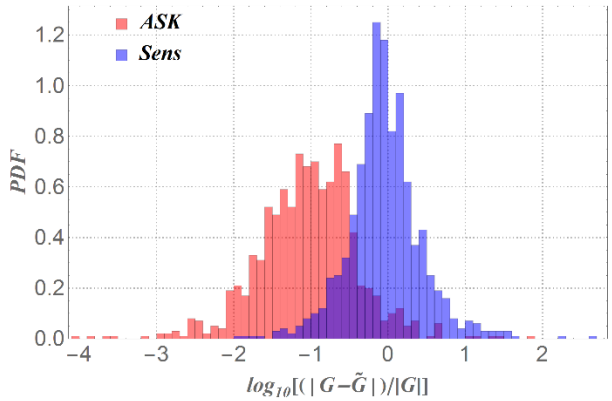

Figure 3: Histogram of the log of the relative error in the testing data for kriging

The trained kriging metamodel is used to provide nearly free simulation points for reliability analysis. By adopting PDEM, we can easily capture the PDF and CDF of the extreme value with 1000 extra simulations provided by kriging metamodel. The ASK method is compared with the 10000 trials of MCS, 50 trials of MCS and the sensitivity analysis method. The results in Figure. 4 and Table 1 verified the feasibility and effectiveness of the proposed method.

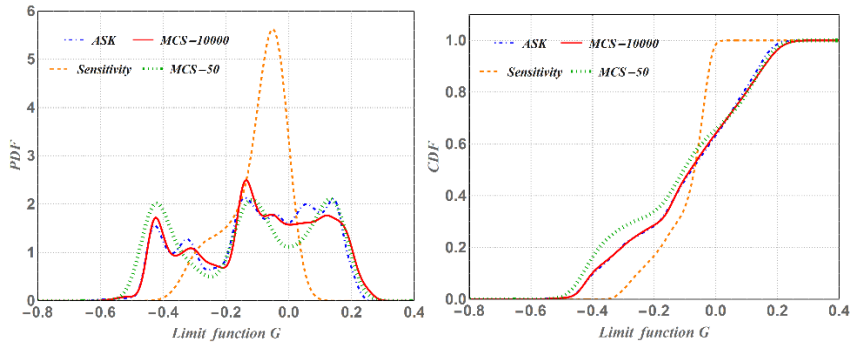

(a) PDF (b) CDF

Figure 4: Comparison of the PDFs and CDFs

Table 1: Comparison of ASK method (number of calls to model is 50) with 10000 trials of Monte Carlo Simulation, 50 trials of Monte Carlo Simulation and the sensitivity analysis (number of calls to model is 50)

Method		K-L distance	Reliability probability	Relative error	Computational time(s)
MCS	10000 trials	-	35.99%	-	0.4056
	50 trials	0.0738	28.95%	19.57%	0.0020
ASK		0.0253	36.85%	2.39%	0.2139
Sensitivity analysis		0.4531	16.85%	53.19%	0.1886

In Table 1, K-L (Kullback–Leibler) information distance is introduced as a quantitative index to evaluate the difference between two probability distribution functions. In Figure. 4, the poor performance of sensitivity analysis method indicates that too much information is lost in this coarse dimension reduction procedure. Although the result of 50 trials of MCS is better than sensitivity analysis method, the simulation limit made it hard to capture the topological characteristics of PDF, particularly when the PDF shows strong multimodality. In general, ASK method reach a good balance between the computational efficiency and accuracy. Compare to the result of 10000 trials of MCS, AKS method exhibit a competitive result with only 50 trials.

Although the computational time of sensitivity analysis method is slightly less than AKS method (12% less), but this can be ignored based on the huge sacrifice on the computational error (22 times). In general, compare to the direct Monte Carlo simulation, ASK method significantly improve the computational efficiency and maintains the high accuracy. As the structural model complexity grows higher, the advantages of ASK will become more distinct.

3 Concluding remarks

This paper presents an Active Subspace Kriging (ASK) method combing with the probability density evolution method (PDEM) to solve high dimensional structural reliability problem. The proposed method can reduce the difficulties in deal with high dimension problem and achieve a tradeoff between calculation accuracy and computational efficiency. A series system with four branches is studied to prove the proposed method is of high accuracy and efficiency. With only 50 calls to the numerical model in both examples, the ASK method shows better performance compare to the control group of methods. Two different dimension reduction method are illustrated in the numerical example, showing that incorrect dimension reduction can lead to invalid kriging regression.

Accordingly, some issue need to be further studied. For instance, a more accurate gradient approximation method can be used in the method. Besides, the minimum number of calls to the numerical model for excavating reliable active subspace is waiting to be studied. The application of ASK method in overcoming high dimension issue in optimization problem is an ongoing investigation.

4 References

Bourinet, J-M, François Deheeger, and Maurice Lemaire. 2011. "Assessing small failure probabilities by combined subset simulation and support vector machines." Structural Safety no. 33 (6):343-353.

Chowdhury, Rajib, BN Rao, and A Meher Prasad. 2009. "High-dimensional model representation for structural reliability analysis." Communications in Numerical Methods in Engineering no. 25 (4):301-337.

Constantine, Paul G. 2015. Active subspaces: Emerging ideas for dimension reduction in parameter studies. Vol. 2: SIAM.

Ghanem, Roger, and Pol D Spanos. 1990. "Polynomial chaos in stochastic finite elements."

Kaymaz, Irfan. 2005. "Application of kriging method to structural reliability problems." Structural Safety no. 27 (2):133-151.

Kleiber, Michał, and Tran Duong Hien. 1992. The stochastic finite element method: basic perturbation technique and computer implementation: Wiley.

Li, Jie, and Jianbing Chen. 2009. Stochastic dynamics of structures: John Wiley & Sons.

Lophaven, Søren Nymand, Hans Bruun Nielsen, and Jacob Søndergaard. 2002. "DACE-A Matlab Kriging toolbox, version 2.0."

Papadrakakis, Manolis, Vissarion Papadopoulos, and Nikos D Lagaros. 1996. "Structural reliability analyis of elastic-plastic structures using neural networks and Monte Carlo simulation." Computer methods in applied mechanics and engineering no. 136 (1-2):145-163.

Pianosi, Francesca, Fanny Sarrazin, and Thorsten Wagener. 2015. "A Matlab toolbox for global sensitivity analysis." Environmental Modelling & Software no. 70:80-85.

Russi, Trent Michael. 2010. Uncertainty quantification with experimental data and complex system models, UC Berkeley.

Schuëller, GI, HJ Pradlwarter, and Phaedon-Stelios Koutsourelakis. 2004. "A critical appraisal of reliability estimation procedures for high dimensions." Probabilistic engineering mechanics no. 19 (4):463-474.

Schueremans, Luc, and Dionys Van Gemert. 2005. "Benefit of splines and neural networks in simulation based structural reliability analysis." Structural safety no. 27 (3):246-261.

Vitali, Roberto. 2000. Response surface methods for high dimensional structural design problems: University of Florida Gainesville, FL, USA.

Joshua I. Weinstein, “The Market in Plato’s *Republic*,” *Classical Philology* 104 (2009): 440.

International Symposium on Reliability of Multi-disciplinary Engineering Systems under Uncertainty (ISRMES2019), 8-11 December 2019, Taipei
Chen, S. S. & Ang, Alfredo. H-S. (Editors)

NUMERICAL STUDIES ON THE PROBABILITY OF TRUE DAMAGE DETECTION FOR BUILDINGS UNDER UNCERTAIN SOIL PROPERTIES AND MEASUREMENT NOISES

Jun-Yang Shi[1]
[1] Taiwan Building Technology Center, National Taiwan University of Science and Technology, Taipei, Taiwan
E-mail: jyshi@mail.ntust.edu.tw

Abstract: Buildings are a significant part of civil infrastructure, which may experience natural hazards over their lifespan. The natural hazards imposed to building structures make it increasingly important to monitor structural health in a longer lifetime period. Several methods have been developed on global condition assessment for structures in recent years. This paper aims to investigate the effectiveness of three vibration-based damage detection (VBDD) methods for building structures embedded in soil through numerical studies. The effects of uncertain soil rigidies and simulated measurement noises on the detection probability of the VBDD methods are also studied. The numerical results show that the soil rigidities considerably influence the effectiveness of the damage detection methods due to dynamic soil-structure interaction. In addition, the increasing measurement noises are found to not only significantly reduce the mean detection probability but also enlarge the variation of the detection probability for all three methods used in this study. Therefore, the impacts of soil uncertainties and measurement noises shall be well considered in the development of robust health monitoring methods for building structures.

Keywords: damage assessment, detection probability, vibration, soil-structure interaction

1 Introduction

To ensure the safety of important civil infrastructures, several methods have been developed on continuous monitoring, damage detection, and global condition assessment for those structures. Meanwhile, vibration-based damage detection (VBDD) methods have been rapidly developed in the last few decades, which investigate changes in the dynamic responses (such as natural frequencies, mode shapes and modal damping) of structures to detect, localize and quantify structural damage. The developments of VBDD methods have been reviewed in the recent study by Farrar and Worden (2012). Recently, several VBDD methods (Sampaio et al, 1999.; Maia et al., 2003; Ratcliffe, 2000; Liu et al., 2009) have been developed by using frequency response function (FRFs) without the need of any modal identification process. The FRF-based method uses measured actual data for damage detection, which represents a considerable advantage in comparison to the mode-shape-based methods. Sampaio et al. (1999) used the curvature of FRF shapes to develop a damage index to find damage locations in the simulated and experimental beams. They found that the damage detection method based on the curvature of FRF shapes performed better than that based on the modal curvature. Liu et al. (2009) presented a scheme of using FRF shapes and FRF curvatures for damage localization. By applying the proposed scheme to a simulated cantilever beam, they found that the consideration of the imaginary part of FRF shapes and normalization of FRF before comparison can effectively improve the accuracy of damage detection. Researchers have also developed damage identification algorithms to directly analyze the FRFs of structures by using advanced techniques such as substructure-based approach (Lin et al., 2012), principal component analysis

(Bandara et al., 2014) and signal process technique (Lee and Eun, 2015). It seems that significant efforts have been devoted to developing VBDD methods by analyzing the curvature changes of the dynamic responses. The existing analytical and experimental studies also clearly demonstrated that either the modal curvature or the curvature of FRFs can be deemed as a good indicator of damage localization in beam-like structures on a rigid base. In engineering practice, the soil rigidity can affect the dynamic response of the buildings through the dynamic soil-structure interaction for general building structures. However, most of recent studies have paid less attention to study the effect of the soil rigidity on the performance of damage detection methods. Besides, in the structural health monitoring process, the measurement data are frequently contaminated by noise due to test environment and electronic devices. It is unavoidable to explore the structural damage with noise-polluted data in engineering practice. Therefore, this study aims to investigate the effectiveness of three VBDD methods on the damage localizations in a multi-story building embedded in a soil medium through numerical studies. The effects of uncertain soil rigidities and measurement noises on the detection probability of the VBDD method are further considered in conducted numerical simulations.The impacts of the soil uncertainties and measurement noise on the effectiveness and robustness of the VBDD methods are to be investigated in this study.

2 Vibration-based damage detection methods

In recent years, a few VBDD methods have been developed using the frequency response function (FRF) without the need of any modal identification techniques. Those methods directly used measured raw data for damage detection, which may represent a considerable advantage in comparison to the mode-shape-based methods. The FRF-based damage detection methods investigate the variations of FRF for all frequencies in the measurement range rather than just modal frequencies. There are three existing FRF-based methods used in this study and the brief concept for each method is given in the following subsections.

2.1 FRF curvature method

Sampaio et al. (1999) proposed the FRF curvature method to detect the damage location by finding at which the maximum of a damage index occurs. The damage index is defined as follows.

$$S_j = \sum_i \left(\Delta\kappa_j\right)_i, \qquad \Delta\kappa_j = \left\| \kappa_j^H - \kappa_j^D \right\| \tag{1}$$

where κ_j represent the curvature of FRF shapes at location j; the subscripts H and D denotes the healthy state and damaged state of the structure; and $(\Delta\kappa)_i$ represents the change of the curvature corresponding to the i-th forcing frequency. The curvature of FRF shapes are just calculated by using central difference method.

2.2 FRF-based damage index method

Maia et al. (2003) presented the FRF-based damage index method to find the damage location which has the maximum of the normalized damage index in terms of the curvature of FRF shapes, as shown below.

$$FRF\_DI_j = \sum_i \left(\beta_j\right)_i, \quad \beta_j = \frac{\left[\left(\kappa_j^D\right)^2 + \sum_j \left(\kappa_j^D\right)^2\right] \sum_j \left(\kappa_j^H\right)^2}{\left[\left(\kappa_j^H\right)^2 + \sum_j \left(\kappa_j^H\right)^2\right] \sum_j \left(\kappa_j^D\right)^2} \tag{2}$$

In above equation, the central difference method was also used to evaluate the curvature of FRF shape.

2.3 Advanced FRF curvature method

The previous work of the authors (Chen et al., 2019) proposed an interpolation method to evaluate the curvature of mode shapes and FRFs of a building-soil system. The interpolated displacement function employed a cubic polynomial function while the coefficients of the function are determined by considering appropriate continuity and boundary conditions. The curvature of the displacement FRF functions can be then evaluated at continuous locations. To develop an advanced FRF curvature method for damage detection, the previous work further presented a new damage indicator using continuous curvatures of the displacement FRF functions. The damage indicator evaluated the changes of the curvature at each story for the building structure staying between the healthy and damaged state, as shown below.

$$DI_j = \sum_i \left(\int_0^{h_j} \left| \kappa_j^H - \kappa_j^D \right|^2 dz \right)_i \tag{3}$$

where $_j$ denotes the curvature function of the displacement FRF within the *j*-th story and h_j indicates the story height. The curvature function is computed by finding the second derivate of the cubic polynomial function, i.e.,

$$\kappa(z) = 6az + 2b \tag{4}$$

where *z* denotes the distance measured from the floor level; *a* and *b* represents the coefficients of the cubic polynomial function used to interpolate the displacement FRFs at each floor level (Chen *et al.*, 2019).

3 Results and discussions

This study carries out numerical simulations to investigate the detection probability of all three damage detection methods illustrated in previous section. Consider a 10-story shear structure embedded in a uniform soil medium. The modeling parameters for the upper structure, foundation and the soil medium are listed in Table 1. Notice that the shear-wave velocity of soil affecting the soil rigidity is simulated as a random variable within a log-normal distribution. This study analyzes one of the most common damage scenarios which simulate the damaged base floor having a 10% stiffness loss. The damage scenario is designed to model the change in the lateral stiffness of the damaged story as a percentage reduction of the undamaged one. A computer program SASSI developed by Lysmer *et al.* (1981) is used in this study to analyze the displacement FRF for the considered building-soil structure subjected to harmonic excitations in horizontal direction. The damage indicators are then calculated using the curvatures of the FRFs analyzed from SASSI. In addition, the effect of simulated noise on the damage localization results is also investigated in this section. Because of the complex vibration measurement, any

single type of random noise may be experienced in the field. For simplicity, this study uses uniform errors with zero mean to simulate the measurement noise. In consideration of the building-soil system, each FRF shape is assumed to have a constant signal-to-noise ratio (SNR) as a result of adding a series of uniformly distributed random numbers to the displacement amplitudes analyzed from SASSI. The SNR is defined as a ratio of signal power to noise power (Vaseghi, 2008), which is often expressed in the logarithmic decibel scale as follows:

$$SNR = 10Log_{10}\left(\frac{A_{signal}}{A_{noise}}\right)^2 \tag{5}$$

where A represents the root mean square (RMS) amplitude. This study considers simulation cases with different SNRs which are 40, 30, 20 and 14 dB. For each SNR, there are 10^4 simulation runs to be conducted in this study. Notice that as the SNR lower as the noise stronger. The numerical results are shown later to examine the accuracy of the three FRF-based VBDD methods for the considered building-soil system.

Table 1. Parametric values of the building-soil model

Simulation zone	Modeling parameter	Simulation value
Upper structure	Story mass	100 Mg
	Story stiffness	100,000 kN/m
	Story height	3 m
Foundation	Dimension	20 m × 20 m
	Embedment depth	10 m
	Foundation mass	1000 Mg
Soil medium	Poisson's ratio	0.33
	Shear-wave velocity	Random variable
	Material density	2 Mg/m^3

Figures 1-3 show the mean value and coefficient of variation (COV) for the detection probability using three methods under the uncertain shear-wave velocity of soil (V_s) and the simulated random noise. The COV of the shear-wave velocity are considered as 0.1, 0.2, and 0.3, respectively. The detection probability is defined as a ratio of the total counts of successful damage localization to the total number of simulation runs. Observe that the advanced FRF curvature method shows a higher mean detection probability and a much lower COV as compared with the two existing methods. For the noise level with a SNR higher than 20 dB, the advanced method is also found to give a considerably lower COV as compared with the FRF curvature method. In addition, the COV of detection probability using the advanced FRF curvature method is remarkably less than the COV of the shear-wave velocity (input source). In contrast, the COV of detection probability using the other two methods could be significantly greater than the COV of the input source even though zero simulated noise is considered. Besides, the probability distribution of detected floor using the three methods is displayed in Figure 4. The predication results of the advanced method are found to primarily localize at the first two floors; however, that of the other two methods seem to have a quite flat distribution ranging from the second to the top floors. Hence, the results imply that the advanced FRF curvature method provides more robust damage localization in successful predictions than the two existing methods when applying to building-soil systems under uncertain soil rigidities and

random measurement noise.

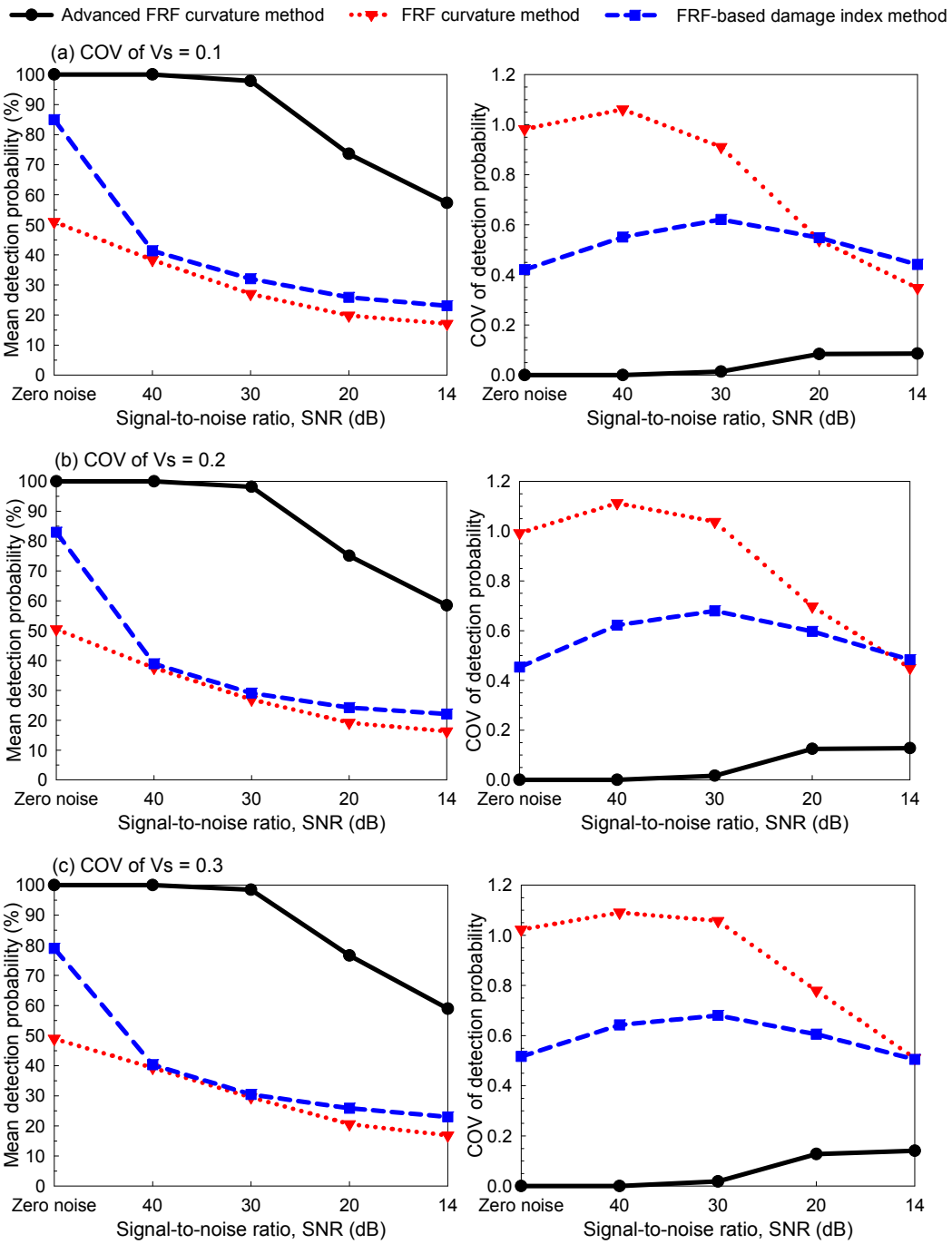

Figure 1. Mean value and COV of the detection probability using thress damage deteciton methods

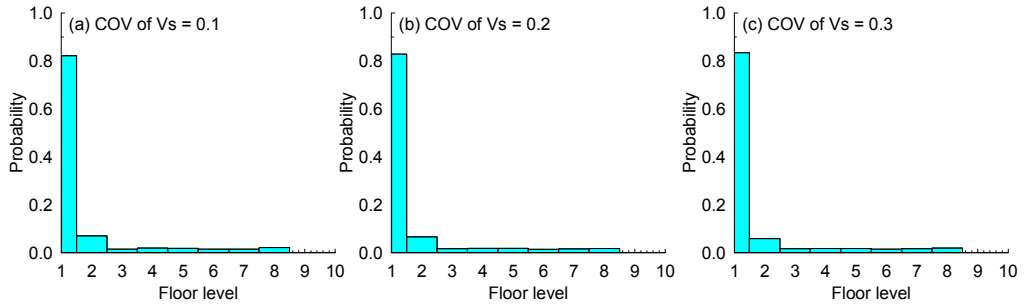

Figure 2. Probability distribution of detected floor using the advanced FRF curvature method

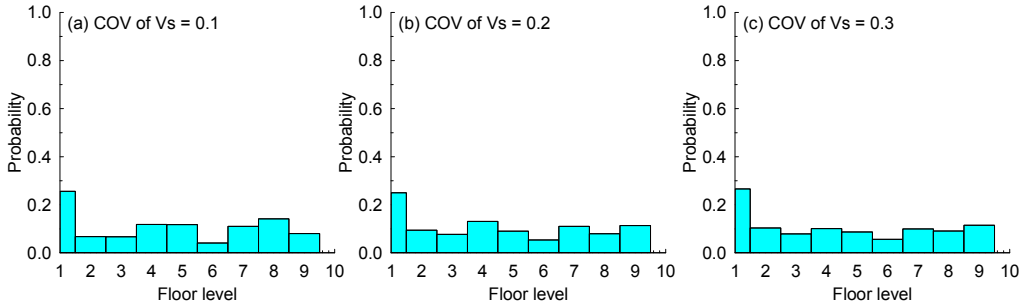

Figure 3. Probability distribution of detected floor using the FRF curvature method

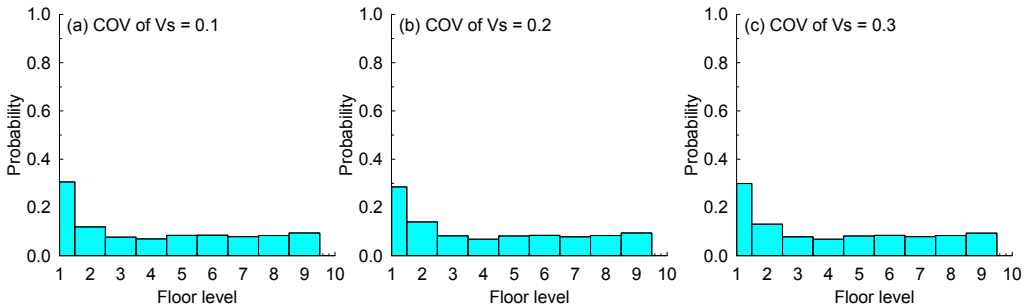

Figure 4. Probability distribution of detected floor using the FRF-based damage index method

4 Conclusions

This paper conducts a numerical study to investigate the correct probability of three vibration-based damage detection methods for a multi-story building embedded in soil. The effects of uncertain soil rigidities and measurement noises on the detection probability are simultaneously considered in numerical simulations. The results show that the mean detection probability using existing methods could be reduced by the combined impacts through the soil uncertainties and measurement noise. In addition, the increasing noise levels are found to not only significantly reduce the mean detection probability but also enlarge the variation of the detection probability with certain level for all three methods considered. Finally, it is also noted that the advanced FRF curvature method proposed in the previous work provides more robust damage

localization in successful predictions than the two other methods considered in this work.

5 References

Bandara, R.P., Chan, T.H., and Thambiratnam, D.P., "Frequency Response Function Based Damage Identification Using Principal Component Analysis and Pattern Recognition Technique," *Engineering Structures* 66 (2014): 116-128.

Building Seismic Safety Council. *NEHRP Recommended Provisions for Seismic Regulations for New Buildings and Other Structures and Accompanying Commentary and Maps*, FEMA 450, 2003.

Chen, S. S., Shi, J. Y., and Wu, Y. Y., "Numerical damage localisation for building systems including dynamic soil-structure interaction," *Structure and Infrastructure Engineering* 15 (2019): 362-375.

Farrar, C. R., and Worden, K. *Structural Health Monitoring: A Machine Learning Perspective*. John Wiley & Sons, 2012.

Lee, E.T., and Eun, H. C., "Damage Detection of Steel Beam Using Frequency Response Function Measurement Data and Fractal Dimension," *Journal of Vibration and Acoustics* 137 (2015): 034503.

Lin, T.K., Hung, S.L., and Huang, C.S., "Detection Of Damage Location Using A Novel Substructure-Based Frequency Response Function Approach with A Wireless Sensing System," *International Journal of Structural Stability and Dynamics* 12 (2012): Paper 1250029.

Liu, X., Lieven, N.A.J., and Escamilla-Ambrosio, P.J., "Frequency Response Function Shape-Based Methods For Structural Damage Localisation," *Mechanical Systems and Signal Processing* 23 (2009): 1243-1259.

Lysmer, J., Tabatabaie-Raissi, M., Tajirian, F., Vahdani, S. and Ostadan F. *SASSI: A System For Analysis of Soil-Structure Interaction Problems*. University of California, Berkeley, US, 1981.

Maia, N.M.M., Silva, J.M.M., Almas, E.A.M., and Sampaio, R.P.C., "Damage Detection In Structures: From Mode Shape To Frequency Response Function Methods," *Mechanical Systems and Signal Processing* 17 (2003): 489-498.

Ratcliffe, C.P., "A Frequency And Curvature Based Experimental Method For Locating Damage In Structures," *Journal of Vibration and Acoustics* 122 (2000): 324-329.

Sampaio, R.P.C., Maia, N.M.M, and Silva, J.M.M., "Damage Detection Using The Frequency-Response-Function Curvature Method," *Journal of Sound and Vibration* 226 (1999): 1029-1042.

Vaseghi, S. V. *Advanced digital signal processing and noise reduction*. John Wiley & Sons, 2008.